CHARACTERIZATION OF LINEAR FRICTION WELDED IN-SERVICE INCONEL 718 SUPERALLOY

by

Mathew MacMaster Smith

A THESIS SUBMITTED IN PARTIAL FULFILLMENT OF
THE REQUIREMENTS FOR THE DEGREE OF

DOCTOR OF PHILOSOPHY

in

THE COLLEGE OF GRADUATE STUDIES

(MECHANICAL ENGINEERING)

THE UNIVERSITY OF BRITISH COLUMBIA
(OKANAGAN)

April 2017

The undersigned certify that they have read, and recommend to the College of Graduate Studies for acceptance, a thesis entitled:

Characterization of Linear Friction Welded In-Service Inconel 718 Superalloy

submitted by **Mathew MacMaster Smith** in partial fulfillment of the

requirements of the degree of **Doctor of Philosophy in Mechanical Engineering**.

Dr. Lukas Bichler, School of Engineering, Mechanical Engineering - Materials

Supervisor, Professor (please print name and faculty/school above the line)

Dr. Dimitry Sediako, School of Engineering, Mechanical Engineering - Materials

Supervisory Committee Member, Professor (please print name and faculty/school in the line above)

Dr. Ray Taheri, School of Engineering, Mechanical Engineering

Supervisory Committee Member, Professor (please print name and faculty/school in the line above)

Dr. Dwayne Tannant, School of Engineering, Civil Engineering

University Examiner, Professor (please print name and faculty/school in the line above)

Dr. Myriam Brochu, Ecole Polytecnique de Montreal

External Examiner, Professor (please print name and university in the line above)

April 26, 2017

(Date Submitted to Grad Studies)

Additional Committee Members include:

(please print name and faculty/school in the line above)

(please print name and faculty/school in the line above)

Abstract

The focus of this thesis was to study the suitability of the linear friction welding (LFWing) process to manufacture or repair of Inconel® 718 superalloy (IN 718) aero engine BLISKs. This was achieved by simulating a LFW joint made of virgin (V) and in-service (IS) (from samples extracted from an actual turbine disk) IN 718 material.

An in-depth microstructural characterization of the V and IS material in the as-received, as-welded and post weld heat treated (PWHT) conditions was carried out. Quantitative analysis of the phase constituents, such as the δ phase, MC-type carbides, MN-type nitrides and the γ grain size of the as-welded and PWHT samples was performed using electron backscattered diffraction (EBSD), scanning electron microscopy (SEM) and energy dispersive spectroscopy (EDS) analyses. Mechanical testing also revealed that variation in the γ grain size, as well as the distribution and the volume fraction of the precipitates had a significant impact on the alloy's hardness and tensile properties. Defect analysis of the as-welded samples revealed that the weld interface was free of oxides, voids, contamination and liquation of secondary phases (e.g., carbides and Laves phases). Grain refinement of the γ grains was observed at the weld interface and was related to the occurrence of dynamic recrystallization during the LFWing process.

Quantitative analysis of the residual strains and stresses in the as-received, as-welded and PWHT samples was achieved using the neutron diffraction technique. The results revealed that careful selection of the beam gauge volume and stress-free lattice spacing were essential for accurate stress analysis. The results suggested the residual stress increased in magnitude from the base metal and reached a peak at the weld interface. The peak magnitudes of the residual stresses were below the yield strength of IN 718. The results of

this work are of significant importance when developing manufacturing and repair processes for IN 718 material components.

Preface

Parts of Section 4.1 were published in an international conference proceeding: M. Smith, L. Bichler, S. Yannacopoulos, J. Gholipour and P. Wanjara, "Characterization of in-service and virgin Inconel 718 superalloy," in 2014 *Conference of Metallurgists*, Vancouver, 2014. I was responsible for the analysis of IN 718 as-received samples, including sample preparation, data acquisition and interpretation. I was also responsible for writing the manuscript, including drafting/editing and revising at all stages of the writing process. My co-author and principal supervisor Dr. Lukas Bichler and Dr. Spiro Yannacopoulos from the School of Engineering, UBC, were involved in editing the manuscript. Dr. Javad Gholipour Baradari and Dr. Priti Wanjara from NRC-Aerospace were responsible for LFWing of the IN 718 samples and editing the manuscript.

Also, parts of Section 4.1 were published as a refereed journal article: M. Smith, L. Bichler, J. Gholipour and P. Wanjara, "Mechanical properties and microstructural evolution of in-service Inconel 718 superalloy repaired by linear friction welding," *International Journal of Advanced Manufacturing*, [Available Online] http://dx.doi.org/10.1007/s00170-016-9515-2. I was responsible for the analysis of IN 718 as-welded and PWHT samples, including sample preparation, PWHTing of the as-welded samples, data acquisition and interpretation. I was also responsible for writing the manuscript, including drafting/editing and revising at all stages of the writing process. My co-author and principal supervisor Dr. Lukas Bichler from the School of Engineering, UBC was involved in editing the manuscript. Dr. Javad Gholipour-Baradari and Dr. Priti Wanjara from NRC-Aerospace were responsible for LFWing of the IN 718 samples and editing the manuscript.

Parts of Chapter 5: were published as a refereed journal article: M. Smith, J.-B. Levesque, L. Bichler, D. Sediako, J. Gholipour and P. Wanjara, "Residual stress analysis in linear friction wedled in-service Inconel 718 superalloy via neutron diffraction and contour method approaches," *Material Science and Engineering A*, 2017 as well as included in an international conference proceeding: M. Smith, L. Bichler, J. Gholipour and P. Wanjara, "Measurement of residual stresses in linear friction welded in-service Inconel 718 superalloy," in Thermec 2016, Graz, 2016. I was responsible for the analysis of IN 718 as-received, as-welded and PWHT samples, including sample preparation, PWHTing of the as-welded samples, data acquisition and interpretation. I was also responsible for writing the manuscript, including drafting/editing and revising at all stages of the writing process. My co-author and principal supervisor Dr. Lukas Bichler from the School of Engineering, UBC was involved in editing the manuscript. Dr. Javad Gholipour and Dr. Priti Wanjara from NRC – Aerospace were responsible for LFWing of the IN 718 samples and editing the manuscript. My co-supervisor Dr. Dimitry Sediako from the School of Engineering, UBC (formally employed at the Canadian Neutron Laboratories) assisted with the neutron diffraction experiments as well as with editing of the manuscript. Jean-Benoît Lévesque from Quebec Hydro was responsible for performing the contour method analysis and editing of the manuscript.

Table Of Contents

List of Tables

List of Figures

Nomenclature

Symbol	Definition	Units
d	Lattice spacing	m
d_0	Stress free lattice spacing	m
E	Young's modulus	GPa
E_{hkl}	Young's modulus for a particular family of planes	GPa
G	Shear modulus	GPa
T_m	Bulk material melting temperature	°C

Greek Symbol	Definition	Units
ε	Strain	
σ	Stress	MPa
ν	Poisson's Ratio	

Term	Definition
As-Received	As-received material obtained from a commercial supplier of superalloy materials.
Base Material	Unaffected material in LFWed samples.
Diffusion	The process by which atoms move through a solid, liquid or gas.
Dissolution	The process by which solids, liquids or gasses become solutes (dissolved components) in another compound (solid, liquid or gas).
Error	95% confidence interval (C.I.), which states that there is a 0.95 probability that the true average will be within the given range.
MC-Type Carbide	Carbides where the metal element "M" can be titanium, tantalum, niobium, hafnium, thorium or zirconium.
MN-Type Nitride	Nitrides where the metal element "M" can be titanium, niobium or zirconium.
Uncertainty	The variation in calculating strains based on the peak positions, which are determined by how well the data is fitted by the Gaussian curve.
Weld Affected Region	Area of a welded sample that has a perceptible microstructural change (from the initial material's microstructure) due to the application of heat and pressure from the welding process.
Weld Interface	The point corresponding to $x = 0$ along the x-direction where the two welded materials meet.

Acronym	Definition
AR	As-received (material in the as-received condition)
BM	Base Material (Unaffected material in LFWed Samples)
BLISK	***Bl***ade + d***isk*** (blade and disk as a single component)
CFW	Continuous Drive Friction Welding
CTE	Coefficient of Thermal Expansion
CNBC	Canadian Neutron Beam Centre
DB	Diffracted Beam
DRX	Dynamic Recrystallization
EBSD	Electron Back-Scattered Diffraction
FEG-SEM	Field Emission Gun Scanning Electron Microscope
FSW	Friction Stir Welding
FWHM	Full Width Half Maximum
FZ	Fusion Zone
HAZ	Heat Affected Zone
IFW	Inertia Friction Welding
IR	Infrared
IS	In-Service Material
LFW	Linear Friction Welding
ND	Neutron Diffraction
PMZ	Partially-melted Zone
PWHT	Post Weld Heat Treatment
SAC	Strain Age Cracking
SEM	Scanning Electron Microscope
ST	Solution Treatment
STA	Solution Treatment and Direct Aging
ST + DA	Solution Treatment and Double Aging
TMAZ	Thermomechanically Affected Zone
UTS	Ultimate Tensile Strength
V	Virgin Material
YS	Yield Strength

Acknowledgements

I am profoundly grateful to my principal advisor Dr. Lukas Bichler for his continual guidance and perspective on various aspects that greatly assisted in the completion of this work as well as his tireless efforts to support not only my research but also my own well being. His kindness and positive attitude made this project a very enjoyable learning experience and I am truly thankful I had the opportunity to work with him as part of my academic career. I am also deeply appreciative to Dr. Bichler for providing the funding to support all aspects of this research. I would also like to thank my co-advisor Dr. Dimitry Sediako for his tireless efforts and assistance in acquiring the neutron diffraction data at the Canadian Nuclear Laboratories located in Chalk River, Ontario.

I would also like to thank Dr. Priti Wanjara and Dr. Javad Gholipour and the technical staff at the National Research Council of Canada - Aerospace located in Montreal, Quebec for providing the in-service material and the facilities to weld the samples used in this work. Without the support they provided, this work would not have been possible

I would also like to thank Dr. Jonathan Durocher and StandardAero for their support and guidance to ensure this work reflected actual industry practices. I would also like to acknowledge the financial support by the National Science and Engineering Research Council of Canada (NSERC) provided through the Engage Grant funding program.

I am grateful for the assistance received by the Michelle Tofteland, David Arkinstall and Durwin Bossy at The University of British Columbia - Okanagan for equipment training and assistance with various aspects of this project. In addition, I would also like to thank Alan Machin at Ryerson University who performed the tensile tests in this work.

Finally I would like to thank my parents, for their continued support throughout my university career, and God for giving me the patience, knowledge and understanding required to see this project through to completion.

To my Mom and Dad

Chapter 1: Introduction

Inconel® 718 (a.k.a. Alloy 718 or IN 718) superalloy is commonly used in high temperature applications, such as compressor/turbine blades, hot liner cowling and vane/disk material in jet engines and in some specialty components for space applications (e.g., space shuttle flow liners) due to its excellent high temperature strength and corrosion resistance [*1*] [*2*] [*3*]. The superior high temperature mechanical and chemical properties of IN 718 are attributable to the alloy's complex composition and microstructure.

The nickel (Ni) - Iron (Fe) - Chromium (Cr) based IN 718 alloy contains strengthening precipitates (~15 % volume fraction [*4*]) in the form of metastable body centered tetragonal (bct) γ'' (stoichiometry Ni_3Nb) and a small quantity (~4 % volume fraction [*4*]) of face centered cubic (fcc) γ' (stoichiometry $Ni_3(Al,Ti)$) in the fcc γ matrix [*1*] [*5*]. During long-term exposure to elevated temperatures, the metastable γ'' phase transforms into the stable orthorhombic δ phase. The δ phase (stoichiometry Ni_3Nb), in addition to MC-type carbides and MN-type nitrides precipitate primarily at the grain boundaries, where they act as grain refiners and contribute to enhancing the material's creep strength at elevated temperatures through grain boundary pinning [*1*] [*5*]. However, high volume fractions of the δ phase have been shown to decrease the potential mechanical properties of the alloy [*6*] [*7*]. Additional alloying elements (e.g., Co, Mo and Fe) strengthen the material through solid solution hardening, while Cr provides oxidation and corrosion resistance through the formation of passive oxide films (e.g., Cr_2O_3) when IN 718 is exposed to elevated temperatures [*5*] [*8*].

The thermal and mechanical processes and environments have an important effect on the microstructure and mechanical properties of the alloy. The specific characteristic of the microstructure is of critical importance when considering various manufacturing and repair

processes, such as welding of the IN 718 alloy. Undesirable or uncontrolled variation in the microstructure may facilitate detrimental phase changes and high residual stresses leading to cracking during manufacturing, repair or service.

Recently, IN 718 has been considered for creating BLISKs for aero engines, where the blade and disk are integrated into a single part, thereby reducing the material and overall engine weight [*9*]. BLISKs are fabricated from a single forged/machined part or by welding blades directly onto the disk material, as shown in Figure 1 [*9*] [*10*].

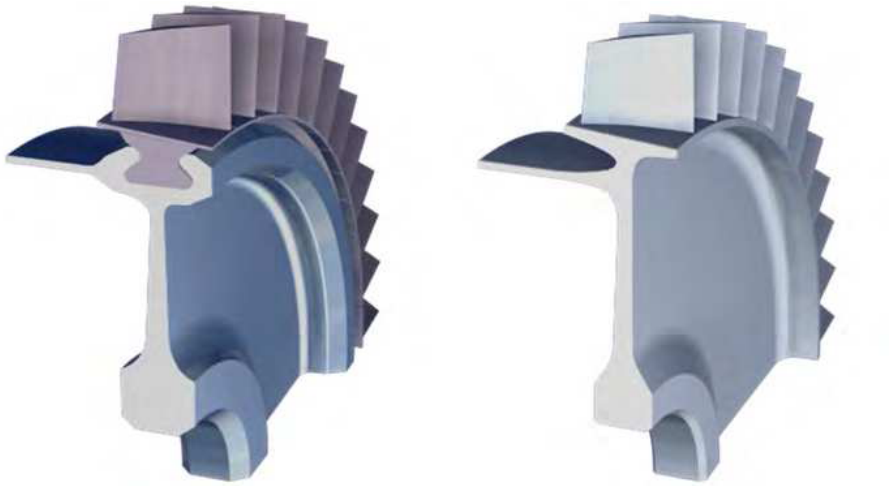

Figure 1: Aero engine turbine/compressor: Left – Traditional blade & disk assembly. Right – New BLISK component [*10*]. (© 2011 Antonio M. Mateo Garcia. Originally published in A. Mateo Garcia, "BLISK fabrication by linear friction welding," *Advances in Gas Turbine Technology*, pp. 411-434, 2011. Under CC BY 3.0 license. Available from DOI: 10.5772/21278.)

Traditionally, the manufacturing of new BLISKs was done using conventional welding methods (e.g., TIG, electron beam, etc.). However, more recent developments have trended towards the use of solid-state welding techniques, such as inertia friction or linear friction welding (LFWing) in an effort to reduce the number of defects associated with traditional welding techniques [*10*].

In order for LFWing to be used as an approved and certified method to repair IN 718 BLISKs, extensive characterization regarding the effect of the welding process on the

superalloy's mechanical properties is required. This typically involves extensive experimentation on LFWed samples including: tensile, hardness, residual stress and oxidation tests to characterize how the microstructural changes that occur during the welding process influence the material's ability to perform under service conditions.

An advantage of friction welding (compared to fusion welding) is the elimination of cracking associated with the melting and solidification within the fusion zone (FZ) and partially melt zone (PMZ), which are created during fusion welding. Also, during friction welding, the lower processing temperatures (compared to fusion welding) eliminate solidification cracking [*11*] [*12*] [*13*]. Furthermore, the lower temperatures and the application of a compressive forging force results in short cycle times that produce a small heat affected zone (HAZ) and reduce the occurrence of post weld heat treatment (PWHT) cracking and liquation cracking [*11*]. Proper control of the weld parameters (such as oscillation/rotational speed, axial pressure, force duration, welding time, amplitude, frequency and burn off/upset distance), have allowed friction welding techniques to be able to join dissimilar metals, such as RR1000 and CMSX-4 [*14*] and Alloy 720Li and IN 718 [*15*] successfully, in addition to difficult to weld superalloys RR1000 [*16*] [*17*] [*18*] [*19*], WASPALOY [*20*] [*21*], IN 738 [*22*], Alloy 720Li [*19*], CMSX-486 [*23*], as well as commonly used superalloys IN 718 [*19*] [*24*] [*25*] [*26*] [*27*] and aerospace grade Ti-alloys [*28*] [*29*].

The ability to weld many commonly used aerospace alloys with minimized occurrence of defects is of particular interest to aerospace manufactures and repair industries. Also, since no shielding gas, fumes, radiation or electrical hazards are present, friction welding is considerably safer for the operator [*10*] [*12*].

The attractiveness of friction welding processes to the aerospace industry compared to other fusion welding techniques stem from the following:

1) Cracking associated with melting the metal is eliminated, and other weld defects (PWHT and liquation cracking) are minimized with proper control of weld parameters.
2) Joining of dissimilar and difficult to weld alloys is possible.
3) No special atmosphere or fluxes/filler materials are required.
4) Minimal material preparation, high reproducibility, high productivity (short cycle times) result in cost effective manufacturing and/or repair.

However, improper control of the friction welding process parameters (e.g., exceeding the optimum joining temperature), miss-alignment of the work pieces and/or contamination of the weld, often introduce defects and flaws into friction welds.

1.1 Scope of Research

The focus of the present research was on simulating the repair of an IN 718 BLISK using the LFWing process. This was achieved by welding in-service (IS) and virgin (V) IN 718 materials together. The work was carried out in partnership between The University of British Columbia (Kelowna, BC), the National Research Council of Canada – Aerospace (Montreal, PQ) and with industry partner StandardAero Ltd. (Winnipeg, MB), who provided consultation on current industry practices for repair of aero-engines.

This thesis focused on characterizing the microstructural changes and residual stresses that occur in IN 718 as a result of the LFWing process and subsequent heat treatment. Specifically, the objectives of this PhD thesis were to:

- Use LFWing to join in-service and virgin IN 718 material and study how the difference in initial material microstructure contributed to microstructure evolution and mechanical performance of the welded samples.
- Quantify residual stresses and strains in the welded and PWHT samples.

1.2 Originality and Novelty of Research

Due to the rarity of procuring IN 718 material that has been exposed to service conditions (in-service material) and removed from service prior to its end-of-life (or time expiration limit), there is currently no known literature on characterizing the microstructure of in-service or LFWed in-service IN 718 material. There is no known literature on the residual stress and strain comparison between in-service and virgin samples or on the residual stress and strains in LFWed (as-welded or PWHT) in-service material.

Chapter 2: Literature Review

The following chapter provides a literature review related to IN 718 superalloy and its processing and property attributes. Also, some background on friction welding and residual stress measurement using the neutron diffraction technique is provided.

2.1 Superalloys

After the creation of the first jet engine for use on the German ME 262 fighter jet, aero-engine materials continued to support a never-ending quest to improve engine power (thrust) and efficiency by enabling higher temperatures within the combustion chambers [*30*]. Material limitations became obvious as the ever-increasing combustion temperatures made the hot gas stream of jet engines a more aggressive environment for the components of the jet engine to operate in. In addition to the high temperatures, some hot gas stream components (e.g., turbine blades and disks) also need to withstand very high dynamic loads generated by the high rotational speeds during engine service (up to 150 000 rpm for small 'micro-turbines') [*31*], which often result in failure due to creep or thermomechanical fatigue of the engine components. Additionally, elevated temperatures (exceeding 500 °C) may also result in accelerated corrosion through hot corrosion or high temperature oxidation [*32*]. Therefore, selecting or designing a material for engine components heavily depends on the operating environment the component will experience during its service life. However, the following general design requirements must be considered for materials operating within a jet engine [*33*]:

1) High mechanical property stability at elevated temperatures: i.e., high strength, high resistance to creep and thermomechanical fatigue.

2) High chemical stability at elevated temperatures: i.e., resistance to hot corrosion and high temperature oxidation during initial exposure and continued protection during service.

Materials satisfying the above criteria are often called superalloys. Modern superalloys can maintain favorable strength, corrosion and creep resistance up to $0.9T_m$ (where T_m is the absolute melting temperature of the alloy in Kelvin) [*33*].

Typically, superalloys fall into one of three categories: (i) nickel-based, (ii) iron-based and (iii) cobalt-based [*5*]. The focus of this work is on nickel-based superalloys, which are solid solution strengthened due to high solubility of alloying elements in the stable fcc Ni based matrix [*5*] [*31*]. This high solubility allows substantial precipitate hardening, giving nickel-based superalloys excellent high temperature strength, corrosion resistance and creep resistance [*5*]. However, the final mechanical, chemical and thermal properties of any superalloy greatly depend on the presence and relative amounts of various alloying elements.

2.1.1 IN 718 Superalloy Composition

The following section outlines the main role of alloying elements that are commonly added to the IN 718 superalloy.

Nickel (Ni): Forms the matrix of the alloy and accounts for 40 – 60 wt% of the total alloy composition. Ni is used as the matrix phase, because it has a high solubility for solid strengthening elements (e.g., Co, Fe, Cr, Mo, Al, Ti and Ta) without creating phase instability during exposure to elevated temperatures. This stability is due to Ni's nearly full valence electron shell. Also, the solid solution strengthening elements create localized strain

fields within the Ni lattice, which interact and hinder dislocation motion, thus increasing the strength of the alloy [*5*].

Chromium (Cr): Chromium accounts for 17 – 21 wt% of the total alloy composition. Cr provides strength via solid solution strengthening of the matrix. Additionally, Cr provides moderate high temperature oxidation resistance for environments under 1000 °C. At temperatures above 1000 °C, the protective Cr_2O_3 layer vaporizes to become volatile CrO_3 [*5*] [*34*].

Iron (Fe): Iron accounts for 5 – 22 wt% of the total alloy composition. Fe improves the alloy's strength by solid solution strengthening of the matrix. Additionally, Fe aids in the precipitation of the bct coherent primary strengthening precipitate γ'' phase (Ni_3Nb) rather than the in-coherent orthorhombic δ phase [*5*].

Tantalum (Ta): Tantalum accounts for up to 12 wt% of the total alloy composition and is mainly included to enhance the strength of IN 718 by solid solution strengthening of the Ni matrix. Ta is also a strong former of MC type carbides, which reduce grain boundary sliding during exposure to elevated temperatures [*5*].

Niobium (Nb): Niobium accounts for 3.15 – 5.50 wt% of the total alloy composition. Nb is added to enhance IN 718's strength by forming the main strengthening precipitate γ'' (Ni_3Nb). The γ'' phase strengthens the alloy through high coherency strains between the precipitates and the matrix. In addition, Nb also forms the δ phase (Ni_3Nb), which does not inherently add strength to the alloy, but is present in small volumes to act as a grain refiner and to improve the creep resistance of the alloy by pinning the grain boundaries. Nb is also found in carbides and other intermetallic phases that can form in IN 718 depending on the exact composition and thermal history of the alloy [*5*]. Nb enrichment when the δ phase

dissolves and Nb segregates to the grain boundary may also be detrimental to IN 718, because the Nb can act as a melting point depressant. Therefore, enrichment of the grain boundaries with Nb may result in grain boundary liquation [*20*] [*24*].

Molybdenum (Mo): Molybdenum accounts for 2.80 – 3.30 wt% of the total alloy composition. Mo provides increased strength though solid solution strengthening of the matrix. Mo is also a strong carbide former (M_6C type), which reduces grain boundary sliding during exposure to elevated temperatures [*5*].

Titanium (Ti): Titanium accounts for 0.65 – 1.15 wt% of the total alloy composition and supports the formation of the secondary strengthening precipitate γ' phase [$Ni_3(Al,Ti)$] in IN 718. In addition, Ti can also form carbides and nitrides in IN 718, which reduces the grain boundary sliding during exposure to elevated temperatures [*5*].

Aluminum (Al): Aluminum accounts for 0.2 – 0.8 wt% of the total alloy composition. Al provides increased strength of IN 718, since it contributes to the formation of the coherent γ' phase [$Ni_3(Al,Ti)$] within the γ matrix [*5*].

Cobalt (Co): Cobalt accounts for up to 1.0 wt% of the total alloy composition. Co is included to enhance the precipitation of the γ' phase by reducing the solubility of the γ' forming elements like aluminum and titanium in the Ni matrix, thereby increasing the alloy's strength. Furthermore, Co raises the solvus temperature of the γ' phase, which increases the high temperature stability of the strengthening precipitate. Co also contributes to IN 718's strength directly by acting as a solid solution strengthening element [*5*].

Carbon (C): Carbon accounts for up to 0.08 wt% of the total alloy composition. C is included to enable the formation of carbides/carbonitrides at the grain boundaries. C can also help reduce grain boundary sliding through the formation of various carbides/nitrides/borides

[*35*] [*36*]. As a result, grain boundary strength and resistance to slip is increased, therefore improving the high temperature strength and creep properties of IN 718 [*5*]. However, the addition of B, C (and even Zr and Hf) also decreases the incipient melting temperature of the superalloy, thereby increasing the difficulty to fully solution heat treat engine components [*5*].

Other trace alloying elements such as manganese (Mn), phosphorus (P), sulfur (S) silicon (Si), boron (B) and copper (Cu) may be added to tailor IN 718's properties to meet specific mechanical, thermal or chemical properties for a given application. However, too much of these elements (for example S > 0.008 wt%, P > 0.025 wt% and B > 0.003 wt%) may cause fusion-zone cracking during welding. Therefore, judicious care must be taken to only add enough of these elements to grain the required beneficial properties without sacrificing the performance and manufacturability of the alloy [*37*].

2.1.2 IN 718 Superalloy Microstructure and Phases

The mechanical properties of superalloys depend on the microstructure and phases that form as a result of the material's manufacturing, service history (thermal and loading conditions) and composition. The following section outlines some of the major phases in the IN 718 superalloy. The microstructural features covered represent those that have a major influence on IN 718's mechanical properties and are responsive to thermal processes, such as heat treatments or mechanical processes that involve thermal gradients, like welding.

The IN 718 superalloys have alloying elements partition to one or more of the following phases:

Gamma Matrix (γ): A nickel based continuous phase (fcc) that contains high concentrations of solid-solution elements (Co, Fe, Cr, Mo, Al, Ti and Ta). The solid solution strengthening elements occupy substitutional sites (vacancies) within the Ni lattice and create localized strain fields within the matrix. The solute induced strain fields hinder dislocation motion, thus resulting in increased strength of the IN 718 superalloy [*5*] [*35*] [*38*].

Gamma Prime (γ′): A coherent strengthening precipitate formed upon cooling of the γ matrix supersaturated solid solution that contains high concentrations of Ti and Al. The γ' phase has nominal composition of Ni_3(Al, Ti) and a fcc crystal structure [*5*] [*33*]. Since the lattice miss-match between the $\gamma - \gamma'$ phases is ~0.4 % – 0.5 % [*4*] [*38*], low coherency strains result in a lower interfacial energy and improved stability at elevated temperatures [*31*]. Due to the low coherency strains, the γ' precipitates primarily strengthen the alloy by the precipitate shearing mechanism [*4*]. The γ' phase comprises ~4 % – 5 % of the volume fraction of the IN 718 superalloy [*1*] [*4*].

Gamma Double Prime (γ″): A coherent metastable phase (with respect to the matrix) that precipitates when the IN 718 superalloy is cooled from a supersaturated solid solution (γ or matrix phase) with high concentrations of Nb in the presences of Fe. The γ'' phase has a nominal stoichiometry of Ni_3Nb and a bct crystal structure [*5*]. Unlike γ', which has rapid precipitation kinetics, γ'' precipitates slowly, resulting in increased resistance to strain-age cracking (SAC) of the IN 718 superalloy [*5*] [*7*]. Furthermore, the high lattice miss-match between the $\gamma - \gamma''$ phases (~2.86%) provides strength to the alloy [*4*] [*39*]. Since the volume fraction of γ'' is also relatively high (~15% – 20%), the γ'' phase is considered the primary strengthening precipitate in the IN 718 superalloy [*1*] [*40*] [*41*].

Delta Phase (δ): The δ phase is a stable form of the γ'' phase, which precipitates over extended periods of time at elevated temperatures (phase transformation from γ'' to δ phase) or during cooling after specific heat treatments, where the γ matrix is a supersaturated solid solution containing high concentrations of Nb. The δ phase may also preferentially precipitate upon cooling in the absence of Fe in the alloy or directly from the matrix at temperatures over 900 °C [*1*] [*5*] [*7*] [*41*] [*42*]. The δ phase is an in-coherent (with respect to the matrix) orthorhombic phase with the nominal stoichiometry of Ni_3Nb [*1*] [*7*]. Unlike the γ' and γ'' phases, the δ phase does not add inherent strength to the alloy, but acts as a grain refiner and increases IN 718's resistance to creep through grain boundary pinning. If the volume fraction of the δ phase becomes too high, it reduces the potential properties of the alloy by consuming Nb rather than allowing further precipitation of the primary strengthening precipitates (e.g., γ''). Reduction in the mechanical properties as a result of over precipitation of the δ phase is commonly referred to as 'δ-phase embrittlement' in the open literature [*1*] [*7*] [*41*].

Carbides: In the IN 718 superalloy, the addition of carbon up to 0.08 wt% causes a reaction between the reactive elements (Ti, Ta, Mo and sometimes Cr) to form carbides with a blocky morphology [*5*]. Typically, low volume fractions of MC-type carbides are purposely formed (where M represents the reactive metal) to reduce grain boundary sliding. However, similar to the δ phase, high volume fractions of carbides have been shown to result in premature component failure. Failure due to high volume fractions of carbides has been shown to be a result of enrichment of carbides with Nb rather than allowing the additional formation of the main strengthening precipitate γ''. In addition, large volume fractions of carbides may also lead to greater volume of liquid along the grain boundaries if conditions

are suitable for carbide liquation, thus leading to a reduction in mechanical performance during service [*5*] [*24*]. During extended exposure to elevated temperatures (service or during heat treatments), the MC carbides may decompose to form more stable $M_{23}C_6$ or M_6C carbides [*5*].

2.1.2.1 Stability of γ'' and δ Phases in IN 718

Saunders *et al.* [*43*] studied the stability of various phases in IN 718 over a wide temperature range under equilibrium and non-equilibrium conditions by performing Thermo-Calc simulations. Specifically, the evolution of the δ phase and the γ'' phase was determined as a function of temperature, as shown in Figure 2.

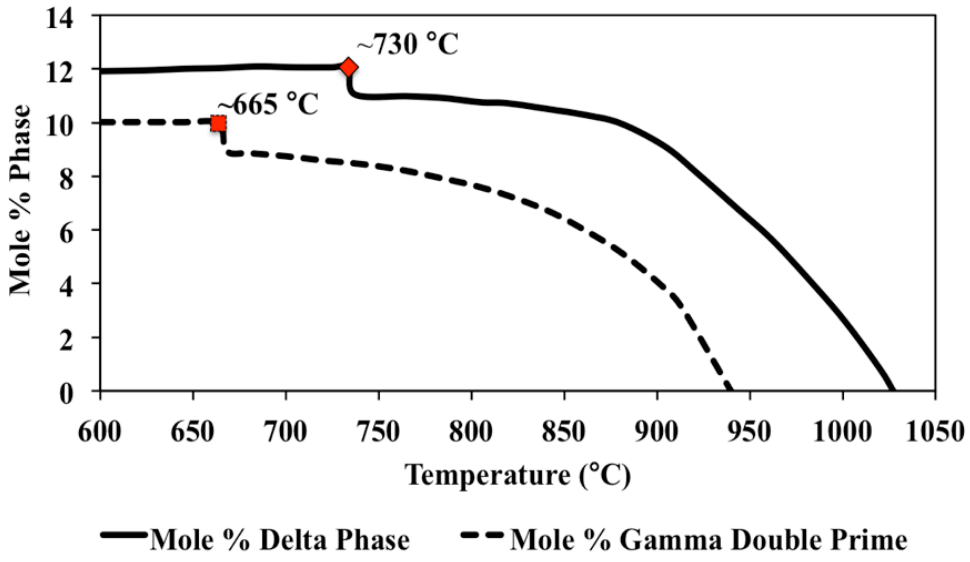

Figure 2: Variation in mole percent of the δ phase under equilibrium and the γ'' phase under non-equilibrium conditions based on Thermo-Calc simulations for IN 718. Data taken from [*43*].

The stability of the δ phase precipitation under equilibrium conditions in IN 718 is shown by the solid black line in Figure 2, while the non-equilibrium precipitation of the meta-stable γ'' is shown as the dashed line. Under non-equilibrium conditions, δ phase

precipitation is completely suppressed [*43*]. From Figure 2, under equilibrium conditions, a measureable decrease in the volume fraction of the δ phase (observed as a ~1 mole % decrease) occurs at ~730 °C. A continuous decrease in volume fraction is expected until the δ phase solvus is reached at ~1030 °C (reported experimentally as 995 °C – 1035 °C depending on the composition of IN 718 [*1*] [*2*]). Similarly, under non-equilibrium conditions, a measureable decrease in the volume fraction of meta-stable γ'' (observed as a ~1 mole % decrease) occurs at ~665 °C. A continuous decrease in volume fraction of γ'' is expected until the γ'' solvus is reached at ~940 °C (reported experimentally as 885 °C – 946 °C depending on the composition of IN 718 [*1*] [*24*]).

It should be noted, that the results of Saunders *et al.* [*43*], were reported for conditions that did not consider the transformation of meta-stable γ'' to its stable form (δ phase) at elevated temperatures and long exposure durations. Furthermore, the conditions of the simulations were not necessarily analogous to the environmental conditions experienced by actual material during service (e.g., the effect of load during service on the precipitates was not considered). However, these simulations were intended to provide a representation of the boundary limits on precipitation, where one phase preferentially forms at the expense of the other. From Saunders *et al.* [*43*], the simulations illustrate that a measureable decrease in the δ phase volume fraction from its peak value (decrease in the δ phase stability) is expected for temperatures exceeding ~730 °C. Further, a decrease in the peak γ'' volume fraction (decrease in γ'' stability) would be expected at around ~665 °C.

2.2 Fusion Welding of Superalloys

The use of welding as a viable joining process was not made until the latter half of the 1800's, due to issues with weld quality and reproducibility. Miossan in 1881 was the first to develop a carbon electric arc as the heat source to melt metal and later Bernandos applied this new technology to welding metals in 1887. Later, Slavianoff experimented with consumable metal electrodes, which subsequently lead to the first industrial metal-electric-arc welding United States patents by Coffin in 1889 [*11*].

Around the same time as the development of the carbon electric arc by Miossan, Le Chatelier developed the first oxyacetylene blowpipe torch, which later became the basis for modern torch welding systems. At the time, the portability and relatively low cost associated with oxyacetylene welds over electric arc welds nearly lead to the discontinuation of electric arc welds altogether. However, in 1914, Kjellberg introduced gas shielding for electric arc welding processes, which vastly improved the quality of electric arc welds [*11*]. Since then, many different welding processes have been developed for many applications in numerous industries.

2.2.1 Traditional Fusion Welding Techniques in the Aerospace Industry

Common welding processes used in the aerospace industry include: gas tungsten arc welding (GTAW or TIG), electron beam (e-beam) welding and laser beam welding. The advantages and limitations of joining materials with these welding techniques are well documented in the published literature [*5*] [*11*] [*12*] [*13*]. In the case of TIG, e-beam and laser techniques, the general process by which welding is achieved relies on heat generation by an external source and the melting of the materials to be joined to form a permanent joint.

Fusion welding uses the liquid material to fill gaps between the metals being welded and achieve excellent metallurgical bonding at the interface. The liquid metal, serves not only to aid the diffusion, mixing and flow of material to form a solid joint, it may also act as a fluxing agent to clean the joint surfaces in the early stages of welding [*11*].

Irrespective of how the liquid interacts with the material, any application of heat within a localized region results in a severe thermal gradient in the base metal leading to changes in final microstructure and mechanical properties in the vicinity of the weld interface.

2.2.2 Fusion Weld Microstructure

Since the material is exposed to localized heating in the vicinity of the weld during fusion welding, a distinct microstructure will evolve along the thermal gradient as a direct result of the influence of heat on the material [*11*]. For pure metals, when the temperature exceeds the melting point, complete liquation of the metal occurs. For an alloy where the temperature exceeds the solidus temperature, melting begins and continues until the liquidus temperature. Therefore, alloys will have liquid and solid material present concurrently over a range of temperatures. When the weld begins to cool and solidify, a new microstructure that is distinct from the parent (base) material develops and depends on the fusion welding technique used and the process parameters. The region where melting of the material occurs is termed the FZ and is shown in Figure 3. For alloys, the region next to the FZ where the temperature falls between the solidus and liquidus temperatures of the alloy, a PMZ develops. The next region to the PMZ is the HAZ, where the temperature remains below the solidus temperature of the alloy (i.e., the temperature is not sufficiently high to cause localized melting), but is often sufficient to result in observable microstructural changes. Examples of such solid-phase microstructural changes may include: grain growth or

alteration in precipitate size, morphology and volume fraction. It is noteworthy that for pure metals, which melt at a distinct temperature, the PMZ does not form. At locations where the temperature does not rise sufficiently to cause any perceptible change in the microstructure, the unaffected base material (BM) retains its original structure, as shown in Figure 3 [*11*].

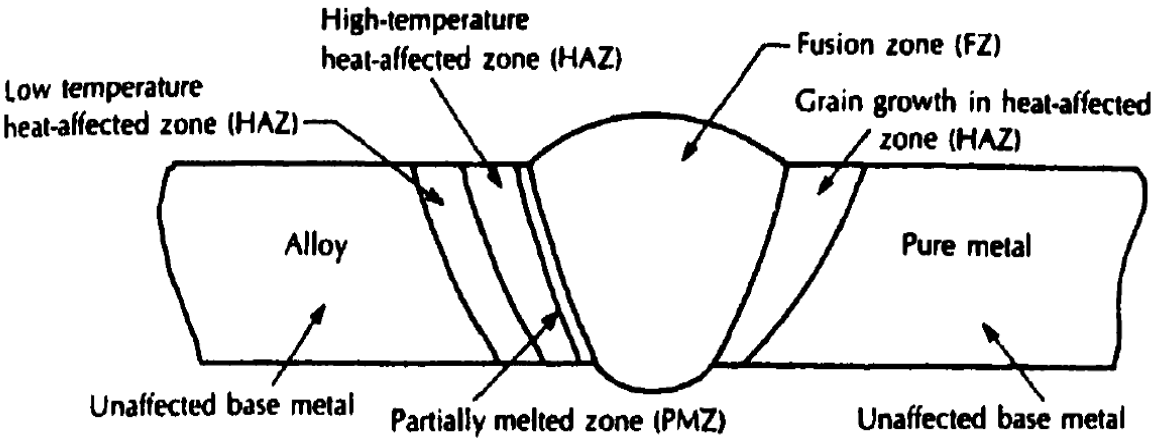

Figure 3: Fusion weld regions for alloys and pure metals [*11*]. (Joining of Advanced Materials, Robert Messler, Jr., Chapter 6: Welding as a Joining Process, Pg. 193, © 1993, with permission from Elsevier. http://www.elsevier.com)

For all fusion welding processes, the number, size and morphology of the various weld regions is influenced by: the material being joined, the welding technique used, as well as the welding parameters (including the weld environment) and the thermal gradients [*11*] [*44*] [*45*]. As a result, the simplified diagram in Figure 3 becomes more complex with distinct microstructures evolving in the unique weld regions, as illustrated in Figure 4.

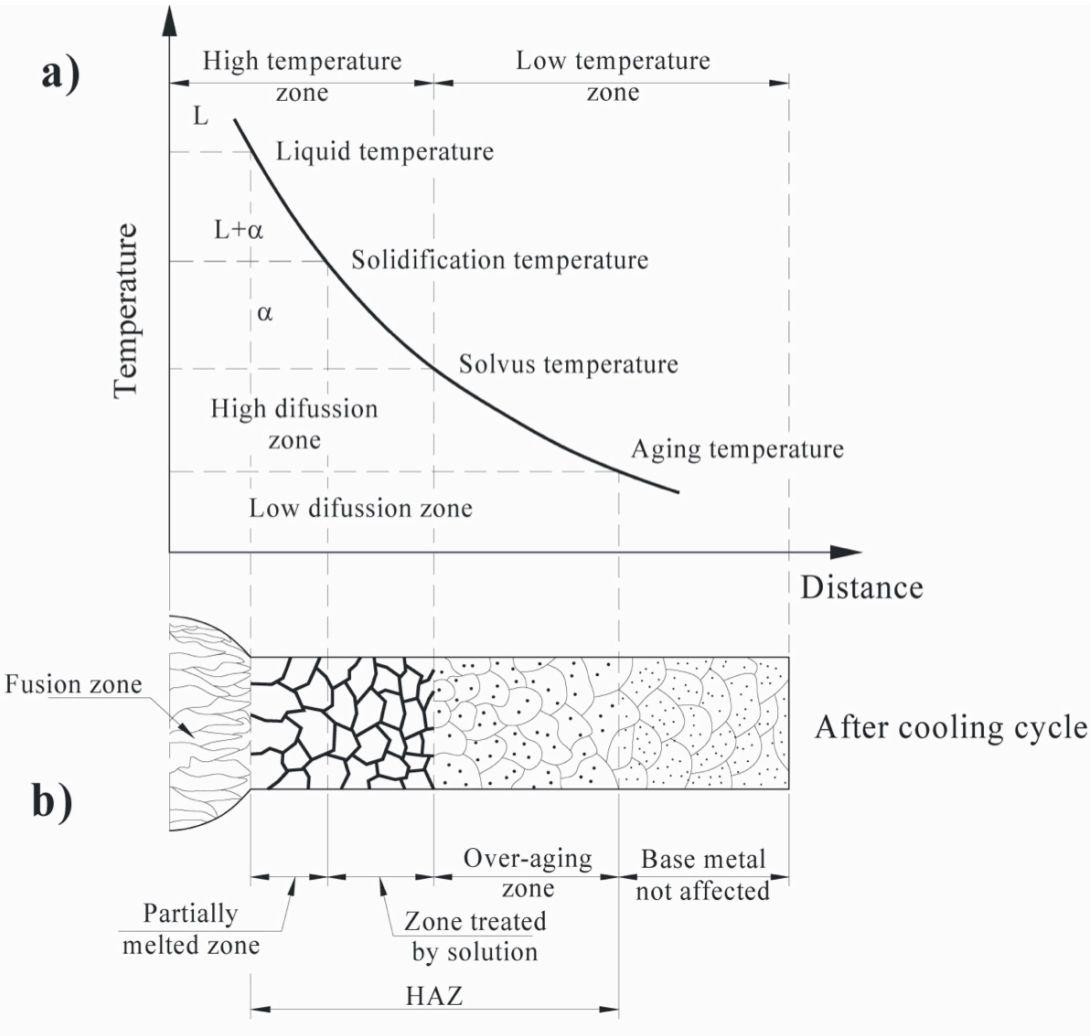

Figure 4: Fusion weld region showing thermal gradient within each weld region and its corresponding microstructure and related temperature. Dots represent precipitates [*45*]: a) Temperature of the weld, b) Weld location in a sample and the representative microstructure. (© 2014 R. Ambriz and D. Jaramillo, Originally published in R. Ambriz and D. Jaramillo, "Chapter 2: Mechanical behavior of precipitation hardened aluminum alloys welds," in *Light metal alloys applications*, W. Monteiro, Ed.: INTECH, 2014 under Creative Commons Attribution 3.0 Unported license. Available from DOI: 10.5772/58418.)

When the temperature exceeds the solvus temperature, the precipitates in precipitate hardened superalloys may dissolve [*11*]. An illustration of precipitate dissolution within the weld region can be seen in Figure 4 in the zone treated by solution (HAZ). For the other regions (overaged and base material) shown in Figure 4, the precipitates are represented by small dots. The dissolution (and overaging) of the strengthening precipitates within the immediate vicinity of the weld interface produces localized softening of the material, schematically illustrated in Figure 5 [*11*].

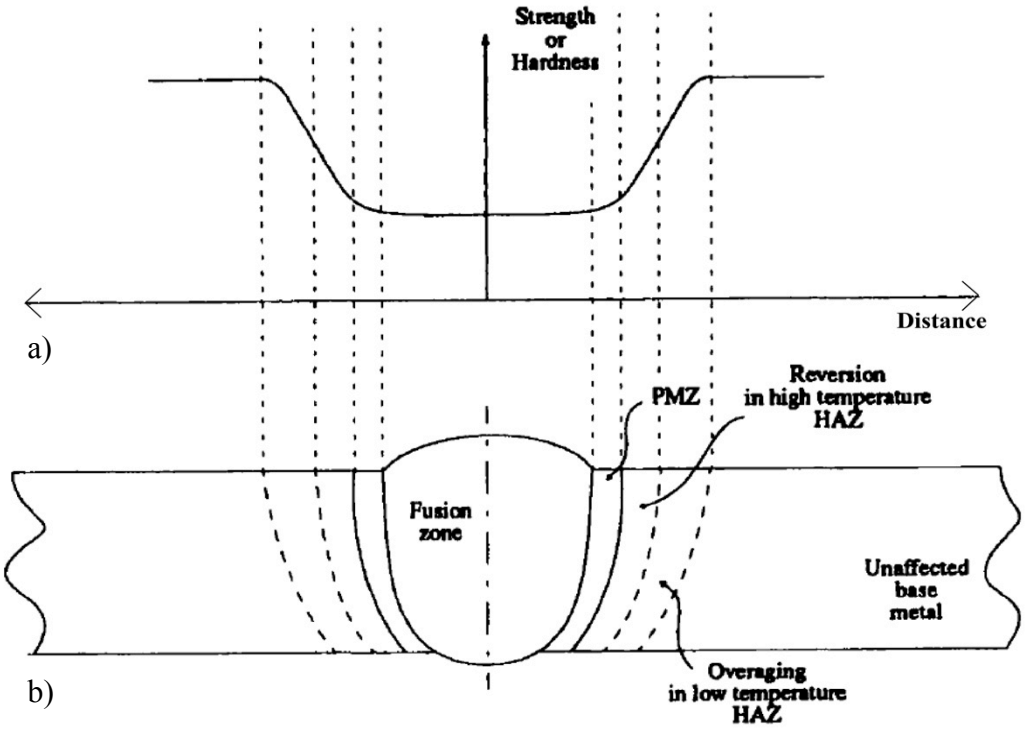

Figure 5: Loss of mechanical properties within the weld interface due to the dissolution of the strengthening precipitates [*11*]: a) Hardness trend across the weld, b) Location of hardness measurements in welded sample. Note: 'reversion' in figure label refers to dissolution of strengthening precipitates. (Robert W. Messler, Jr. Principles of Welding Processes, Physics, Chemistry and Metallurgy, © 1999 John Wiley & Sons, Inc. Reproduced with permission from Wiley Books).

To counter this undesirable variation in hardness, a PWHT is required, but often results in unwanted changes to the base material as well. A few options are available to combat this issue. First, the temperatures of the welding operation can be reduced below the precipitate phase's solvus or overaging temperatures. Second, the time at elevated temperatures during welding can be minimized [*11*].

The first approach, for fusion welding, is not practical since the very nature of fusion welds requires high temperatures capable of melting the materials to be joined. Since, by nature the melting temperature of an alloy is above the solidus and ageing temperatures, the only way to avoid temperatures that surpass the solvus or overaging temperatures would be to use a solid-state welding process (discussed in Section 2.3) [*11*]. However, the use of solid-state welding processes, where the process temperatures are lower than in fusion welding, does not guarantee that precipitate dissolution will not occur. Solid-state welding of precipitate hardened superalloys in the heat treated state (with an optimum precipitate size, morphology and volume fraction) may result in some loss of mechanical properties across the weld interface due to precipitate dissolution, as was reported by various authors [*16*] [*22*] [*24*] [*25*]. The second, and more practical method to retain an optimal microstructure, is to select a fusion welding process that is capable of heating and cooling the material rapidly to reduce the time the material spends above the solvus temperature, thereby minimizing the time when diffusion controlled kinetic processes can occur [*11*]. This is often achieved by using laser or electron beam welding, where high energy is concentrated on a small area to facilitate rapid melting and joining of the material [*13*].

Alternatively, rather than aging the material prior to welding, the weldment can be aged after welding (i.e., weld the component in the solution heat treated condition followed by

post weld ageing heat treatment). However, during this treatment, cracks or shape distortions can develop in the weld, potentially resulting in a complete loss of the component. If the material cannot be fully heat treated after welding, then a localized heat treatment can restore some of the mechanical properties that were lost during welding. However, localized heat treatments will not provide optimal properties and may cause further loss of strength if not performed correctly [*11*].

In an attempt to reduce some of the detrimental effects resulting from fusion welding techniques, current welding research seeks to develop novel methods to join metals without melting. This has put a new emphasis on the age-old technology of forge welding, which is now known as solid state welding.

2.3 Solid State Welding of Superalloys

With respect to fusion welding, the application of a particular fusion welding technique to a specific component or part will undoubtedly have to take into account the added effects of pre and/or post weld processing conditions required to maintain the component's desired properties. As discussed in Section 2.2.2, these added heat treatments often lead to unfavorable microstructural changes within the unaffected base material. As a result, cheaper and faster welding techniques (such as TIG welding) are no longer an attractive option, leading to the use of more expensive and time consuming welding techniques for critical aerospace components (such as e-beam or laser beam welding). The use of e-beam and laser welding can become very costly and may not allow for some components (like BLISKs) to be manufactured or repaired [*13*].

In an effort to avoid flaws associated with melting the materials being joined, research on solid state welding for materials that are highly susceptible to HAZ cracking or for components that cannot undergo the necessary pre or post weld processing due to the formation of detrimental microstructural changes is of interest [*23*]. Solid state welding refers to any metal joining process that facilitates a solid and coherent joint between two alloys without bulk melting of the materials. Solid state welding can use friction, generated by the relative motion between the two materials being welded, as the primary and only heat source (known as friction welding). Typical friction welding techniques used in industry include: inertia/continuous drive and linear friction welding [*11*] [*12*] [*13*]. For these friction welding techniques, the general process is as follows [*10*] [*11*] [*12*]:

1) Relative motion via oscillation/rotation between the two work pieces results in increased temperature at the point of contact.
2) While the oscillation/rotational motion continues, an applied compressive force brings the work piece interfaces together to allow for cleaning of the faying surfaces from contamination (grease, oxides, etc.) by extrusion of flash material from the interface. This step also provides a perfectly even and complete surface contact between the two work pieces. At this stage, viscoplastic flow and intermixing of the material occurs.
3) Oscillatory/rotational motion is stopped and a forging compressive force is applied to deform the work pieces and promote viscoplastic flow of material and increased diffusion of atoms.
4) Cooling of the welded work pieces after joining is complete.

Parameters such as oscillation/rotational speed, axial pressure, force duration, welding time, oscillation amplitude and frequency, as well as the burn off/upset distance are controlled to provide the necessary heat (where the alloy flows plastically) and pressure (where intimate contact between the two weld interfaces allows for atomic diffusion and proper intermixing of plastically deformed material) to create a coherent joint [*11*] [*12*].

Even though the temperatures that evolve during friction welding are not high enough to melt the material, substantial thermal gradients are created, resulting in the possibility of some cracking associated with phase liquation occurring in the HAZ of some alloys (see Section 2.4.2 for more details on liquation cracking) [*22*] [*23*]. As a result of the high thermal gradients and the application of pressure during welding, a unique microstructure across the weld interface is also created.

2.3.1 Microstructure of Solid-State Welds

Microstructural changes occur across the weld interface as a result of high thermal gradients and the application of a compressive forging force during friction welding. As illustrated in Figure 6, regions with a unique microstructure develop and are generally termed the: dynamically recrystallized (DRX) region at the interface of the original surfaces, thermomechanically affected zone (TMAZ) (a.k.a. high-temperature heat affected zone), the low-temperature HAZ (referred to as the HAZ in this work) and the unaffected base material (BM).

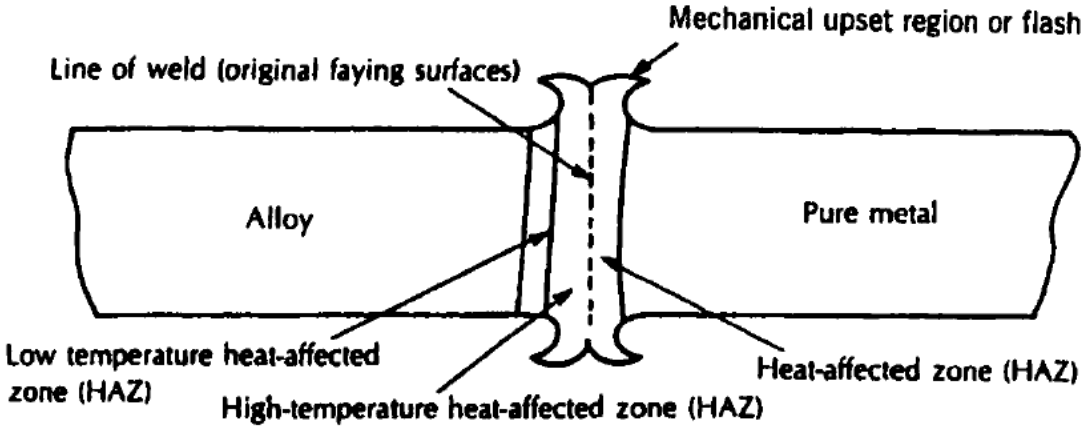

Figure 6: LFWed sample showing the various regions across the weld interface [*11*]. (Joining of Advanced Materials, Robert Messler, Jr., Chapter 6: Welding as a Joining Process, Pg. 193, © 1993, with permission from Elsevier. http://www.elsevier.com)

Typically, the weld-affected region for friction welding processes range between 3 – 10 mm in size [*16*] [*20*] [*24*] [*25*] [*26*] for welds with similar metals and up to 15 mm for welds with dissimilar metals [*15*]. By comparison, TIG welding can have weld affected regions between 10 – 100 mm wide, while electron beam and laser fusion welding can have weld affected regions as narrow as 0.1 – 1 mm [*13*].

Although the weld affected region and the HAZ are relatively small in friction welded materials, cracking in the vicinity of the weld may occur. Despite the temperature used during friction welding being lower than the bulk melting temperature of the welded alloys, the temperature is still sufficiently high within the HAZ to cause significant precipitate dissolution and subsequent rapid re-precipitation during PWHT, which may initiate cracking. In addition, the temperature achieved in friction welding may also reach sufficient levels to allow localized liquation of low melting point compounds (e.g., carbides) creating a liquid film along the grain boundaries within the HAZ. This intergranular liquid can lead to liquation cracking when tensile load develops in the welded component during cooling.

Therefore, it becomes important to reduce the extent of the weld-affected region to minimize the area where defects may form, which is often achieved by lowering the process temperatures [*11*].

2.3.2 Linear Friction Welding

In general, a LFW process starts by aligning two work pieces in culets. One of the work pieces is oscillated linearly against the faying surface of the other fixed work piece. When the desired temperature is reached, oscillation is stopped and an axial compressive force is applied to consolidate the pieces. Typically, the oscillation displacement is between 1 – 3 mm with frequencies between 25 – 125 Hz and a maximum axial compressive welding stress between 100 – 450 MPa [*10*]. A schematic illustration of the LFW setup is shown in Figure 7.

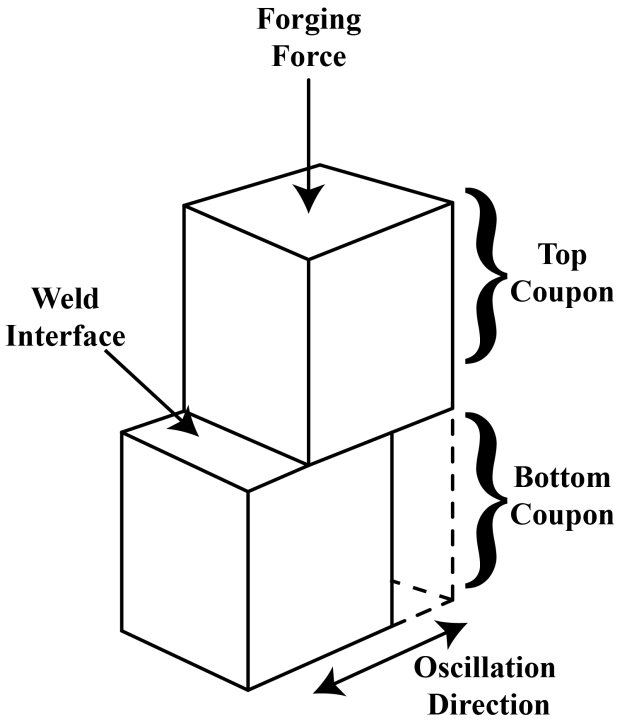

Figure 7: LFW work piece setup.

Part consolidation during LFW occurs in four distinct stages [*46*] [*47*]:

1) The work pieces are brought together such that their faying surfaces are in contact and under slight pressure to allow friction to generate heat. During this stage, the contact area between the two work pieces increases due to surface wear. No shortening of the material is experienced at this stage. However, sufficient axial force is required to generate the necessary heat for softening necessary for the next stage.
2) During the second stage, large material particles begin to be extruded from the weld interface and the contact area between the faying surfaces of the work pieces is considered to be 100% of the cross-sectional area of the work pieces. The temperature continues to rise until the material reaches a point where a thin plastic layer develops at the weld interface.
3) Once the plastic layer develops, the relative oscillation motion between the two work pieces begins to extrude highly plasticized material from the weld interface and forms the flash. This results in minor axial shortening of the work pieces.
4) To consolidate the weld, the oscillation is typically stopped within ~1 second and a rapid application of the final compressive forging load is applied to the perfectly aligned work pieces. After a few seconds, the load is removed from the newly joined material, which is then allowed to cool to room temperature.

The overall welding process only takes a few seconds to complete, but can be used to join difficult to weld superalloys (WASPALOY [*20*] [*21*], IN 738 [*22*], CMSX-486 [*23*]), as

well as dissimilar superalloys (RR1000 and CMSX-4 [*14*]) and other superalloys (IN 718 [*24*] [*25*] [*27*]), as well as aerospace grade Ti-alloys [*28*] [*29*].

The first important use of LFWing in the aerospace industry was for repairing damaged blades of aircraft engines that were made of difficult to weld nickel superalloys and aerospace grade Ti-alloys. Currently, LFWing is used for manufacturing new Ti-alloy compressor BLISKs [*10*] [*13*] and has become of particular interest as a potential repair process for BLISKs due to the significant reduction in weld defects compared to fusion welding techniques [*13*] [*21*].

2.4 Welding Defects

With all welding techniques, the evolution of defects is a possibility. In many cases weld contamination and improper fusion may occur if the weld setup and welding operation are not performed correctly. There are, however, other weld defects that can arise due to various mechanisms associated with the welding technique itself. For example, in most fusion welds, cracking in the HAZ region due to liquation may occur. In literature, the mechanisms of each type of flaw have been studied in depth for many different alloys [*6*] [*11*] [*12*] [*13*] [*15*] [*48*]. These studies have resulted in the development of various welding parameters and PWHT procedures for specific alloys to reduce the occurrence of welding flaws associated with the various welding techniques. Some of the more common weld defects associated with solid-state welding are discussed in the following sections.

2.4.1 Weld Contamination

Typically, there are three types of contaminants that may enter a weld: (i) voids and gas porosity, (ii) foreign metal contaminants and (iii) other non-metallic contaminants [*11*].

Gas porosity or voids are typically associated with fusion welding, where gas pockets are trapped in the FZ due to the reduction in solubility of gas in a liquid metal with decreasing temperature or as a result of the solidification process [*11*] [*12*]. Since the LFWing process does not melt the metal, gas porosity is not a common issue.

Foreign metal and other non-metallic inclusions, such as slag, oxides, dirt or other debris on the weld surface may be swept into or created in the weld zone during welding. Similar to the inclusion of pores in the weld, the inclusion of such debris can result in a formation of stress concentrations when the joint is loaded. Typically, the inclusion of foreign debris into a weld can be avoided by having a clean workpiece free of water, oxide scales, dirt, grease and other contamination [*11*].

2.4.2 Cracking of Weld Region

Cracks are among the most dangerous weld defects because there are no acceptable limits for crack inclusion within a weld. The occurrence of cracks within a weld depends on: the critical stress and strain, the stress and strain rate, temperature ramp/cooling rate, the initial composition and microstructure of the material and the geometry of the weld [*11*] [*44*].

Weld cracking can be classified into two categories: (i) cold cracks, which form in the weld or HAZ after the metal has solidified and cooled to room temperature and (ii) hot cracks, which form at high temperatures within the HAZ of the weld at temperatures above the alloy's solvus temperature [*44*].

Cold cracking in welds can be prevented by following proper welding procedures and ensuring a clean weld surface (free of any moisture, grease, oil or other hydrogen containing compounds). Alternatively, heating the material after welding to allow for hydrogen to diffuse out of the metal will also help to mitigate cold cracking [*44*].

Hot cracking is a generalized expression used to describe all cracks within the HAZ of the weld that form at elevated temperatures (above the alloy's solvus temperature) or during PWHT [*44*]. Depending on the welding technique used, the material and the welding parameters, various hot cracks can occur, such as strain- age (PWHT) cracking or HAZ liquation cracking.

2.4.2.1 HAZ Liquation and Liquation Cracking

HAZ liquation occurs when localized melting of low melting point constituents (e.g., carbides and borides) occurs. Liquation has been reported in numerous nickel based superalloy systems including: Inconel 738 [*22*] [*49*], Inconel 738 LC [*50*], CMSX-486 [*23*], Alloy 900 Series [*51*] and Inconel 718 [*52*] [*53*] [*54*] [*55*]. For cracking to occur after a phase has liquated, several conditions must be met. First, a liquid film must wet the grain boundaries. Second, a critical tensile stress at the liquid/matrix interface must be reached in order for a crack to open and propagate [*12*] [*30*].

HAZ liquation is known to occur by non-equilibrium phase transformations below the alloy's bulk solidus (subsolidus liquation) and at equilibrium melting above the alloy's bulk solidus when sufficient time is allowed for precipitates to melt (supersolidus liquation). Subsolidus liquation mechanisms can be grouped into two categories: (i) grain boundary penetration or (ii) grain boundary liquation.

Subsolidus non-equilibrium HAZ liquation is generally considered more detrimental in relation to cracking since it [*30*]:

1) Influences the nature of melting at supersolidus temperatures by altering the diffusion kinetics during subsequent heating by establishing non-equilibrium film along the grain boundaries at lower temperatures.

2) Extends the effective melting temperature range of the alloy, thereby increasing the duration where HAZ liquation cracking may occur.

Even if a critical stress is not achieved at the liquid/matrix interface to create a crack, the formation of a liquid may also have a detrimental effect on the alloy's bulk material properties, such as the production of a brittle or otherwise mechanically unfavorable re-solidified material during cooling. Therefore, knowledge of the various parameters that influence liquation of secondary phases and the initiation and propagation of cracks resulting from such liquid is critical to mitigate the loss of the weld integrity.

2.5 Liquation Mechanisms

Liquation occurring at non-equilibrium subsolidus temperatures and heating/cooling rates can be classified into two categories: (i) grain boundary penetration or (ii) grain boundary segregation. Both mechanisms may be active in the HAZ during welding [*30*]. The following sections outline some of the mechanisms by which non-equilibrium subsolidus liquation occurs, as well as parameters that affect an alloy's susceptibility to liquation cracking.

2.5.1 Grain Boundary Penetration

Grain boundary penetration involves a phenomenon called constitutional liquation of second phase particles, where low melting point particles melt and form a continuous liquid film [*30*]. Under equilibrium conditions, slow heating of an alloy to elevated temperatures enables the alloy's second phase particles to dissolve by diffusion into the matrix before a eutectic type reaction takes place. However, during constitutional liquation, rapid heating

causes the particles to liquate faster than diffusion can occur, resulting in a eutectic reaction between the second phase particles and the matrix [*12*] [*30*]. Since HAZ cracking is an intergranular defect, penetration of the grain boundary by the liquid film is usually a precursor to crack formation [*12*]. The amount of liquid that forms along the particle-matrix interface depends on the heating rate, initial particle size and the dissolution kinetics of the constituent particle at elevated temperatures [*12*] [*30*].

To nucleate a crack, a substantially thick liquid must remain on the grain boundaries, while tensile stresses develop in the material during cooling. Once the tensile stresses reach the critical magnitude, the crack opens and propagates through the intergranular liquid/grain boundary interface [*21*] [*50*] [*56*].

2.5.1.1 Constitutional Liquation

First experimentally observed and characterized by Pepe and Savage [*57*] [*58*] in 18-Ni maraging steels, constitutional liquation has been accepted by many scholars, researchers and others within the scientific community to explain non-equilibrium liquation in a variety of alloys. Constitutional liquation has been observed to occur in many material processing operations, including welding operations, hot rolling, forging, drawing and extrusion [*11*].

Constitutional liquation can be explained by examining a simple binary alloy with $\boldsymbol{\beta}$ phase particle of composition $C_{\alpha\beta}$ precipitating within the $\boldsymbol{\alpha}$ matrix with an initial alloy of composition C, as seen in Figure 8. When this alloy is heated slowly (equilibrium heating), the solubility of $\boldsymbol{\beta}$ in the $\boldsymbol{\alpha}$ matrix steadily increases. As such, the $\boldsymbol{\beta}$ phase particle shrinks as $\boldsymbol{\beta}$ atoms diffuse into the matrix solid solution. This increase in solubility continues until the equilibrium solvus temperature, T_2, (shown in Figure 8a) is reached where the last remaining

β phase disappears into solid solution with the matrix and creates a homogeneous single solid phase ***α*** with the same initial composition as the bulk alloy, *C* [*11*].

During rapid (non-equilibrium) heating of the ***β*** phase above an alloy's solvus temperature to T_3 (shown in Figure 8a), dissolution of ***β*** occurs since this phase becomes unstable at this temperature. Since the ***β*** phase particle is dissolving, the overall size of this particle will begin to decrease as more of the solute atoms go into solid solution with the ***α*** matrix. As the temperature increases and dissolution continues, solute ***β*** atoms diffuse into the surrounding ***α*** matrix material, giving rise to a concentration gradient of ***β*** atoms in the ***α*** matrix. The maximum ***β*** concentration evolves at the interface of the particle and the matrix and decreases as distance from ***β*** particle nucleus increases. As the temperature approaches the eutectic temperature, T_e, the ***β*** phase particles continue to shrink and the gradient of ***β*** atoms in the matrix continues to increase. However, there is a concentration gradient of ***β*** atoms between the ***β*** phase and the matrix that, at T_e, will allow for a liquid to form. Therefore, the ***β*** phase particle still remaining will be surrounded by a liquid phase. With continued heating, above T_e but below the solidus temperature, the liquid region between the remaining particle and the matrix material continues to grow. This liquid has a varying composition from the ***β*** particle/liquid interface to the liquid/matrix interface, since the ***β*** atoms continue to diffuse into the liquid and the matrix material, as illustrated in Figure 8b. Once the particle completely dissolves, the liquid film produced will undergo gradual compositional change and eventually disappear (by continued diffusion into the ***α*** matrix) assuming sufficient time at any isothermal temperature below the equilibrium solidus temperature [*11*].

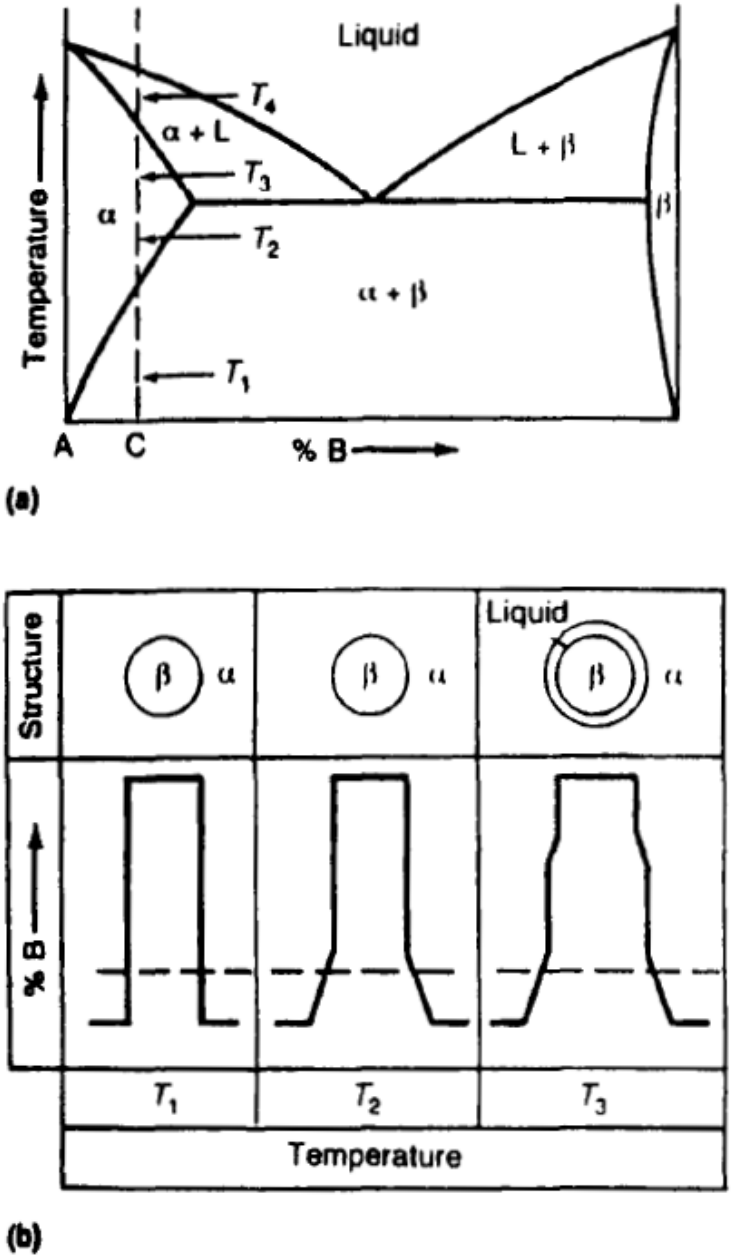

Figure 8: Constitutional liquation of a hypothetical phase *B* in matrix *A*: a) Schematic of constitutional liquation of *β* particle in a binary system and b) Concentration gradients in front of the liquating *β* particle [*52*]. (T. Sims, S. Norman, S. Stoloff and W. Hagel, Superalloys II: High temperature materials for aerospace and industrial power, © 1987 John Wile & Sons, Incorporated. Reproduced with the permission of Wiley Books).

The magnitude of the concentration gradients that result from the dissolution of the ***B*** phase precipitates are governed by [*57*]:

1) Heating rates – faster heating rates result in a steeper concentration gradient.
2) The mobility of ***β*** atoms into the ***α*** matrix – faster diffusion of atoms results in a shallower concentration gradient.

Constitutional liquation can occur at any temperature between T_e and the solidus temperature if the heating rate is sufficiently fast to hinder normal diffusion processes and allow the low melting point phase to exist beyond T_e where eutectic type reactions can occur with the matrix. Constitutional liquation has been observed in many different precipitate hardened alloys, including superalloys [*22*] [*23*] [*50*] [*54*] [*55*] [*58*] [*59*] [*60*] where rapid heating precluded complete dissolution of the precipitates prior to reaching T_e. Constitutional liquation is nefarious, since it results in localized melting of the material during high temperature processing of alloys and cannot be easily detected [*11*].

2.5.2 Grain Boundary Segregation

Grain boundary segregation involves the diffusion of active elements (like Nb, B and S [*53*] [*54*] [*57*] [*58*] [*61*] [*62*]) to the grain boundary during exposure to elevated temperatures where they: (i) may form constitutionally liquating compounds or, (ii) may act as a melting point depressant (in Ni alloys) or, (iii) if present in the liquid formed during liquidation of Nb-rich intermetallics, these elements may alter the properties of the liquid film [*30*].

Elements can diffuse to the grain boundary by two diffusion-controlled mechanisms, equilibrium segregation and non-equilibrium segregation [*30*]. Equilibrium segregation

occurs when a sufficiently high temperature is maintained to allow solute atoms to diffuse from within the grain to the grain boundary, where their absorption reduces the boundary's free energy. However, this mechanism is limited to a few atomic layers from the grain boundary.

Non-equilibrium segregation occurs during the cooling stage following annealing or hot plastic deformation of the material. This mechanism requires the formation of solute-vacancy complexes and a presence of concentration gradients between the grain boundary and the grain's interior. A concentration gradient is formed by the destruction of vacancies at the grain boundaries during cooling. As the vacancies move, they drag solute atoms, resulting in the enrichment of these atoms at the grain boundary [*30*] [*63*].

In practice, the contributions of both grain boundary segregation mechanisms can be difficult to distinguish. For example, enrichment of the grain boundary region by boron in cast IN 718 was reported by Huang *et al.* [*54*] to occur by both equilibrium and non-equilibrium mechanisms. The presence of boron at the grain boundary was shown to negatively influence IN 718's ability to resist liquation cracking. The degree to which each mechanism contributed to the overall diffusion of boron was shown to be dependent on both the maximum temperature and the cooling rate experienced by the material. It was found that equilibrium segregation increased as temperature decreased, while non-equilibrium segregation increased as temperature increased. Non-equilibrium segregation was also reported to be affected by the cooling rate, where mid-range cooling rates (e.g., air cooling at 20 °C/s) allowed for sufficient time to form solute-vacancy complexes, which were not observed at higher cooling rates (e.g., 400 °C/s) [*54*]. Thus, in an effort to control liquation, and liquation cracking, it is necessary to understand how the microstructure, alloy

composition and the heating/cooling rates influence the onset of liquation or the initiation of a critical tensile stress.

2.5.3 Parameters Affecting Liquation Cracking

Even though liquation of low melting point precipitates in an alloy may occur, it does not necessarily result in cracking. There are a number of contributing factors that have been shown experimentally to influence an alloy's susceptibility to liquation cracking.

Grain Size: Thompson *et al.* [*59*] suggested that alloys with a large grain size will accumulate thicker layers of liquid for a given volume fraction of precipitates due to smaller grain boundary surface area. As a result, the thicker liquid layer takes longer to completely solidify, which prolongs the existence of intergranular liquid. Any mechanism that prolongs isolated intergranular liquid films may allow sufficient time for the critical tensile magnitudes to be achieved, and therefore increase the possibility of liquation cracking [*12*].

Size of Precipitates: A large volume fraction or a large initial size of liquating particles can generate a thicker liquid film on the grain boundaries. For analogous reasons as discussed for the effect of grain size, the thicker liquid film takes longer to solidify and may result in cracking if a substantial tensile stress develops prior to its complete solidification [*12*] [*55*]. Larger particles also take longer to completely dissolve and therefore may be present at higher temperatures during rapid heating where liquation may occur [*60*].

Rate of Particle Dissolution: Precipitates with high dissolution rates are not likely to exist above the solvus temperature and therefore the precipitates will not have the opportunity to react with the matrix and from intergranular liquid [*12*].

Type of Precipitate: Within the HAZ of the weld, there are two types of precipitates that may liquate: (i) constitutionally liquating precipitates and (ii) equilibrium melting precipitates [*11*] [*12*]. As discussed previously, equilibrium melting precipitates are those that melt when the temperature exceeds the alloy's solidus. Since the temperature that exceed the alloy's bulk solidus are commonly associated with regions (such as the FZ and PMZ) that have large volumes of liquid material (due to bulk melting of the alloy) that may aid in healing any cracks that occur during equilibrium melting of precipitates, cracking is therefore not a major concern in these regions. However, constitutionally liquating precipitates may exist above the bulk solvus for the alloy during non-equilibrium heating. This becomes a particular problem when localized regions away from the liquid reserves of the FZ (or PMZ) develop a liquid film that is not connected to any adjacent reservoir of liquid. This increases the probability of forming cracks or microfissures that cannot be backfilled by the liquid from the fusion zone (or PMZ) [*11*] [*12*].

Soucail and Bienvenu [*60*] performed experimental and numerical simulations on the dissolution of the γ' phase under equilibrium and non-equilibrium heating of a nickel base superalloy. Their results suggested that there was a significant departure from equilibrium dissolution kinetics of the γ' phase during rapid heating, with the temperature for complete solid-state dissolution of the γ' phase increasing as the heating rate increased. Furthermore, the departure was shown to increase as the size of the γ' phase increased [*60*].

Impurities: The effect of impurities on the liquation of precipitates in IN 718 has been the subject of many studies [*53*] [*54*] [*55*]. The results suggest that liquation is not necessarily caused by the presence of impurities in the alloy, but the impurities do enhance liquation by: (i) increasing the wettability of the grain boundaries, (ii) reducing the solidus

temperature, (iii) accelerating precipitation of low melting point phases, and (iv) enabling the formation of liquid on the grain boundaries [*12*] [*53*] [*54*] [*55*].

Impurities have been shown to increase wetting of the grain boundaries in IN 718. For example, Thompson *et al.* [*55*] studied the effect of carbon content on the extent of liquation cracking in cast IN 718 and found that the increase in the volume fraction of liquating Nb-rich carbides was directly proportional to the increase in carbon content. This increase contributed to an increase in HAZ liquation cracking as well. It was also noted that alloys with similar process history and composition had a different liquation cracking susceptibility, due to the variations in the liquating phase volume fractions [*55*].

Huang *et al.* [*54*] simulated the thermal conditions within the HAZ of a weld by subjecting cast IN 718 to varying heat treatments. Secondary ion mass spectroscopy (SIMS) analysis was performed in the vicinity of the grain boundaries of the samples and revealed that boron segregating to the grain boundaries decreased the solidification range of the liquid that developed at the grain boundaries. Also, boron contributed to increased grain boundary wettability. Further, Huang *et al.* [*54*] concluded that boron enrichment at the grain boundaries lowered the stress required to initiate and propagate a crack [*54*].

Temperature and Heating Rate: Exposing IN 718 to temperatures between the eutectic and bulk solidus of the precipitate, with sufficiently fast heating rates, restricts the liquating precipitate from fully dissolving before the precipitate can react with the matrix. This results in the formation of a liquid phase via eutectic type reactions between the precipitate and the matrix. For example, Ola *et al.* [*22*] studied the microstructural changes during LFW of IN 738 Ni-based superalloy. Their Gleeble simulations of the LFW process revealed that the main strengthening precipitate, γ', was present at temperatures exceeding the precipitate's

solvus temperature (given as ~1160 °C) when heating rates of 150 °C/second were imposed. When the alloy was heated to peak temperatures above the $\gamma - \gamma'$ eutectic temperature (given as ~1180 °C), γ' liquation was observed. A similar result was also observed in a separate study by Ola *et al.* [*23*] on LFW of the Ni-based superalloy CMSX-486. The authors observed that the γ' precipitates remained even at the eutectic temperature (given as ~1250 °C) while heating the material at 150 °C/second and reacted with the matrix to create a liquid film. To minimize such liquation and reactions of secondary phase precipitates, the welding temperatures and material heating rates should be controlled to remain below critical values of the specific alloy [*22*] [*23*] [*58*] [*60*].

Presence of Critical Tensile Stress: The evolution of a critical tensile stress at the liquid/matrix interface is required for a crack to open and propagate.

Experiments performed by Ola *et al.* [*22*] [*23*] showed that the application of a compressive stress during solid-state welding increased the back-diffusion of solutes from the liquid into the surrounding matrix, thereby eliminating the liquid and reducing the effect of liquation cracking within HAZ of linear friction welded IN 738. In addition, the authors observed that the application of external compressive stress reduced the nucleation and growth of cracks [*22*] [*23*].

It is therefore important to consider not only the initial microstructure of the material to be welded, but also how the microstructure changes during welding and how the changes in the microstructure influence the characteristics of the weld defects.

2.6 Dynamic Recrystallization Mechanisms

A decrease in the material properties due to microstructural changes is not exclusive to recovery and recrystallization processes during post processing heat treatments. Dynamic recovery and dynamic recrystallization may occur while deforming a material at elevated temperatures during metalworking operations (such as hot forging and rolling operations) [*64*]. Dynamic recrystallization (DRX) is frequently observed during hot deformation processes in materials where the recovery process is slow and the material retains large amounts of stored energy (i.e., in low stacking fault energy materials such as Ni and Ni-based superalloys) [*2*] [*64*] [*65*] [*66*]. Dynamic recrystallization occurs after dynamic recovery of a material during the deformation processes, when a specific critical temperature, strain rate, and deformation are achieved. DRX often results in the formation of new grains [*64*]. The mechanisms of DRX can be divided into two categories: (i) discontinuous dynamic recrystallization (DDRX) and (ii) continuous dynamic recrystallization (CDRX). Depending on the type of dynamic recrystallization occurring, several mechanisms have been proposed to explain the recrystallization process. DDRX has been suggested to occur by the necklace mechanism (discussed further in Section 2.6.1), while CDRX was proposed to occur via two mechanisms: (i) progressive lattice rotation, and (ii) geometric dynamic recrystallization (discussed further in Section 2.6.2) [*64*]. Figure 9 illustrates the various proposed mechanisms for each category of dynamic recrystallization.

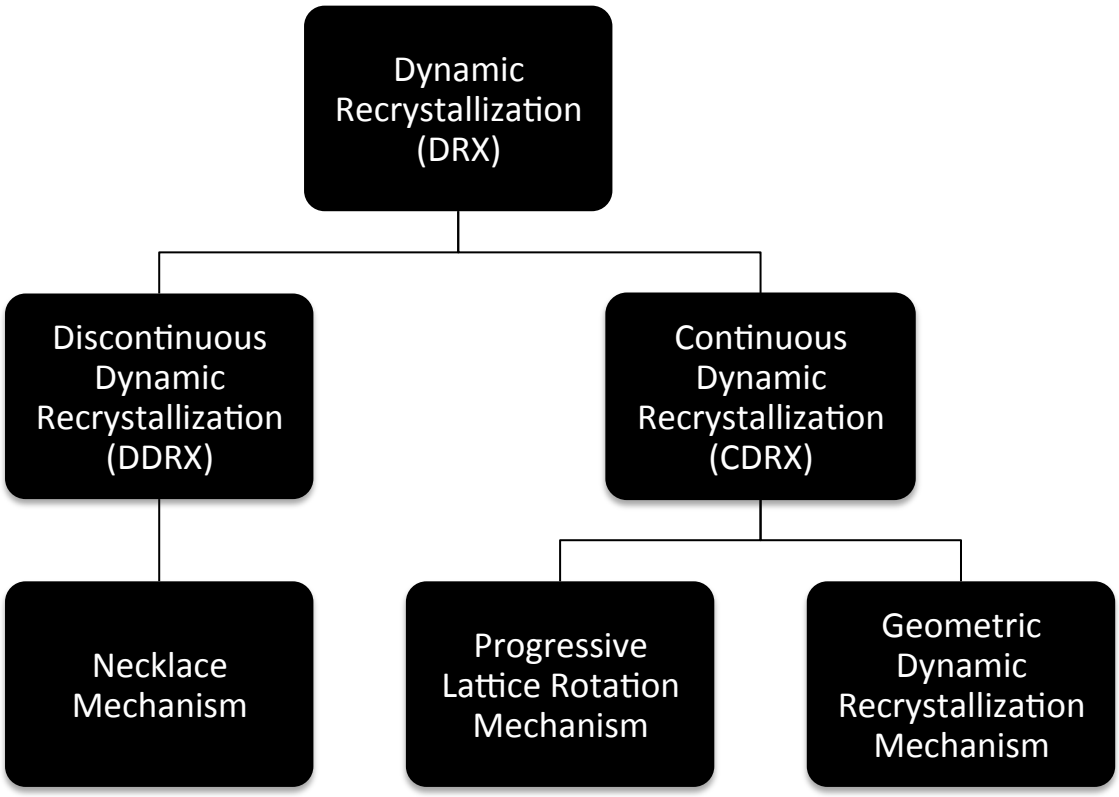

Figure 9: Various mechanisms contributing to dynamic recrystallization in materials during elevated temperature deformation.

Although dynamic recovery and dynamic recrystallization processes are important for industrial processes, the exact initiation mechanisms and driving forces are not well understood in the open literature. This is because recovery and recrystallization processes often occur simultaneously [*64*]. Therefore, the mechanisms proposed in the literature are often based on post dynamic recovery and dynamic recrystallization observations from experiments using simple materials (single phase alloys or pure metals) or based on numerical models derived from a known theory on 'idealized' models, which do not accurately reflect an actual material behavior (especially for the case of highly alloyed superalloys) [*64*]. However, the mechanisms proposed provide a general understanding of how a material's microstructure changes during dynamic recrystallization.

2.6.1 Discontinuous Dynamic Recrystallization (DDRX)

Discontinuous dynamic recrystallization (DDRX) occurs in materials with slow recovery processes (i.e., where dislocations remained locked in the grains during heat treatment) during deformation at high temperatures (1100 °C for IN 718 [*65*]). Recrystallization may occur once a critical temperature, strain rate and strain (dislocation density) are achieved, thus allowing new grains to form on old high angle grain boundaries following the necklace mechanism, illustrated in Figure 10.

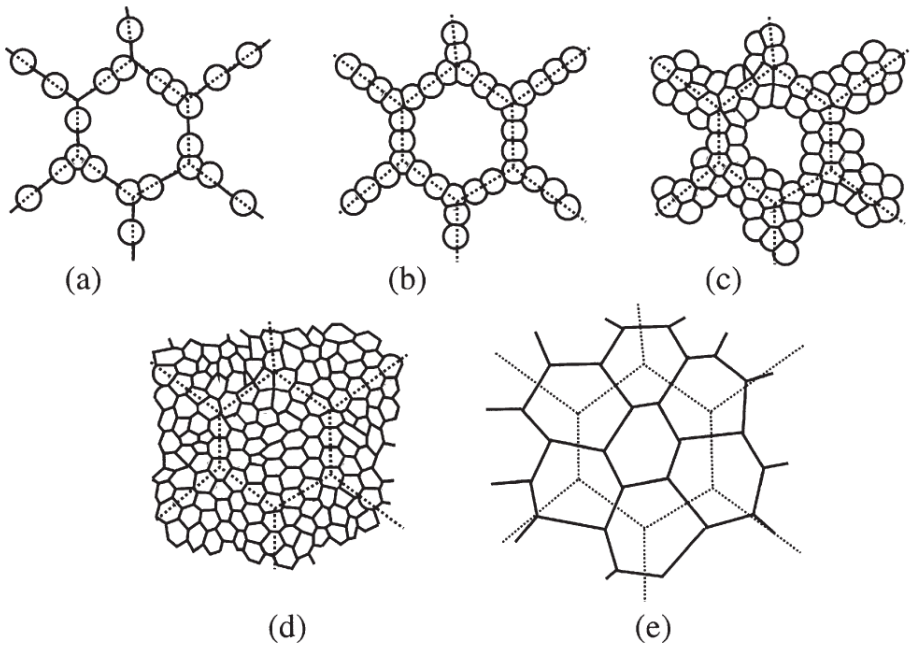

Figure 10: Microstructure evolution during DRX: a) – d) large initial grains (dashed lines) being consumed by the small recrystallized grains (solid lines) during the DRX process, e) Small initial grains (dashed lines) consumed by the recrystallized grains (solid lines) during the DRX process [*64*]. (Reprinted from Recrystallization and related annealing phenomena, 2nd Edition, F. Humphreys and M. Hatherly, Chapter 13: Hot deformation and dynamic restoration, pp 431, (2004) with permission from Elsevier. http://www.elsevier.com).

As shown in Figure 10, the new recrystallized grains form on the initial high angle grain boundaries and are thought to originate as a result of grain boundary bulging. Grain boundary bulging is often observed experimentally as grains with serrated edges [*64*] [*65*]. As the grain boundary moves (driven by the difference in the dislocation density of the recrystallized and

non-recrystallized grains), the dislocation density behind the boundary is reduced to near zero values (as a result of the recrystallization process). As deformation continues, the dislocation density behind the moving boundary increases, approaching that of the non-recrystallized material and thus the driving force for continued grain growth decreases.

The initiation of DDRX is often only observed for low stacking fault energy materials, where recovery mechanisms are slow. Slow material recovery results in higher dislocation densities, which are necessary to initiate dynamic recrystallization. For materials that have a high stacking fault energy, the recovery process occurs more rapidly due to more dislocation climb and cross-slip may occur. In such cases, the critical dislocation density is not achieved and DDRX does not occur (only dynamic recovery).

2.6.2 Continuous Dynamic Recrystallization (CDRX)

Continuous dynamic recrystallization (CDRX) is often the dominant mechanism of dynamic recrystallization for materials subjected to high strain rates and relatively low temperatures (950 °C for IN 718) [*65*] [*66*]. However, it has been found that the dominant DRX (i.e., either DDRX or CDRX) mechanism in IN 718 depends on the hot processing conditions (i.e., temperature, strain, strain rate) [*65*] [*66*] as well as the state of the material (i.e., the microstructure) [*2*]. It has also been suggested that both CDRX and DDRX may be active simultaneously in some instances [*2*].

The grains that form during CDRX often have high angle grain boundaries. CDRX process gets its namesake as a result of having no separate nucleation and growth steps (i.e., the process is continuous). CDRX can be divided into two mechanisms: (i) progressive lattice rotation and (ii) geometric dynamic recrystallization.

2.6.2.1 Progressive Lattice Rotation

Progressive lattice rotation is a strain induced continuous dynamic recrystallization mechanism. The exact mechanisms governing this process are not clear in the literature but the general process involves creating new grains from the subgrains within high angle boundaries during the deformation of a material. The creation of new grains occurs by progressive rotation of subgrains that are adjacent to existing grain boundaries. This type of CDRX is usually found in materials where dislocation motion is inhibited (as a result of limited slip systems, second phase particle strengthening or solute drag) [*64*].

2.6.2.2 Geometric Dynamic Recrystallization

Geometric dynamic recrystallization often occurs in materials that are subjected to large strains (true strains ranging between 3% – 7% [*64*]), where high angle grain boundaries (HAGB) are forced closer together during high levels of deformation. The progression of geometric dynamic recrystallization during high strain deformation is illustrated in Figure 11. When the high angle grain boundaries impinge, a new grain structure of mainly high angle grain boundaries is generated [*64*].

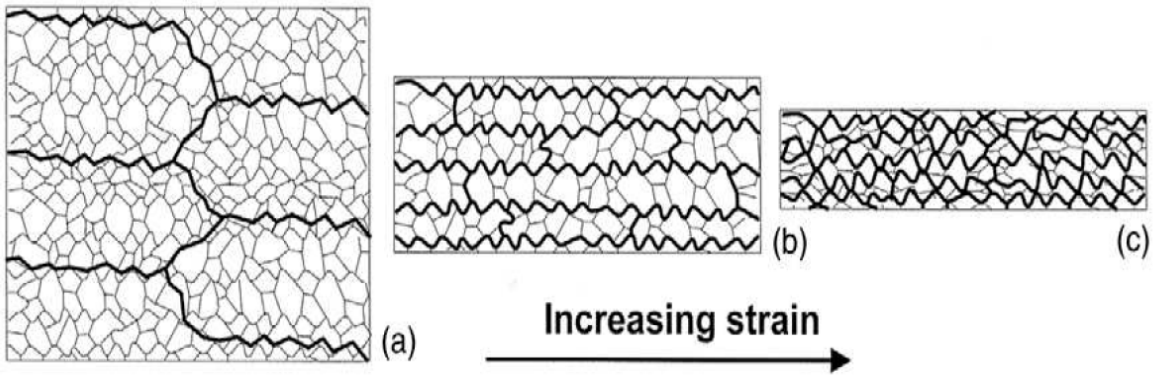

Figure 11: Progression of geometric dynamic recrystallization with increased strain: a) initial microstructure, b) – c) Increased deformation forcing HAGB (dark lines) together [*64*]. (Reprinted from Recrystallization and related annealing phenomena, 2nd Edition, F. Humphreys and M. Hatherly, Chapter 14: Continuous recrystallization during and after large strain deformation, pp 462, (2004) with permission from Elsevier. http://www.elsevier.com).

2.6.3 Effects of DRX on Liquation

The externally applied compressive loading during the linear friction welding process has been shown experimentally to induce DRX and result in grain refinement [*20*] [*21*] [*22*] [*23*] [*24*]. DRX has been experimentally shown to reduce the formation of liquation cracking at the grain boundaries due to: (i) increased grain boundary surface area due to the reduced grain size, (ii) increased migration rates of the smaller grain boundaries resulting in a reduced interaction between secondary liquating phases and the grain boundary, (iii) increased diffusion rates of liquated phases due to the higher grain boundary surface area and (iv) increased grain boundary surface area resulting in a reduced stress acting on individual grain boundaries [*21*].

2.7 Evaluation of Residual Stress and Strain in Welded Superalloys

Residual strain that develops during fusion welding has been extensively studied over the past 20 years using neutron and x-ray diffraction techniques. In the case of new joining techniques, such as LFW, residual stress and strain characterization continues to be of high interest to alloy and technology designers [*17*] [*18*] [*28*] [*67*] [*68*] [*69*].

Residual stresses are self-equilibrating, which means the local tensile and compressive stresses will sum to zero over the net volume of the material. Depending on the length scale over which the residual stresses sum to zero, the residual stresses can be divided into three groups: (i) Type I macrostresses (i.e., variation in stress over the length of the bulk sample), (ii) Type II intergranular stresses (i.e., variation in stress magnitude between adjacent grains) and (iii) Type III atomic stresses (i.e., variation in stress magnitude on the atomic scale that result from coherency strains and dislocation strain fields within a grain) [*70*]. Residual stresses may be created within a material by mechanical deformation (e.g., forging, rolling, bending drawing, shot peening, etc.), chemical/phase changes (e.g., precipitation hardening, phase transformations, radiation damage, nitriding, etc.) or thermal effects (e.g., thermal gradients that result in localized variation in expansion or contraction of the crystal lattice, differences in the coefficient of thermal expansion between material/phases during heating/cooling, etc.) [*71*]. Typically, during welding, the creation of localized thermal gradients results in a significant variation in the microstructure, which results in the evolution of residual stresses in the material.

Measurement of the various types of residual stresses is achieved by selecting a characteristic gauge volume to correspond with the length scale of the residual stress type of

interest. If the measurement volume is larger than the characteristic gauge volume, the residual stress will not be recorded. However, in multiphase and/or polycrystalline alloys the effects of Type II and Type III residual stresses may be incorporated into the measurement of Type I residual stresses via peak broadening. For example, in Ni-based superalloys where the γ and γ' phases are present, the Type II residual stresses are typically superimposed on the Type I residual stresses. This superposition occurs due to both the γ (matrix) and γ' phases being cubic and coherent, but their lattice parameters are not exactly the same (i.e., there are some coherency strains between the two phases). Therefore, a non-zero average Type II macrostresses leads to an average background residual stress in each phase and is detected as peak broadening during neutron diffraction experiments [*70*]. For the purpose of this work, analysis of Type I residual stresses was considered the primary focus. Still, it is recognized that Inconel 718 is a multiphase superalloy with Type II and III residual stresses likely contributing to the Type I residual stresses. However, Type II and III residual stress analysis was beyond the scope of this research.

From an industrial perspective, establishing proper welding parameters is of critical importance in order to minimize the residual stresses in welded parts. Since turbine blade materials are typically exposed to high temperatures and loading during service, inadequate relief of (Type I) residual stresses may cause distortion or deformation of the blades during service. The use of proper PWHT to effectively relieve residual stresses prior to service is therefore important. Neutron diffraction is a powerful tool used to quantify elastic residual stresses and strains in a material, thus assisting with the development of welding parameters and PWHT cycles.

Preuss *et al.* [*17*] used neutron diffraction to study the evolution of residual stresses in inertia friction welded RR1000 superalloy joints. The authors determined that the conventional PWHT used for RR1000 did not sufficiently relieve the residual stresses in the welded material and suggested that a 50 °C increase in the standard PWHT temperature was required in order to adequately reduce the residual stresses from welding.

In the same study, Preuss *et al.* [*17*] found that the thermal gradient in the weld region resulted in a localized variation in the stress free lattice parameter due to element segregation. It was shown by the authors that if the measurement of the stress free d_0 spacing did not properly account for the variation in the lattice parameter across the weld interface, the resulting calculated stresses were not accurate. This is a significant finding. Since most superalloys are precipitate hardened, it is necessary to minimize the temperature and duration of heat treatment so as not to overage the material. If the stresses are overestimated, then higher PWHT temperatures and longer durations may be used erroneously, leading to an undesired degradation of the material properties (e.g., strength, hardness).

The following section outlines the theory of neutron diffraction, interaction of neutrons with matter and the use of neutron diffraction to measure residual stresses and strains.

2.7.1 Interaction of Neutrons with Matter

Neutrons have no electrical charge and therefore are not influenced by the electron cloud of an atom. The size of the nucleus of an atom is approximately 100 000x smaller than the distances between adjacent nuclei, which allows the neutrons to travel relatively long atomic distances without being absorbed or diffracted by the host atoms [*72*].

Neutrons are considered to exhibit a wave-particle duality and their interactions with matter are governed by quantum mechanics. There are several different types of scattering

events that can occur. Typically, scattering refers to the altering of a particle's direction of travel by an interaction with an atom, while diffraction is considered an altering of a wave's direction of travel due to an interaction with a series of atoms. Since neutrons exhibit a wave-particle duality, in most texts "scattering" and "diffraction" are used interchangeably [*72*] [*73*]. However, it is also noted that in some literature diffraction is referred to as a special type of scattering (elastic coherent scattering), where a pattern due to constructive interference of waves that are in-phase emerges after neutrons interact with a material [*72*]. For the purpose of this work, scattering will follow the particle naming convention and diffraction will follow the wave naming convention regardless of the material the neutrons are interacting with.

2.7.1.1 Neutron Sources

There are two types of neutron sources. First, spallation sources of neutrons use a high-energy beam of protons that is directed to a source material (uranium) to initiate radioactive decay. This decay subsequently releases a large number of neutrons of various wavelengths. These neutrons are directed and collimated toward the sample being analyzed [*70*] [*71*]. Spallation sources are typically used for time-of-flight neutron diffraction experiments. Time-of-flight diffraction works based on the principle that each neutron with a unique wavelength generated at the source travels at a different velocity. Measuring the time it takes each neutron to diffract for a specific distance traveled, the wavelength can be matched to the detected diffraction peak. Knowing the wavelength and the angle of diffraction, the interplanar spacing (*d*-spacing) for the diffracting plane(s) can be found, which then can be used to measure the residual strain and calculate the residual stress [*70*] [*71*].

The second type of neutron source is a nuclear reactor, where neutrons are constantly generated from a nuclear fission reaction of uranium. These neutrons have a continuous spectrum of wavelengths and are often called "white" neutrons. These neutrons are collimated and directed to a monochromator crystal, where a single wavelength is selected. The single wavelength neutron beam is then further collimated to the proper interaction volume and directed towards the sample being analyzed, as shown in Figure 12 [*70*] [*71*].

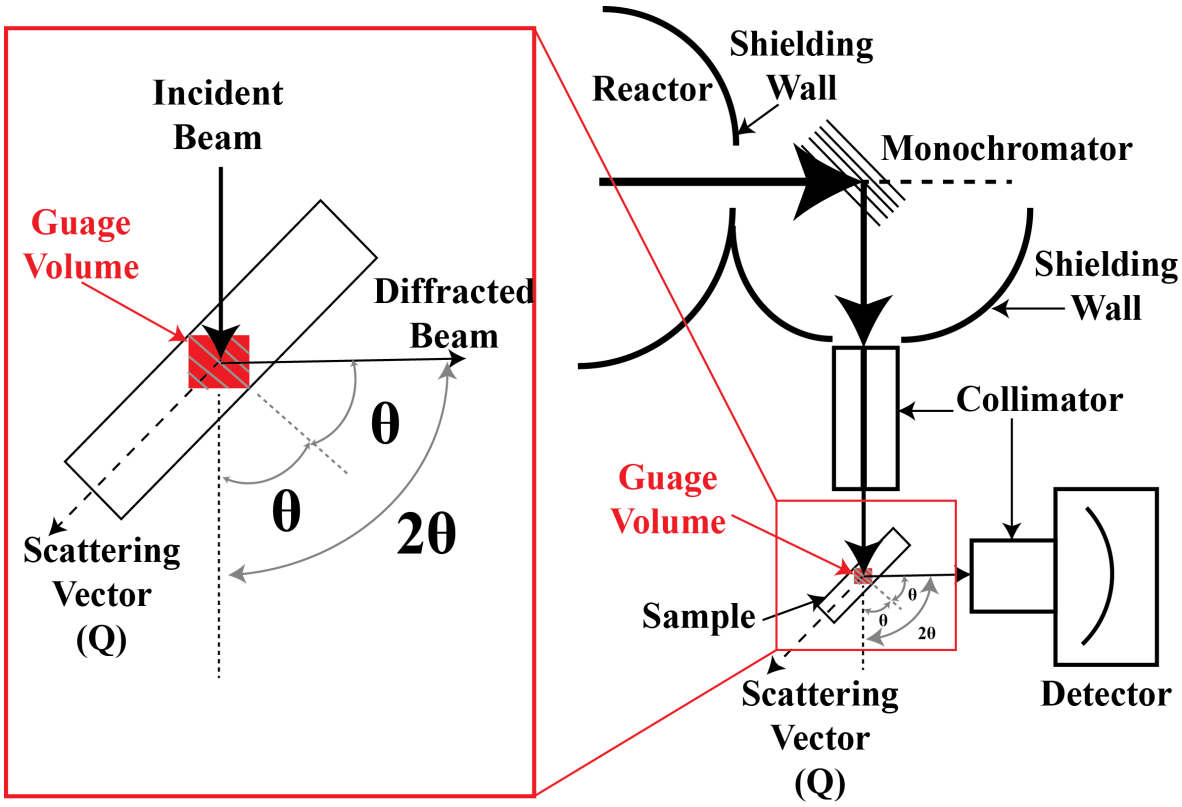

Figure 12: Experimental apparatus for neutron diffraction from a nuclear source.

Since only one plane is diffracting in a crystal for a given wavelength, only one diffracting angle needs to be monitored, which makes the measurement of interplanar spacing relatively simple [*70*] [*71*].

For both spallation and nuclear source diffraction experiments, the strain can be measured by performing diffraction experiments on: (i) a stress free and (ii) stressed sample. Then, by measuring the difference in the *d*-spacing obtained from diffraction theory (Bragg's law), the residual elastic strain and stress can be calculated for a location of interest [*71*].

2.7.1.2 Neutron Diffraction Theory

For constructive interference to occur, the path length difference traveled between two adjacent beams must be an integer multiple of the wavelength, as shown in Figure 13. Otherwise, due to destructive interference between the diffracted waves, the diffracted beam will have a minimal intensity [*72*] [*74*].

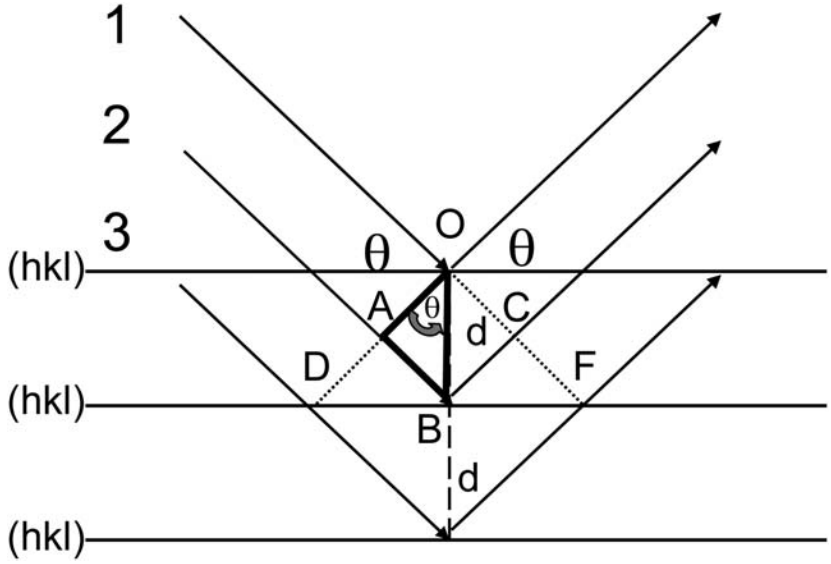

Figure 13: Incident beam of particles interacting with planes of atoms used to describe Bragg's law by path length difference method. (Reproduced from [*75*] with permission of The Royal Society of Chemistry. http://dx.doi.org/10.1039/C0NR00561D).

The condition to detect a Bragg peak can be defined as follows [*74*]. The path difference $\overline{AB} + \overline{BC}$ must be an integer multiple of the wavelength, $n\lambda$.

$$n\lambda = \overline{AB} + \overline{BC} \tag{1}$$

Based on trigonometry of the diffracting incident beam 2 shown in Figure 13, the path segments $\overline{AB}$ and $\overline{BC}$ can be expressed in terms of the interplanar spacing, *d,* and the angle of diffraction, θ*:*

$$\overline{AB} = d \sin\theta \tag{2}$$

$$\overline{BC} = d\ sin\theta \tag{3}$$

Substituting Equations (2) and (3) into Equation (1) yields:

$$n\lambda = d\ sin\theta + d\ sin\theta \tag{4}$$

which simplifies to the expression given for Bragg's Law:

$$n\lambda = 2d\ sin\theta \tag{5}$$

Bragg's Law, Equation (5), describes the relationship between neutron wavelength, angle of diffraction and the interplanar spacing of atoms in a crystal lattice. Bragg's law can be used for phase identification (i.e., measurement of the diffraction angle), wavelength

calibration (i.e., measurement of the beam wavelength) or lattice strain measurements (i.e., measurement of the *d*-spacing). The use of Bragg's law for the measurement of interplanar spacing between a stressed and un-stressed (stress free) material is the basis for the peak-shift method for determining elastic residual strain in a material. The accuracy of the measured strain and calculated stress depends on the accuracy to which the angle of diffraction is determined from the raw diffraction data. Strain measurement often involves careful consideration of the peak position and contributions to peak broadening due to material-neutron interactions, as discussed in the following section.

2.7.1.3 Diffraction Peaks and Peak Broadening

The peak position (diffraction angle) and peak width can provide information regarding the state of the material. Depending on the relative changes in these parameters between ideal (i.e., stress free, no texture, etc.) and actual samples, the state of the material including strain, texture, grain size and contributions from Type II and III residual stress can be inferred. However, other effects, such as crystal mosaics and variations in the neutron wavelength can also influence the profile of the diffracted peak. As a result, prudent attention to which contributions have resulted in the observed changes in the diffraction data is required for accurate analysis. Typical neutron diffraction data that has been curve fitted showing the parameters of interest and the information provided is shown in Figure 14.

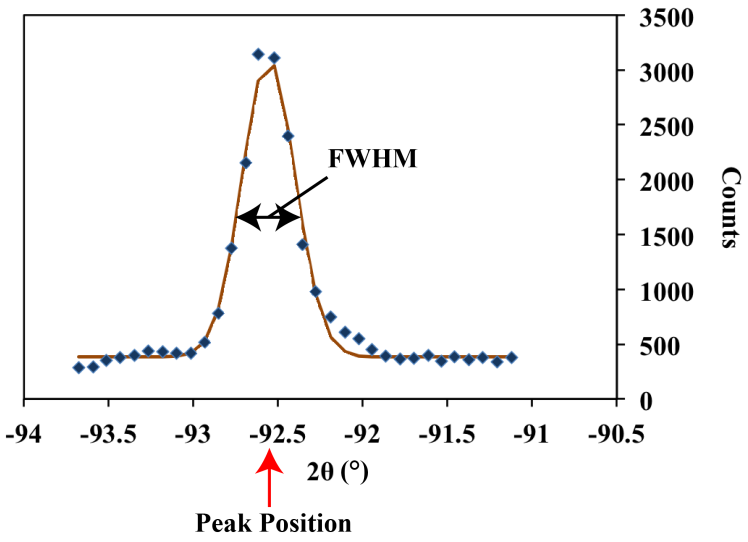

Figure 14: Single diffraction peak taken along *x*-direction stress analysis of ST + DA IS as-received material.

Residual Strain: When a material is plastically deformed, slip occurs within the crystal lattice of the material and results in changes in the shape of the grains. The extent of the grain deformation is a result of the applied load, as well as the nature of the interactions between adjacent grains (since each grain retains grain boundary contact with its neighbors). The interactions between grains limit the degree to which each grain can deform (when loaded) and recover (when unloaded) in a polycrystalline material. As a result, when the load is removed from the material, the crystal lattices of the grains are typically left in a bent, twisted or a generally deformed state and some elastic strain may become 'locked' in the material. Thus, the material is said to have retained residual strain. Since the residual strain deforms the crystal lattice, a diffraction experiment will result in a diffraction angle at a slightly different position as compared to an un-strained sample of the same material [*71*] [*76*] [*77*]. The change in the diffraction angle position as a result of residual strain is

illustrated in Figure 15. More details on how residual strain and stress is determined from diffraction data is provided in Section 2.7.1.4.

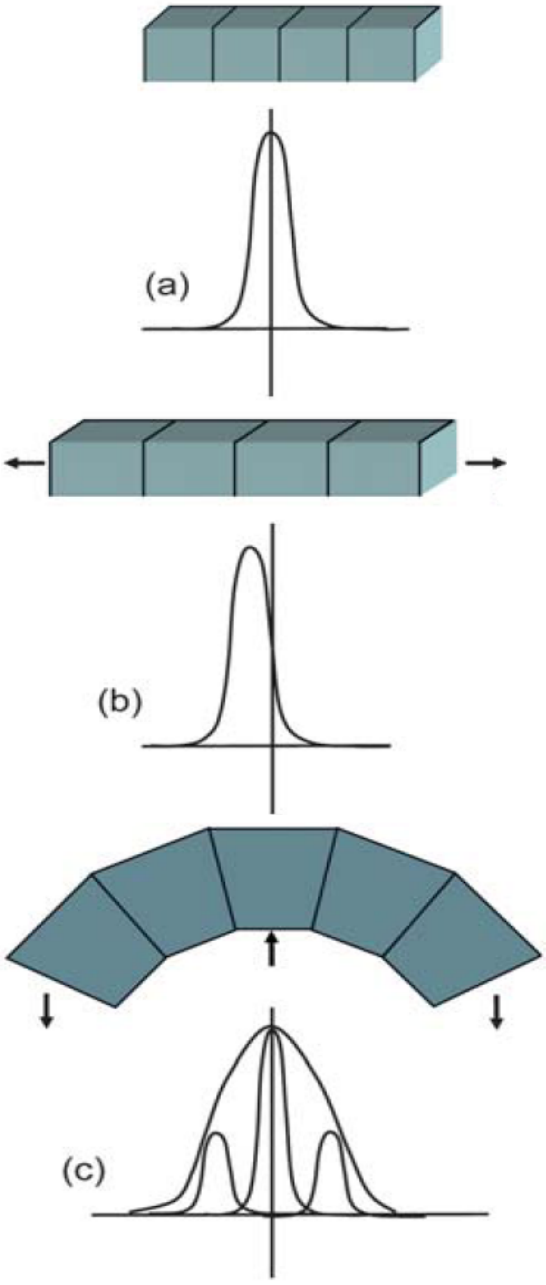

Figure 15: Effect of strain on the crystal lattice: a) No strain, b) Uniform strain across the crystal lattice, c) Non-uniform strain across the crystal lattice. (Adapted from [*75*] with permission of The Royal Society of Chemistry http://dx.doi.org/10.1039/C0NR00561D).

Crystallographic Texture: Similar to strain, preferred orientation of the crystals within a polycrystalline material (known as crystallographic texture) will result in more or less grains (depending on the orientation with respect to the beam) to contribute to a single diffraction peak per unit volume, as compared to the same material with perfectly equiaxed randomly distributed grains. This will result in an increased (or decreased) number of counts (or peak intensity) as compared to the same material without texture [*77*]. The difference in peak position between a material with texture (and no stress) and one with stress (and no texture) with respect to a material with stress free randomly distributed crystal structure is illustrated in Figure 16.

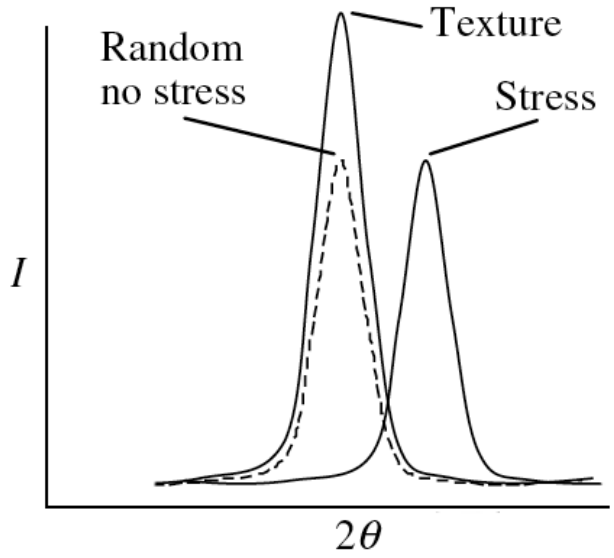

Figure 16: Effect of crystallographic texture on diffraction intensity [*77*]. (Bob B. He, Two-Dimensional X-ray Diffraction, © 2009 Wiley & Sons, Inc., Reproduced with permission from Wiley Books).

Grain Size: The effect of the grain size on the diffraction data may not be as apparent as that from strain or texture effects. However, as the number of diffracting grains increases per unit volume (smaller grain size), the slight variations between diffracting grain interplanar

spacing also increases. The difference between interplanar spacing, based on Bragg's law (Equation 5), results in different diffraction angles for each contributing grain. This creates a fuller diffraction peak profile, which may obscure the individual contributing peaks (as illustrated in Figure 17b), which may be visible when fewer grains (larger grain size) are diffracting (as illustrated in Figure 17a) [*75*] [*78*]. The broader diffraction peak profile is typically reflected as an increase in full width half maximum (FWHM) magnitude.

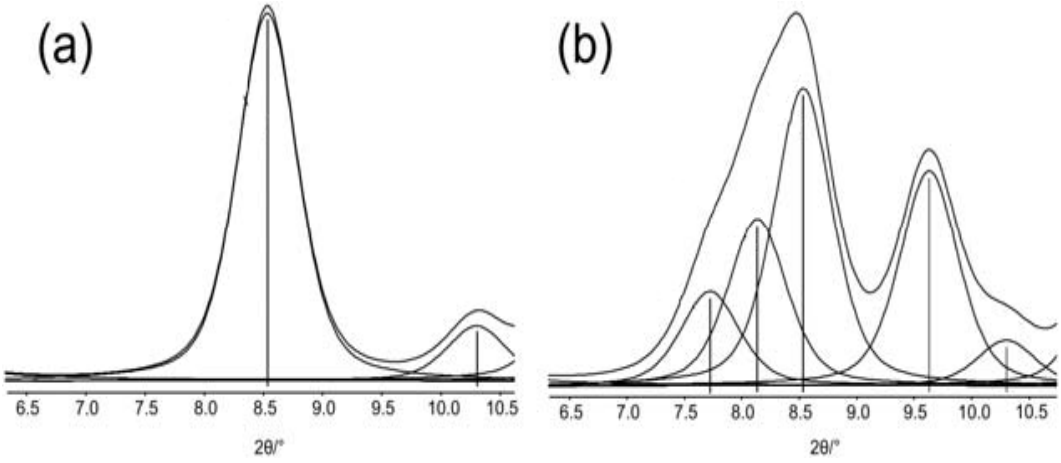

Figure 17: Effect of grain size on the diffraction peak profile: a) Single diffraction peak at 2θ = 8.5°, b) Three reflections that are obscured by a single peak. (Reproduced from [*75*] with permission of The Royal Society of Chemistry http://dx.doi.org/10.1039/C0NR00561D).

For most metallic materials, there is a range of grain sizes that contribute to the diffraction profile. As seen in Figure 18, small grains contribute to the edges of the peak, making the peak more inclusive of the grain distribution in the bulk material, while the larger crystals contribute more to the center of the peak. The effect of the grain size and the distribution of grain size on the diffraction profile is also shown in Figure 18.

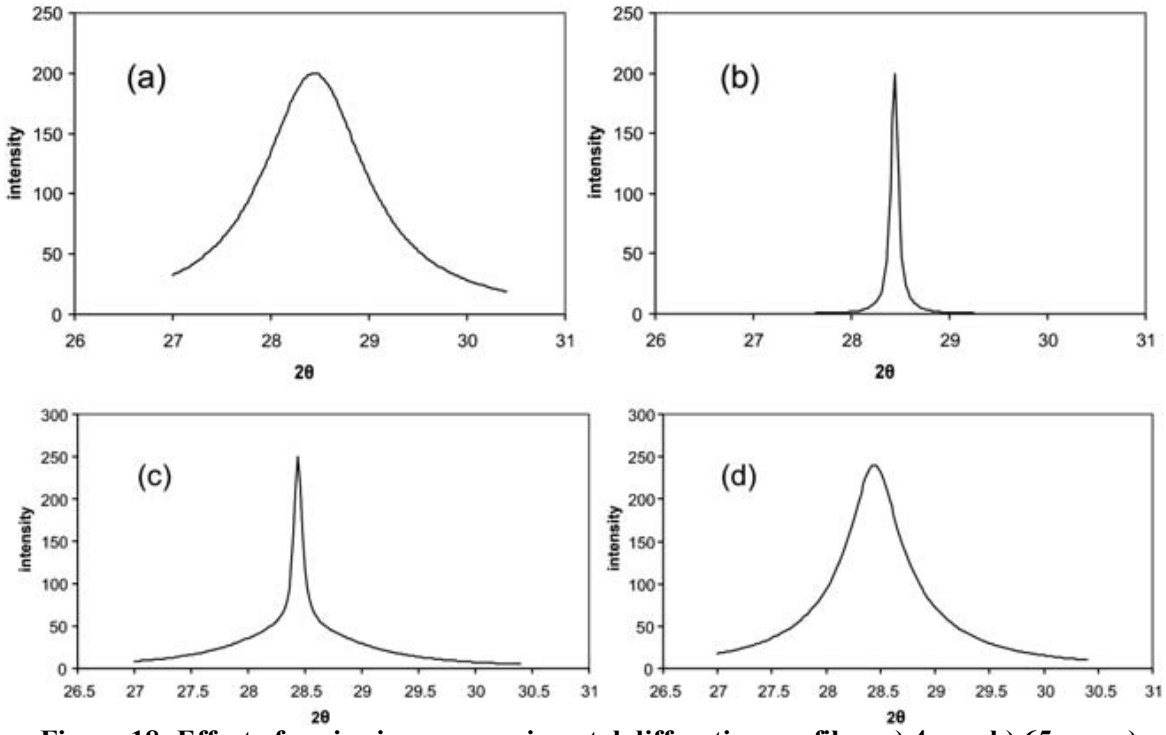

Figure 18: Effect of grain size on experimental diffraction profiles: a) 4 nm, b) 65 nm, c) Mixture of 4 nm and 65 nm grains and d) Mixture of 4 nm and 11 nm grains. (Reproduced from [*75*] with permission of The Royal Society of Chemistry http://dx.doi.org/10.1039/C0NR00561D).

As more grains contribute to diffraction, the intensity of the overall diffraction peak increases. However, it should also be noted that Type II and III residual stresses may contribute to peak broadening and their relative contributions to the overall peak profile may change as the number of diffracting grains varies (for a constant gauge volume). Therefore, peak broadening due to grain size effects is difficult to determine and often requires significant data manipulation and numerical methods to study. Typically, the neutron diffraction technique increases in accuracy as more grains contribute to diffraction (i.e., a more representative average residual stress of the bulk material is obtained).

Crystal Structure: Since crystallographically perfect materials do not exist, there are always some variations within a material's grain crystal lattice. Stacking faults or dislocations that develop during the material's manufacture and service history may cause deviations or defects in the crystal structure. Depending on the arrangement of these defects, a single grain may have several arrangements of the lattice structure, which produce a mosaic effect, as shown in Figure 19.

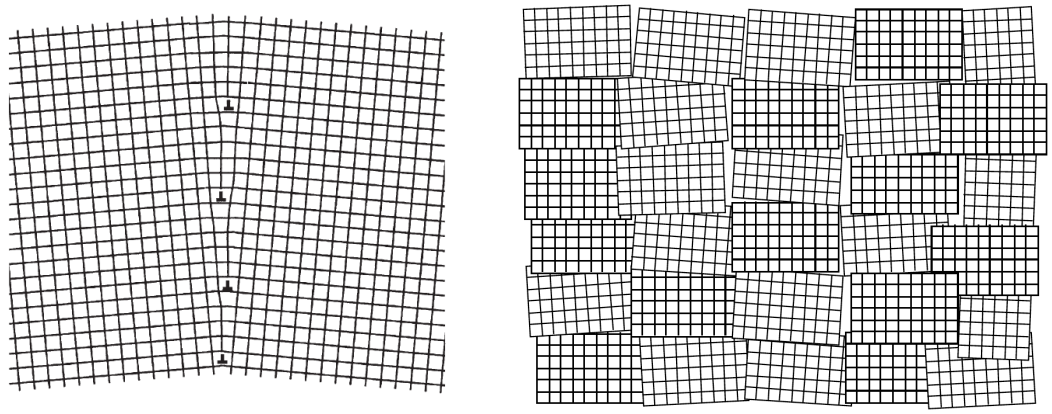

a) b)

Figure 19: Incident (I) and diffracted (D) neutrons and the variation in diffraction angle (Black and Orange θ) for: a) Tilt boundaries resulting from vertical stacking of several dislocations [*64*], b) Grain mosaic structure resulting from numerous tilt boundaries [*77*]. (a - Reprinted from Recrystallization and related annealing phenomena, 2nd Edition, F. Humphreys and M. Hatherly, Chapter 4: The structure and energy of grain boundaries, pp 95, (2004) with permission from Elsevier [*64*]. b - Reproduced from Two-dimensional x-ray diffraction, B. He, John, Wiley & Sons, INC., 2009 with permission from Wiley Books [*77*].)

When the incident neutrons diffract from various crystal orientation in the mosaic structure, a change in the diffraction angle of the detected diffracted neutron beam will result. As such, neutron diffraction measurements on imperfect (mosaic) grain structures result in peak broadening, rather than a single peak at the diffraction angle of interest, as shown in Figure 20.

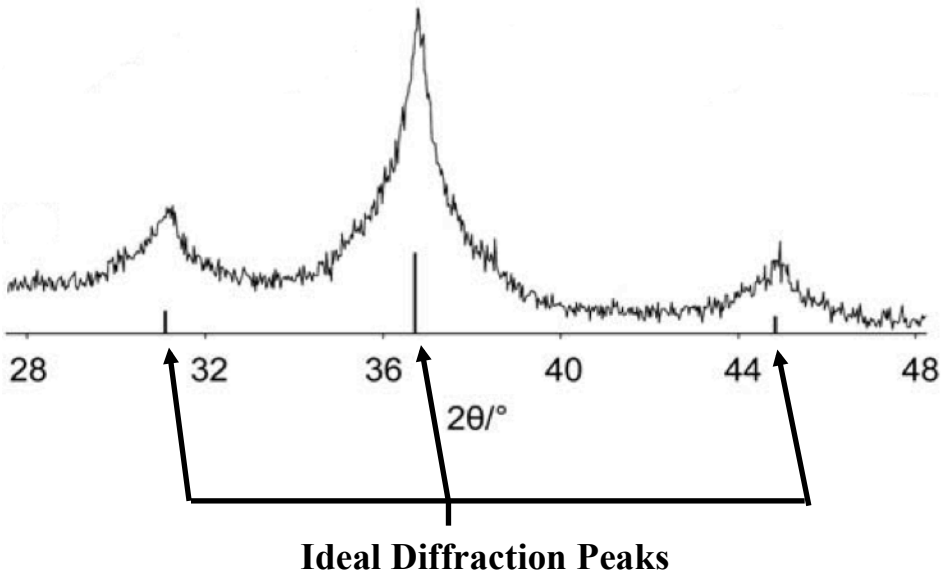

Figure 20: Experimental diffraction peak for Co_3O_4 powder. Theoretical (ideal) peaks shown as bars under the patterns. (Adapted from [*75*] with permission of The Royal Society of Chemistry http://dx.doi.org/10.1039/C0NR00561D).

Multiple peaks (as seen in Figure 17b) may also result from diffraction contributions from several planes of a particular phase in the material. How close the peaks are is dependent on the crystal structure of the particular diffracting phases [*75*].

Other Effects: Other effects such as variation in the neutron beam collimation (i.e., not all the neutrons within the collimated beam are parallel and impinge on the material surface at the same angle) and the variation in the neutron beam wavelength (i.e., not a single monochromatic beam of neutrons, but a beam with some variation in the wavelength) will also contribute to peak broadening. However, since these effects are a result of the experimental setup and not neutron-material interactions, these effects would be common to all experiments performed using the same experimental setup and equipment settings. Therefore, steps should be taken to minimize contributions to peak broadening from these

effects, by following proper experimental setup and calibration procedures prior to performing any neutron diffraction experiments.

2.7.1.4 Residual Stress Measurement using Neutron Diffraction

When a crystalline material is subjected to tensile loading, the crystal lattice expands along the loading axis from its stress-free natural state and contracts for compressive load. The resulting expansion or contraction of the crystal lattice and associated variation in the interplanar spacing can be quantified using the peak-shift method summarized in Equation (6) [*71*]:

$$\epsilon = \frac{d_{hkl} - d_{0-hkl}}{d_{0-hkl}} \tag{6}$$

where d_{hkl} is the inter-planar spacing for the (*hkl*) plane in the stressed sample and $d_{0\text{-hkl}}$ is the stress free inter-planar spacing for the (*hkl*) plane.

For isotropic materials, the corresponding stresses along the orthogonal *x*-, *y*- and *z*-directions can be calculated using the generalized Hooke's law shown in Equation (7) [*71*] for the *x*-direction.

$$\sigma_X = \frac{E_{hkl}}{(1+\nu_{hkl})(1-2\nu_{hkl})}[(1-\nu_{hkl})\,\epsilon_X + \nu_{hkl}(\epsilon_Y + \epsilon_Z)] \tag{7}$$

where ε_x, ε_y, ε_z are the strains in the *x*-, *y*- and *z*-directions, σ_X is the stress in the *x*-direction, E_{hkl} and υ_{hkl} are the Young's modulus and Poisson's ratio for the plane of interest, respectively. Stress in the *y*- and *z*-directions can be found in a similar manner.

Chapter 3: Experimental Procedure

This chapter describes the procedure for the experiments performed in this research.

3.1 IN 718 Material Samples

Commercially available rolled slab of virgin (V) IN 718 superalloy was obtained from Rolled Alloys (Edmonton, Alberta) in the solution annealed state (i.e.,1 hour solution heat treatment (ST) at 968 °C, followed by water quenching to room temperature). This heat treatment is often used in the aerospace industry to increase the workability of the alloy. The composition of the virgin IN 718 alloy is provided in Table 1, as per the manufacturer's material specification sheet.

Table 1: Composition of virgin IN 718 provided by the supplier (in wt.%) [*79*].

Ni	Cr	Fe	Nb	Mo	Ti	Al	Cu
54.01	18.57	17.09	5.21	2.87	0.96	0.58	0.24

Co	Si	Mn	C	P	Ta	B	S
0.17	0.10	0.08	0.03	0.009	0.003	0.002	0.0004

Additionally, IN 718 was obtained from the NRC and used in the calibration and optimization of the weld equipment parameters. This NRC V material was termed "Raw" in this thesis. The composition of the NRC material fell within the commercially accepted limits for IN 718.

In-service (IS) IN 718 material was also used and examined in this research. The IS material samples were extracted from two forged aero-engine turbine disks that were removed from service prior to their end-of-life (or time expiration limit). The disks were supplied by the NRC in the ST condition, which followed standard aerospace industry

practices to ST the IN 718 disks upon removal from service in preparation for repair. The ST was performed at 954 °C for 1 hour in vacuum, followed by cooling to 538 °C at a rate of 16 °C/min in an argon (Ar) atmosphere, and then rapid cooling in Ar to room temperature.

It was assumed that both forged disks underwent standard industry casting, forging and heat treatment processes prior to service. The exact operating environment and the number of cycles of the disks are confidential. However, it was assumed that the material was exposed to temperatures close to the peak operating temperature of IN 718 of ~650 °C [*5*].

Sections of the disks that were used for microstructural analysis are shown in Figure 21.

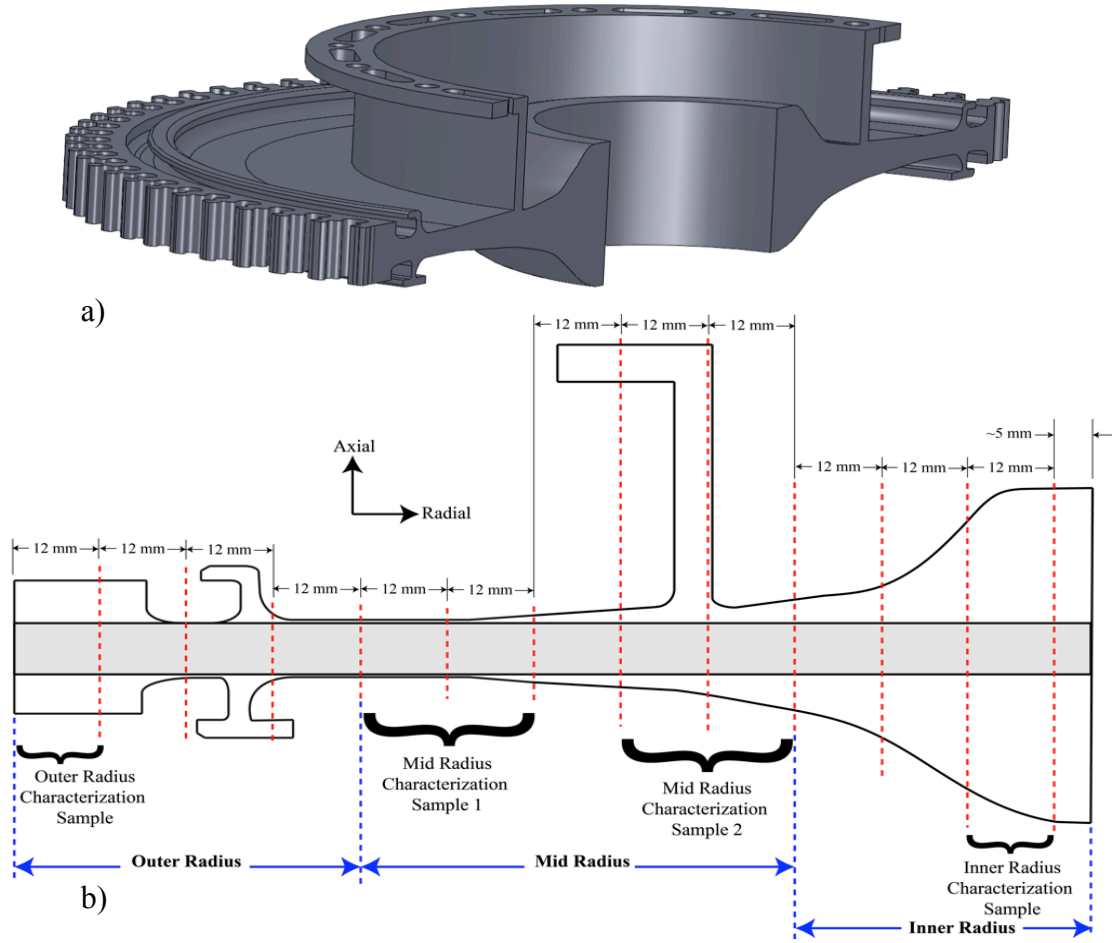

Figure 21: Geometry of the in-service disk turbine: a) Disk cross-section, b) Cross-section showing regions for metallurgical characterization. The shaded region shows the region used for characterization on the extracted samples.

Samples for microstructural analysis were sectioned from the V and IS as-received materials using a slow speed diamond cut-off saw and wire electrodischarge machining (EDM), respectively. The naming schemes used to identify the regions extracted from the IS disks throughout this work were denoted as: outer radius, mid radius 1, mid radius 2 and inner radius, as seen in Figure 21.

IN 718 coupons that were used for LFW were extracted from the V as-received material using a water-jet and machined to final dimensions on a mill. In the case of the IS samples for LFW, wire EDM (performed at the NRC) was used due to the complex geometry of the disks. The final dimensions of all the test coupons were 34 x 12.5 x 9 mm.

3.2 LFWing and PWHT of IN 718 Alloy

Prior to welding of the test coupons, the faying surfaces on each coupon to be welded were first ground with 800-grit SiC abrasive paper, which was followed by a thorough cleaning with acetone to remove any oxides or contamination on the surfaces. The coupons were then placed in the clamping fixture of the LFW process development system (PDS) at the Aerospace Structures, Materials and Manufacturing facility at the National Research Council Canada – Aerospace (Montreal, Quebec). The LFWing process was performed under ambient conditions without any shielding gas protection.

The LFW PDS consists of two actuators: (i) the forge actuator, which applied a downward pressure on the top stationary coupon and (ii) the in-plane actuator, which oscillated the lower coupon in the horizontal direction [*80*]. As illustrated in Figure 22, the oscillation of the lower coupon occurred in the direction parallel to the width of the coupon

(*y*-direction). For the V-IS samples, the bottom coupon corresponded to the IS material. The PDS weld parameters were programmed to proprietary conditions and two sets of joints were processed: V-V and V-IS (as-welded sample shown in Figure 22b).

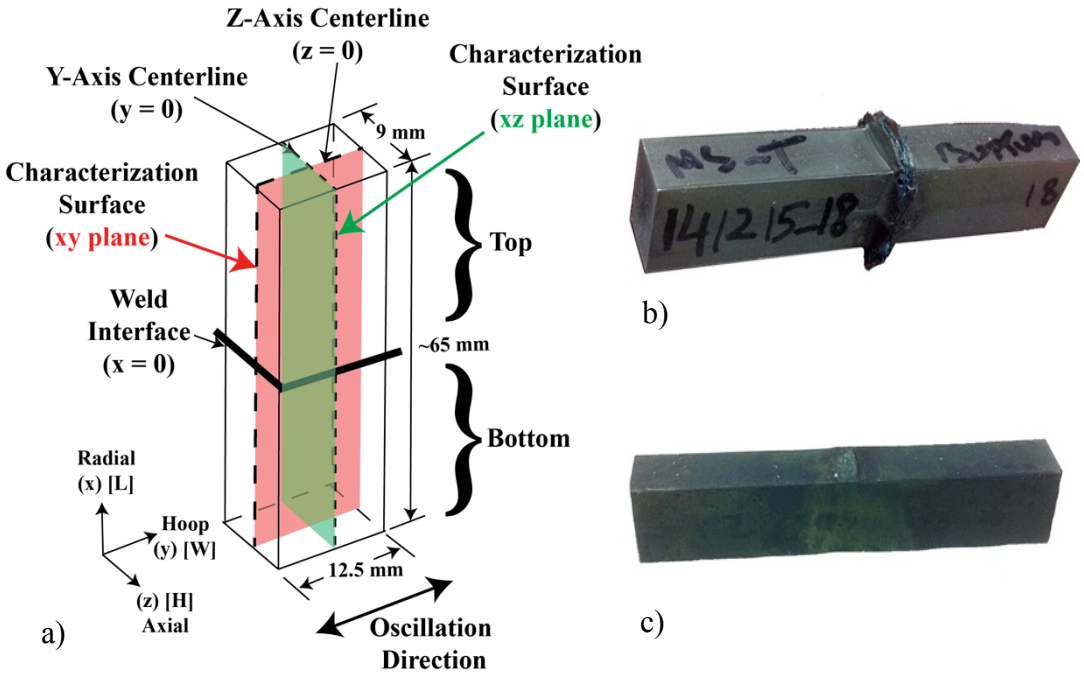

Figure 22: LFW sample geometry: a) Schematic of a LFWed sample showing the geometry, weld oscillation direction, and surface plane used for material characterization, b) As-welded sample, c) PWHTed sample with the flash removed [*81*]. (The International Journal of Advanced Manufacturing Technology, Mechanical properties and microstructural evolution of in-service Inconel 718 superalloy repaired by linear friction welding, 2016, pp. 1-16, M. Smith, L. Bichler, J. Gholipour and P. Wanjara, © Her Majesty the Queen in Right of Canada 2016. With permission of Springer).

Some LFWed samples were also subjected to PWHT consisting of ST and double aging (DA) heat treatments (ST + DA). A representative PWHT sample is shown in Figure 22c. The ST consisted of holding the welded samples at 1020 °C for 1 hour in an argon atmosphere, followed by air cooling to room temperature. The DA heat treatment consisted of holding the welded samples at 745 °C for 8 hours under an argon atmosphere, followed by

furnace cooling at a rate of 25 °C/min to 645 °C and soaking at this temperature, while maintaining an argon atmosphere for 8 hours, followed by air cooling to room temperature.

Alignment of the weld interface was done by two methods, which depended on the analysis that was being performed subsequent to welding. For microstructural analysis, the weld interface was found by setting $x = 0$ at the point where the straight oxide inclusion protruded into the sample from the flash, as shown in Figure 23 (area used for alignment is highlighted by the red box in Figure 23a). For analysis of the samples where microstructural features could not be directly assessed (hardness tests, tensile tests and neutron diffraction), the weld interface was aligned based on visual inspection of the interface region in the flash. Alignment of the sample for microstructural and mechanical property characterization was maintained for all testing and analysis, where the weld interface was defined as $x = 0$ (shown in Figure 22a and Figure 23). Depending on the characterization surface used (*xy* or *xz* planes) the centerline corresponded to $y = 0$ or $z = 0$, respectively (centerline shown in Figure 22a) and the "core region" was defined as the region ± 2 mm from the centerline (shown in Figure 23a), which corresponded to the largest region free from edge effects.

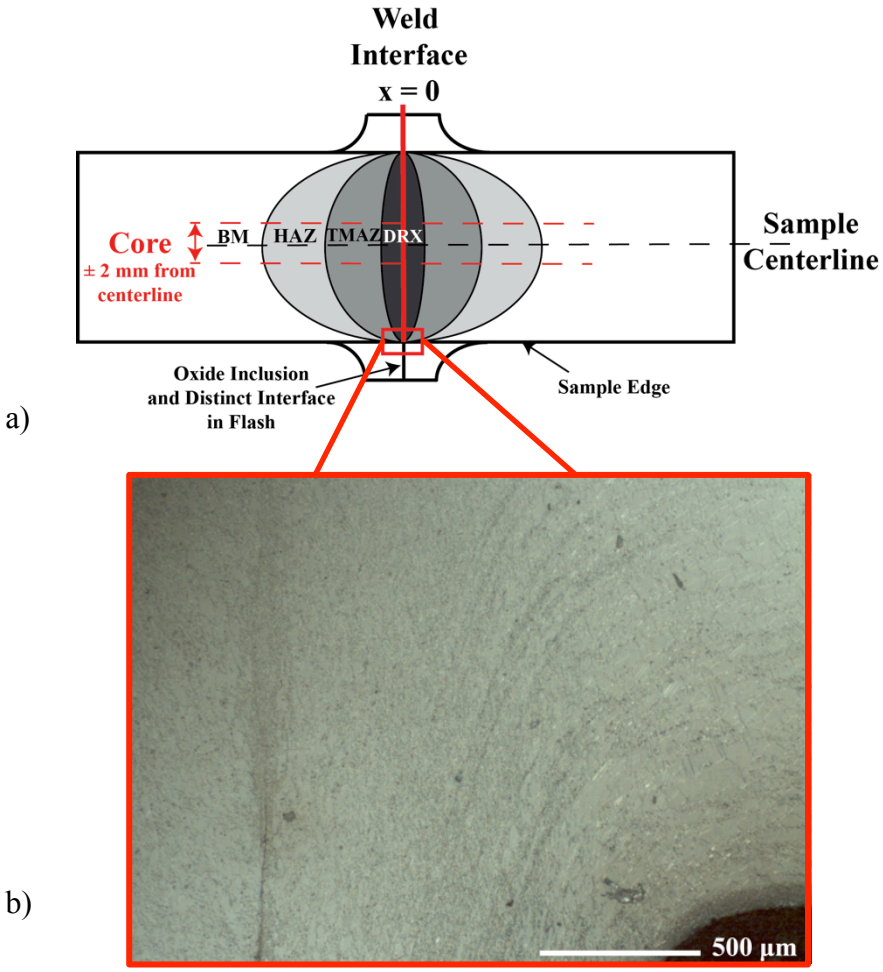

Figure 23: LFW sample microstructural development: a) Organization of weld regions and alignment of the weld interface, b) Optical micrograph of the flash and weld interface - highlighted red box region from a).

A FLIR SC8303 infrared (IR) camera with an indium antimonide detector and an image capture resolution of 1024 x 1024 pixels was used to measure the temperature at the weld interface during welding. Calibration of the IR camera was performed by the manufacturer (FLIR) and was confirmed by emissivity testing prior to the LFW experiments. Emissivity tests were conducted at NRC – Aerospace by heating a test superalloy (with a properly calibrated thermocouple attached) to several temperatures. The thermocouple reading was

then compared to the IR camera temperature reading. Good agreement between the two methods was observed.

The IR camera was focused on the region between the two grips of the PDS where the material underwent plastic deformation and upsetting during the welding process (i.e., the weld interface region). IR data post processing was performed using ResearchIR Max software. IR video post processing snapshots are shown in Figure 24. For post processing, three locations of interest were selected using the IR ResearchIR Max software, as indicated by the green, red and blue cross-hairs in Figure 24. The cross-hairs were placed in regions where high temperatures were observed during the LFWing process. Based on the FLIR thermal analysis guidelines in the ResearcIR Max software [*82*], pixel averaging provided more accurate temperature measurement, as compared to a single pixel measurement. Therefore, each of the cross-hairs monitored an area equivalent to 3 x 3 pixels in the captured image and averaged the representative pixel temperatures, which was subsequently plotted. Since the locations selected by the cross-hairs were static with respect to the IR camera, (i.e., they did not move with the sample during LFWing), the exact location selected for each cross-hair corresponded to the location where high temperatures were observed during some point in the welding process. This can be seen in Figure 24c where the green and blue cross-hairs are observed to correspond to the locations of high temperature when t = ~6.5 seconds, while the red cross-hair only corresponds to a location of high temperature when t = ~4 seconds (shown in Figure 24b).

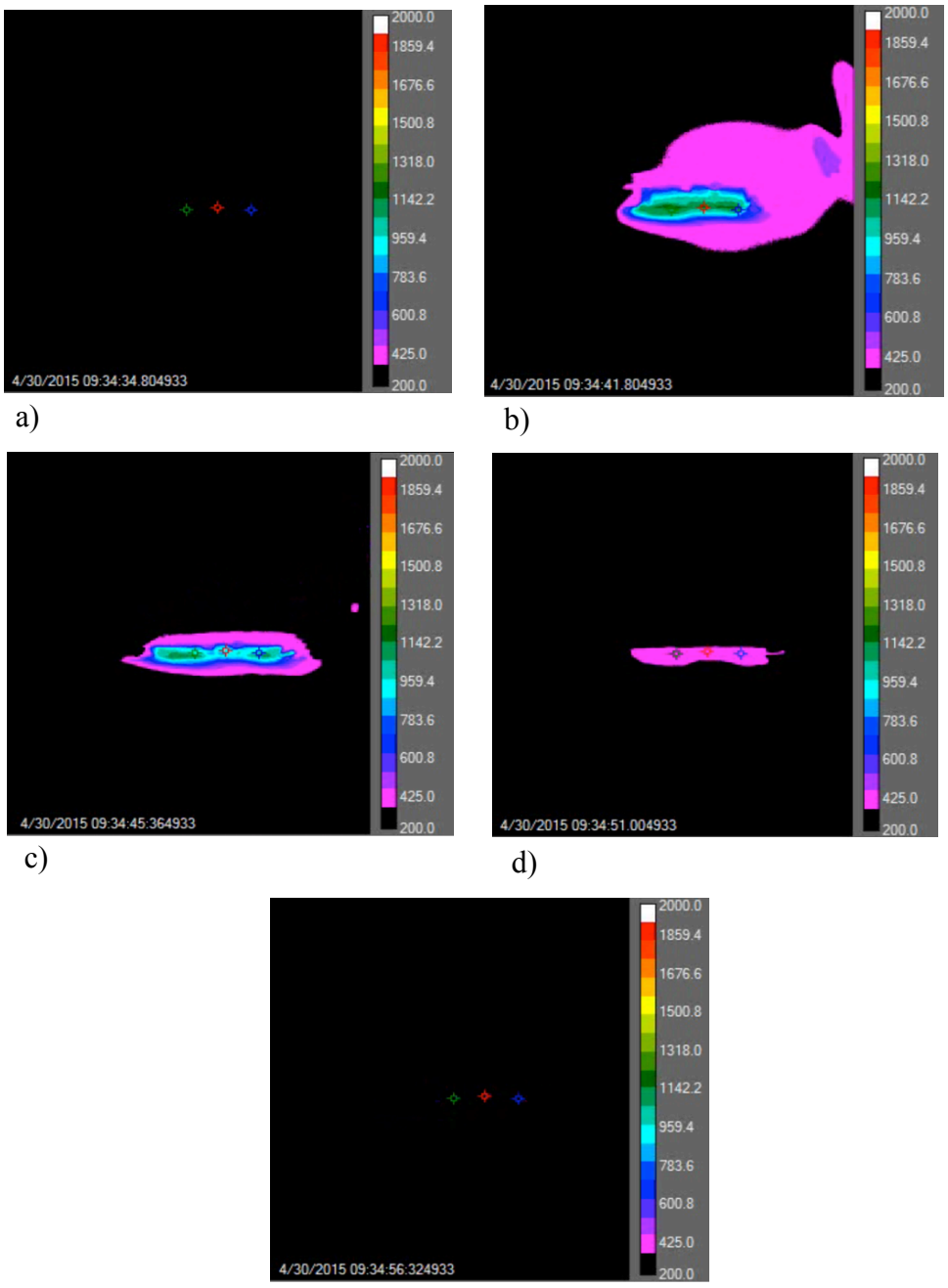

Figure 24: IR data post processing showing three 3 x 3 pixel averaging sites of interest (green, red and blue cross-hairs): a) Time (t) = 0 seconds, b) t = ~4 seconds (peak temperature), c) t = ~6.5 seconds (start of forging stage), d) t = ~11.5 seconds (forging force released), e) t = ~16 seconds (temperature below thermal range of IR camera.

Of the three generated temperature profiles, the profile that reached the highest temperature was used and reported as the peak temperature obtained from the 3 x 3 pixel averaging. The peak (single pixel) temperature during the welding process was also found by monitoring the entire weld region and reported as the peak temperature obtained from a single pixel.

3.3 Microhardness Measurement

Vickers microhardness was measured for the V as-received material, IS as-received material, V-V and V-IS as-welded samples and V-V and V-IS PWHT samples. Measurements were made using a Wilson VH3100 machine at The University of British Columbia – Okanagan Campus. The Vickers hardness equipment was calibrated using an ASTM standard calibration block. A 15 second dwell time, with an indent spacing of 350 μm and a load of 500 g was used for all measurements.

The microhardness profiles for the as-received material samples were measured across the center of the sample (as shown in Figure 25a). The minimum test point separation distance for all measurements was greater than five times the diagonal measurement of the indent in order to avoid skewing the hardness data by contributions from the neighbouring indent strain fields.

The distribution of test points for the as-welded and PWHT samples covered the surface of the samples; spanning a distance of ± 6 mm from the weld interface for the as-welded samples. The PWHT heat treatment resulted in uniform microstructure closer to the weld interface as compared to the as-welded samples. Therefore, to reduce the number of measurements, hardness was measured as far as ± 5 mm from the weld interface. The lines of

indentations reached up to 500 μm from the edge of the sample with each row spaced 500 μm apart, as shown in Figure 25. Thus, the microhardness profiles were collected across the unaffected based material, as well as the weld region. The raw data was then used to create a 2-dimensional and 3-dimensional map showing hardness distribution across each sample.

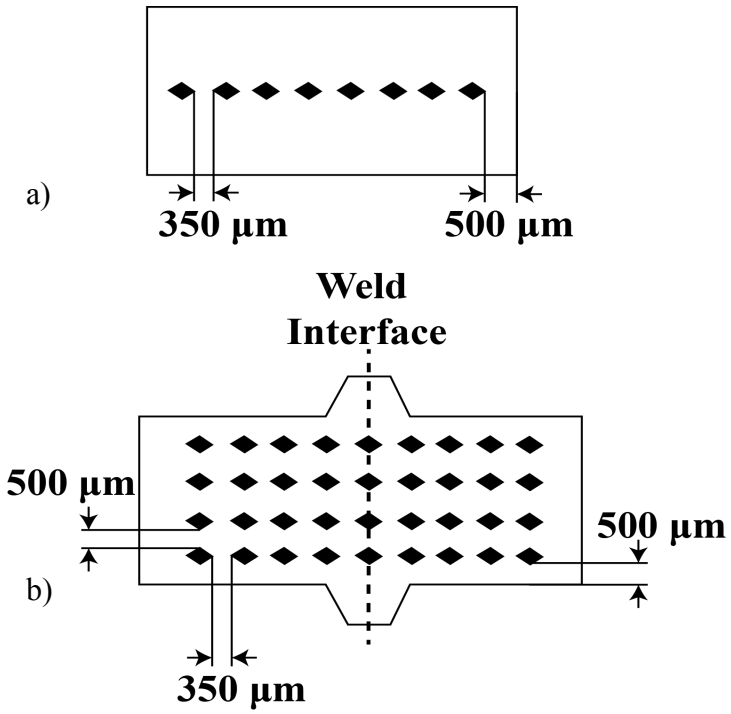

Figure 25: Distribution of hardness measurements for: a) As-received, b) As-welded and PWHT samples.

Similarly to the as-received material hardness profiles, the minimum indentation separation distance for all measurements was at least five times the diagonal measurement of the indent to avoid contributions from the neighbouring strain fields [*83*].

3.4 Tensile Test

Tensile tests were performed on three samples each of the V and IS as-received materials, as-welded samples (V-V and V-IS) and PWHT samples (V -V and V-IS) according to ASTM Standard E8M – 04 [*84*].

The virgin as-received, as-welded and PWHT IN 718 samples were machined in accordance with ASTM standards [*84*] for round sub-size samples with a 4 mm sample diameter. The grip length was 17 mm with a gauge length of 26 mm, as shown in Figure 26a.

Due to material and geometry limitations, flat sub-size specimens were extracted by EDM from the IN 718 disks. The IS tensile specimens were machined according to ASTM standards [*84*] for flat sub-sized samples with a 6 mm width, 6 mm thickness and a 25 mm gauge length, as shown in Figure 26b.

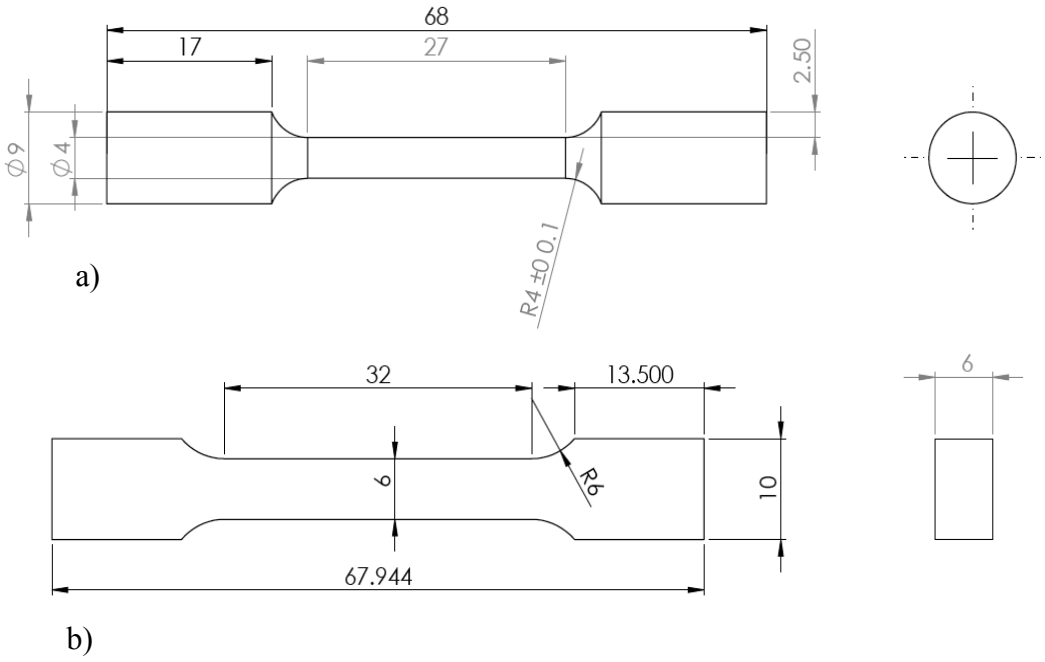

Figure 26: Dimensions of sub size tensile samples: a) Round, b) Flat. All dimensions are shown in mm.

The tensile tests were carried out at Ryerson University at room temperature using a United STM-50 frame with a mechanical extensometer to measure strain. United Testing Systems Canada Limited calibrated the United STM-50 test frame and the mechanical extensometer on an annual basis. Testing was conducted using displacement control at a rate of 2 mm/min.

3.5 Residual Stress and Strain Evaluation

Non-destructive residual strain mapping of the LFWed samples was performed using neutron diffraction at the Canadian Nuclear Laboratories (CNL) (Chalk River, Ontario) on the L3 beamline. A general overview of the samples and spectrometer is provided in Figure 27 to Figure 29.

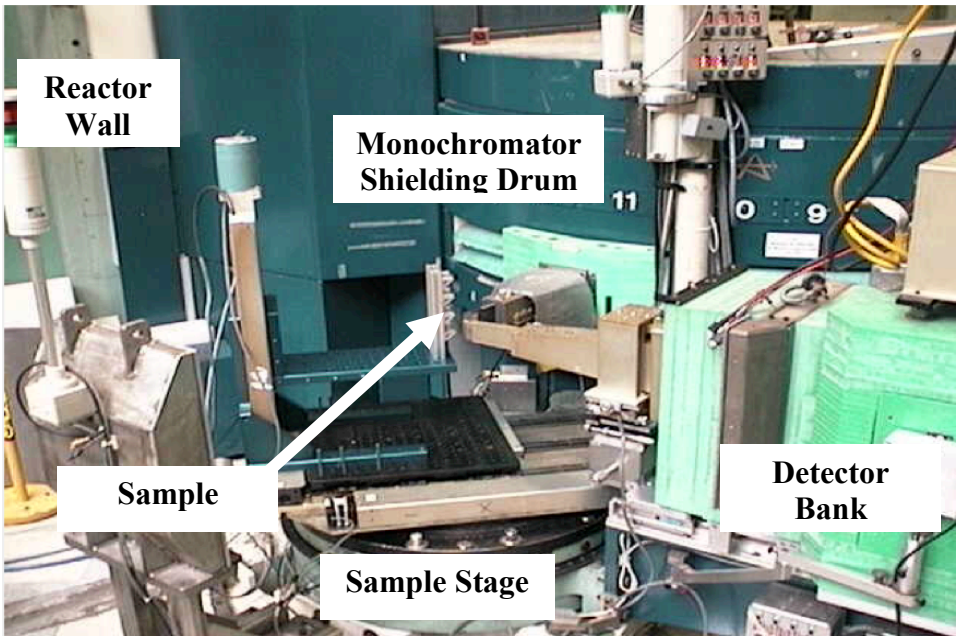

Figure 27: L3 triple axis spectrometer at CNL in Chalk River, ON.

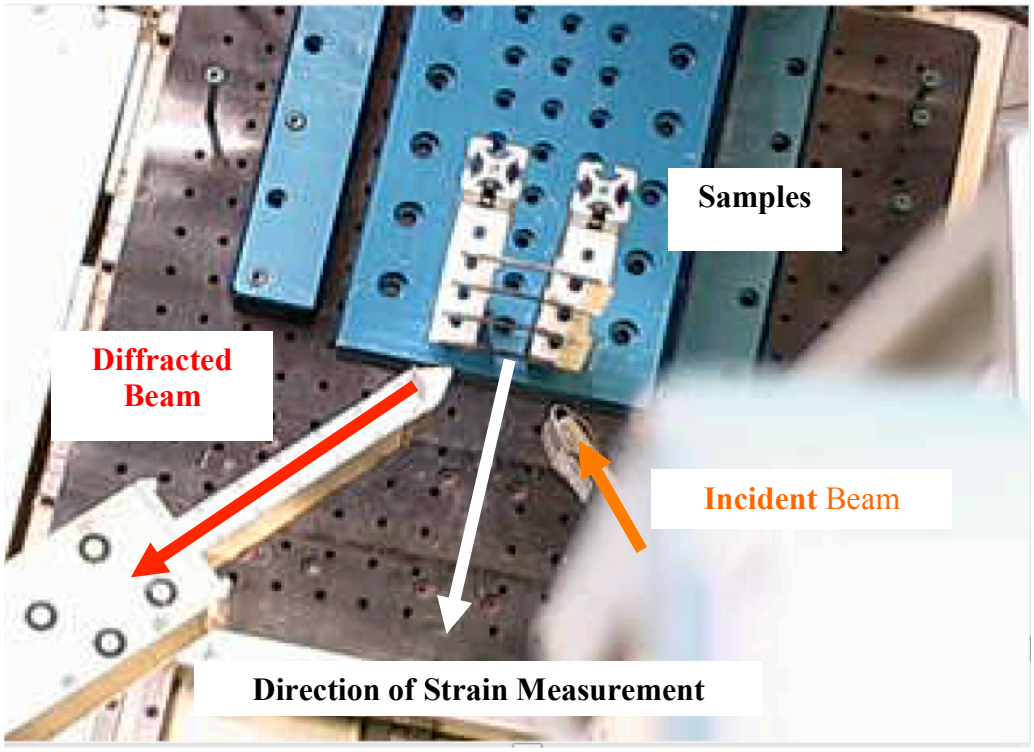

Figure 28: Sample arrangement for strain measurement.

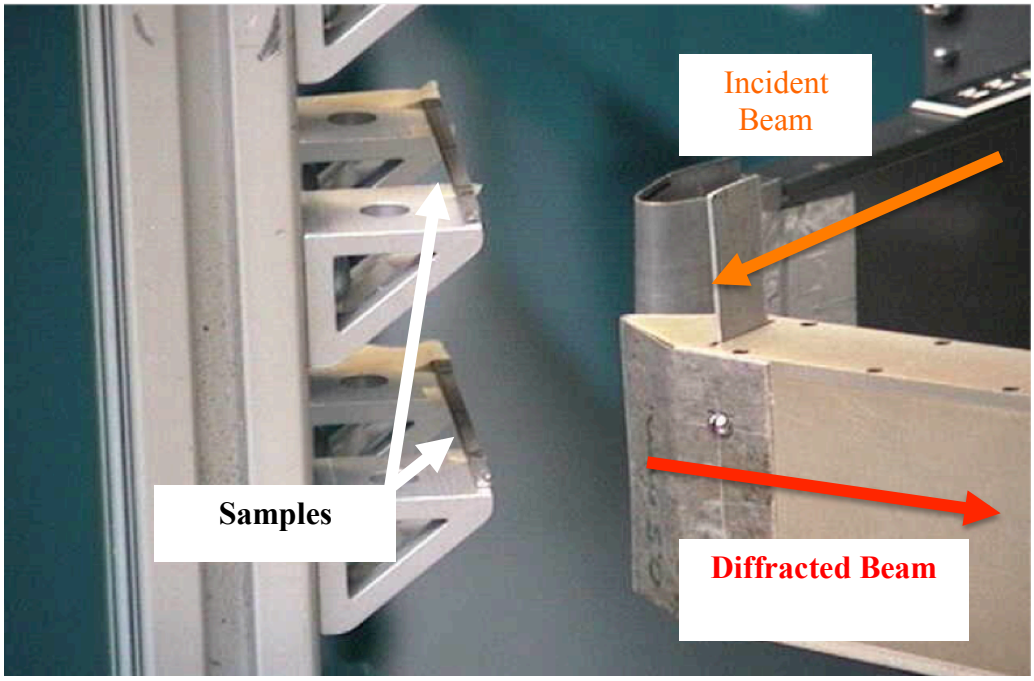

Figure 29: Side view of sample arrangement for strain measurement.

The as-welded and PWHTed samples, along with their stress free matchstick samples were aligned (using the optical alignment equipment designed for alignment of the spectrometer) on the sample stage so that the center of the flash corresponded to a position of $x = 0$ (to keep the neutron diffraction experiments consistent with all other experiments performed in this work). The neutron beam gauge volume was centered along the core of the material (to minimize edge effects in the strain measurements).

3.5.1 Neutron Diffraction Experiment Set-up and Calibration

Prior to calibration of the wavelength, the spectrometer was aligned following procedures outlined in CNL's standard set-up guide by R. Rogge *et al.* [*85*] under the supervision of CNL staff.

Neutron experiments were conducted for a total of 10 weeks of continuous scan time. The neutron diffraction experiments were performed in multiple sets of experiments. Before each set of experiments, the wavelength was calibrated with a germanium monochromatic crystal. The wavelengths used in the diffraction experiments were 1.5704 Å, 1.5697 Å, 1.5702 Å, 1.5695 Å and 1.5702 Å, while the strain was measured from the {311} planes.

The exact wavelength of the incident neutron beam was obtained from a wavelength calibration test performed prior to scanning the samples. Ultra-high purity Ni powder was used for calibration, where the exact diffraction angle (for a given wavelength and crystallographic plane) and interplanar spacing for several crystallographic planes were known. A Microsoft excel macro available to CNL staff was used to find the correct wavelength based on comparisons between theoretical and actual diffraction angles.

3.5.2 Neutron Beam Geometry

The general neutron beam geometry is shown in Figure 30. Initially, the neutron beam was shaped (using a collimator) to a width and height of 0.5 mm and 4.6 mm, respectively.

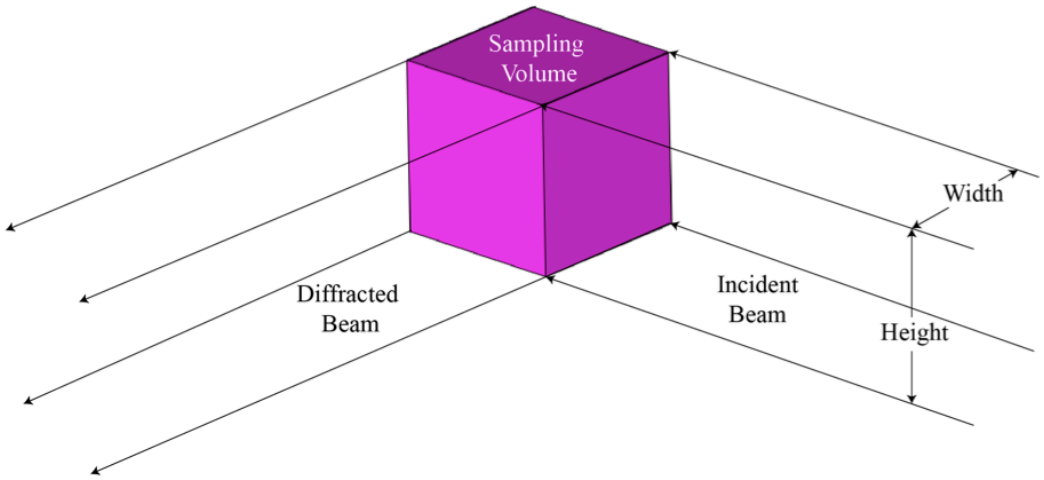

Figure 30: Neutron beam gauge volume.

However, microscopic analysis of the weld regions revealed that a 0.5 mm beam had significant overlap with multiple weld regions (i.e., HAZ, TMAZ and DRX).

As a result, a second set of neutron diffraction residual stress scans (high-resolution scans) was performed with a beam width of 0.3 mm X 4.6 mm in order to more accurately measure the lattice strain in the distinct weld regions.

3.5.3 Selection of Scan Locations

For the V-IS as-welded samples, a value of residual stress in the V base material away from the weld region (at x = -5 mm) was first obtained. Then, mapping along a line from x = -1.5 mm in 0.5 mm increments for the low resolution scans and 0.3 mm increments for the high resolution scans was carried out to x = 1.5 mm, as shown in Figure 31. Similarly, a final measurement was done on the IS material side at x = 5 mm. A similar procedure was

performed on the V-V as-welded and the V-V and V-IS PWHT samples. Two measurements in random locations in three orthogonal directions were also taken in each of the V and IS as-received material coupons. These measurements revealed the magnitude of the residual stresses in the materials in the as-received condition.

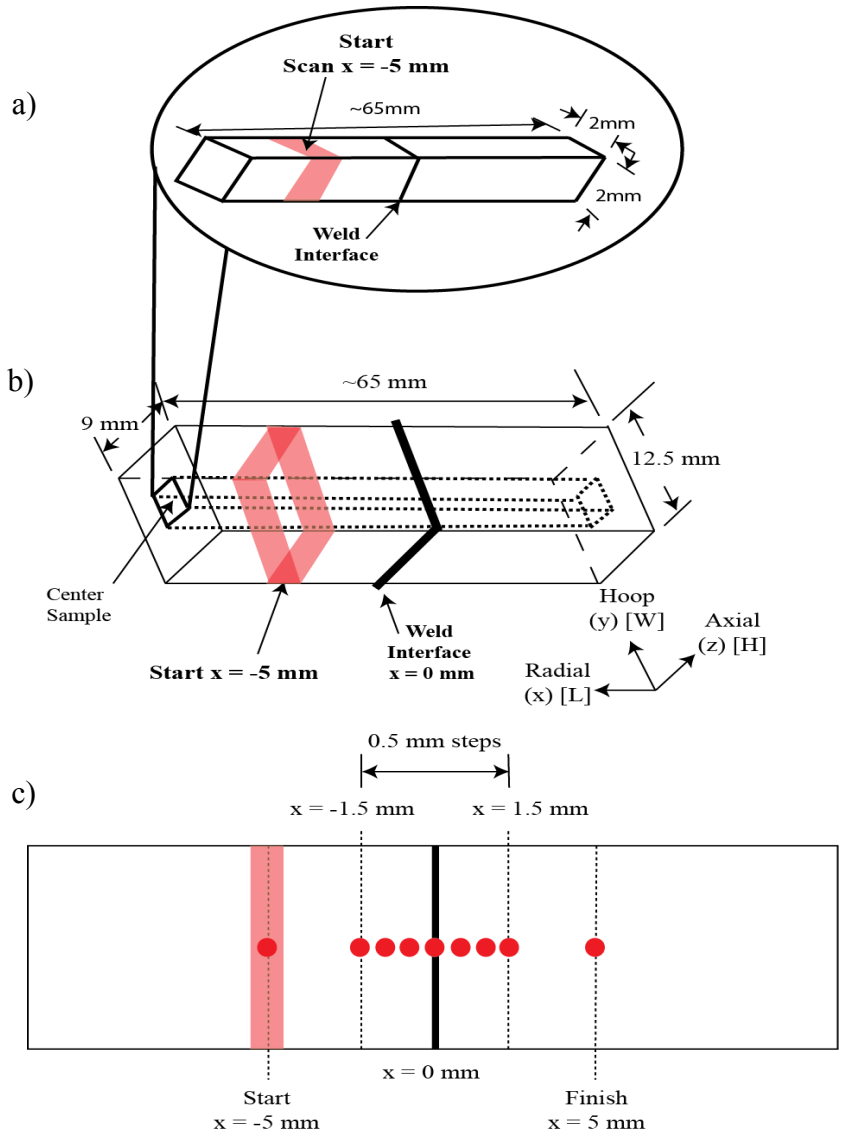

Figure 31: LFW sample showing regions of interest for neutron diffraction experiments: a) Matchstick stress free (d_0) sample taken from the core of as-welded sample, b) As-welded sample geometry, c) Scan locations of interest (red dots) along *x*-direction [*86*]. (Residual stress analysis in linear friction welded in-service Inconel 718 superalloy via neutron diffraction and contour method approaches, Vol. 691, M. Smith, J. -B. Levesque, L. Bichler, D. Sediako, J. Gholipour and P. Wanjara, pp. 168-179, Crown Copyright © 2017, with permission from Elsevier).

At every location, elastic residual strain was measured in three orthogonal directions (*x*, *y* and *z*) to enable the calculation of the elastic residual stresses at that location. In order to use the peak-shift method, a stress free matchstick sample (with associated stress free inter-planar spacing or d_0-spacing) was required. To obtain the d_0-spacing, a matchstick specimen was cut from the welded samples, as seen in Figure 31. For the as-welded and PWHT samples, scans in the *y*-direction and *z*-direction were made across a stress-free matchstick sample. The locations of the scans in the stress-free matchstick sample in the *y*-direction and *z*-direction were made at precisely the same locations as the scans in the stressed samples. The *y*-direction and *z*-direction stress-free values were then averaged for each location along the stress free sample and used as d_0-spacing for the calculation of strain and stress. For the PWHT samples, scans in the stress-free matchstick sample and stressed sample followed the same scan locations and procedure as the as-welded samples.

All strain values reported in this thesis correspond to strain from the {311} planes. The corresponding stresses at each scan location in the *x*-, *y*- and *z*-directions in the stressed samples were calculated using a generalized Hooke's law, Equation (7), where the values of the Young's modulus and Poisson's ratio were 194 GPa and 0.310 for the {311} reflection, respectively [*67*] [*68*].

3.5.4 Neutron Diffraction Data Statistical Interpretation

Statistical analysis of the raw neutron diffraction data was performed in order to validate the measured residual strain at each point. The first step was to set the number of neutrons that would pass through the incident beam collimator and subsequently interact with the sample. This value was called the beam count monitor value. The neutrons were counted

with a beryllium window monitor placed in the path of the incident neutrons. When the specific monitor value (number of neutrons) was reached at a given location of interest, the controller would move to the next measurement location on the sample. By changing the monitor value, adjustments were made to provide adequate peak-to-background counting statistics.

The location of the diffracted peak was measured with a neutron detector, which consisted of 32 wires. The center wire of the detector was aligned with the theoretical Bragg's peak position for the {311} plane. The wires were uniformly spaced to provide an angular span of ± 1.3° from the theoretical Bragg's peak position. An example of unprocessed diffraction data is shown in Figure 32.

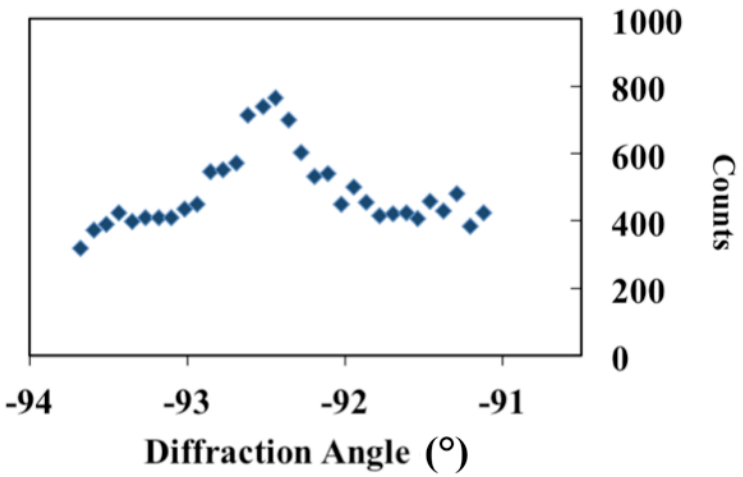

Figure 32: Raw neutron data.

For the low resolution scans, the monitor value of 810 000 (~2 hours per point) provided a good peak-to-background ratio. In some cases, the monitor value had to be increased to 1 224 000 (~3.25 hours per point) to allow for a valid statistical analysis of the data. For the low resolution and matchstick samples, a monitor value of 450 000 – 810 000 (~1.25 – 2 hours per point) provided adequate counting statistics.

The raw neutron count data was then fitted with a Gaussian curve using a linear least squares (Newton-Raphson) algorithm. Raw data fitted with a Gaussian curve using the Microsoft Excel macro is shown in Figure 33.

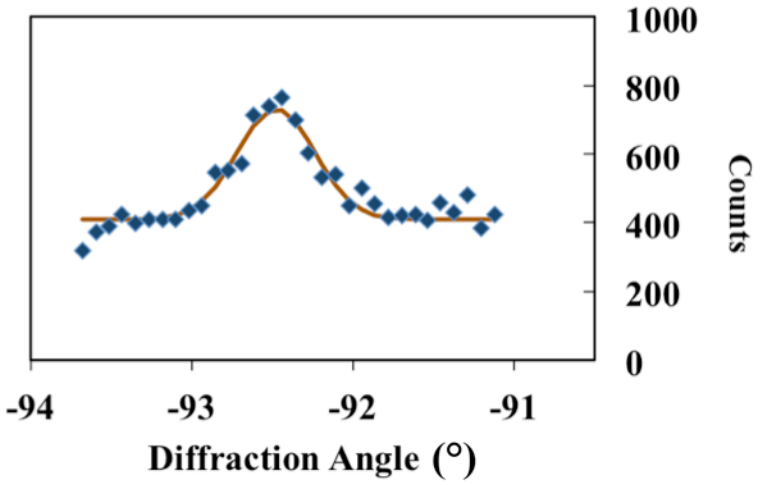

Figure 33: Gaussian fitting of raw neutron data.

The Gaussian fitting returned several parameters characterizing the diffraction peak. These parameters included:

1) Peak Position: The central position of the diffracted peak resulting from the fitted curve.
2) Integrated Intensity: The integrated area under the diffraction peak resulting from the fitted curve. This value was normalized based on the Monitor value that was used for the measurement.
3) Full width half maximum (FWHM): A measurement of the width of the peak taken at a location corresponding to half the peak height.

Prior to analyzing the diffraction data, each diffraction peak was judiciously examined to meet the selection criteria in Table 2. If the diffraction data did not meet the selection

criteria, a second scan was performed (using the same monitor value) and the data from the two scans combined and subsequently analyzed.

Table 2: Neutron diffraction peak selection criteria.

Parameter	Selection Criteria
Diffraction Counts	The peak from the Gaussian fit should be at least 100 counts higher than the background.
Integrated Intensity	Should be at least 1.0 or higher

If the combined diffraction data still did not meet the selection criteria, the point was scanned for a longer duration (increased Monitor values) until the selection criteria was satisfied.

After each point was accepted based on the selection criteria, the *d*-spacing was calculated using Equation (5) and the residual strain and stress calculated using Equation (6) and (7), respectively.

3.6 Microscopy Techniques

Standard metallographic preparation procedures were used to grind and polish the V and IS as-received samples, as-welded (V-V and V-IS) and PWHTed (V-V and V-IS) samples, as described in ASTM Standard E3 – 01 [*87*]. Samples were ground using SiC abrasive paper under flowing water. 120 grit SiC abrasive paper was used to remove the as-cut surface. Sequential grinding using 240, 400, 600 grit SiC abrasive paper was used to grind the surface and prepare it for polishing. Polishing was performed using 9 μm, 6 μm and 3 μm diamond paste suspended in diamond extender solution.

The grain boundaries in the IN 718 samples were revealed using an electro-etching technique on the polished surface following the processes outlined in ASTM Standard E 407-99 [*88*]. General microstructure electro-etching consisted of submerging the samples in 10 g

oxalic acid dissolved in 100 mL deionized water. A voltage of 8 V was applied for 25 seconds using a stainless steel cathode and a pure nickel anode [*88*]. Finer structures (MN, MC, γ', γ'' and δ phase) in all samples were revealed using a modified electroetching procedure with a solution of 8 ml H_2SO_4 and 100 ml H_2O at 2 V for 5 seconds using a pure titanium cathode and a pure nickel anode [*88*].

For EBSD analysis, electropolishing after manual polishing to 3 μm was done using a modified procedure from that described in [*89*] using a solution of 20 % H_2SO_4 and 80 % methanol at 25 V for 5 - 25 seconds (depending on the size of the sample) using a stainless steel anode and cathode. This produced up to a 98 % index rate at most EBSD scan locations.

A high-resolution Tescan Mira3 XMU field emission gun scanning electron microscope (FEG-SEM) at an accelerating voltage of 20 kV was used in secondary electron (SE) and backscattered electron (BSE) imaging modes to reveal microstructural features. Compositional analysis was achieved through x-ray energy dispersive spectroscopy (EDS) analysis.

Grain size measurements on the V and IS materials were carried out using the three-circle method using ten randomly chosen micrograph fields for each sample, following the principles described in ASTM Standard E112 – 96 [*90*] and validated using EBSD.

The EBSD studies were performed at an accelerating voltage of 20 kV using a Tescan Mira3 XMU FEG-SEM equipped with an HKLNordlysis Max EBSD detector and Oxford AZtecHKL EBSD acquisition system. During EBSD mapping, the electron beam scanned the polished surface of the sample tilted at 70° towards the detector. EBSD patterns were detected by a CCD camera, while the background was subtracted during post-processing with the Oxford Channel 5 HKL software used for data acquisition and analysis. For the V as-

received material, the scanned area for the EBSD maps was 457 μm x 305 μm with a step size of 0.6 μm, while for the IS as-received material, the scanned area was 135 μm x 135 μm with a step size of 0.2 μm. The scanned area for each EBSD site map across the weld interface for the as-welded samples was 138.7 μm × 138.7 μm with a step size of 0.2 μm. By contrast, for the PWHTed samples five different sites were examined across the weld interface. The scanned area for each EBSD site map across the PWHT weld interface was 1000 μm × 1000 μm with a step size of 5 μm.

The global texture of the γ phase (matrix) in the samples was determined. The pole figures reported in this work relate to {100}, {110} and {111} planes of the γ phase, corresponding to the normal of the polished surface.

Volume fractions of the various precipitates were determined following the principles outlined in ASTM Standard E562 – 02 [*91*] using ten randomly chosen micrograph fields. The volume fraction was determined assuming that the area fraction was equivalent to the volume fraction [*91*]. Precipitate size and interparticle spacing were measured from FEG-SEM micrographs using the Buehler OmniMet image analysis software. Measurements were made from 10 randomly selected micrograph fields, for 10 randomly selected particles. The interparticle spacing was measured to be the distance from the selected particle to the next nearest particle (of the same phase).

Chapter 4: Phase I: Microstructural Characterization

The following chapter outlines the results of microstructural and mechanical property characterization for the V and IS as-received material, as well as the as-welded and PWHT V-V and V-IS welds.

Selected results presented in this chapter were published in the following publications:

M. Smith, L. Bichler, S. Yannacopoulos, J. Gholipour and P. Wanjara, "Characterization of in-service and virgin Inconel 718 superalloy," in 2014 *Conference of Metallurgists*, Vancouver, 2014.

M. Smith, L. Bichler, J. Gholipour and P. Wanjara, "Mechanical properties and microstructural evolution of in-service Inconel 718 superalloy repaired by linear friction welding," *International Journal of Advanced Manufacturing*, 2016, [Available Online] http://dx.doi.org/10.1007/s00170-016-9515-2.

4.1 As-Received Material Characterization

The following section presents the results of the V and IS IN 718 as-received material microstructural and mechanical property characterization. SEM, EDS and EBSD microstructural results are presented and discussed along with room temperature hardness and tensile strength results.

4.1.1 As-Received Material Microstructure

Characterization of the δ phase, MC carbides and MN nitrides in the V and IS as-received IN 718 was accomplished by high resolution FEG-SEM analysis. Figure 34 shows representative micrographs of the microstructure of the V and IS material.

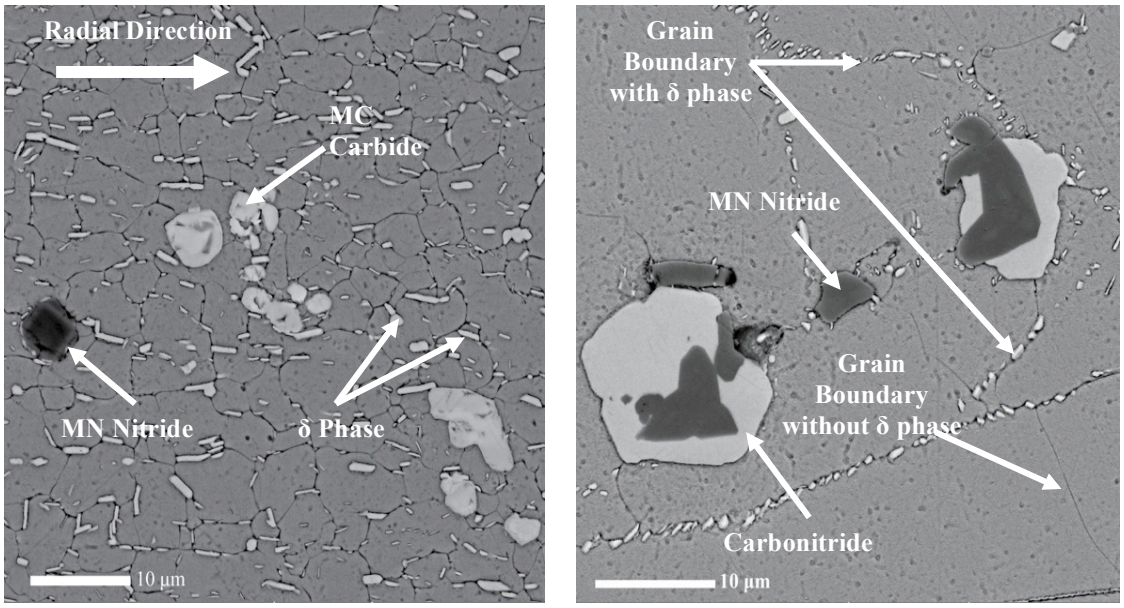

a) b)

Figure 34: FEG-SEM micrographs (BSE) representing: a) IS as-received material, b) V as-received material showing γ grain boundaries with and without the δ phase.

As seen in Figure 34a, the IS as-received material had many rod-like precipitates that were observed at the inter- and intra-granular locations. In the V as-received material, these precipitates were observed only along some grain boundaries. Based on a comparison of their morphology and composition (summarized in Table 3) with literature, these precipitates were identified as the δ phase [*1*] [*5*].

In both the V and IS as-received materials, several large blocky precipitates with irregular edges (white particles in Figure 34) were observed. These large blocky particles were often near precipitates that had rectangular and well defined edges (black precipitates in

Figure 34). In some instances, both the white and black particles appeared to be combined into one single precipitate, as seen in Figure 34b. Literature suggests that in IN 718, carbides typically appear as large globular or blocky particles in the matrix and are rich in Nb, while nitrides have a more defined, sharp rectangular appearance and are rich in Ti [*5*] [*27*]. Based on the morphology and composition (summarized in Table 3), the large white precipitates were identified as carbides (NbC), while the darker black precipitates were nitrides (TiN).

At higher magnifications, very small spherical precipitates were observed throughout the microstructure, as shown in Figure 35. Due to their size, compositional analysis on individual particles was not possible. However, based on their morphology and size, these precipitates were likely the γ' and γ'' phases, which are frequently observed in the IN 718 superalloy. In the literature, these phases were reported to have a disk-like or globular morphology [*1*] [*5*].

Table 3: Precipitate compositional range in V and IS materials compared to literature [*92*] [*93*] [*94*] [*95*]. Compound column shows: type of precipitate (material type) units.

Compound	Nb	Ti	Ni	Cr	Fe	N
δ phase (V) at%	5.1 – 11.1	1.4 – 2.2	56.9 – 63.5	11.7 – 19.1	9.7 – 15.7	-
δ phase (IS) at%	18.6 – 19.7	3.5 – 3.7	61.7 – 68.0	4.1 – 6.4	4.5 – 6.4	-
NbC (V) at%	82.0 – 83.4	13.2 – 11.6	2.5 – 3.0	1.0 – 1.1	0.8 – 1.2	-
NbC (IS) at%	78.7 – 84.2	9.4 – 6.1	2.7 – 3.9	1.2 – 1.1	0.6 – 1.3	-
TiN (V) at%	1.7 – 2.1	43.0 – 48.8	1.1 – 1.9	0.6 – 1.2	0.8 – 0.3	35.6 – 38.5
TiN (IS) at%	2.4 – 3.2	43.0 – 48.8	0.4 – 0.6	0.3 – 0.5	0.1 – 0.2	42.1 – 48.1
δ phase (V) wt%	7.9 – 16.7	1.2 – 1.7	56.8 – 60.7	9.9 – 16.9	8.8 – 14.9	-
δ phase (IS) wt%	26.8 – 28.2	2.6 – 2.7	55.9 – 61.8	3.3 – 5.8	3.9 – 5.5	-
NbC (V) wt%	89.4 – 90.2	6.6 – 7.4	1.7 – 2.0	0.65 – 0.7	0.6 – 0.8	-
NbC (IS) wt%	87.5 – 90.6	5.2 – 9.4	1.7 – 2.7	0.7 – 0.8	0.5 – 0.8	-
TiN (V) wt%	4.7 – 6.2	65.1 – 71.7	1.9 – 3.5	0.9 – 1.9	0.5 – 1.4	15.5 – 17.4
TiN (IS) wt%	7.6 – 10.7	53.3 – 64.9	0.8 – 1.4	0.5– 0.8	0.3 – 0.4	19.9 – 24.3
δ phase [*94*] at%	14.5 – 20.4	2.6 – 3.0	59.3 – 64.9	3.4 – 11.4	5.3 – 9.7	-
NbC [*93*] at%	78.0 – 84.0	8.0 – 12.0	2.0 – 4.0	3.0 – 4.5	0.5 – 1.0	
TiN [*92*] wt%	11.6 – 19.6	54.1 – 59.5	-	-	-	24.7 – 31.9

Due to their fine size, a detailed quantitative examination (volume fraction) of the γ' and γ'' phases was not possible in this work. This was due in part to the considerable difficulty in resolving and distinguishing the individual phases with sufficient resolution with the FEG-SEM, as seen in Figure 35.

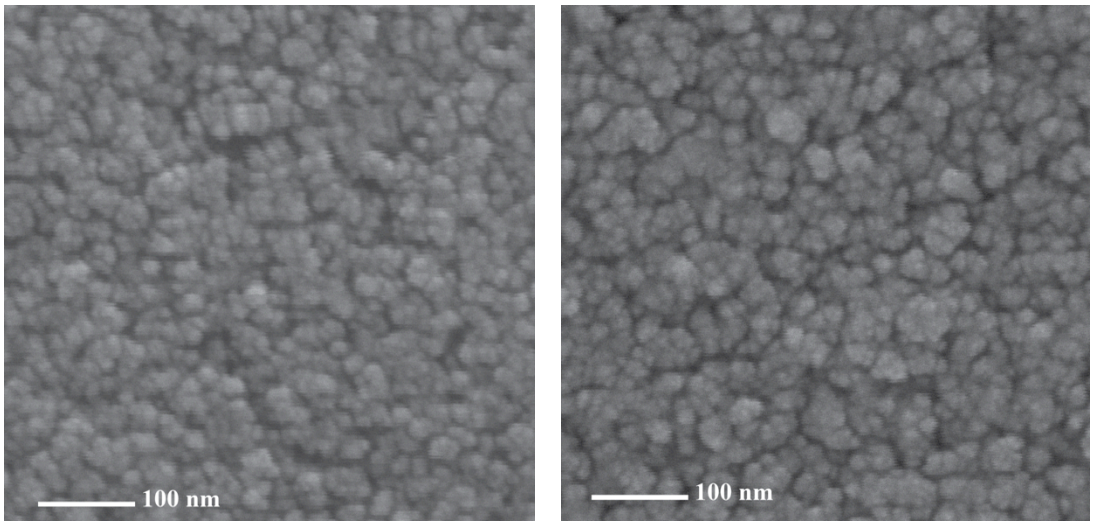

a) b)

Figure 35: FEG-SEM images of the γ' and γ'' phases in the: a) V as-received material, b) IS as-received material.

However, the γ' and γ'' phase size (combined average) was < 30 nm at all locations within the two IS disks, as well as in the V as-received material samples. This size range is in agreement with the reported optimum size for these precipitates (30 – 40 nm for best IN 718 alloy mechanical properties [*1*]).

Microstructural studies of IN 718 presented in the literature suggest that the presence, distribution, morphology and volume fraction of the various precipitates in IN 718 are highly dependent on the composition of the alloy [*1*] [*5*] [*27*].

4.1.1.1 δ Phase Characterization

Microstructural characterization of the V and IS as-received samples suggests that the distribution of the δ phase was significantly different between these materials. The V as-received material δ phase was observed to mostly occupy intergranular regions with infrequent δ phase precipitates detected in the intragranular regions. For the IS material, δ phase was observed to be dispersed throughout the γ matrix, occupying both intergranular and intragranular regions, as seen in Figure 34a and Figure 37. It was also observed that the δ phase aligned along the radial direction of the IN 718 disk.

Two distinct sets of grains were observed within the V material. First, large grains with visible δ phase precipitates along the grain boundaries. Second, smaller grains with their grain boundaries completely void of the δ phase precipitates, as seen in Figure 34b and Figure 36. Possible reasons for the development of the two sets of grains in the V material are discussed in Section 4.1.1.3.

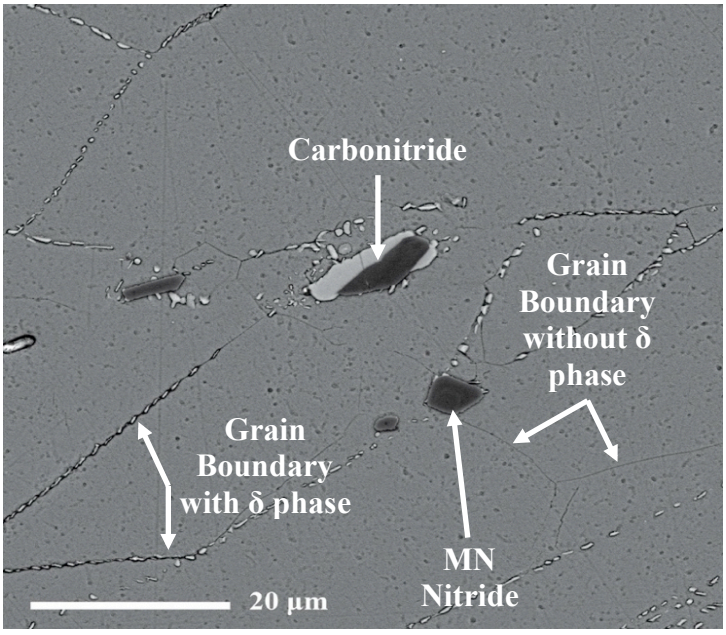

Figure 36: FEG-SEM micrographs (BSE) of V as-received material showing two sets of grain boundaries.

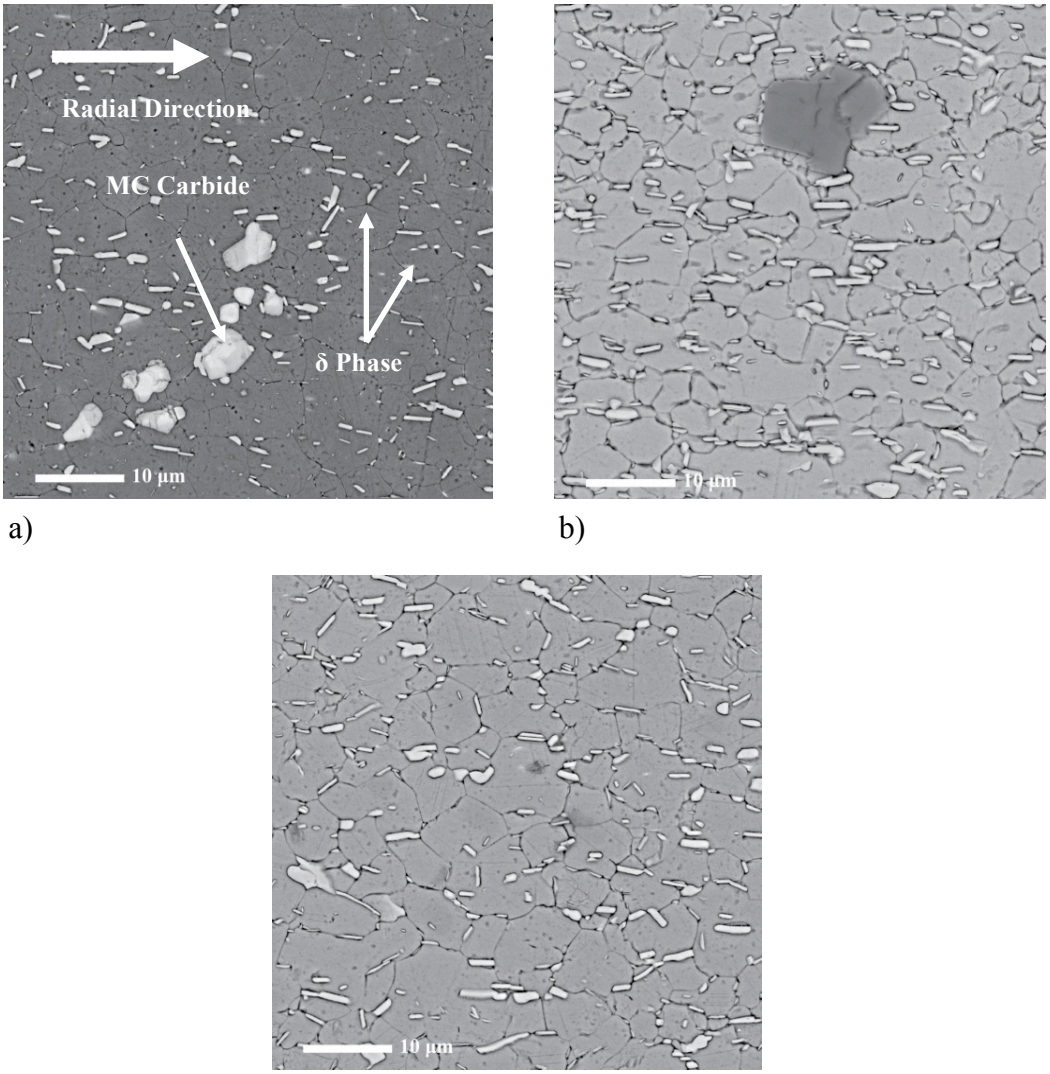

Figure 37: FEG-SEM micrographs (BSE) of IS as-received material showing: a) Outer radius, b) Mid radius, c) Inner radius. Radial direction indicated is the same for all micrographs.

Figure 38 shows the average δ phase volume fraction, interparticle spacing and the width in the V and IS materials. It should be noted that the ASTM Standard E562 – 02 used for measuring the volume fraction of various phases is only valid for randomly distributed particles. Since the δ phase in the V as-received material was observed to precipitate preferentially along the grain boundaries, the average volume fraction for the virgin as-received material reported in Figure 38c may have some inaccuracy.

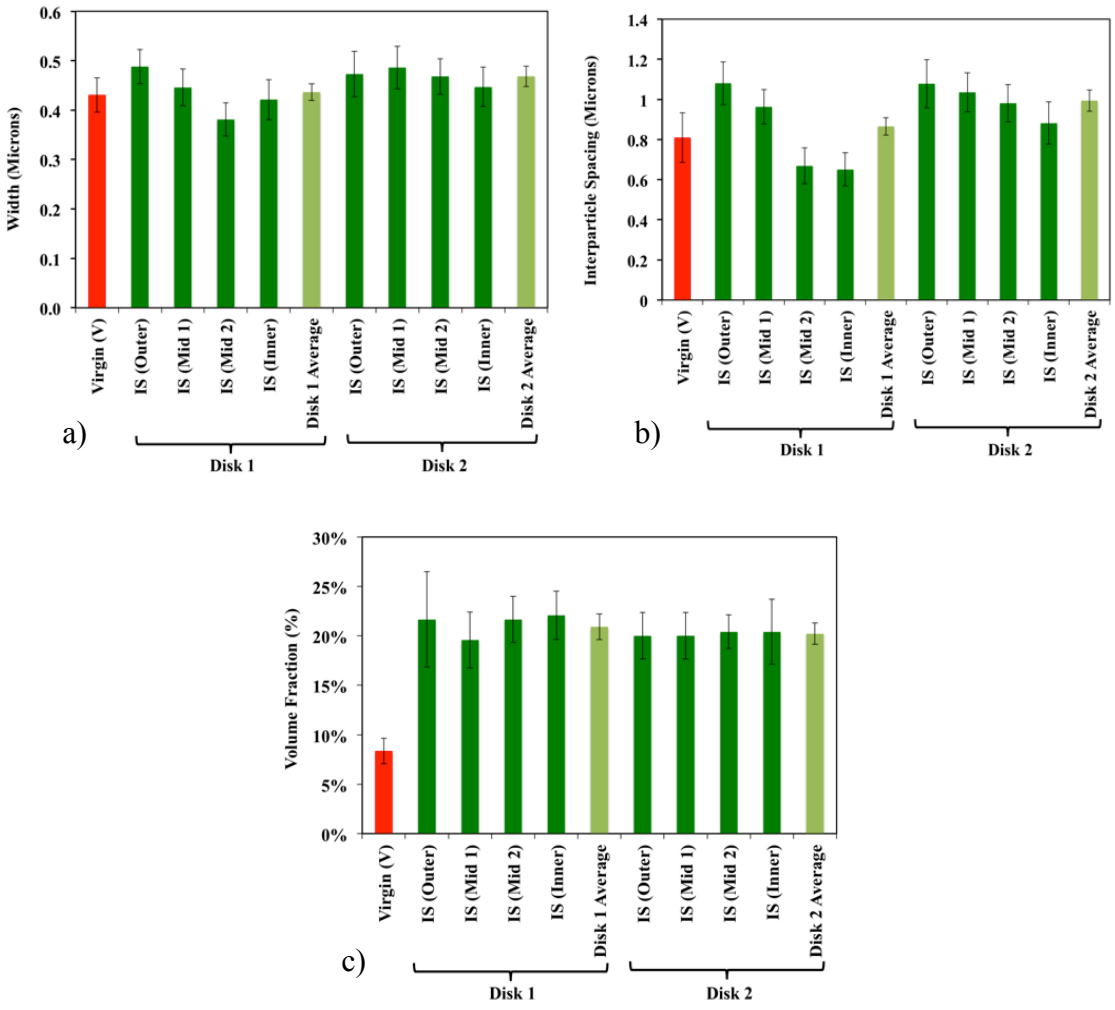

Figure 38: FEG-SEM characterization of δ phase in the V as-received material and two IS disks: a) Width of δ phase, b) Interparticle spacing of δ phase, c) Volume fraction of δ phase. Error bars show the 95% confidence interval [*95*].

The width and interparticle spacing of the δ phase in the IS as-received material, as seen in Figure 34a and b, was greater than in the V as-received IN 718. This observation is consistent with literature, where increasing the alloy's exposure time at elevated temperatures increased the δ phase size and volume fraction [*7*] [*96*].

IN 718 is designed to precipitate the δ phase preferentially along the grain boundaries in order to inhibit grain boundary sliding and grain growth at elevated temperatures [*1*] [*5*]. Typically, the δ phase precipitation in the intergranular or intragranular regions is achieved with heat treatments between 995 °C – 1035 °C, corresponding to temperatures just below the δ phase solvus for IN 718 [*1*]. Judicious control of the heat treatment time and temperature is required to properly adjust the δ phase volume fraction, size and morphology, which are highly dependent on the amount of Nb present in the alloy [*2*] [*5*] [*41*] [*97*]. If proper control of the heat treatment is not achieved, over precipitation of the δ phase may result. High volume fractions of the δ phase prior to service may lead to a reduction in the potential mechanical properties of the alloy as a direct result of Nb diffusion into the δ phase rather than into γ'' (the primary strengthening precipitate in IN 718) [*41*].

In the current study, the forging and forming process of the disk prior to service may have partially attributed to the δ phase reaching the saturation limit in the IS as-received material near the edges of the disk. Chamanfar *et al.* [*1*] observed an increase in the δ phase volume fractions at the edges of forged IN 718 material. However, contrary to the observations made by Chamanfar *et al.* [*1*], the outer edges of the forged disk in the current work did not show any significant increase in the δ phase volume fraction compared to the inner regions of the disk. This suggests that the IS material may have reached the δ phase

saturation limit at the various locations across the disk at different times prior to removal of the disk from service.

Azadian *et al.* [*96*] studied the δ phase precipitation in IN 718 at various temperatures and durations. Their results suggested that the theoretical maximum δ phase volume fraction (13 %) could be extended to a peak of 20 %. The authors suggested that the extension was a direct result of other solute elements diffusing into the δ phase lattice. In the present work, the initial assumption of the maximum service temperature was assumed to be ~650 °C for the IS material, which is significantly lower than the δ phase solvus temperature (995 °C – 1035 °C [*1*] [*2*]). As a result, the δ phase dissolution did not likely occur during service and the δ phase precipitation continued until the 20 % peak volume fraction was achieved across the entire disk prior to removal from service. Results from the δ phase volume fraction analysis (Figure 38c) support this assumption, since the δ phase precipitation was observed to be at the saturation limit of ~20 % across the entire disk.

4.1.1.2 MC Carbide and MN Nitride Characterization

Carbides and nitrides were observed to be uniformly distributed throughout both as-received materials and had a similar morphology, as seen in Figure 39. Figure 40 summarizes the average size and volume fraction of the carbides and nitrides in the as-received materials.

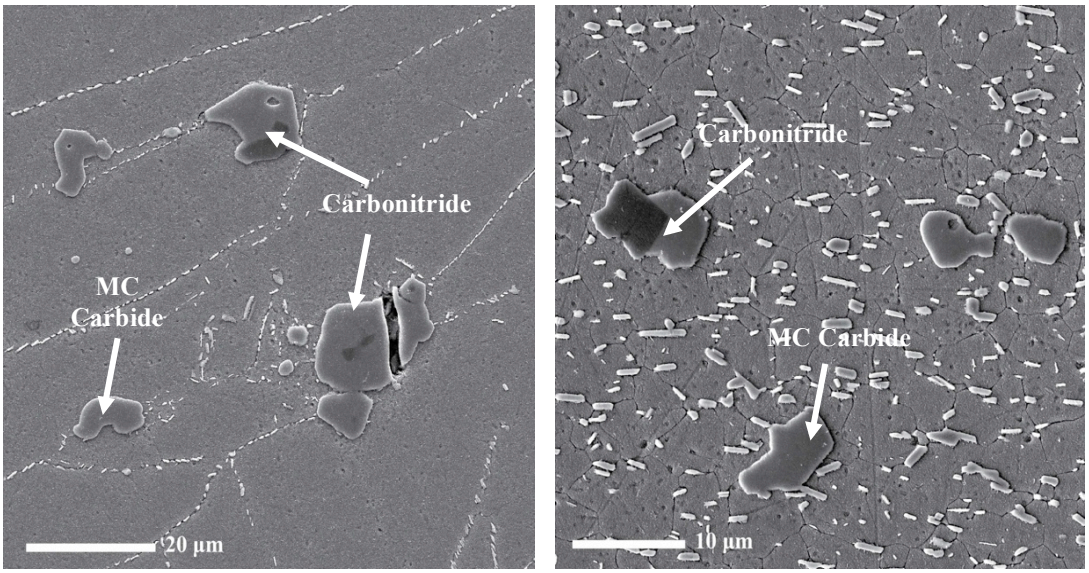

a) b)

Figure 39: FEG-SEM micrographs (SE) of carbides and nitrides in: a) V as-received material, b) IS as-received material.

As shown in Figure 40a and Figure 40c, the average size and volume fraction of the carbides was lower in the IS as-received IN 718 material when compared to the V as-received material. The difference in carbide average size and volume fraction may be attributed to the long exposure of the IS material to elevated temperatures. Carbide dissolution (size reduction) has been suggested in the literature [*5*] to occur when IN 718 is exposed to service temperatures.

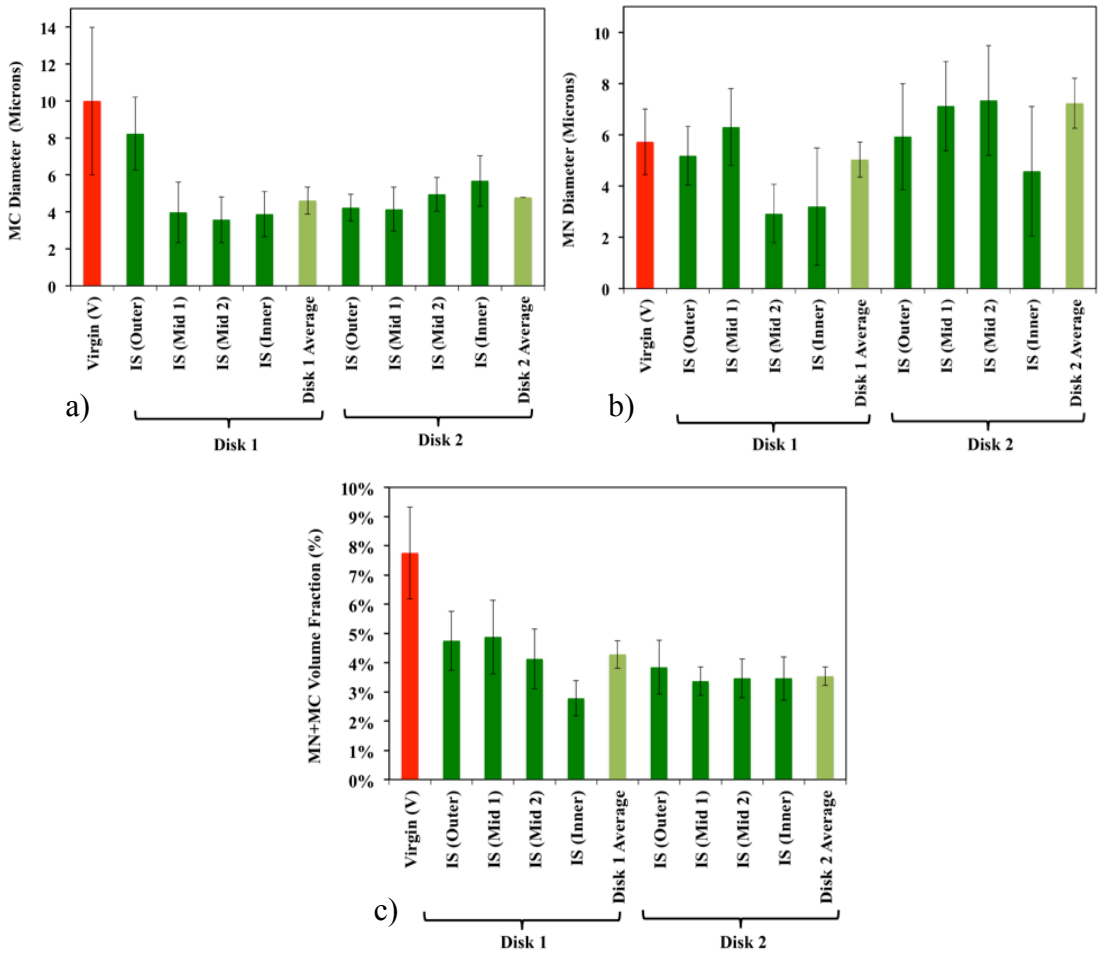

Figure 40: FEG-SEM characterization of carbides and nitrides in the V as-received material and two IS disks: a) Average size of the MC carbide, b) Average size of the MN nitride, c) Average volume fraction of the MC + MN. Error bars show the 95% confidence interval [*95*].

4.1.1.3 Grain Size Characterization

The larger grains in the V material (observed with the δ phase precipitation along the grain boundaries, as shown in Figure 41a) were found to be ~44 μm in diameter, which was in agreement with the reported grain size by the manufacturer (reported as 44 μm) [*79*]. The V material grain size measurements in Figure 42 also include the smaller grains (i.e. grains that did not have the δ phase precipitating along the grain boundaries, as shown in Figure

41b). The grain size results obtained via the ASTM standard are consistent with EBSD results.

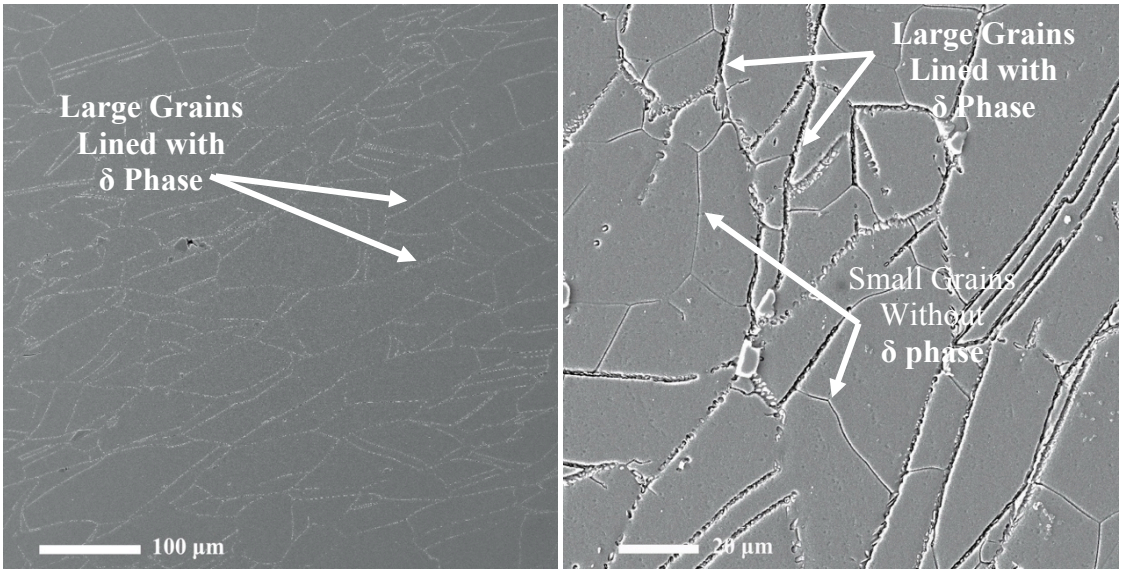

a) b)

Figure 41: FEG-SEM micrographs (SE) of V as-received material: a) Large grains with *δ* phase precipitates, b) Over etched sample showing small grains (without *δ* phase) and large grains (with *δ* phase).

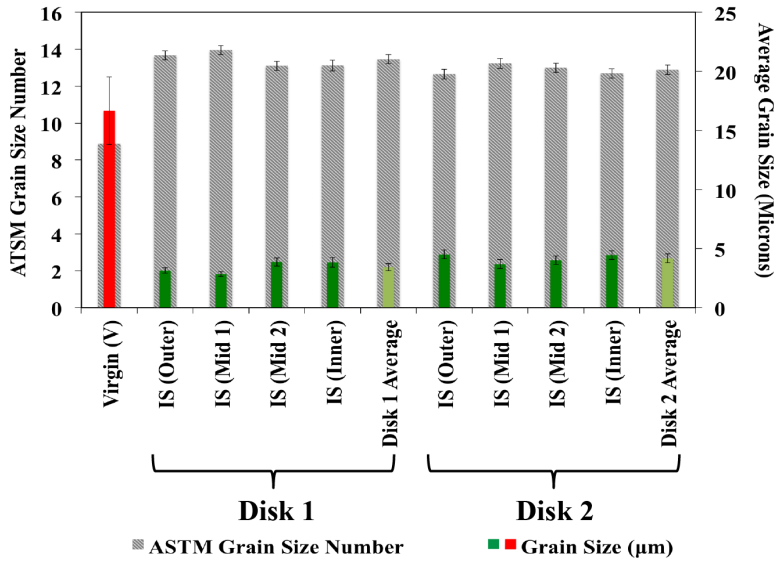

Figure 42: ASTM average grain size in the V material and two IS disks. Error bars show the 95% confidence interval [*95*].

Based on the V material ST performed by the supplier (described in Section 3.1) and the time temperature transformation (TTT) diagram for IN 718 (Figure 43), the smaller grains observed were possibly recrystallized grains that formed during the ST. It should be noted that depending on the composition of the alloy, the lines shown in Figure 43 might shift slightly [*5*] [*41*]. Thus, from the TTT diagram for IN 718 shown in Figure 43, for a one hour ST at 968 °C the intersection of the dashed red trend line occurs along the border of the grain boundary δ phase precipitation. Consequently, depending on the exact composition of the initial alloy, it would be expected that there would be no δ phase precipitation or only a slight δ phase precipitation along the grain boundaries. Based on the actual microstructural observations of the V as-received material (Figure 41b), no δ phase precipitates formed during the heat treatment. Therefore, during heat treatment after forming the bar stock, the recrystallized grains were free of the δ phase. Also, since the temperature was well below the δ phase solvus temperature (995 °C – 1035 °C [*1*] [*2*]) required to dissolve the already existing δ phase along the grain boundaries, the grain boundary δ phase that existed prior to the heat treatment remained unaffected.

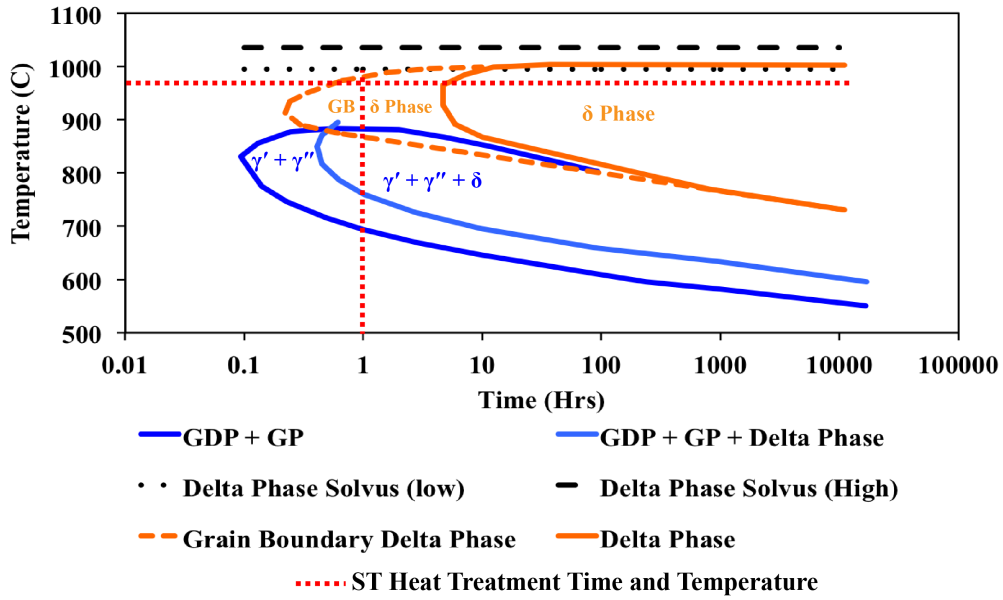

Figure 43: Time temperature transformation (TTT) diagram for IN 718. Data taken from [*5*] [*41*].

Figure 42 shows a significant difference (~80 %) in the grain size between the V and IS as-received materials. The smaller grain size in the IS material may be attributed to: (i) forming/heat treatment of the disk prior to service (i.e., material with deformed grains will nucleate and grow new strain free grains during heat treatment), (ii) disk service conditions (i.e., some DRX may occur during service during high loading and exposure to high temperature), (iii) post-service handling of the disk (i.e., heat treatment of a material that has sufficient strain to cause recrystallization during exposure to elevated temperature).

Minimal variation in the grain size was observed between the outer, mid and inner radius of the IS IN 718 disks. The lack of appreciable variation in the grain size across the IS disks implies that the post service heat treatment was successful in creating and/or maintaining a consistent grain size across the full radius of the disk.

Grain texture analysis was also carried out using EBSD. Representative EBSD area maps are given in Figure 44 and Figure 45 for the V and IS materials, respectively.

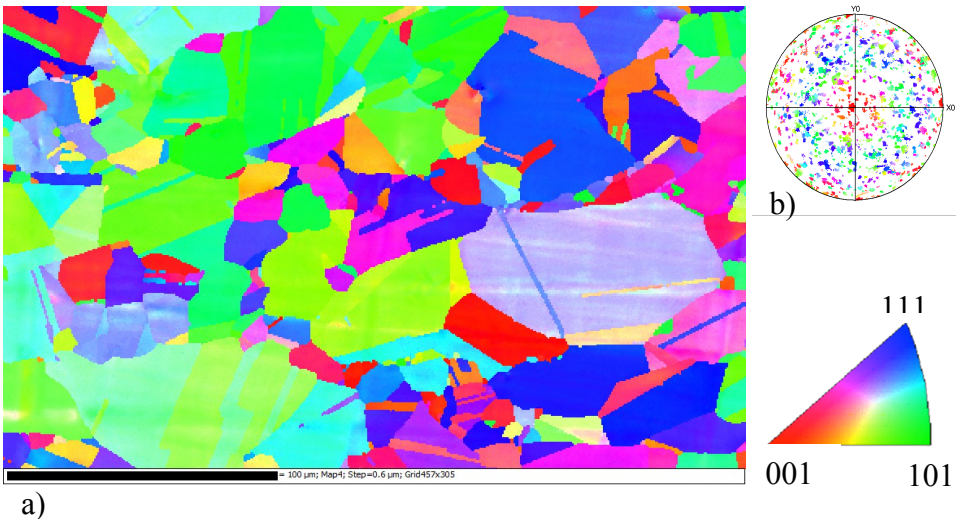

Figure 44: a) EBSD area map of the V as-received IN 718 material, b) Pole figure of the (001) plane. The inverse pole figure corresponds to the direction normal to the polished surface. Scale bar represents 100 µm.

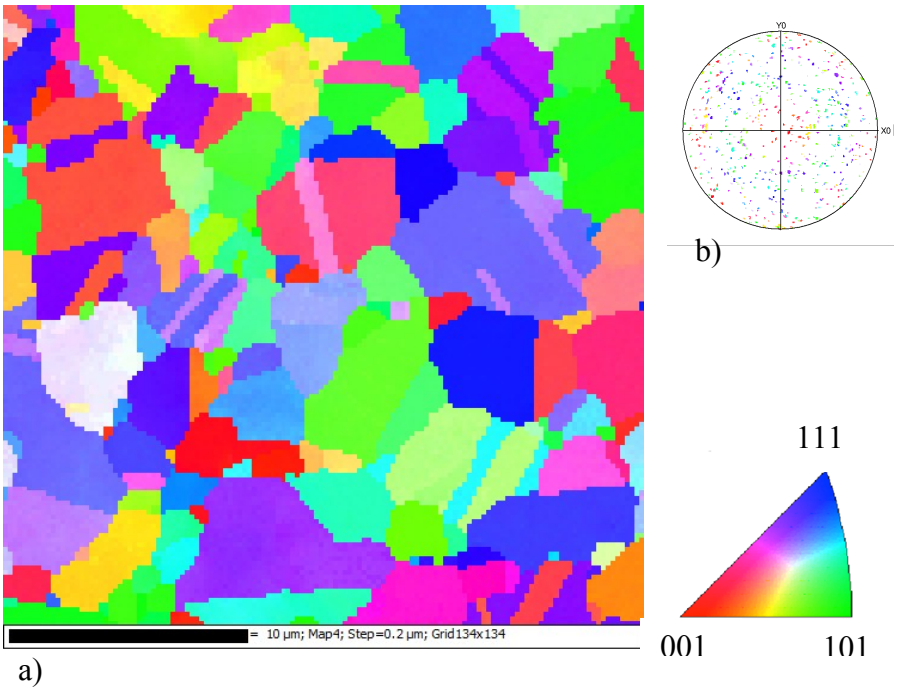

Figure 45: a) EBSD area map of the IS as-received mid radius 1 sample, b) Pole figure of the (001) plane. The inverse pole figure corresponds to the direction normal to the polished surface. Scale bar represents 10 µm.

The results in Figure 44 and Figure 45 indicate that the grains in the V and IS materials had no preferred crystallographic orientation. Thus, the ST that both materials were subjected to prior to analysis may have contributed to the random grain orientation. Furthermore, the extended exposure to elevated service temperatures experienced by the IS IN 718 material may have also resulted in the removal of any texture that was present as a result of the forging operations.

4.1.2 As-Received IN 718 Hardness and Tensile Strength

The following section presents the results of the room temperature mechanical property evaluation (hardness, yield and tensile strength) for the V and IS IN 718 as-received materials.

4.1.2.1 Hardness

Figure 46 summarizes the V and IS as-received IN 718 material average hardness. The hardness of the IS disks was ~25 % higher than that of the V material. The higher hardness of the in-service material may be partially attributed to the smaller grain size, as discussed in Section 4.3.4.1. Despite the significant variation in maximum hardness measured between the materials, the hardness values were within IN 718's reported hardness range found in the literature (174 HV – 430 HV). The large range of hardness values reported in the literature reflects IN 718's sensitivity to process and thermal history, composition and operational environmental conditions [*1*] [*24*] [*26*].

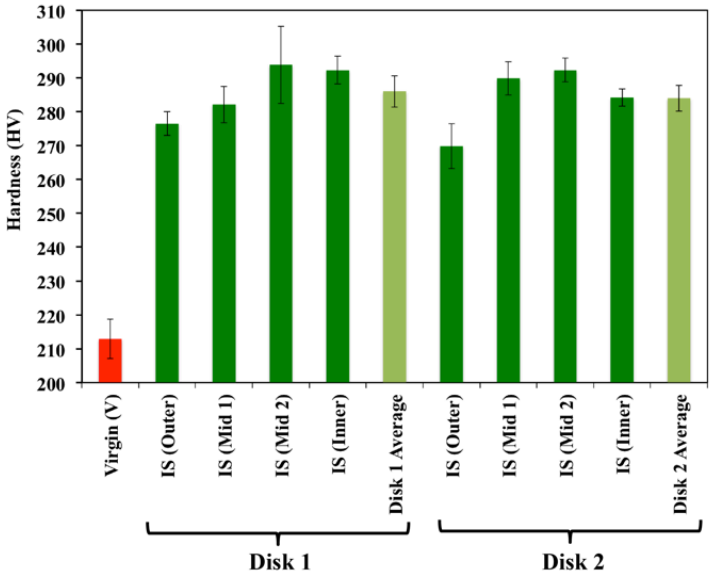

Figure 46: As-received V and IS material average hardness. Error bars show the 95% confidence interval [*95*].

Experimental work by Chamanfar *et al.* [*1*] on microstructural characterization of forged and heat treated IN 718 demonstrated that the hardness of IN 718 increased with: (i) an increase in the δ phase and secondary carbide volume fractions, and (ii) a decrease in the grain size.

Table 4 summarizes the results reported by Chamanfar *et al.* [*1*] for the average δ phase and secondary carbide volume fractions and average grain size as compared to the current study.

Table 4: Summary of microstructural features found by Chamanfar *et al.* [*1*] as compared to the current work.

Material	Average δ Phase Volume Fraction (%)	Average Volume Fraction of Carbides (%)	Average Grain Size (μm)	Hardness (HV)
As-forged [*1*]	2	0.5	12	321
Heat Treated [*1*]	8	2	19	388
IS* (Current Study)	21.25 ± 2.87	3.91 ± 0.67	3.79 ± 0.33	285 ± 4.00

*Note the IS as-received carbide volume fraction also includes nitrides as well.

Comparison between the precipitate volume fractions and the grain size summarized in Table 4, it may be anticipated based on the observations of Chamanfar *et al.* [*1*] that the hardness of the IS as-received material in the current work should be greater than 388 HV. The higher anticipated hardness of the IS material stems from a direct result of the significantly higher δ phase (165 % – 960 % above those observed by Chamanfar *et al.* [*1*]), carbide volume fractions (~95 % – 680 % above those observed by Chamanfar *et al.* [*1*]) and the considerably smaller grain size (~68 % – 80 % smaller than those observed by Chamanfar *et al.* [*1*]). However, due to the complex interaction between the combined effect of the phases and the grain size to the overall mechanical properties of IN 718, a higher hardness was not observed in the IS as-received material in the current study. In fact, an ~11 % – 26 % decrease in hardness was observed compared to the hardness reported by Chamanfar *et al.* [*1*]. This decrease in hardness can be explained by considering that IN 718 is primarily strengthened by the γ'' phase with additional strength originating from other phases such as γ', carbides, nitrides and the δ phase. If the secondary phase volume fractions (carbides, nitrides and, especially the δ phase) increase beyond optimal levels, the effect of grain boundary pinning from these phases becomes overshadowed by the loss of primary strengthening precipitate forming elements such as Nb [*41*] [*98*]. A direct relationship between a reduction in creep strength resulting from grain boundary softening caused by local Nb depletion from δ phase precipitation was reported by Brooks and Bridges [*98*]. Therefore, the mechanical properties of IN 718 are likely influenced by other parameters in addition to those reported by Chamanfar *et al.* [*1*]. A more in depth discussion on the factors that influence the hardness of IN 718 is provided in Section 4.3.4.1.

Due to the considerable difficulty associated with resolving the γ' and γ'' phases in this work (discussed in Section 4.1.1), additional characterization of the V material and IS disks is required to further understand the relationship between the microstructure and mechanical properties. Furthermore, the direct impact of the δ phase, specifically the influence of varying the volume fraction, size and morphology of the δ phase on the mechanical properties of IN 718 remains unclear in the literature [*6*] [*7*]. Therefore, due to the influence of the compositional variations, heat treatment duration/peak temperature/ramp rates, as well as the effect of the service environment on the morphology of IN 718 constituents, there remains considerable difficulty with comparing the mechanisms contributing to the mechanical properties (e.g., yield strength, tensile strength, etc.) of IN 718 between the various studies available in the literature.

4.1.2.2 Tensile Properties

The tensile properties of the V and IS as-received IN 718 materials are summarized in Figure 47. The IS IN 718 material exhibited a higher yield (61 % increase), ultimate tensile strengths (25 % increase) and a lower ductility (35 % decrease) in comparison to the V material. The higher strength of the IS material was likely the result of the smaller grain size compared with the V material. While the hardness of the IS IN 718 material was ~32 % higher than that of the V material, the tensile properties were only ~25 % (200 MPa) higher. As shown in Figure 47, the tensile properties of both the V and IS as-received material samples were similar to those reported in the literature for comparable heat treatments (ST material). However, the yield strength and UTS was significantly lower than that of the solution treated and direct aged (STA) and the solution treated and double aged (ST + DA) heat treated materials [*24*] [*26*]. The lower mechanical properties of the ST material

compared to the STA and ST + DA material is in agreement with literature since the STA and ST + DA heat treatment are designed to create an optimum microstructure resulting in enhanced strength and hardness by solutionizing the δ phase and promoting the formation of higher volume fractions of γ'' [*1*]. Although the strength of the as-received materials in the ST condition was lower than in the ST + DA and STA conditions, the ductility of the ST base material was roughly 30 % – 60 % higher than in the case of the ST + DA and the STA materials. Thus, IN 718 is significantly more ductile in the ST rather than in the aged condition. More details on how heat treatments alter the microstructure of IN 718 are presented in Section 4.3.3.

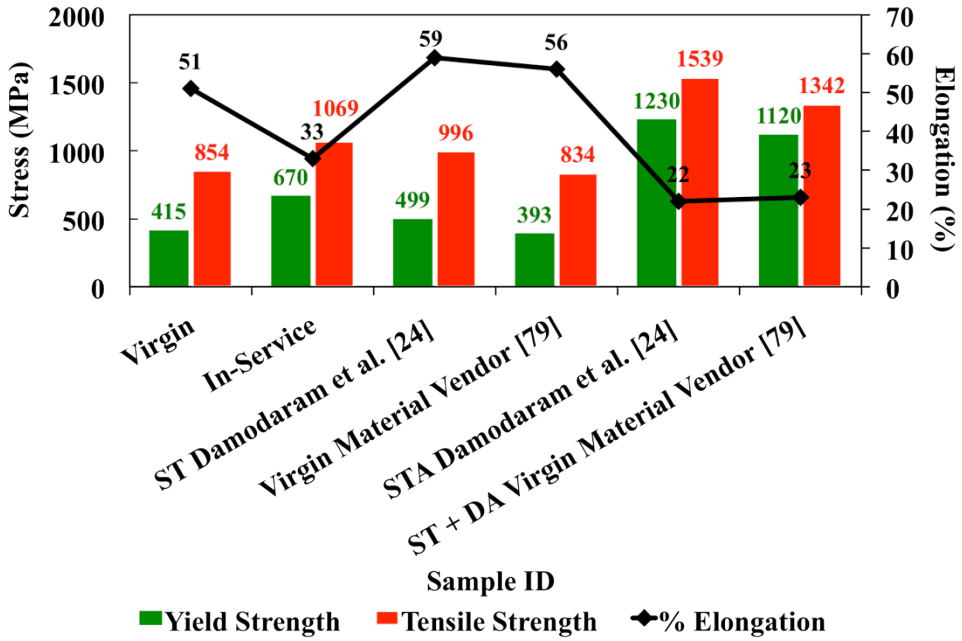

Figure 47: Mechanical properties (average yield strength, ultimate tensile strength, and total percent elongation) for the V and IS as-received materials in the solution treated conditions compared with ST, STA and ST + DA conditions reported in literature [*24*] [*79*]. Error bars show the 95% confidence interval.

The higher hardness and tensile strength of the IS material as compared to the V material suggests that the IS disks had not reached the service life expiration limit, since a

deterioration of mechanical properties in the IS material (i.e., lower or similar tensile strength compared to the V material) would be expected if the disks had reached their service life expiration limit.

4.2 In-Service Disk Evaluation

Since a significant decrease from the maximum δ phase volume fraction (~20 %) was not observed in the current work (as discussed in Section 4.1.1.1), the operational temperatures of the IS disks likely did not exceed 730 °C for any substantial length of time (as suggested by the stability of the γ'' and δ phase data by Saunders *et al.* [*43*] presented in Figure 2 and discussed in Section 2.1.2.1). Also, as illustrated in Figure 2, at temperatures above ~665 °C a reduction in the γ'' volume fraction is observed, which also corresponds to a reduction in alloy strength, as shown in Figure 48 [*5*]. Since the IS disk was subjected to high dynamic loading during the operation of the jet engine, which would require maximum strength from the alloy during service (i.e., maximum volume fraction of the γ'' phase), it is therefore unlikely that the peak service temperature exceeded the initially assumed maximum operating temperature of ~650 °C.

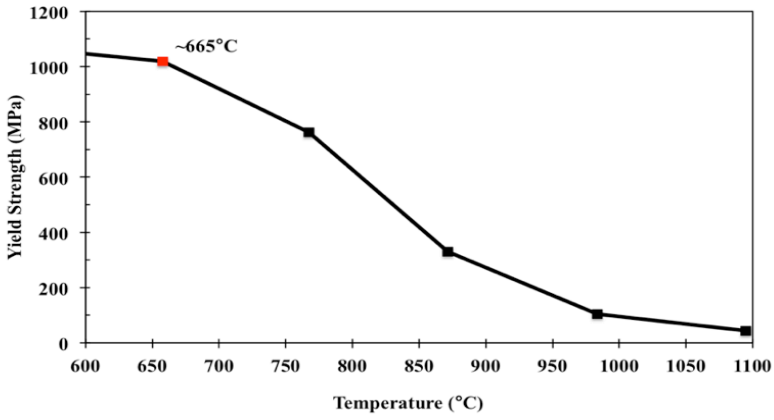

Figure 48: Effect of temperature on the yield strength of ST + DA IN 718. Data taken from [*5*].

The conclusion regarding the assumed maximum service temperature is further supported by the mechanical performance of the IS material, as compared to the V material used in the current study and other materials discussed in the literature. The hardness and the tensile strength of the IS material was higher than the V material (in the as-received conditions), but were still comparable to literature [*1*] [*24*] [*26*] [*79*]. This suggests that the mechanical properties of the IS material have not degraded during service, as would be expected for material that had reached its end-of-life limit or exceeded an operating temperature greater than 650 °C for long durations.

Consequently, the IS IN 718 disks characterized in this work are representative of a material that would undergo a repair processes (for example LFW repair of BLISKs) in an industrial setting. Understanding of an in-service material's microstructure in the pre-repair state is of importance when designing proper repair process parameters. Lack of proper understanding of a material's microstructure can result in detrimental phase changes during repair processes, which would lead to high residual stresses or result in un-wanted microstructural transformations, all of which may lead to premature failure during post repair service.

4.3 As-Welded & PWHT Sample Characterization

The following section outlines the results of microstructural and mechanical property characterization for the V-V and V-IS IN 718 welds in the as-welded and PWHT conditions. However, a discussion on the selection of the LFW process parameters is discussed first.

4.3.1 Selection of LFW Parameters

Initial testing was carried out to determine suitable process parameters for LFWing. Due to the critical nature of aero-components operating in jet engines, the presences of defects within a weld, such as voids, cracks, oxides, would have serious influence on the performance of the welds and could lead to premature component failure (as discussed in Section 2.4). Furthermore, aeroengine material is designed to have specific properties (i.e., mechanical, thermal, chemical, etc.) for each component. A modification of these properties through the application of heat during welding may result in unfavorable microstructural changes, leading to unfavorable alterations to the designed mechanical properties of the material. Therefore, one of the considerations was to minimize the size of the weld affected region created during LFW. Figure 49 shows one half of the weld affected region (i.e., the distance from the weld interface to the unaffected base material) observed under an optical microscope. Among other parameters, the presence of defects, such as voids, cracks and oxides within the welded material was examined and minimized.

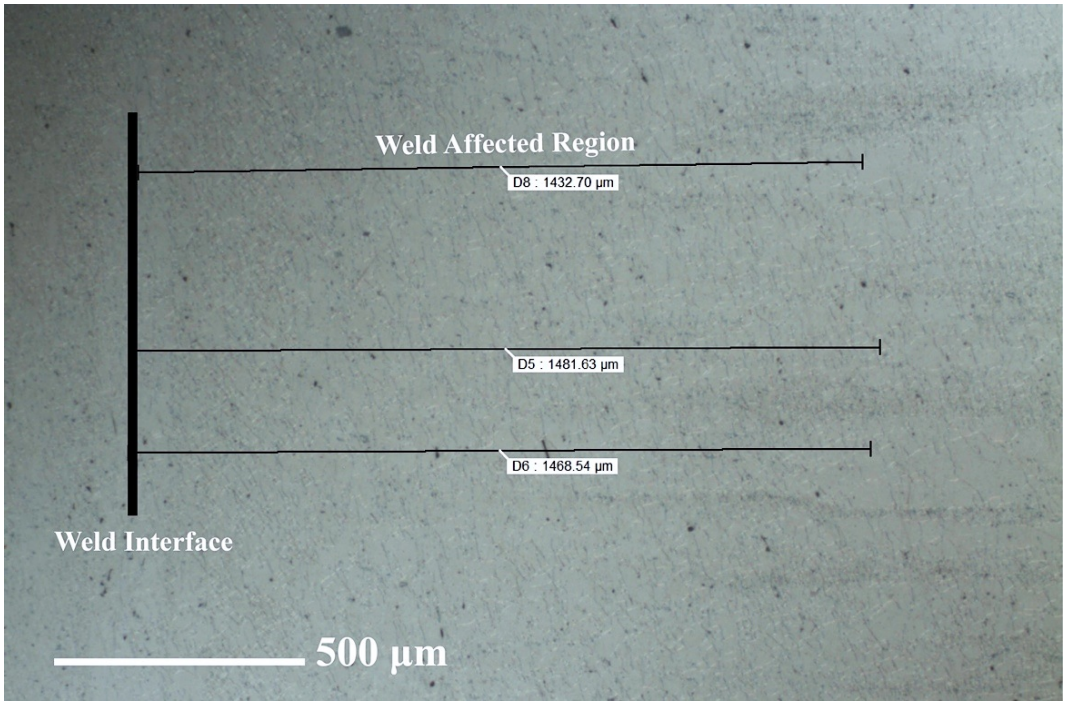

Figure 49: Optical micrograph showing half of the total weld affected region (distance from the weld interface to unaffected base material).

The weld parameter selection process was carried out in two experimental phases. During the first phase (calibration phase) the IN 718 material was varied, while the weld parameters were held constant. For this stage, the materials used included: (i) V – virgin as-received IN 718, (ii) V_{NRC} – IN 718 material from a virgin material batch supplied by the NRC and (iii) IS – in-service IN 718 taken from the aero engine disks.

During the second phase (optimization phase), the IN 718 material remained the same, while the weld parameters were varied. For this phase, the material used was the V_{NRC} IN 718 supplied by the NRC. In total, 16 test runs were performed. The exact magnitude and the combination of the specific weld parameters (e.g., frequency, pressure, duration, etc.) that were varied, as well as the final weld parameters selected for LFWing are proprietary.

FEG-SEM and EDS analyses were used to characterize the weld interface microstructure and determine if any voids, contamination or oxides were present in the weld (criterion #1). Optical microscopy was used to evaluate the size of the weld affected region by measuring the distance from the weld interface to the start of the unaffected base material (i.e., half of the weld affected region) for each test sample (criterion #2). The weld affected region measurements for the optimization and calibration tests are presented in Figure 50.

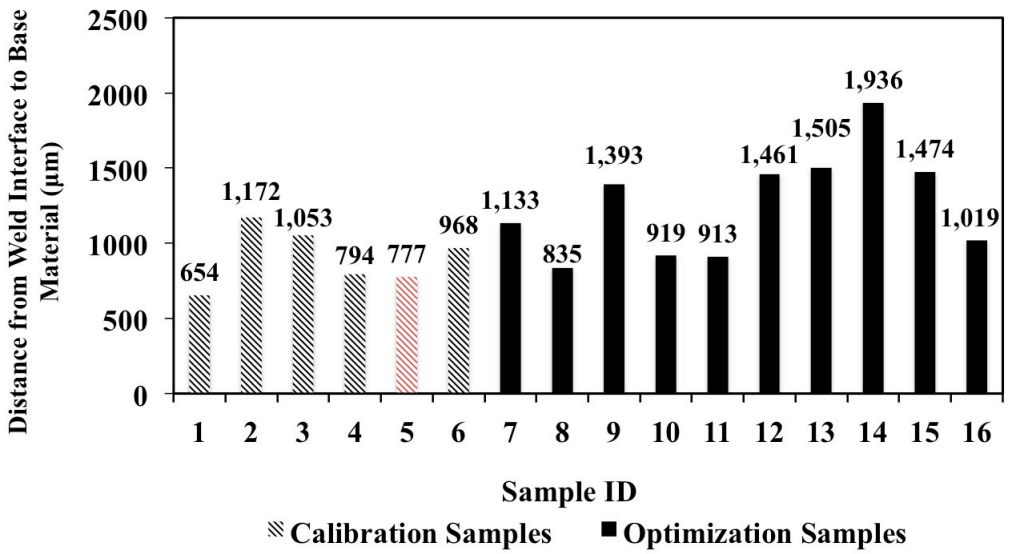

Figure 50: Average width of the weld affected material (from the weld interface to unaffected base material) for the calibration and optimization samples.

With the exception of calibration Sample #5 (shown as red hashed bar in Figure 50) the welded samples were defect free with no voids, cracks or oxides at the core of the weld interface, as seen in Figure 51a. It was determined that the inclusion of oxides at the weld interface of calibration Sample #5 was due to a misalignment of the sample coupons prior to welding.

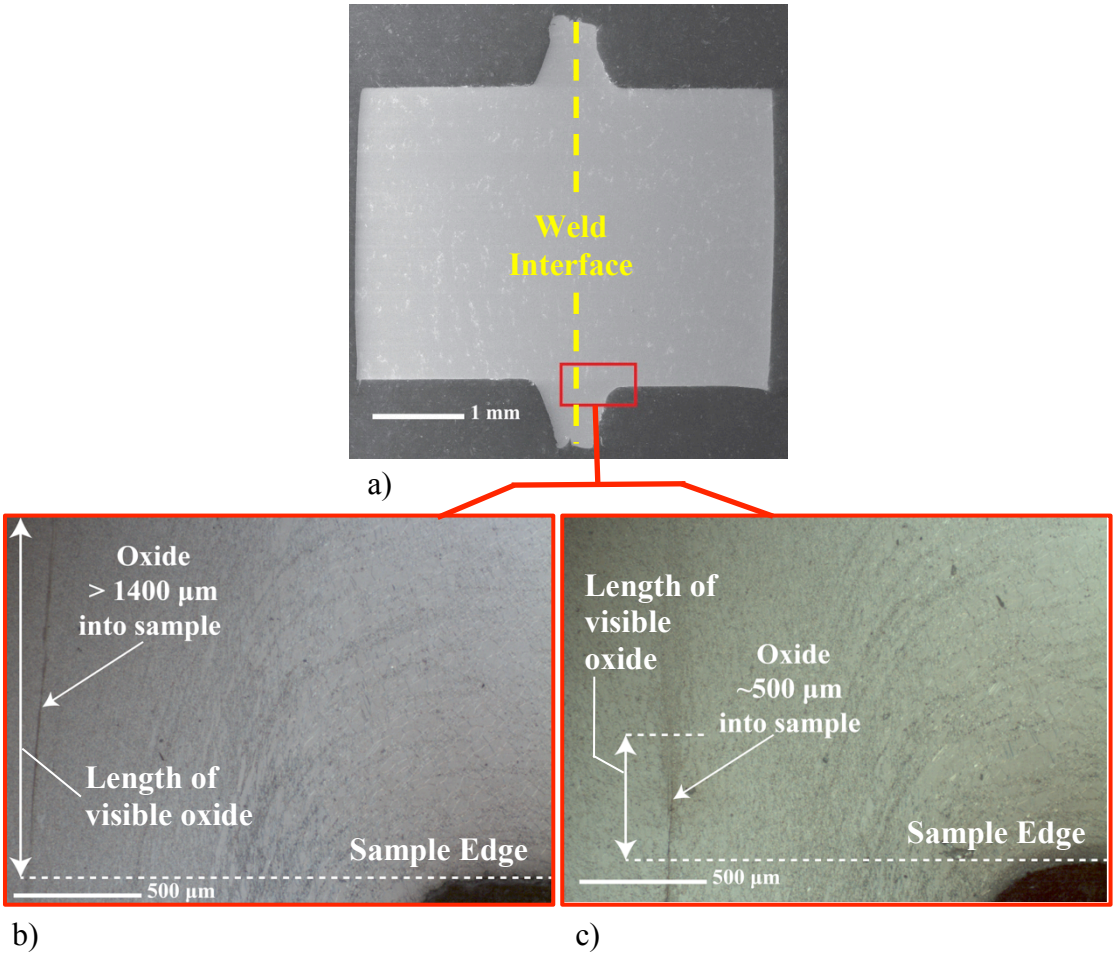

Figure 51: Oxide inclusions in the sample from the flash: a) FEG-SEM micrograph (SE) of the LFW sample, red box - region of interest, b) Optical micrograph of optimization sample #8 with oxide inclusion at the weld interface, c) Optical micrograph of optimization sample #10 with minor oxide inclusion at the weld interface.

For all samples, it was observed that the oxides that were extruded into the flash during welding penetrated into the sample to a varying degree (shown in Figure 51b and c). The extent to which the oxide penetrated into the sample was observed to be dependent on the weld parameters used, but was independent of the IN 718 material.

Since the extent of oxide penetration into the sample did not depend on the material used (i.e., for the same weld parameters and different materials the distance the oxide penetrated

into the sample remained the same), suggests that the LFW process is robust enough to accept variations in material composition. This is a significant result, since slight material compositional differences between engine components are often encountered in an industrial setting during repair.

Based on the optimization and calibration tests, Sample #1 met all the criteria and therefore the same LFW parameters were used for LFW processing of all samples.

4.3.2 LFW Temperature Evolution

An infrared (IR) imaging system was used to examine the development of a thermal gradient on the surface of the samples between the weld interface and the base material during LFWing. Evolution of the thermal gradient was correlated to the relative motion and high friction created between the two materials being welded. The maximum temperature (as recorded by an individual pixel) by the IR camera system during the LFWing process was 1185 °C for the V-V samples and 1176 °C for the V-IS samples, as shown in Figure 52. This result is consistent with the literature [*20*] [*26*] [*27*], where the maximum interface temperature for friction welding of IN 718 was reported to be between 1100 °C and 1200 °C. Upon completion of the burn-off stage, where the oscillation was stopped (and forging stage began) a rapid decrease in the temperature was observed, as seen in Figure 52. The initial temperature trend line (dashed) and the end of the final cooling curve, shown in Figure 52, were restricted to a minimum temperature of ~300 °C, which was the minimum temperature detected by the system.

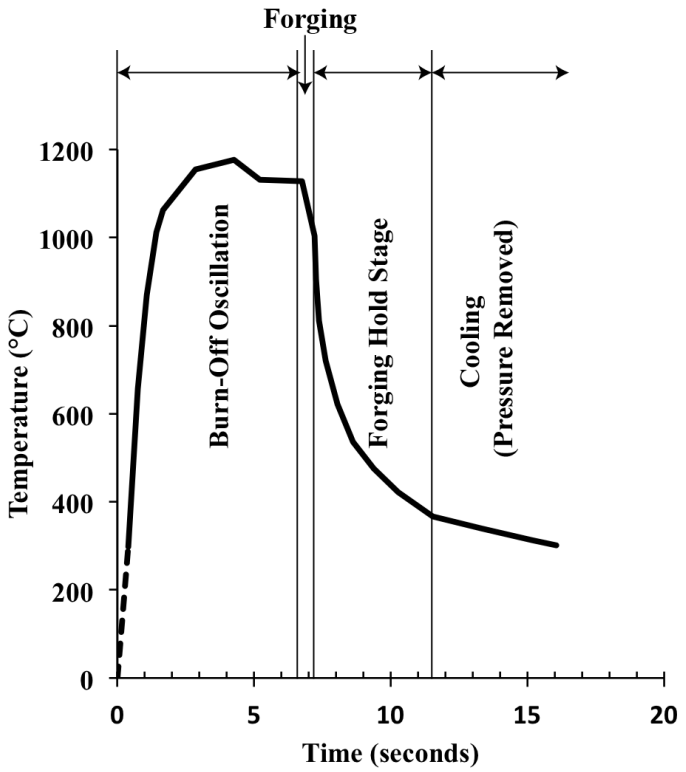

Figure 52: LFW interface temperature trend taken from IR camera for the V-IS sample [*81*]. (The International Journal of Advanced Manufacturing Technology, Mechanical properties and microstructural evolution of in-service Inconel 718 superalloy repaired by linear friction welding, 2016, pp. 1-16, M. Smith, L. Bichler, J. Gholipour and P. Wanjara, © Her Majesty the Queen in Right of Canada 2016. With permission of Springer).

Chamanfar *et al.* [*20*] suggested that for friction welding processes, the temperatures should reach ~50 °C – 60 °C below the bulk solidus temperature of the material to ensure sufficient softening/plasticization of the weld interface to produce a high quality weld. In the current work, the maximum local average temperature on the sample surface at the interface was ~1130 °C (obtained from 3 x 3 pixel averaging), which was ~130 °C below the bulk solidus temperature of IN 718 (reported as 1260 °C [*79*]). Due to the occurrence of the flash folding over, especially at the onset of the forging stage where the flash obscured the interface temperatures from the IR camera, it is therefore possible that some measurement

errors were present. It should be noted, however, that the temperatures detected on the sample surface were likely lower than temperatures reached at positions located mid-depth and mid-width of the sample at the weld interface, as reported in [*20*]. Nevertheless, some single pixels did indicate a maximum interface surface temperature ranging between 1176 °C – 1185 °C, which is in agreement with temperatures reported by other authors during LFWing [*26*] [*27*].

4.3.3 Microstructural Characterization of LFWed and PWHTed Samples

The LFWing process created highly localized thermal and strain gradients across the weld interface due to the rapid heating, cooling and applied compressive loading, which resulted in a significant variation in the microstructure in the vicinity of the weld region. Interestingly, a lens-shape profile developed for each of the weld regions, which may have been a result of the oscillatory motion of the lower coupon during welding, as illustrated in Figure 23a.

Microstructural analysis across the weld region at the centerline of the sample, (highlighted as the red box shown in Figure 53), was performed on the V-V and V-IS as-welded samples. As depicted in Figure 54 and tabulated in Table 5, the average grain size in the unaffected base material (BM) was ~15 μm and ~4 μm for the V and IS material, respectively. The grain size gradually evolved to ~4.5 μm in the DRX region for both the V-V and V-IS as-welded samples. Table 5 also shows the approximate widths of each of the respective weld regions for the as-welded condition.

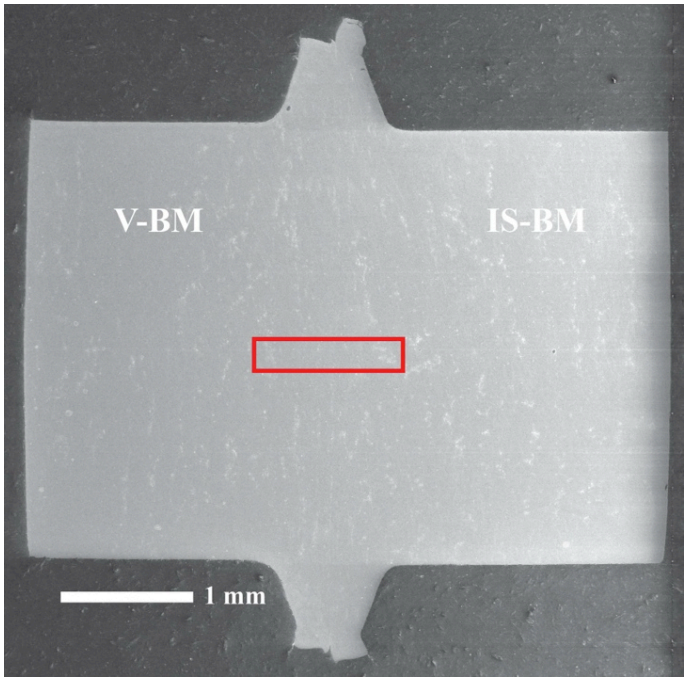

Figure 53: Region (red box) where a microstructural analysis was performed on the as-welded and PWHT samples [*81*]. (The International Journal of Advanced Manufacturing Technology, Mechanical properties and microstructural evolution of in-service Inconel 718 superalloy repaired by linear friction welding, 2016, pp. 1-16, M. Smith, L. Bichler, J. Gholipour and P. Wanjara, © Her Majesty the Queen in Right of Canada 2016. With permission of Springer).

Table 5: Relative width and average *γ* grain size of the different weld regions for as-welded V-V and V-IS from EBSD analysis [*81*]. (The International Journal of Advanced Manufacturing Technology, Mechanical properties and microstructural evolution of in-service Inconel 718 superalloy repaired by linear friction welding, 2016, pp. 1-16, M. Smith, L. Bichler, J. Gholipour and P. Wanjara, © Her Majesty the Queen in Right of Canada 2016. With permission of Springer).

		V-V As-Welded			V-IS As-Welded		
Material Side	Region	Region Width (mm)	Distance From Weld Interface (mm)	Average Grain Size (μm)	Region Width (mm)	Distance From Weld Interface (mm)	Average Grain Size (μm)
V	BM	0.55	-1.50 – -0.95	10.1 ± 4.6	0.44	-1.52 – -1.06	15.7 ± 7.6
	HAZ	0.34	-0.84 – -0.51	8.1 ± 2.2	0.33	-0.95 – -0.62	8.4 ± 2.2
	TMAZ	0.22	-0.40 – -0.18	6.8 ± 1.0	0.33	-0.51 – -0.18	8.6 ± 1.3
	DRX	0.33	-0.06 – 0.25	4.5 ± 0.2	0.33	-0.07 – 0.26	4.9 ± 0.4
V/IS	TMAZ	0.22	0.36 – 0.57	6.4 ± 1.0	0.22	0.37 – 0.58	5.4 ± 0.4
	HAZ	0.22	0.69 – 0.91	8.8 ± 2.1	0.22	0.70 – 0.92	5.0 ± 0.3
	BM	0.47	1.02 – 1.49	11.4 ± 5.0	0.47	1.03 – 1.50	3.8 ± 0.2

*EBSD grain size was verified with hand calculations following the principles described in ASTM Standard E 112 + 96.

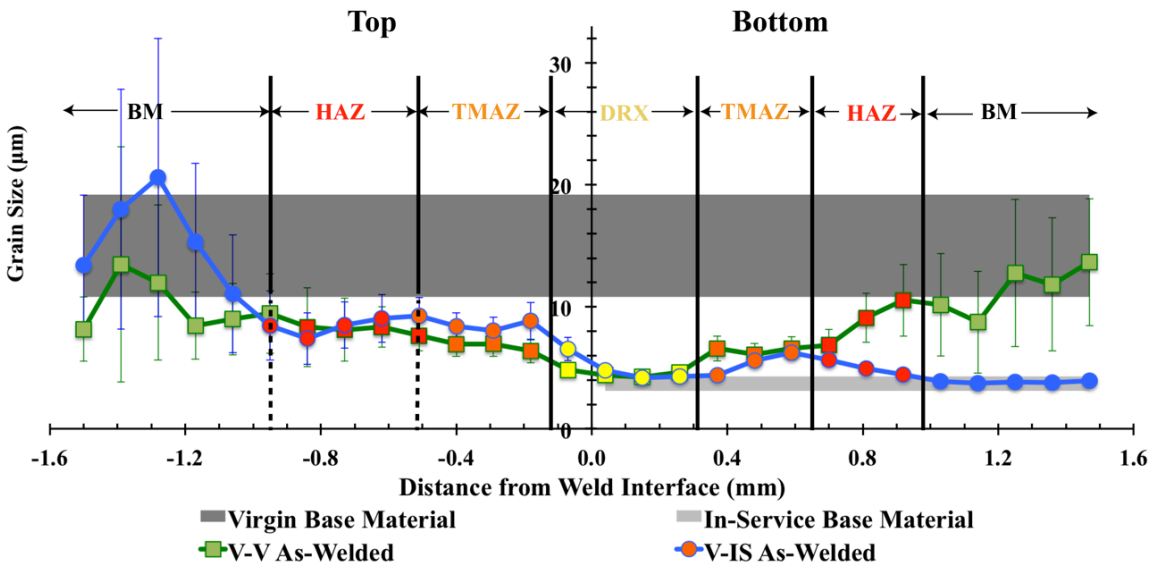

Figure 54: As-welded grain size trends determined using EBSD for the V-IS and V-V as-welded. IN 718 V and IS as-received BM average grain size including the 95% confidence interval is shown as the shaded regions. Marker color indicates the different weld regions: Yellow – DRX, Orange – TMAZ, Red - HAZ and BM as trend line color. Error bars show the 95% confidence interval [*86*]. (Residual stress analysis in linear friction welded in-service Inconel 718 superalloy via neutron diffraction and contour method approaches, Vol. 691, M. Smith, J. -B. Levesque, L. Bichler, D. Sediako, J. Gholipour and P. Wanjara, pp. 168-179, Crown Copyright © 2017, with permission from Elsevier).

EBSD merged maps across the weld interface of the as-welded V-V and V-IS samples are presented in Appendix A. A representative EBSD map in Figure 55a for the V-IS as-welded material shows a grain structure similar to that of the V IN 718 as-received material (seen in Figure 44). Such a grain structure was present in the V-IS material from -1.5 mm to -1.06 mm from the weld interface and had an average grain size of 15 ± 7.6 µm. This region is referred to as the V unaffected base material (V BM). As seen in Figure 55b, moving closer towards the interface, a noticeable change in the grain structure was observed at -0.95 mm to -0.62 mm from the weld interface. This region is referred to as the HAZ. Compared to the V BM, the grains were finer in the HAZ and had an average size of 8.4 ± 2.2 µm. The next region, termed as the TMAZ was at -0.51 mm to -0.18 mm from the weld interface. In this region, the grains appeared slightly compressed (shown in Figure 55c) and had an average

grain size of 8.6 ± 1.3 μm. The smaller grain size at the weld interface (which extended from -0.07 mm to 0.26 mm) was the terminal point of a steady decrease in the grain size from 15.7 ± 7.6 μm in the V BM to 4.9 ± 0.4 μm at the weld interface, as seen in Figure 54. Other researchers who studied friction welding processes of various superalloys have also reported the occurrence of a significant reduction in the grain size at the weld interface [*21*] [*26*] [*27*] and attributed the reduction to DRX processes (discussed in Section 2.6). The extent of grain refinement at the weld interface has been reported in the literature to be dependent on the duration of the welding process, the maximum temperature achieved, total strain and the strain rate [*21*]. Hence, by comparing the observed microstructure and recorded maximum temperature in the current work to the published data on LFW of IN 718, it is reasonable to assume that DRX occurred at the weld interface in the V-V and V-IS welds.

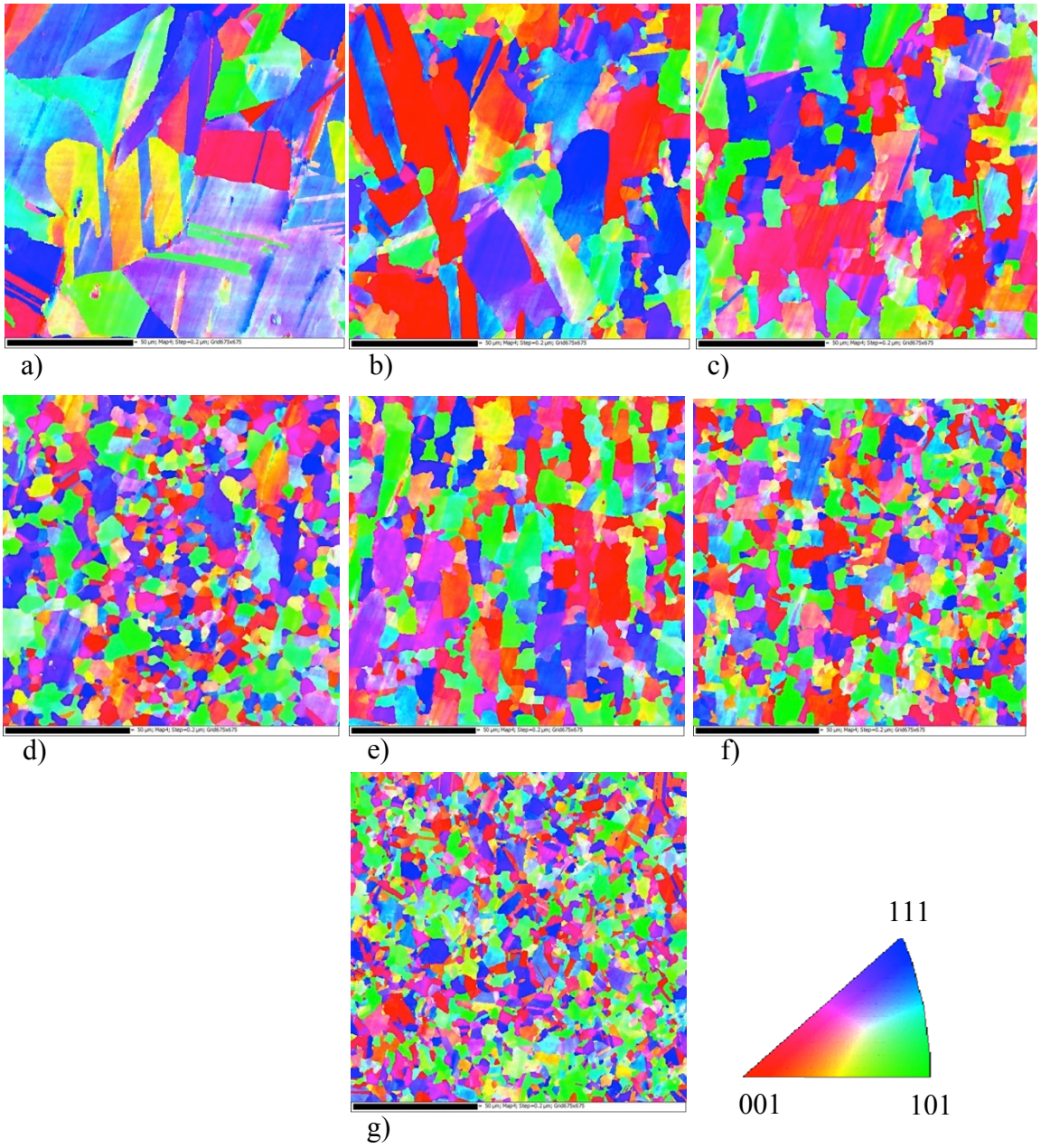

Figure 55: Representative EBSD maps taken from various sites within each weld region of V-IS: a) V-BM, b) V-HAZ, c) V-TMAZ, d) V-DRX, e) IS-TMAZ, f) IS-HAZ, g) IS-BM. V-V had similar EBSD maps to those shown in a) – d) and was symmetrical but offset over the weld interface. The inverse pole figure indicates the direction normal to the polished surface. Scale bars represent 50 µm [*81*]. (The International Journal of Advanced Manufacturing Technology, Mechanical properties and microstructural evolution of in-service Inconel 718 superalloy repaired by linear friction welding, 2016, pp. 1-16, M. Smith, L. Bichler, J. Gholipour and P. Wanjara, © Her Majesty the Queen in Right of Canada 2016. With permission of Springer).

On the IS side of the weld, the TMAZ region, with its compressed grains, was observed from 0.37 mm to 0.59 mm from the weld interface (seen in Figure 55e). As compared to the DRX region, the average grain size in the TMAZ increased (5.4 ± 0.4 μm). Following the TMAZ, the HAZ region in the IS material was seen at 0.70 mm to 0.92 mm from the interface. The average grain size in the HAZ was 5.0 ± 0.3 μm. Finally, at a distance of 1.03 mm to 1.5 mm from the weld interface, the grain size was observed to remain constant at 3.8 ± 0.2 μm, which was comparable to the IS IN 718 as-received material. Therefore, microstructural grain size analysis suggests the weld affected region spanned less than ±1.5 mm from the weld interface. The grain size evolution in the V-V as-welded sample followed a similar trend as observed on the V side of the V-IS weld, as seen in Figure 55a – d.

The offset observed in the grain size evolution in the as-welded samples (seen in Figure 54) may be related to the different thermomechanical process conditions experienced by the top coupon (subjected to applied compressive force) versus the oscillating bottom coupon during welding. Chamanfar *et al.* [*99*] reported and explained a similar occurrence of offsetting in LFWed WASPALOY.

In order to characterize the changes that occur within the weld region during subsequent heat treatment, some LFWed samples were subjected to a standard industry PWHT. EBSD area maps across the weld interface for the V-V PWHTed and V-IS PWHTed samples are shown in Figure 56 (full EBSD merged maps for these samples are shown in Appendix B). The PWHT grain size evolution across the weld interface is summarized in Figure 57. The grain size reported for the V-V PWHTed and V-IS PWHTed materials, as well as the ST + DA V and IS as-received materials (Figure 57) were determined through EBSD only, due to

significant experimental challenges associated with etching the grain boundaries sufficiently for proper three-circle method (ASTM Standard E112 – 96) analysis after heat treatment.

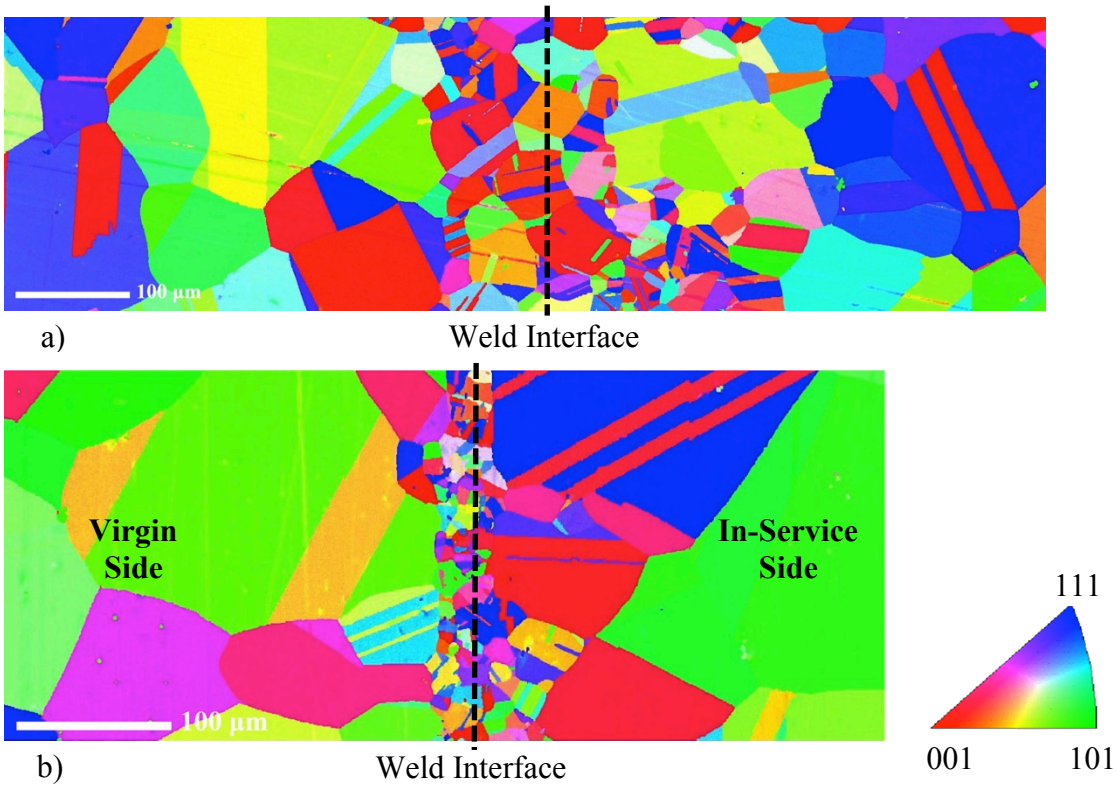

Figure 56: EBSD area map across the weld interface of the PWHTed samples: a) V-V, b) V-IS. The inverse pole figure corresponds to the direction normal to the polished surface. Scale bars represent 100 µm [*81*]. (The International Journal of Advanced Manufacturing Technology, Mechanical properties and microstructural evolution of in-service Inconel 718 superalloy repaired by linear friction welding, 2016, pp. 1-16, M. Smith, L. Bichler, J. Gholipour and P. Wanjara, © Her Majesty the Queen in Right of Canada 2016. With permission of Springer).

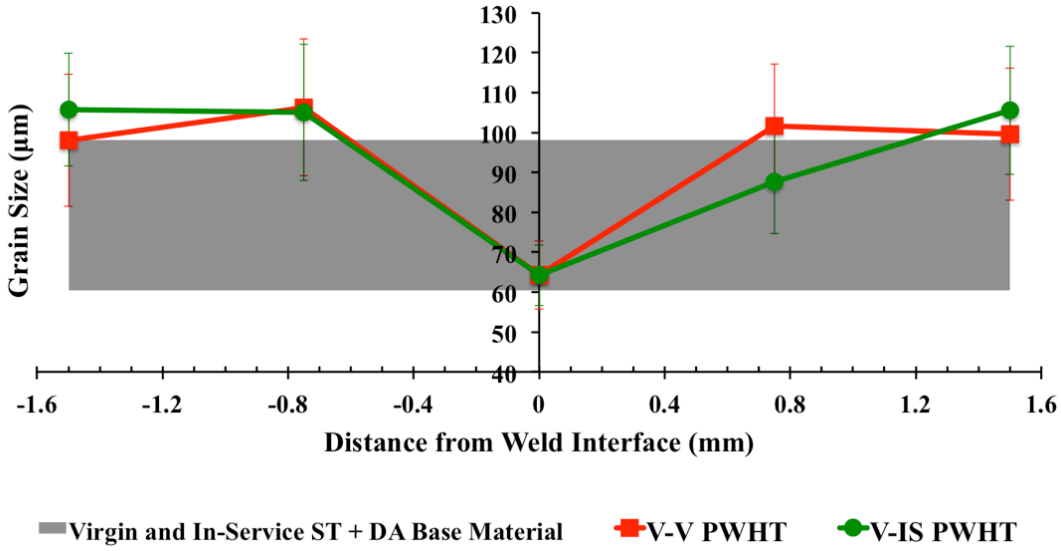

Figure 57: EBSD grain size distribution for PWHTed V-V and V-IS samples relative to the as-received and ST + DA base materials. Base material average grain size, including the 95% confidence interval is shown as shaded regions. Error bars show the 95% confidence interval [*81*]. (The International Journal of Advanced Manufacturing Technology, Mechanical properties and microstructural evolution of in-service Inconel 718 superalloy repaired by linear friction welding, 2016, pp. 1-16, M. Smith, L. Bichler, J. Gholipour and P. Wanjara, © Her Majesty the Queen in Right of Canada 2016. With permission of Springer).

The grain size variation between the V-V PWHTed and V-IS PWHTed samples was minimal and relatively consistent across the weld interface, as seen in Figure 56 and Figure 57. Interestingly, the HAZ and TMAZ regions were not detected in the PWHTed samples. Only a slight difference in the grain size was detected at the weld interface, where smaller grains (65 ± 7.6 µm) were clearly visible. The width of this reduced grain size region at the weld interface was ~50 µm and ~200 µm for the PWHTed V-IS and V-V welds, respectively. The grains observed outside of the weld interface region were significantly larger (100 ± 61 µm). The grain sizes observed in the PWHTed samples (excluding the weld interface region) were slightly larger than the grain size of the V and IS as-received materials that were subjected to the same heat treatment (i.e., ST + DA), which were observed to have

a grain size of 79 ± 23 μm and 78 ± 21 μm, respectively. Therefore, the PWHTed samples underwent some additional grain growth during heat treatment as compared to the as-received samples subjected to ST + DA.

EBSD texture analysis was performed to evaluate the possibility of crystallographic texture evolution in the V-V and V-IS as-welded and PWHTed samples. Figure 58 shows representative pole figure contours for the V-IS as-welded material weld regions (V-BM, HAZ, TMAZ, DRX and IS-BM). Figure 59 shows representative pole figure contours for the PWHTed samples. Based on the EBSD analysis, a random orientation of the grains was observed at all locations in the as-welded and PWHT samples and no crystallographic texture was detected.

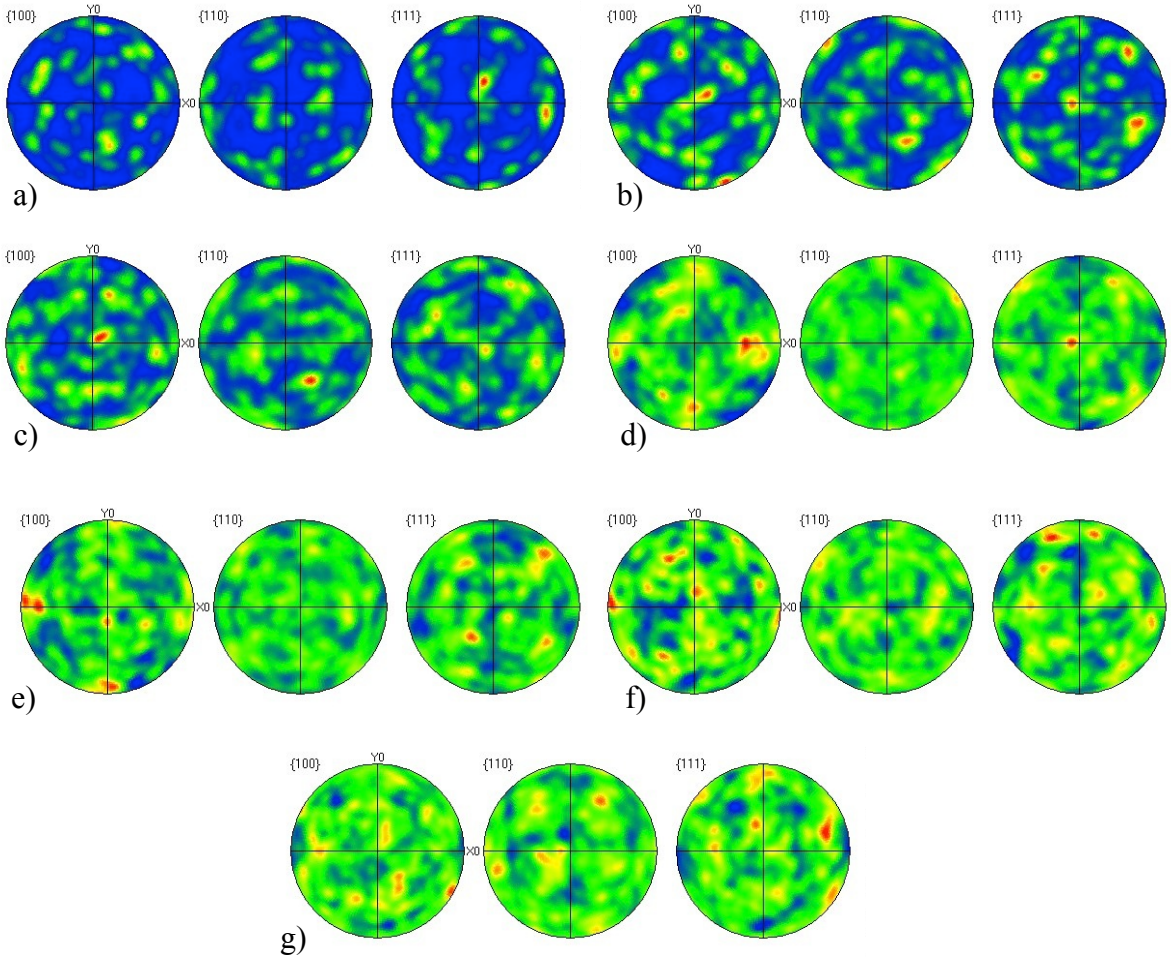

Figure 58: Representative pole figure contours taken from V-IS as-welded sample: a) V-BM, b) V-HAZ, c) V-TMAZ, d) DRX, e) IS-TMAZ, f) IS-HAZ, g) IS-BM. V-V as-welded material had similar pole figure contours to those shown in a) – d) and was symmetrical, but offset over the weld interface [*81*]. (The International Journal of Advanced Manufacturing Technology, Mechanical properties and microstructural evolution of in-service Inconel 718 superalloy repaired by linear friction welding, 2016, pp. 1-16, M. Smith, L. Bichler, J. Gholipour and P. Wanjara, © Her Majesty the Queen in Right of Canada 2016. With permission of Springer).

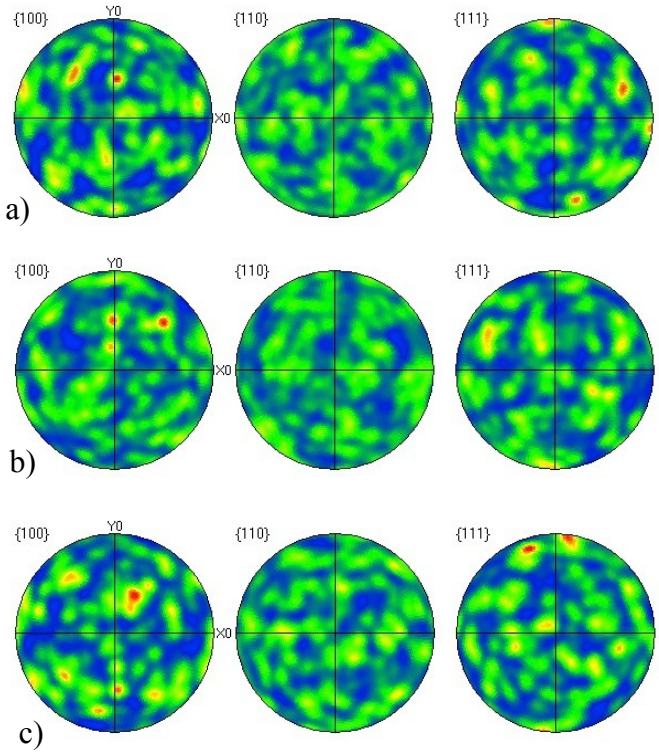

Figure 59: Representative pole figure contours taken from V-IS PWHT sample: a) V-BM, b) Weld interface, c) IS-BM. V-V PWHT material had similar pole figure contours to those shown in a) – c) [*81*]. (The International Journal of Advanced Manufacturing Technology, Mechanical properties and microstructural evolution of in-service Inconel 718 superalloy repaired by linear friction welding, 2016, pp. 1-16, M. Smith, L. Bichler, J. Gholipour and P. Wanjara, © Her Majesty the Queen in Right of Canada 2016. With permission of Springer).

Microstructural characterization of the strengthening precipitates (γ' and γ'') was performed on the as-received material (as shown in Figure 35) and the as-welded samples in each of the weld regions, as shown in Figure 60.

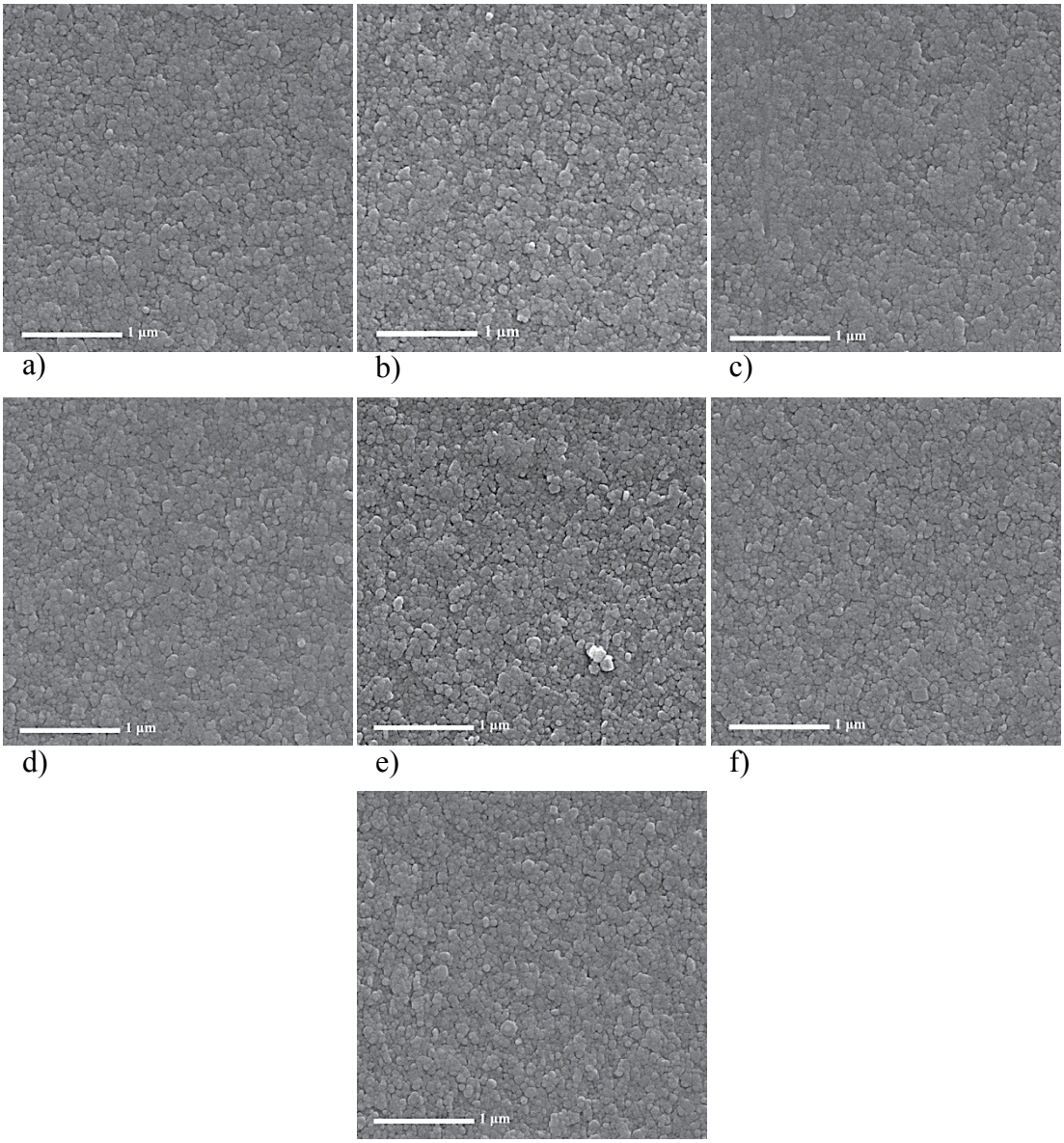

Figure 60: FEG-SEM micrographs (SE) of the γ' and γ'' phases in the V-IS as-welded sample in each of the weld regions: a) V-BM, b) V-HAZ, c) V-TMAZ, d) DRX, e) IS-TMAZ, f) IS-HAZ, g) IS-BM.

The γ' and γ'' precipitate size in the IS disk base material was observed to be constant across the entire radius of the disks and was similar to the γ' and γ'' sizes measured in the V as-received material. As seen in Table 6, the precipitate size in the as-welded V-V and V-IS

material was comparable to the as-received materials and was close to the ideal 30 – 40 nm size for optimum mechanical properties of IN 718 [*1*].

Table 6: Approximate size of the γ' and γ'' particles in the IN 718 base materials and linear friction welds [*81*]. (The International Journal of Advanced Manufacturing Technology, Mechanical properties and microstructural evolution of in-service Inconel 718 superalloy repaired by linear friction welding, 2016, pp. 1-16, M. Smith, L. Bichler, J. Gholipour and P. Wanjara, © Her Majesty the Queen in Right of Canada 2016. With permission of Springer).

Sample	Diameter (nm)
V-BM (As-Received)	< 30
IS-BM (As-Received)	< 30
V-V*	< 35
V-IS*	< 35

*The size of γ' and γ'' did not change across the weld region (DRX, TMAZ, HAZ and BM)

SEM microstructural characterization was carried out using both SE and BSE imaging modes to reveal the larger precipitates. Representative micrographs for each region of the as-welded V-IS material are shown in Figure 61. Additional SEM merged images across the as-welded V-V and V-IS samples are provided in Appendix C. Microstructural features on the V side of the V-IS sample, shown in Figure 61a – d, were similar to those observed for the as-welded V-V material.

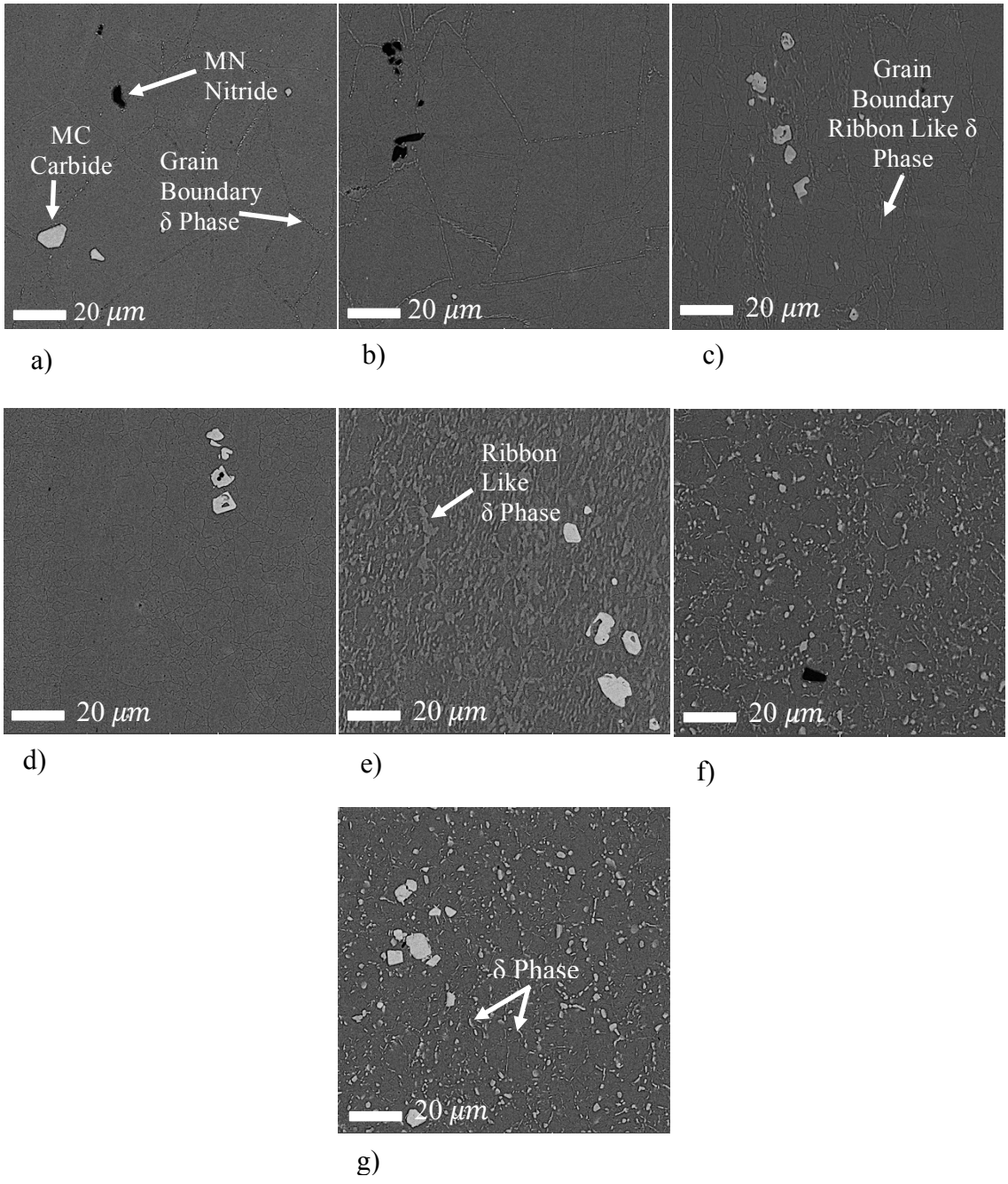

Figure 61: Representative SEM backscatter electron micrographs of the as-welded V-IS sample: a) V-BM, b) V-HAZ, c) V-TMAZ, d) DRX. e) IS-TMAZ, f) IS-HAZ, g) IS-BM [*81*]. (The International Journal of Advanced Manufacturing Technology, Mechanical properties and microstructural evolution of in-service Inconel 718 superalloy repaired by linear friction welding, 2016, pp. 1-16, M. Smith, L. Bichler, J. Gholipour and P. Wanjara, © Her Majesty the Queen in Right of Canada 2016. With permission of Springer).

The δ phase morphology and volume fraction changed significantly across the weld interface. In the unaffected BM, a substantial δ phase precipitation was observed, while in the DRX region, a complete dissolution of the δ phase was observed. A transition zone within the TMAZ in the V and IS sides of the welded samples with partial dissolution of the δ phase was observed. The dissolution resulted in a ribbon like morphology of the δ phase, as seen in Figure 61c and Figure 61e.

The morphology of the MC-type carbides and MN-type nitrides remained constant in all regions of the welded materials. Further, no welding defects, such as cracking, voids, oxides or liquation were observed at the weld interface or within the weld affected area.

The absence of defects in the weld-affected region in the current work cannot be overlooked. Since solid-state welding processes involve lower temperatures compared to fusion welding techniques, microcracking due to melting/solidification is eliminated. The complete elimination of such defects makes friction welding an attractive option for welding solidification crack susceptible superalloys, such as Inconel 738LC, ALLVAC 718PLUS and WASPALOY [*26*] [*48*] [*50*].

Typically, low melting temperature compounds liquate in the TMAZ and/or HAZ regions during fusion welding. The liquid, if present in a substantial volume, can advance through the grain boundaries and create a liquid/grain boundary interface. During cooling, if a critical tensile stress is reached, the formation of micropores will occur and subsequently nucleate microcracks. In general, LFW processes have a lower susceptibility for liquation cracking due to: (i) the application of a compressive load during welding, which reduces the likelihood of reaching the critical tensile stress required to open and propagate a crack, (ii)

the use of lower overall temperatures in solid-state welding reduces the possibility of liquation of precipitates [*20*].

Liquation of γ' and MC type carbides was reported by Ola *et al.* [*22*] [*23*] in the TMAZ and HAZ regions of friction welded CMSX-486 and Inconel 738 superalloys. The precipitates were reported to remain in the alloy at temperatures well above their equilibrium solvus temperature during rapid heating, resulting in eutectic type reactions with the matrix. As discussed in Section 4.3.2, the average interface temperature observed during welding in the current study was ~1130 °C, which was above the γ', γ'', and δ phase equilibrium solvus temperatures for IN 718 (909 °C – 936 °C, 885 °C – 946 °C and 995 °C – 1035 °C, respectively) [*1*] [*2*] [*26*]. However, in the current work liquation was not observed in any of the weld samples, which is consistent with Damodaram *et al.* [*26*] and Mary *et al.* [*25*] [*27*] who also experimented with friction welding of IN 718.

The absence of liquation (and liquation cracking) may be explained by examining the parameters that influence particle liquation and subsequent cracking during friction welding. During LFW, rapid thermal cycles create a substantial divergence from equilibrium conditions, which results in an increase in the complete precipitate dissolution temperature [*22*] [*23*]. Also, slow precipitate dissolution rates, low melting points, high process temperatures and the presence of impurities have been shown to promote non-equilibrium reactions between the precipitates and the matrix [*12*] [*20*] [*21*] [*49*] [*50*]. By scrutinizing the parameters that influence particle survival under non-equilibrium conditions (which help precipitates to survive above the equilibrium eutectic temperature [*49*]) and relating these parameters to the observed microstructural features in this work, the lack of liquation in this work can be explained. First, the Laves phase (which has been reported to liquate in IN 718

[*52*] [*55*]) was not observed in the material due to the alloy composition (Nb was less than 5 wt%) used in this work [*5*] [*41*] [*52*] [*100*]. Second, carbides (MC type) have been reported to liquate at temperatures exceeding 1200 °C [*55*] [*100*]. In the present work, the process temperatures were below 1200 °C, thus carbide liquation was not expected. Third, for the γ', γ'' and the δ phase precipitates, the temperature recorded during welding was above the reported solvus temperature of each of these phases; however, the size of these precipitates was sufficiently small to allow complete dissolution into the matrix before reaching the eutectic temperature. Dissolution rates of these precipitates were likely enhanced with the application of a compressive stress, as suggested by Ola *et al.* [*22*]. Therefore, since the conditions for liquation of the various precipitates were not met, none of the phases present in the materials used in the current work were prone to liquate.

There was some difficulty associated with etching the PWHT material sufficiently to reveal the microstructural features without obscuring the surface with a burn layer that rapidly formed during the etching processes. However, etching was sufficient to reveal a coarsening of the smaller γ' and γ'' precipitates at all locations within the PWHT samples during microstructural analysis, as seen in Figure 62 and summarized in Table 7. Precipitate coarsening may be an indication of δ phase dissolution with an associated release of Nb, leading to the increased formation of γ''.

Table 7: Approximate size of the γ' and γ'' particles in base material (ST + DA) and linear friction welds after PWHT [*81*]. (The International Journal of Advanced Manufacturing Technology, Mechanical properties and microstructural evolution of in-service Inconel 718 superalloy repaired by linear friction welding, 2016, pp. 1-16, M. Smith, L. Bichler, J. Gholipour and P. Wanjara, © Her Majesty the Queen in Right of Canada 2016. With permission of Springer).

Sample	γ' and γ'' Diameter (nm)	Sample	γ' and γ'' Diameter (nm)
V-BM (1020 °C ST + DA)	< 85	IS-BM (1020 °C ST + DA)	< 85
V-V PWHTed	< 100	V-IS PWHTed	< 100
V-V PWHTed Weld Interface	< 140	V-IS PWHTed Weld Interface	< 100

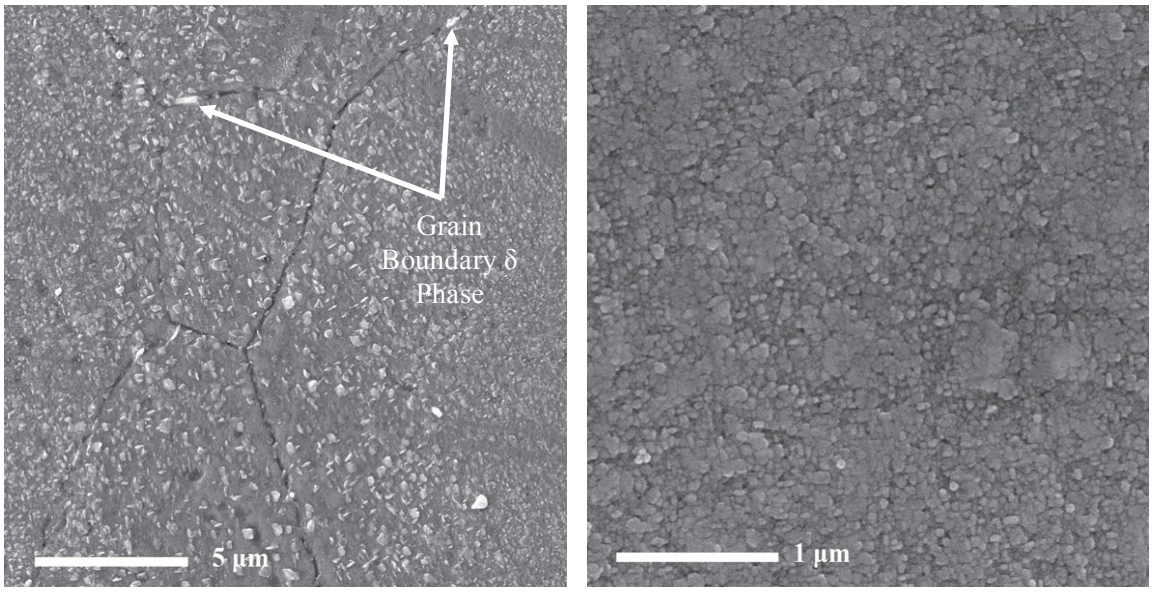

a) b)

Figure 62: FEG-SEM micrographs (SE) of the γ' and γ'' phases in the V-IS PWHT material: a) Weld interface, b) Interior of the grain.

As seen in Figure 62a, some small and randomly distributed δ phase particles were observed scattered along grain boundaries of the PWHTed samples. Based on microstructural examination of the PWHTed samples, it was observed that the standard PWHT was capable of restoring the weld region to a more uniform microstructure by removing the distinct DRX,

HAZ and TMAZ weld regions. Thus, the PWHT parameters examined in this work have successfully re-solutionized the δ phase uniformly even for an initial material with a large variation in the δ phase volume fraction.

4.3.4 Hardness and Mechanical Properties of LFWed Material

The following section presents the results of evaluating the hardness, yield and tensile strength of the V-V and V-IS as-welded and PWHT IN 718 samples.

4.3.4.1 Microhardness Evolution Across the Weld Interface

Figure 63 and Figure 64 show the average microhardness across the weld interface for the as-welded and PWHTed samples, respectively. The hardness trends are based on the average of all measurements made across the weld (as shown in Figure 65 to Figure 68) for each location along the x-direction of the sample. The slight offset of the average hardness from the weld centerline observed in the V-V as-welded material (seen in Figure 63) may be the result of edge effects (uneven increase in hardness magnitudes close to the flash of the weld). This can be observed close to the edge, where the flash was extruded (at y = +5 mm at x = 0 in Figure 65). At this location, the peak hardness magnitude was higher than a y = -5 mm. Therefore, this uneven distribution of peak magnitudes along the x-direction may have attributed to the observed average hardness offset, even though there was some symmetry to the general hardness trend.

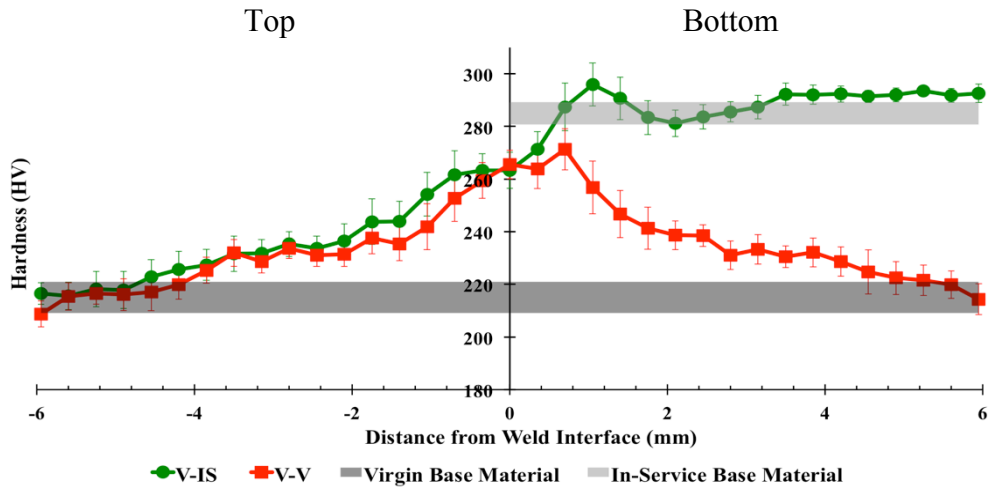

Figure 63: Average Vickers microhardness variation across the as-welded V-V and V-IS samples compared to the as-received base material. Base material average hardness, including 95% confidence interval is shown as shaded regions. Error bars show the 95% confidence interval. Top and bottom indicate the position of sample in the fixture during welding (with V as top coupon) [*81*]. (The International Journal of Advanced Manufacturing Technology, Mechanical properties and microstructural evolution of in-service Inconel 718 superalloy repaired by linear friction welding, 2016, pp. 1-16, M. Smith, L. Bichler, J. Gholipour and P. Wanjara, © Her Majesty the Queen in Right of Canada 2016. With permission of Springer).

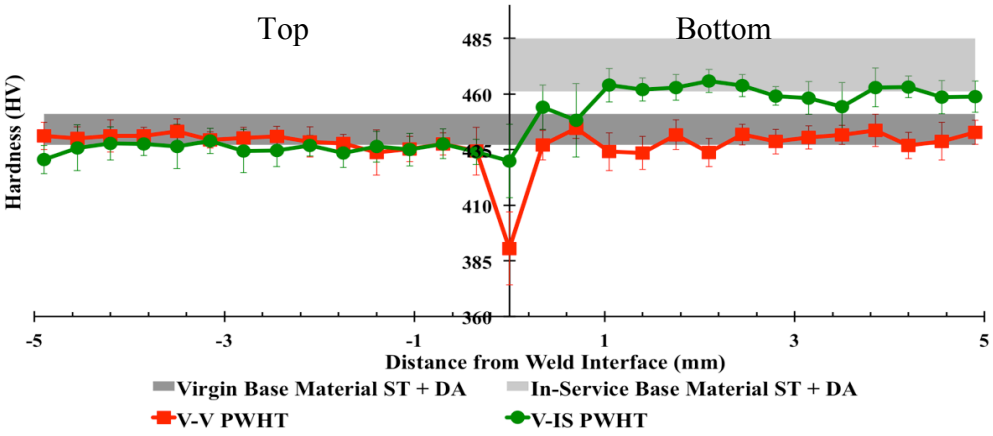

Figure 64: Average Vickers microhardness variation across the PWHTed V-V and V-IS samples compared to PWHT (ST + DA) base material samples. Base material average hardness including 95% confidence interval is shown as shaded regions. Error bars show the 95% confidence interval. Top and bottom indicate the position of sample in the fixture during welding (with V as top coupon) [*81*]. (The International Journal of Advanced Manufacturing Technology, Mechanical properties and microstructural evolution of in-service Inconel 718 superalloy repaired by linear friction welding, 2016, pp. 1-16, M. Smith, L. Bichler, J. Gholipour and P. Wanjara, © Her Majesty the Queen in Right of Canada 2016. With permission of Springer).

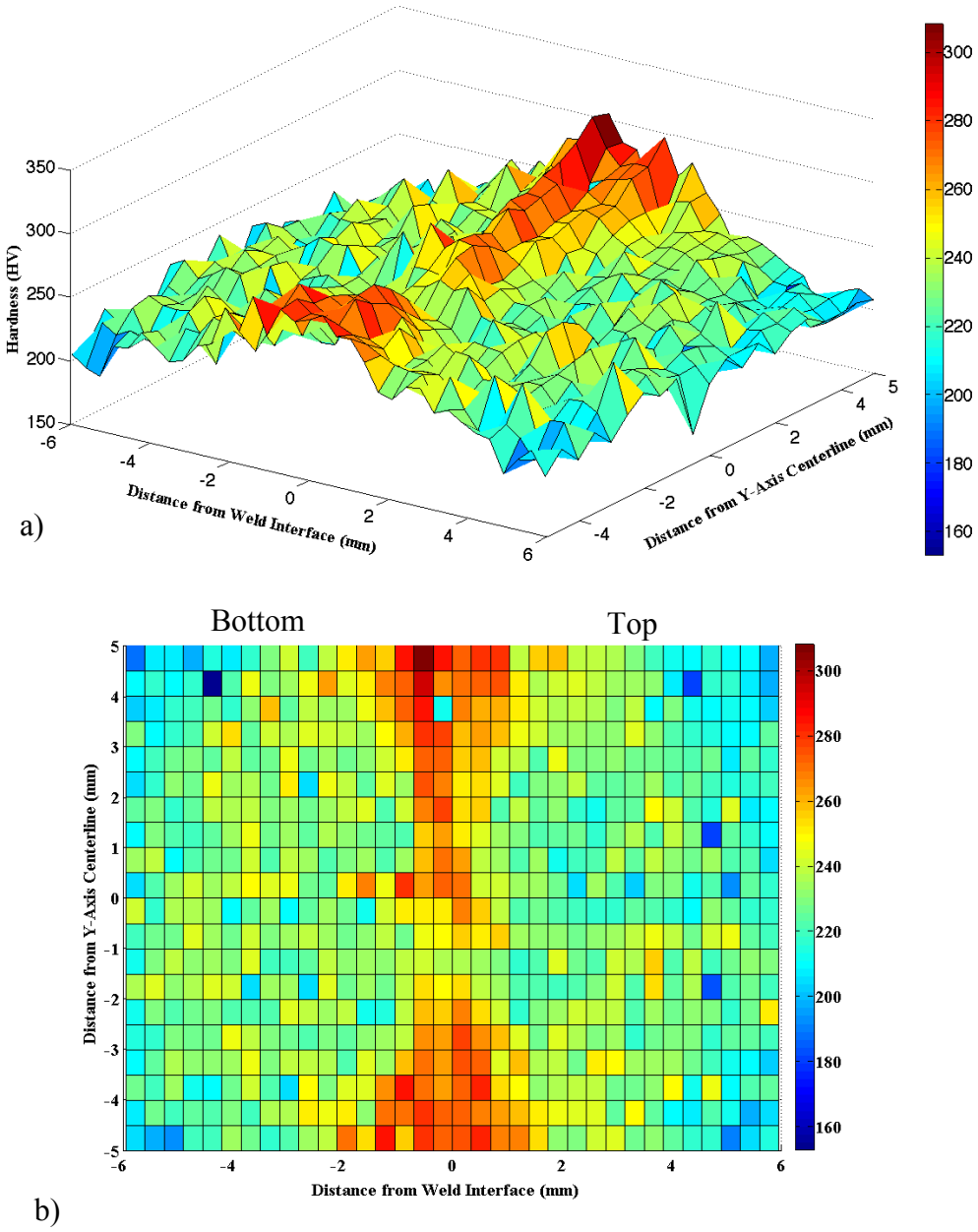

Figure 65: Vickers microhardness maps: a) 3d V-V as-welded hardness map across the weld interface, b) 2D map. Bottom and top indicate the position of sample in the fixture during welding [*81*]. (The International Journal of Advanced Manufacturing Technology, Mechanical properties and microstructural evolution of in-service Inconel 718 superalloy repaired by linear friction welding, 2016, pp. 1-16, M. Smith, L. Bichler, J. Gholipour and P. Wanjara, © Her Majesty the Queen in Right of Canada 2016. With permission of Springer).

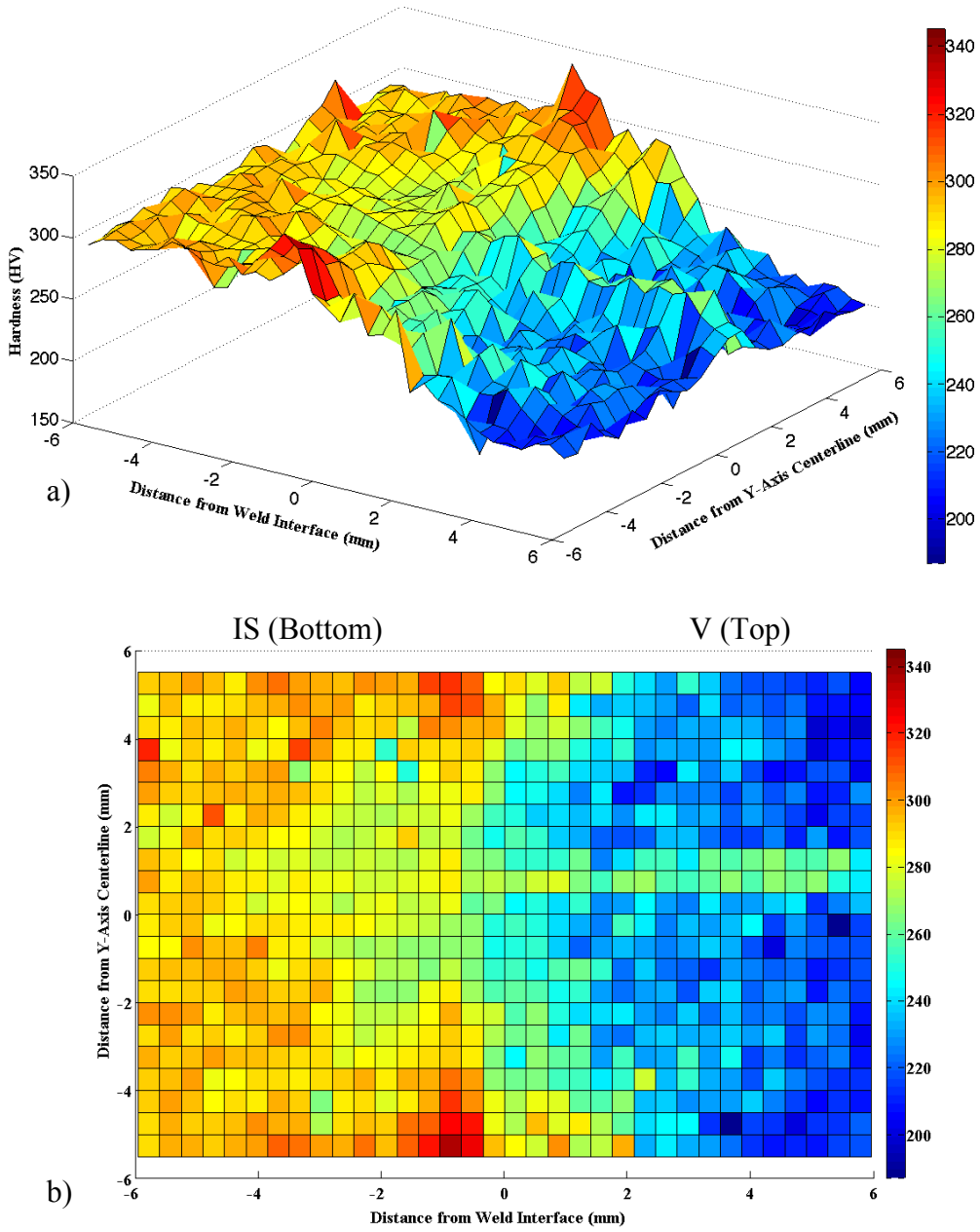

Figure 66: Vickers microhardness maps: a) 3d V-IS as-welded hardness map across the weld interface, b) 2D map. Bottom and top indicate the position of the sample in the fixture during welding [*81*]. (The International Journal of Advanced Manufacturing Technology, Mechanical properties and microstructural evolution of in-service Inconel 718 superalloy repaired by linear friction welding, 2016, pp. 1-16, M. Smith, L. Bichler, J. Gholipour and P. Wanjara, © Her Majesty the Queen in Right of Canada 2016. With permission of Springer).

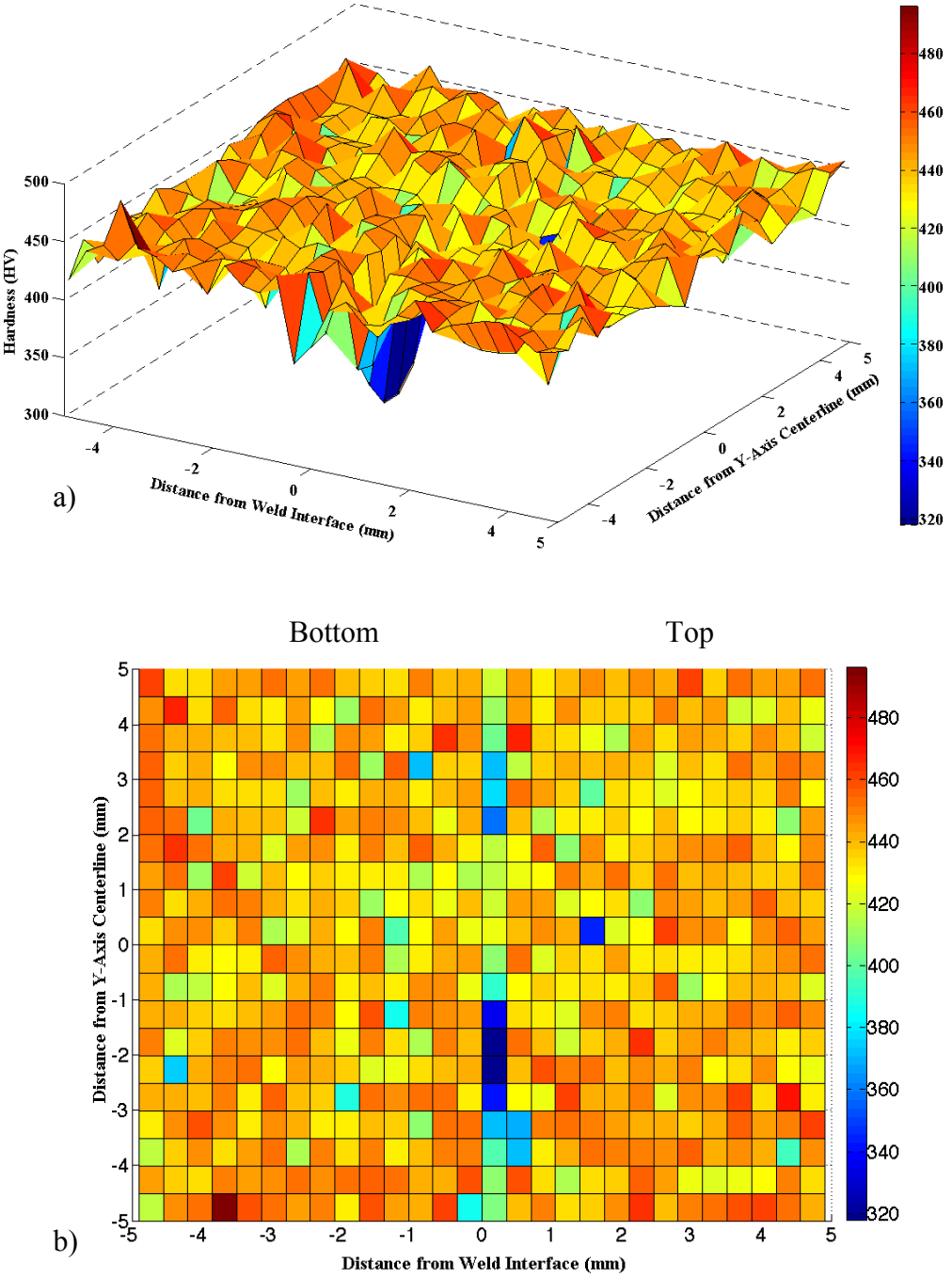

Figure 67: Vickers microhardness maps: a) 3d V-V PWHT hardness map across the weld interface, b) 2D map. Bottom and top indicate the position of the sample in the fixture during welding [*81*]. (The International Journal of Advanced Manufacturing Technology, Mechanical properties and microstructural evolution of in-service Inconel 718 superalloy repaired by linear friction welding, 2016, pp. 1-16, M. Smith, L. Bichler, J. Gholipour and P. Wanjara, © Her Majesty the Queen in Right of Canada 2016. With permission of Springer).

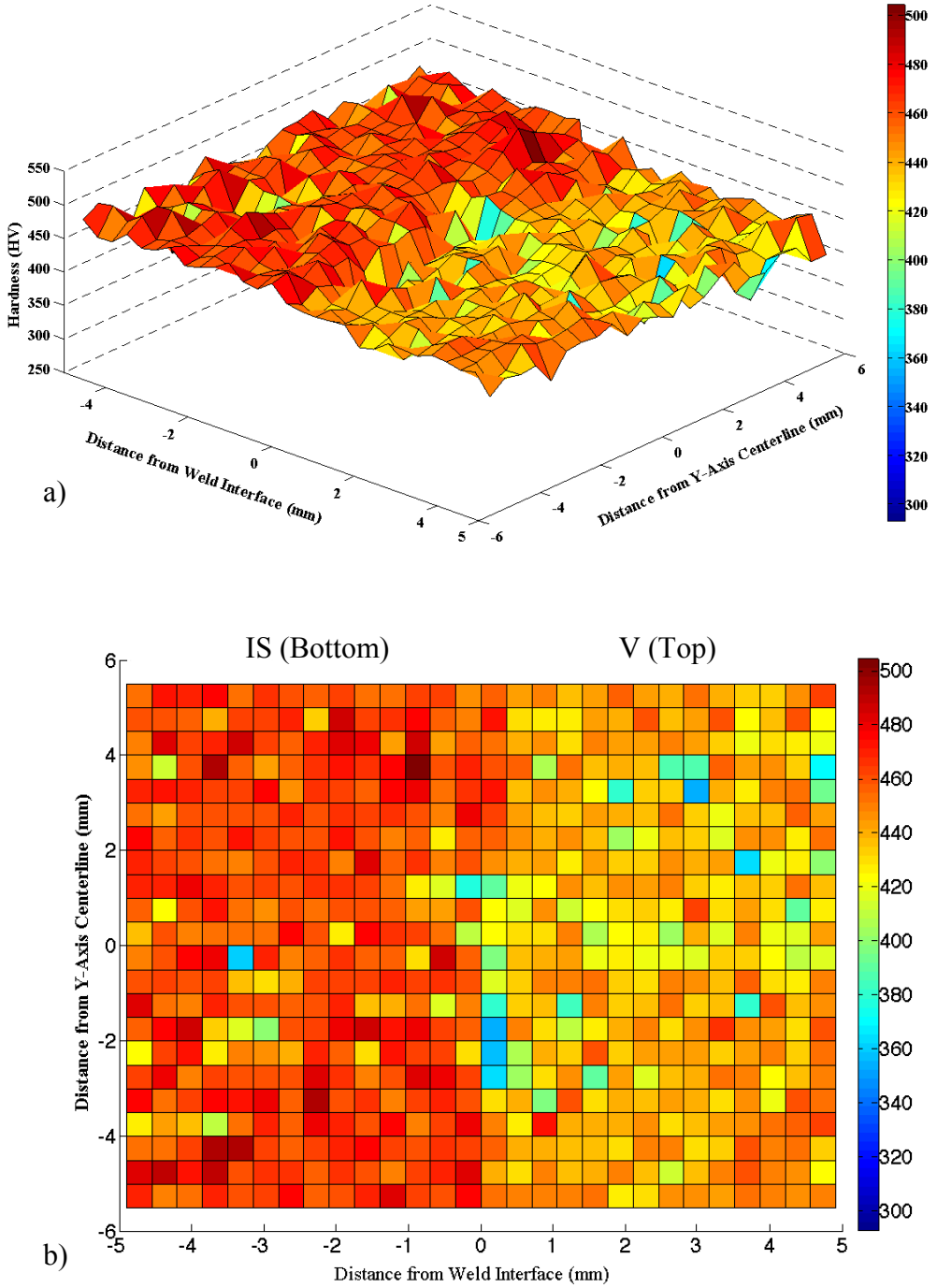

Figure 68: Vickers microhardness maps: a) 3d V-IS PWHT hardness map across the weld interface, b) 2D map. Bottom and top indicate the position of the sample in the fixture during welding [*81*]. (The International Journal of Advanced Manufacturing Technology, Mechanical properties and microstructural evolution of in-service Inconel 718 superalloy repaired by linear friction welding, 2016, pp. 1-16, M. Smith, L. Bichler, J. Gholipour and P. Wanjara, © Her Majesty the Queen in Right of Canada 2016. With permission of Springer).

As seen in Figure 63, the hardness slightly increased across the V-V as-welded weld region ($x = \pm$ 1.5 mm from the weld interface) to a peak hardness of 265 HV, while the base material was 215 HV. The increase in the interface hardness may be partially attributed to the smaller grain size within the HAZ, TMAZ and DRX regions of the weld. This conclusion is reinforced by the strengthening precipitate analysis summarized in Table 6, where the size of the primary strengthening precipitates remained constant across the various weld regions. Therefore, the contribution from variation in strengthening precipitate morphology to the variation in the hardness across the weld region was not as significant as the variations in grain size. Additionally, the partial or full dissolution of the δ phase in the weld regions (discussed in Section 4.3.3) likely allowed for Nb to diffuse into the matrix, thereby permitting an increase in the γ'' volume fraction resulting in a further increase in hardness, as suggested by Smith *et al.* [*41*] who studied the role of Nb in IN 718. The range of hardness values across the weld interface were similar to those reported in the literature [*20*] [*26*].

Analyzing the δ phase volume fraction across the V-IS as-welded sample interface, the IS BM (Figure 61g) had a high volume fraction of the δ phase (~20%), while in the DRX region (Figure 61d) the δ phase was absent. Interestingly, the increase in the γ'' volume fraction as a result of δ phase dissolution in the DRX region did not result in an observable increase in hardness. It was also observed that the average grain size, as well as the average strengthening precipitate size in the DRX and IS BM was consistent. Therefore, the increased hardness on the IS side ($x > 0$ mm) of the V-IS as-welded sample was not expected to be influenced by an increase in strengthening precipitate volume fraction or decreased grain size (as was observed in the V-V as-welded sample). The increase in the hardness

across the weld interface in the V-IS as-welded material was likely the result of other factors (such as variation in composition [*101*]), which were not studied in this work.

The hardness of the PWHT material at *x*-distances greater than 0.35 mm or less than -0.35 mm was similar to the ST + DA as-received material. However, the V-IS PWHT material exhibited a slight increase (~5 %) in hardness on the IS side of the weld, which was still ~2 % below that of the ST + DA IS as-received material. Comparison of the microstructure of the PWHTed samples (Figure 62) to the as-welded samples (Figure 60) revealed significant changes in γ'' and γ' strengthening precipitate morphology and distribution, which may be related to the complete δ phase dissolution in the PWHT samples.

As shown in Figure 64, the hardness of the V-V PWHTed sample was relatively uniform, except at the weld interface. Despite the smaller grain size at the interface, an expected increase in the hardness was not observed. This contradiction may be attributed to significant precipitate coarsening seen at the weld interface (as summarized in Table 7). Precipitate coarsening likely resulted in a loss of coherency strains, which lead to a corresponding decrease in the hardness at the weld interface that was significant enough to overshadow any increase in the hardness resulting from the smaller grain size. Overaging of the strengthening precipitates and subsequent loss of hardness in IN 718 during PWHT was observed by Huang *et al.* [*15*] during their experiments with welding IN 718 to Alloy 720Li using inertia friction welding.

As previously discussed in Section 4.1.2, strengthening mechanisms of IN 718 involve complex interactions between the size and distribution of precipitates (γ', γ'', MC carbides and other phases), the relative γ-γ' and γ-γ'' misfit (or coherency strain between the precipitates and the matrix), residual stress and the grain size [*1*] [*16*] [*20*]. These material

parameters are influenced by the temperature and loading history of the alloy. The complex interaction between the various strengthening mechanisms active in IN 718 was studied by Chaturvedi *et al.* [*4*] and Slama *et al.* [*102*], where various heat treatments were perforemed in an effort to observe the evolution of microstructure and the relation of these changes to mechanical performance. Chaturvedi *et al.* [*4*] reported that the precipitate strengthening mechanisms in IN 718 varied (changing between precipitate shearing and coherency strain strengthening mechanisms) based on the size, morphology and volume fraction of the primary strengthening precipitates γ' and γ'', which were highly influenced by the aging duration and heat treatment peak temperature.

The influence of the thermal history on IN 718's bulk mechanical properties is evident from the recent experiments on friction welding of IN 718 by Damodaram *et al.* [*24*] [*26*] and Preuss *et al.* [*19*]. The authors observed that the effect of various pre- and post-weld heat treatments on the local microstructure (morphology of the strengthening precipitates) and mechanical properties across the weld region were directly and significantly influenced by the heat treatment time, temperature and weld sequence. For example, Damodaram *et al.* [*26*] reported that a PWHT consisting of a STA improved the tensile strength in comparison to the as-welded samples. However, the PWHT consisting of a STA of samples with an existing ST or STA prior to welding resulted in inferior tensile strength compared to samples that were only subjected to aging treatments after welding. The authors attributed the difference in tensile strength to grain coarsening that occurred during the post weld ST stage of the heat treatment.

Therefore, it is highly likely that the hardness trends observed in the current work were related to the γ' and γ'' distribution and morphology effects, as well as solid solution strengthening and grain size [*1*] [*4*] [*16*] [*20*] [*101*] [*102*].

4.3.4.2 LFW Tensile Properties

Room temperature tensile test results of the as-received, as-welded and PWHTed samples are summarized in Table 8.

Table 8: Average tensile properties for the base material, as-welded and PWHTed samples. Error shown is given as 95% confidence interval [*24*] [*26*] [*81*]. (The International Journal of Advanced Manufacturing Technology, Mechanical properties and microstructural evolution of in-service Inconel 718 superalloy repaired by linear friction welding, 2016, pp. 1-16, M. Smith, L. Bichler, J. Gholipour and P. Wanjara, © Her Majesty the Queen in Right of Canada 2016. With permission of Springer).

Sample	Yield Strength (MPa)	Ultimate Tensile Strength (MPa)	% Elongation
V-BM	415 ± 12	854 ± 5	51 ± 4
IS-BM	670 ± 12	1069 ± 2	33 ± 8
V-V LFW	443 ± 21	846 ± 1	48 ± 14
V-IS LFW	478 ± 7	858 ± 11	28 ± 1
V-V PWHT	1085 ± 45	1321 ± 31	20 ± 3
V-IS PWHT	1112 ± 43	1336 ± 23	17 ± 5
IN 718 ST BM [*24*]	499	996	59
LFW + PWHT [*24*]	870	1081	15
ST + LFW + PWHT [*26*]	1254	1480	17

The results for the yield strength, tensile strength and % elongation in the present work are in general agreement with results presented in literature [*26*]. PWHT was observed to significantly improve the tensile strength of both the V-V and V-IS LFWed materials. As discussed previously in Section 4.1.2 and Section 4.3.4.1, the increased mechanical

properties and hardness from PWHT may be partially attributed to the changes in the size, morphology and the volume fraction increase of γ'' resulting from the δ phase dissolution.

There was no observed difference in the tensile strength between the PWHTed samples. This is likely due to the location of material failure, which was observed to be in the V base material in all tensile samples. Since the hardness in the V-V PWHTed sample was the lowest at the weld interface, failure during tensile loading was be expected to occur at the interface region. However, this did not occur and suggests that rapid localized strain hardening within the DRX region may have occurred, leading to a relatively higher localized strength at the interface where finer grains were observed as compared to the surrounding material. Therefore, during loading the stress localized to the weaker V base material, which was then the region most prone failure.

The location of material failure during tensile testing of friction welded IN 718 was observed by Damodaram *et al.* [*24*] [*26*] to vary depending on the heat treatment and welding sequence. Damodaram *et al.* [*26*] observed that IN 718 friction welded samples with an existing pre-weld ST that were subjected to a PWHT consisting of STA (i.e., ST ➔ welded ➔ STA) had lower hardness in the TMAZ as compared to the surrounding base material. However, similar to the observations in this work, Damodaram *et al.* [*26*] reported that the tensile sample failure location was in the base material well away from the weld region and not in the weaker TMAZ. The authors, however, did not provide any explanation as to why failure was not in the weaker TMAZ in their sample.

Since the failure occurred in the unaffected V material for the V-IS as-welded samples, the weld region and the unaffected IS-BM were stronger than the V-BM. This observation is important since it is usually assumed that a material exposed to elevated temperatures for

extended periods typically experiences degradation in mechanical performance. However, contrary to the general assumption, the result of the present work shows that the IS material has retained mechanical properties that were comparable to (and in some cases better than) the V BM in the as-welded and PWHTed conditions. Since the V-BM material was shown to be the weak point in the V-IS welded sample, further damage to the original IS disk is not anticipated during post repair service of LFW repaired BLISK components.

Chapter 5: Phase II: Residual Stress and Strain

Elastic residual strain was measured using the neutron diffraction technique. Subsequent to the initial neutron diffraction experiments (i.e., a low resolution scan using a beam size of 0.5 mm x 4.6 mm), microstructural analysis was performed on the as-welded samples to determine the location of the DRX, TMAZ and HAZ regions. As discussed in Section 4.3.3, the total weld affected region was approximately ±1.5 mm from the weld interface and the size of each weld region was ~0.33 mm. Thus, a second set of experiments with a neutron beam with a width of 0.30 mm was necessary to ensure proper measurement of strain within each of the weld regions (i.e., high resolution scan using a beam size of 0.3 mm x 4.6 mm). Additionally, a strain measurement in the unaffected base material was obtained at ±5 mm from the weld interface.

The following sections provide the results of the measured strain and calculated stress profiles in the as-welded and PWHT samples. Selected results presented in this section were published in the following journals and conferences:

M. Smith, L. Bichler, J. Gholipour and P. Wanjara, "Measurement of residual stresses in linear friction welded in-service Inconel 718 superalloy," in Thermec 2016, Graz, 2016.

M. Smith, J.-B. Levesque , L. Bichler, D. Sediako, J. Gholipour and P. Wanjara, "Residual stress analysis in linear friction welded in-service Inconel 718 superalloy via neutron diffraction and contour method approaches," *Material Science and Engineering A*, 2017 [Available Online] http://dx.doi.org/10.1016/j.msea.2017.03.038.

5.1 Residual Stress and Strain in As-Welded Samples

The following section presents the results of the residual strain mapping of the V-IS and the V-V as-welded samples. Comparison between the measured strain and calculated stress is discussed in addition to a comparison between the high and low resolution neutron diffraction scans and the as-welded and PWHT samples.

5.1.1 Residual Strain in As-Welded Samples

Figure 69 and Figure 70 show the general trend of the residual strains in the as-welded V-V and V-IS samples. In the *y*- and *z*-directions, the strain increased from the BM (far field) to the peak at the weld interface, while in the *x*-direction the strain decreased from the far field to the weld interface. Furthermore, the as-welded materials had a relatively low magnitude of tensile strain along the *x*- and *y*-directions at the weld interface. The strains along the *z*-direction were compressive, as seen in Figure 69 for the V-IS sample and Figure 70 for the V-V sample. Although the general residual strain trends observed for most of the scan locations were similar in both the high and low resolution scans, the magnitude of the residual strain from the low resolution scans was higher than that measured during the high resolution scans in the *x*-direction for the V-IS and *y*-direction for the V-V as-welded samples.

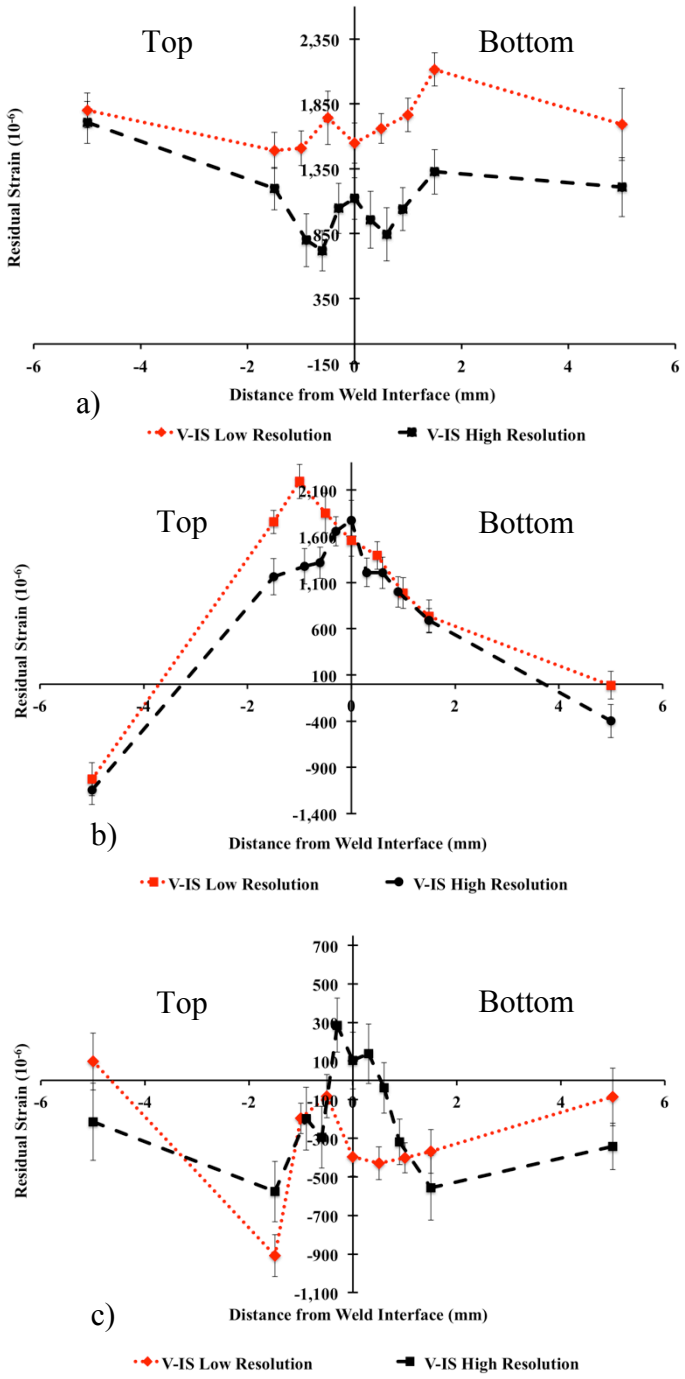

Figure 69: V-IS as-welded residual strain profiles for low resolution (0.5 mm X 4.6 mm beam size) and high resolution (0.3 X 4.6 mm beam size) scans: a) *x*-direction, b) *y*-direction, c) *z*-direction. Error bars show uncertainty. Coupon placement during welding labeled as top and bottom [*86*] [*103*]. (Residual stress analysis in linear friction welded in-service Inconel 718 superalloy via neutron diffraction and contour method approaches, Vol. 691, M. Smith, J. -B. Levesque, L. Bichler, D. Sediako, J. Gholipour and P. Wanjara, pp. 168-179, Crown Copyright © 2017, with permission from Elsevier).

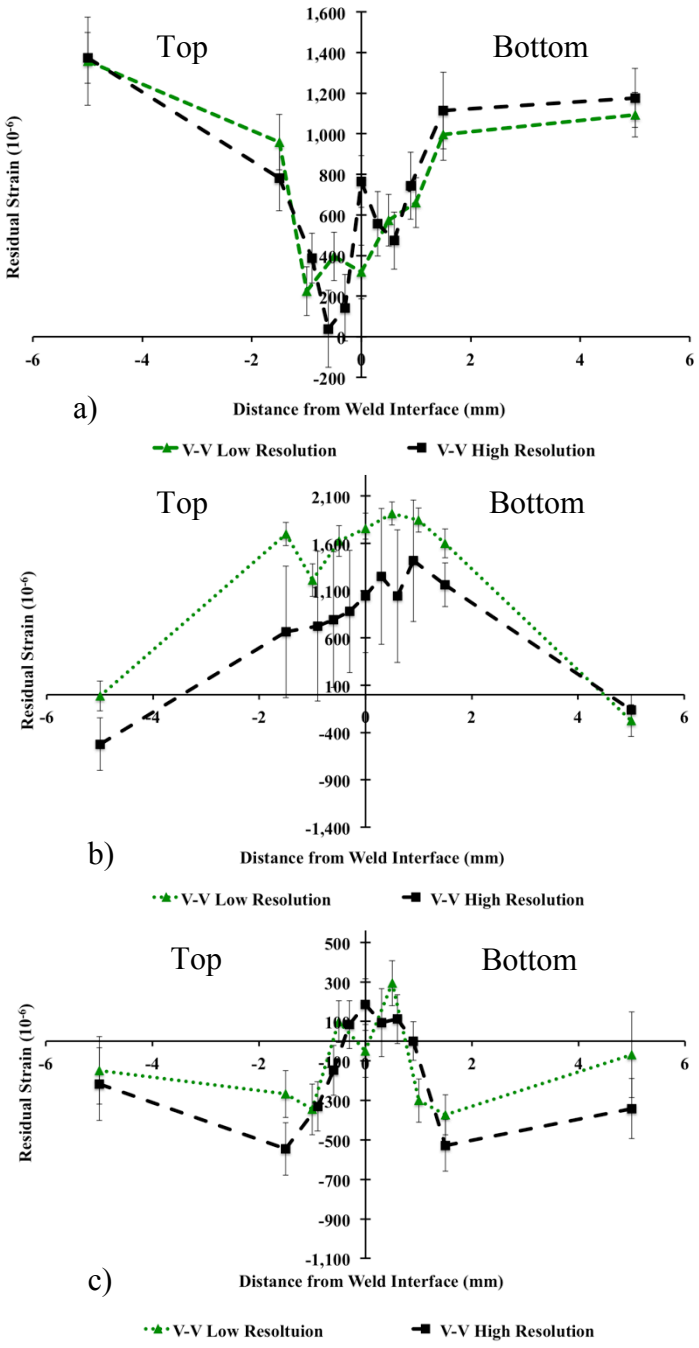

Figure 70: V-V as-welded residual strain profiles for low resolution (0.5 mm X 4.6 mm beam size) and high resolution (0.3 X 4.6 mm beam size) scans: a) *x*-direction, b) *y*-direction, c) *z*-direction. Error bars show uncertainty. Coupon placement during welding labeled as top and bottom [*86*]. (Residual stress analysis in linear friction welded in-service Inconel 718 superalloy via neutron diffraction and contour method approaches, Vol. 691, M. Smith, J. -B. Levesque, L. Bichler, D. Sediako, J. Gholipour and P. Wanjara, pp. 168-179, Crown Copyright © 2017, with permission from Elsevier).

The *x*-direction residual strain magnitudes remained tensile, while the measured residual strain magnitude in the *y*- and *z*-direction approached zero in far field (Figure 69 for the V-IS sample and Figure 70 for the V-V samples). The high residual strain in the *x*-direction may be partially attributed to the LFW process. During welding, a compressive load was applied in the *x*-direction. However, during cooling, the applied load was removed by withdrawing the hydraulic rams, while still holding the sample clamped in the jaws of the welding fixture, resulting in an applied tensile load. As the sample continued to cool, the now tensile residual load may be responsible for the measured tensile residual strain in the *x*-direction.

The peak residual strain was observed at the weld interface along the *y*-direction for both the V-IS and V-V samples, as seen in Figure 69b and Figure 70b, respectively. The *y*-direction corresponded to the axis parallel to the direction of oscillation during welding. Therefore, due to the large plastic deformation, a large amount of elastic tensile residual strain was retained along this direction, which is in agreement with results reported in [*28*]. Also, along the *y*- and *z*-directions, a localized peak residual tensile strain developed at the weld interface. The peak residual strain (and the influence on residual stresses in these directions) may be attributed to large plastic deformation and ensuing flash extrusion along these axes during LFWing.

5.1.2 Residual Stress in As-Welded Samples

Prior to LFW of the V and IS coupons, the magnitude of residual strain and stress in the as-received material was determined following the procedure outlined in Section 3.5. Table 9 and Table 10 summarize the average residual strain and stresses in the three orthogonal directions for V and IS as-received material coupons, respectively.

Table 9: Average residual strain in the as-received material prior to linear friction welding. Presented as strain ± uncertainty [*86*]. (Residual stress analysis in linear friction welded in-service Inconel 718 superalloy via neutron diffraction and contour method approaches, Vol. 691, M. Smith, J. -B. Levesque, L. Bichler, D. Sediako, J. Gholipour and P. Wanjara, pp. 168-179, Crown Copyright © 2017, with permission from Elsevier).

Material	*x*-Direction Strain (10^{-6})	*y*-Direction Strain (10^{-6})	*z*-Direction Strain (10^{-6})
Virgin	152 ± 110	194 ± 128	98 ± 128
In-Service	54 ± 80	333 ± 146	79 ± 111

Table 10: Average residual stress in the as-received material prior to linear friction welding. Presented as strain ± uncertainty [*86*]. (Residual stress analysis in linear friction welded in-service Inconel 718 superalloy via neutron diffraction and contour method approaches, Vol. 691, M. Smith, J. -B. Levesque, L. Bichler, D. Sediako, J. Gholipour and P. Wanjara, pp. 168-179, Crown Copyright © 2017, with permission from Elsevier).

Material	*x*-Direction Stress (MPa)	*y*-Direction Stress (MPa)	*z*-Direction Stress (MPa)
Virgin	76 ± 61	82 ± 63	68 ± 63
In-Service	16 ± 53	74 ± 62	12 ± 57

The uncertainty shown in Table 9 may seem relatively large compared to the measured strain magnitudes. However, having uncertainty values of ±50 – 100 microstrain is common for the neutron diffraction method. The BM uncertainty is consistent with the other scans from the as-welded and PWHT samples presented in this work, as well as with the literature [*28*] [*70*].

The rolling process of the V bar stock (as-received) material during its manufacture may be responsible for the observed minor residual stresses. Similarly, the residual stresses in the IS as-received material may be the remnants of stresses that evolved during forging/forming of the disk, service or during post service handling. The presence of residual stresses in the V and IS as-received material (in the ST condition) prior to welding of the coupons indicates the ST was insufficient to completely remove the residual stresses associated with forming,

service or post service exposure. However, comparison of the low magnitude residual stress in the as-received material (e.g., 76 ± 61 MPa in the *x*-direction of the V as-received material) prior to welding to the high magnitude residual stresses across the weld affected region of the LFWed materials after welding (e.g., 354 ± 123 MPa for the high resolution scan in the *x*-direction of the V-V as-welded material) suggests that the residual stress values in Figure 71 and Figure 72 were imparted by the LFW process.

The high resolution scans in Figure 71 and Figure 72 revealed that the BM (far field measurements) had almost zero stress in the *y*- and *z*-directions for both the as-welded materials, which is in agreement with the stress measurements of the V and IS as-received material prior to welding (summarized in Table 10). In the V-IS sample, the general residual stress trend was found to be tensile in all directions, with a peak at the weld interface. Such a general residual stress trend was in agreement with reported literature for solid state welded superalloys and aerospace grade Ti-alloys [*17*] [*18*] [*28*]. The tensile stresses in the welded samples were likely balanced by compressive stresses at other locations not examined in the current work. The maximum stresses observed across the V-IS weld region were ~530 MPa for the *x*-direction, ~630 MPa for the *y*-direction and ~400 MPa for the *z*-direction, as shown in Figure 71. The maximum stresses across the V-V weld regions were ~375 MPa for the *x*-direction, ~470 MPa for the *y*-direction and ~270 MPa for the *z*-direction, as shown in Figure 72. Unlike the V-IS sample, the V-V sample had the peak stress slightly offset from the weld interface, shifted towards the bottom (oscillating) coupon.

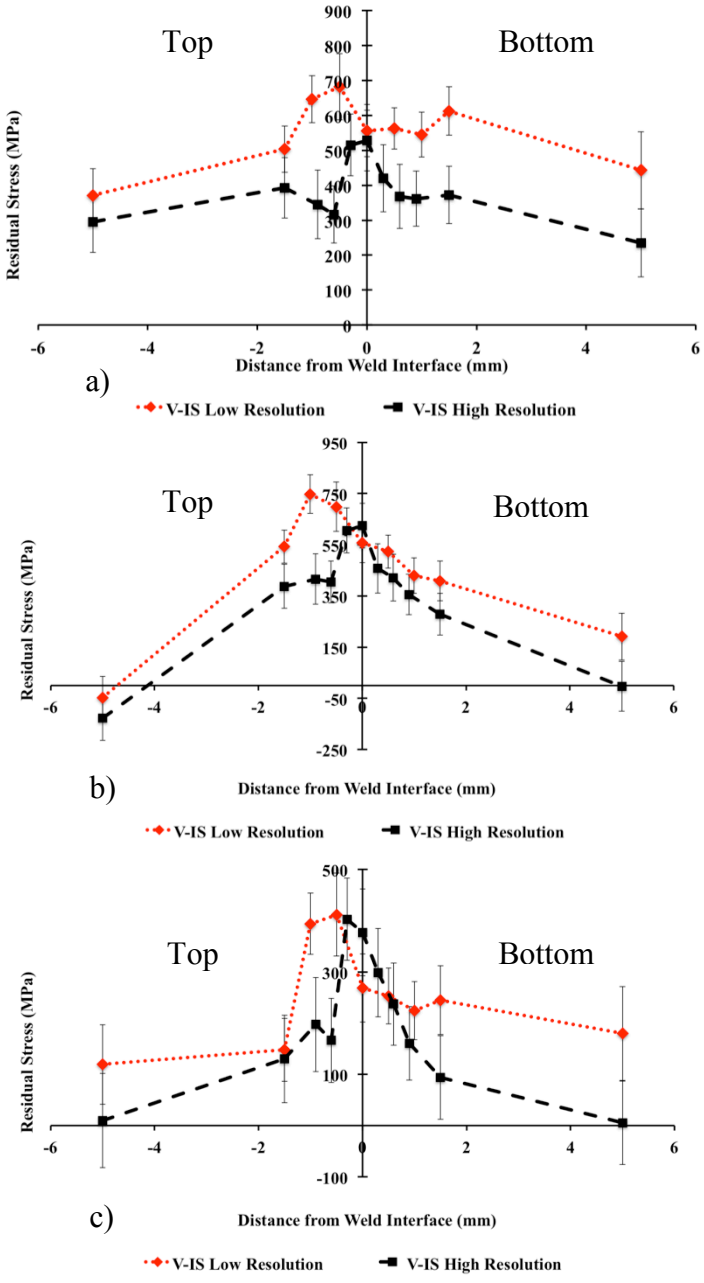

Figure 71: V-IS as-welded residual stress profiles for low resolution (0.5 mm X 4.6 mm beam size) and high resolution (0.3 X 4.6 mm beam size) scans: a) *x*-direction, b) *y*-direction, c) *z*-direction. Error bars show uncertainty. Coupon placement during welding labeled as top and bottom [*86*][*103*]. (Residual stress analysis in linear friction welded in-service Inconel 718 superalloy via neutron diffraction and contour method approaches, Vol. 691, M. Smith, J. -B. Levesque, L. Bichler, D. Sediako, J. Gholipour and P. Wanjara, pp. 168-179, Crown Copyright © 2017, with permission from Elsevier).

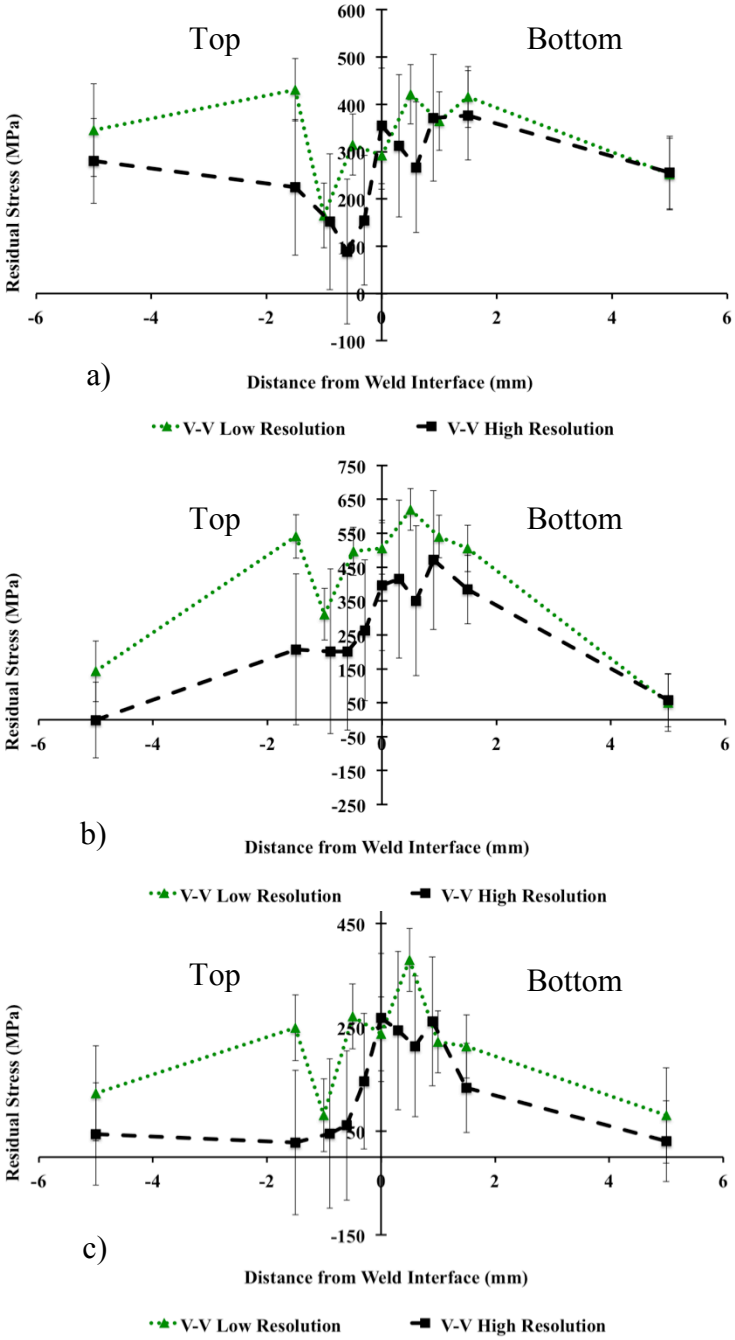

Figure 72: V-V as-welded residual stress profiles for low resolution (0.5 mm X 4.6 mm beam size) and high resolution (0.3 X 4.6 mm beam size) scans: a) *x*-direction, b) *y*-direction, c) *z*-direction. Error bars show uncertainty. Coupon placement during welding labeled as top and bottom [*86*]. (Residual stress analysis in linear friction welded in-service Inconel 718 superalloy via neutron diffraction and contour method approaches, Vol. 691, M. Smith, J. -B. Levesque, L. Bichler, D. Sediako, J. Gholipour and P. Wanjara, pp. 168-179, Crown Copyright © 2017, with permission from Elsevier).

The residual stresses peak offset towards the bottom coupon in the V-V sample (shown in Figure 72a – c may be attributed to several possible factors. First, the alignment of the samples (i.e., locating the weld interface in the stress free (d_0) sample and the stressed (d) sample) was limited to approximately ±0.1 mm due to equipment positioning limitations. Since the stress free sample provides the reference lattice spacing for the strain calculated in the welded samples, the stress free state of the material at each specific location is unique and cannot be substituted for the stress free d_0 value from another location. Likewise, the stressed sample provides the unique and specific lattice spacing created by the thermal and strain gradients during welding at each specific location, which cannot be substituted for another location. Therefore, any variation or shift created due to the physical miss-alignment of the sample with respect to the neutron beam results in a miss-match between the stress free and stressed states of the material. The effect of the variation of the neutron gauge volume on the magnitude of the measured residual strain and calculated residual stress found by the neutron diffraction technique is discussed in Section 5.1.3.

Secondly, the offset may also be attributed to the positioning of the weld coupon during LFWing. Differences in thermomechanical conditions experienced by the top coupon (subjected to applied compressive force) versus the bottom coupon (that oscillated) during welding may have resulted in the observed residual stress offset. Variation in physical positioning and movement during LFW may have shifted the actual development of the weld regions (i.e., each weld region was not centered or directly aligned at the weld interface, as shown in Figure 73), which depends on the thermomechanical response of each coupon during welding. Since the neutron beam was aligned with the weld interface flash, any shift

in the development of the weld regions (DRX, TMAZ, HAZ) along the core of the weld sample at the weld interface may have resulted in an offset of the measured residual stresses.

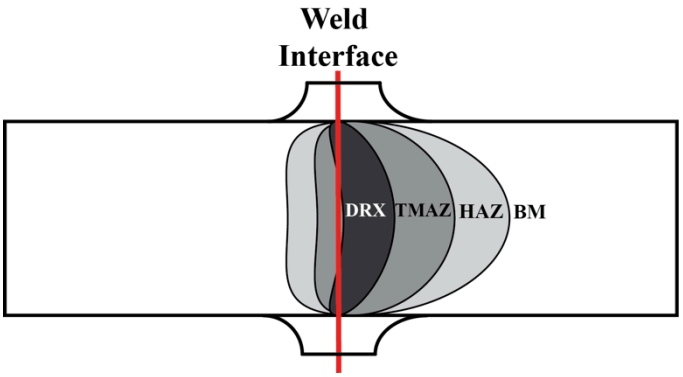

Figure 73: Illustration showing exaggerated weld regions due to variation in thermomechanical response of the weld coupons of a hypothetical LFWed sample. Not to scale.

The existence of an offset as an actual metallurgical occurrence is further supported by the visible microstructural and hardness shift (shown in Figure 54 and Figure 63), where the DRX region and peak hardness were shifted towards the bottom coupon. The lack of influence of coupon position in the case of the V-IS welds may be explained as result of welding two materials with dissimilar initial microstructures. Since the materials have unique elastic-plastic response during welding, the effect of the coupon position during welding was reduced.

The variation in the magnitude of the measurement uncertainty was not consistent across the weld interface, which could be related to the lens-shape of the weld regions. In this work, a neutron beam width of 0.3 mm (high resolution scan) was chosen to ensure that a measurement could be made within each of the weld regions. However, Vickers microhardness mapping across the weld interface, as shown in Figure 65 to Figure 68 revealed that the hardness of the as-welded material varied considerably in the vertical direction (+/- 2.5 mm from the *y*-centerline), which may be attributed to a variation in the

microstructure. The variation in microstructure would undoubtedly influence the d/d_0 values, which may contribute to the observed residual stress offset to the bottom sample and larger error associated with the measured residual strain. Moreover, even though the high resolution neutron beam was collimated to have a width of 0.3 mm, the actual size of the neutron beam that interacted with the sample was possibly slightly bigger due to beam divergence after passing the collimator. The collimator divergence during the current experiments was estimated to be 0.6°, with a sample placement between 25 mm – 35 mm from the collimator. This may have resulted in an overlap with adjacent regions between 0.112 mm – 0.217 mm on either side of the scan location (0.524 mm – 0.734 mm total beam size for the high resolution scans).

The general residual tensile stress trend (i.e., increasing residual stress from the base material to the peak at the weld interface) along the *y*- and *z*-directions for the as-welded material agrees with the published literature, where plastic flow during high temperature processing involved with friction welding resulted in a large flash production and peak residual tensile stresses at the weld interface upon cooling [*18*] [*19*] [*28*]. A similar residual stress trend was reported in Daymond and Bonner's [*28*] experimental work with LFWed Ti-alloys. The authors reported high tensile stresses developed at the weld interface along the axis of flash extrusion, which was attributed to plastic flow during friction welding.

Although an overall compressive force was applied during the LFW process in the current study, the residual stresses were observed to be tensile at the weld interface in all three orthogonal directions. The high residual tensile stress in the present study may be related to the weld sample handling during the forging stage of the LFW process. Similar to the discussion on the residual strains, the retraction of the hydraulic rams during the cooling

stage while still gripping the sample may have contributed to an applied tensile load. Depending on the distance moved by the hydraulic rams, the compressive stress applied during welding may have reverted to an overall tensile stress during sample cooling after welding. Thus, it is important to consider the exact procedure and timing of when the applied forging force is removed during LFWing.

5.1.2.1 Comparison of Residual Stresses to As-received Material Yield Strength

From the room temperature tensile tests, the yield strength (YS) of the V and IS as-received materials was 415 MPa and 670 MPa, respectively. Comparison of the residual stresses to the YS reveals that the residual stresses were below the YS at all locations (and remained within the margin of uncertainty as shown in Figure 75 to Figure 80).

As discussed in Section 4.3, the microstructure across the weld interface significantly changed and as a result the base material mechanical properties likely changed as well. A similar variation in mechanical properties across inertia friction welded RR1000 superalloy was reported by Preuss *et al*. [*17*] [*19*], where a 10 % – 15 % increase in the yield strength was observed across the weld. To verify if an increase in mechanical properties occurred across the LFWed material in the current work, a plot of tensile strength versus Vickers microhardness was made based on the V as-received material data sheet [*79*], as shown in Figure 74.

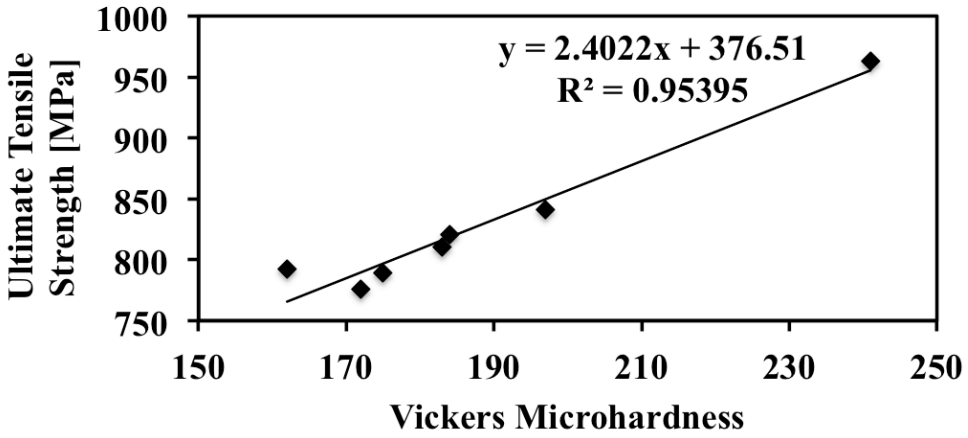

Figure 74: UTS variation as a function of Vickers microhardness for Inconel 718 based on data taken from [*79*] [*86*]. (Residual stress analysis in linear friction welded in-service Inconel 718 superalloy via neutron diffraction and contour method approaches, Vol. 691, M. Smith, J. -B. Levesque, L. Bichler, D. Sediako, J. Gholipour and P. Wanjara, pp. 168-179, Crown Copyright © 2017, with permission from Elsevier).

Using the trend line equation shown in Figure 74 and using the Vickers hardness measurements across the weld interface (as shown in Figure 63), estimation of the local ultimate tensile strength (UTS) across the weld was calculated for the as-welded material. From the room temperature tensile tests conducted on the as-received material (V and IS), the results revealed that the actual YS was consistently ~48 % and ~62 % lower than the UTS for the V and IS as-received materials, respectively. Therefore, using the data from Figure 74 and the relationship between UTS and YS from the room temperature tensile tests, the local YS and UTS based on the hardness trends across the weld interface (referred to as the "estimated YS" and "estimated UTS") was estimated. The estimated YS across the weld interface was calculated by setting the estimated YS 48 % lower than the estimated UTS for the V material and 62 % lower than the estimated UTS for the IS material across the V-V and V-IS as-welded samples. It should be noted that the local YS and UTS of the weld interface for the as-welded material was not measured directly. Estimated YS within the weld region

of the V-V material was kept at 48 % lower than the estimated UTS (since similar materials were joined). For the V-IS weld region, the estimated YS was based on an average difference of 55 % (i.e., average of 48 % and 62 %) lower than the estimated UTS. A comparison between the residual stresses, the estimated UTS and the estimated yield from the hardness trends is shown in Figure 75 to Figure 80 for the V-IS and V-V as-welded materials, respectively.

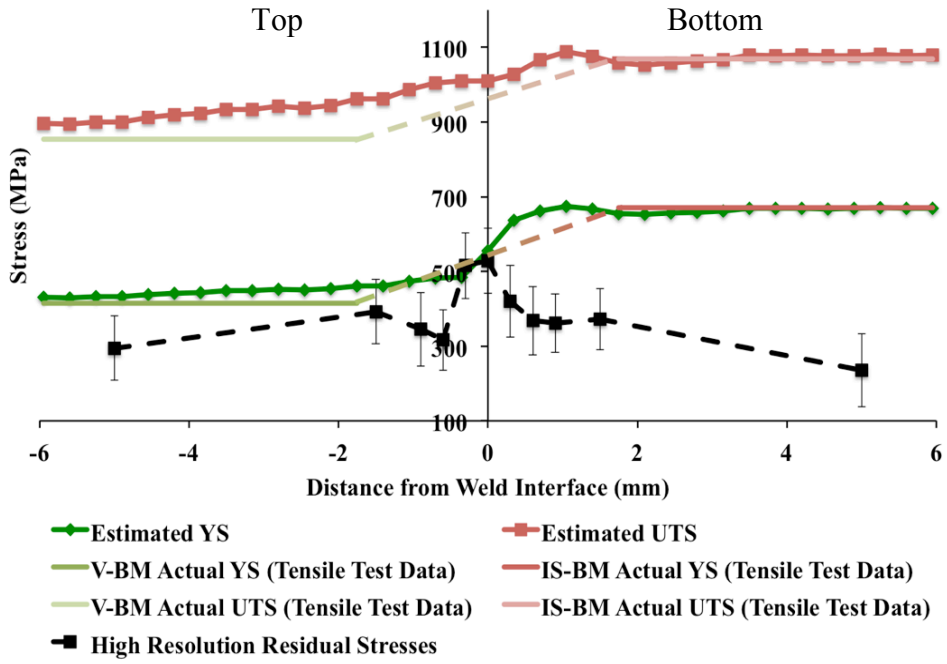

Figure 75: X-direction V-IS high resolution residual stress compared to actual V as-received and IS as-received material yield and UTS from tensile tests and estimations of yield and UTS based on hardness. Error bars show uncertainty. Coupon placement during welding labeled as top and bottom [*86*]. (Residual stress analysis in linear friction welded in-service Inconel 718 superalloy via neutron diffraction and contour method approaches, Vol. 691, M. Smith, J. -B. Levesque, L. Bichler, D. Sediako, J. Gholipour and P. Wanjara, pp. 168-179, Crown Copyright © 2017, with permission from Elsevier).

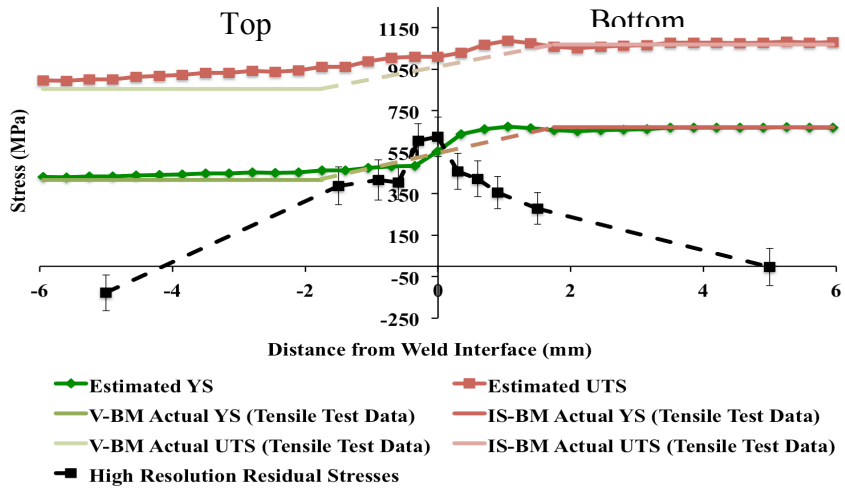

Figure 76: Y-direction V-IS high resolution residual stress compared to actual V as-received and IS as-received material yield and UTS from tensile tests and estimations of yield and UTS based on hardness. Error bars show uncertainty. Coupon placement during welding labeled as top and bottom [*86*]. (Residual stress analysis in linear friction welded in-service Inconel 718 superalloy via neutron diffraction and contour method approaches, Vol. 691, M. Smith, J. -B. Levesque, L. Bichler, D. Sediako, J. Gholipour and P. Wanjara, pp. 168-179, Crown Copyright © 2017, with permission from Elsevier).

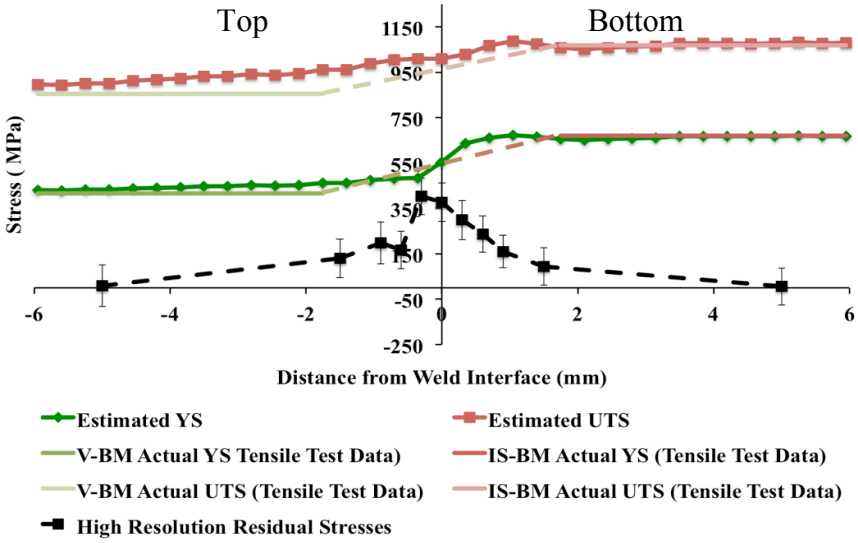

Figure 77: Z-direction V-IS high resolution residual stress compared to actual V as-received and IS as-received material yield and UTS from tensile tests and estimations of yield and UTS based on hardness. Error bars show uncertainty. Coupon placement during welding labeled as top and bottom [*86*]. (Residual stress analysis in linear friction welded in-service Inconel 718 superalloy via neutron diffraction and contour method approaches, Vol. 691, M. Smith, J. -B. Levesque, L. Bichler, D. Sediako, J. Gholipour and P. Wanjara, pp. 168-179, Crown Copyright © 2017, with permission from Elsevier).

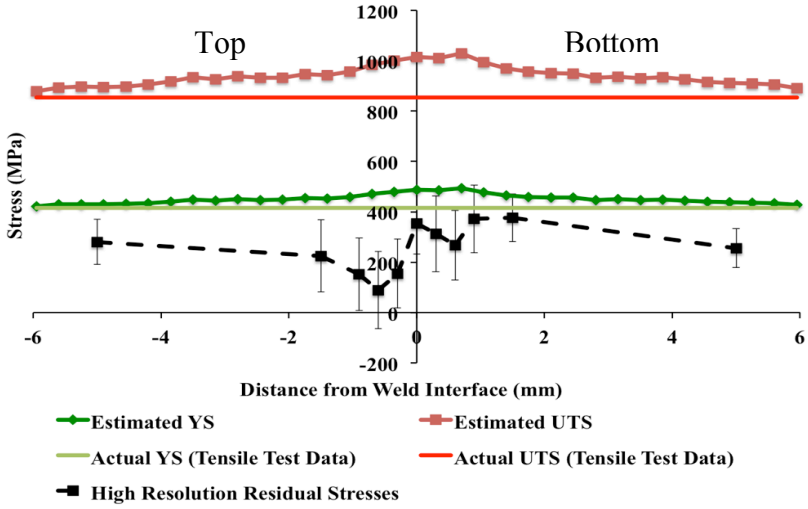

Figure 78: X-direction V-V high resolution residual stress compared to actual V as-received material yield and UTS from tensile tests and estimations of yield and UTS based on hardness. Error bars show uncertainty. Coupon placement during welding labeled as top and bottom [*86*]. (Residual stress analysis in linear friction welded in-service Inconel 718 superalloy via neutron diffraction and contour method approaches, Vol. 691, M. Smith, J. -B. Levesque, L. Bichler, D. Sediako, J. Gholipour and P. Wanjara, pp. 168-179, Crown Copyright © 2017, with permission from Elsevier).

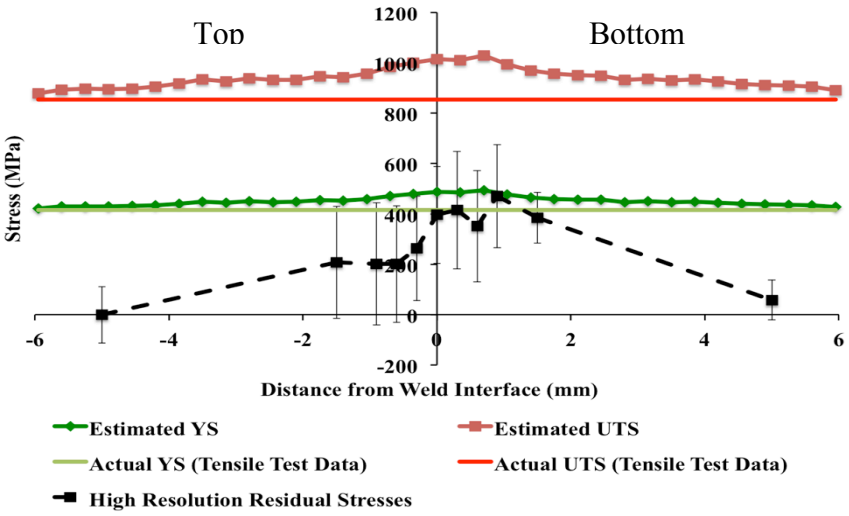

Figure 79: Y-direction V-V high resolution residual stress compared to actual V as-received material yield and UTS from tensile tests and estimations of yield and UTS based on hardness. Error bars show uncertainty. Coupon placement during welding labeled as top and bottom [*86*]. (Residual stress analysis in linear friction welded in-service Inconel 718 superalloy via neutron diffraction and contour method approaches, Vol. 691, M. Smith, J. -B. Levesque, L. Bichler, D. Sediako, J. Gholipour and P. Wanjara, pp. 168-179, Crown Copyright © 2017, with permission from Elsevier).

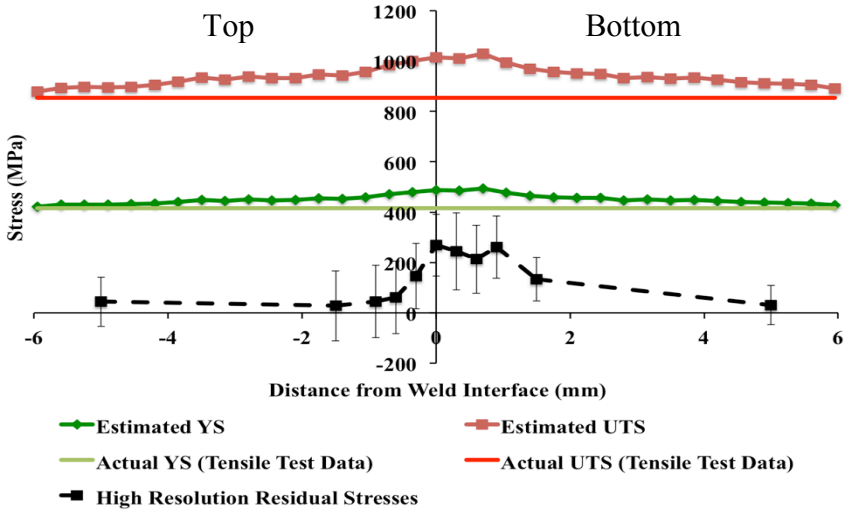

Figure 80: Z-direction V-V high resolution residual stress compared to actual V as-received and IS as-received material yield and UTS from tensile tests and estimations of yield and UTS based on hardness. Error bars show uncertainty. Coupon placement during welding labeled as top and bottom [*86*]. (Residual stress analysis in linear friction welded in-service Inconel 718 superalloy via neutron diffraction and contour method approaches, Vol. 691, M. Smith, J. -B. Levesque, L. Bichler, D. Sediako, J. Gholipour and P. Wanjara, pp. 168-179, Crown Copyright © 2017, with permission from Elsevier).

Comparing the V-V as-welded estimated mechanical properties across the weld to the actual UTS and YS, seen in Figure 78 to Figure 80, it was observed that the estimated weld interface UTS and YS (based on hardness profiles) were ~19% and ~17%, respectively, higher than the UTS and YS of the IN 718 alloy measured by the room temperature tensile tests. These percentage increases were similar to those reported by Preuss *et al*. (where a 10 % – 15 % increase in the YS compared to as-received material was observed across the weld interface) [*17*] [*19*]. Since the V-IS material was mixed at the weld interface, precise estimation of the local YS and UTS and subsequent comparison to the base material is not possible since two distinctly different materials were joined. However, the results of the V-V estimates of the mechanical properties in the current work illustrate how changes in the microstructure at the weld interface influence the mechanical properties in this region. Based

on the estimations, however, the residual stresses at the weld interface were still likely below the 'new' yield point in these regions.

There still remains a significant challenge in correlating the mechanisms that result in the development of residual stresses during linear friction welding of superalloys in the literature. Primarily, the lack of in-depth characterization of the complex microstructural changes that occur in superalloys during the welding processes (as presented and discussed in Section 4.3) is often not provided. Further, common issues in residual stress measurement in the published literature make a direct comparison of results problematic.

5.1.3 High and Low Resolution Scan Comparison

The results of this work on utilizing the high and low resolution scans suggest that relatively large beams (beam sizes 1.5 mm x 1.5 mm or 2 mm x 2 mm) commonly found in the published literature for friction welding without mention of the size of the weld regions being studied pose a challenge for accurate data analysis [*17*] [*18*] [*28*]. Although larger beam sizes improve counting statistics and reduce the scan durations, the relatively large sampling volume of the beam deteriorates the spatial resolution for each weld region, resulting in erroneously calculated residual stresses if the distinct weld regions are smaller than the beam size [*18*].

There is a need to properly account for the variation in the d_0-spacing across the weld interface, in addition to the variation in the size of each weld region [*17*] [*19*] [*104*]. During welding, large thermal gradients are created between the weld interface and the unaffected BM. As a result, various elements may diffuse in and out of substitutional sites within the crystal lattice structure, which results in the expansion or contraction of the stress free lattice

across the weld region. In the reported literature [*28*] [*67*] on the measurement of residual stresses of solid-state processed materials by neutron diffraction, far field d_0-spacing is often used for stress calculations across the entire sample (including the weld region). As a result, the measured *d*-spacing of the stressed sample is compared to an incorrect reference value that may not properly represent a transformed lattice structure due to the influence of localized heat and pressure at the interface. Preuss *et al.* [*17*] [*19*], while studying inertia friction welded RR1000 superalloy, demonstrated the sensitivity of the calculated residual stress measured by neutron diffraction to the variations in the *d*-spacing. A 600 MPa over estimation of the stress at the weld interface was reported by Preuss *et al.* [*17*] [*19*] when a far field d_0-spacing was used rather than the correct value of d_0-spacing across the weld. This overestimation of residual stresses may negatively influence the PWHT by erroneously extending the duration and/or peak, resulting in a degradation of mechanical properties of the final weldment.

Slama *et al.* [*102*] studied the effect of heat treatment time and temperature on the morphology (size and geometry) of the γ' and γ'' phases and related how the variation in the morphology and volume fraction of the γ' and γ'' phases affected the hardness of IN 718. The authors found that the morphology and volume fraction change of the γ' and γ'' phases resulted in an optimum hardness for IN 718 when a short duration at higher heat treatment temperatures (i.e., peak hardness was observed after 50 hours at 680 °C and after 4 hours at 750 °C) was implemented. Slama *et al.* [*102*] also observed that with a continued exposure of IN 718 after peak hardness was achieved, an ~ 20% decrease in hardness due to overaging of the strengthening precipitates occurred. Therefore, the results from Slama *et al.* [*102*], as well as others who investigated the influence of temperature and exposure duration on the

mechanical properties of IN 718 [*1*] [*4*] [*16*] [*20*] [*98*] show that the mechanical properties are influenced by the heat treatment time and peak temperature. As a result, if residual stresses are overestimated from inaccurate measurement of the stress-free d_0-spacing, the subsequent PWHT maximum temperature or duration may be erroneously extended to relieve residual stresses that are not actually in the weldment, resulting in the loss of mechanical properties.

5.2 Residual Stress and Strain in PWHT Samples

The following section provides the results of the residual strain and stress mapping in the V-IS PWHTed and the V-V PWHTed samples. General trends, as well as a comparison between the residual strain and stress is presented and a discussion regarding some of the difficulties associated with acquiring the PWHT diffraction data is highlighted. Furthermore, a comparison between the residual strain and stress of the as-welded and PWHT samples is presented.

5.2.1 PWHTed Samples Residual Stress and Strain General Trends

The residual strain and stress associated with the ST + DA V and IS material prior to welding is summarized in Table 11 and Table 12, respectively.

Table 11: Average residual strain in the ST + DA V and IS material. Presented as strain ± uncertainty.

Material	*x*-Direction Strain (10^{-6})	*y*-Direction Strain (10^{-6})	*z*-Direction Strain (10^{-6})
Virgin	255 ± 72	-139 ± 195	-58 ± 120
In-Service	-266 ± 85	-94 ± 150	-384 ± 96

Table 12: Average residual stress in the ST + DA V and IS material. Presented as strain ± uncertainty.

Material	*x*-Direction Stress (MPa)	*y*-Direction Stress (MPa)	*z*-Direction Stress (MPa)
Virgin	45 ± 57	-14 ± 76	-1.6 ± 65
In-Service	-129 ± 53	-104 ± 62	-147 ± 54

The residual strain and stress in the ST + DA V and IS samples (summarized in Table 11 and Table 12) were mostly compressive, as compared to the as-received samples (summarized in Table 9 and Table 10), which were mostly tensile. The residual stress magnitudes for the V ST + DA sample were relatively closer to zero as compared to the V as-received sample. This suggests that the heat treatment of the V material was more effective in removing the remaining stresses. However, the IS ST + DA sample had higher compressive stress magnitude compared to the as-received IS sample. The higher compressive stress magnitude may be a result of error associated with the measured d or d_0-spacing.

The residual strain and stress for the PWHT V-V and V-IS samples are shown in Figure 81, Figure 82 and Figure 83 for the *x*-, *y*- and *z*-directions, respectively. Based on the results, it was observed that the measured strain and calculated stress values varied across the weld interface, without a general pattern or symmetry between the far field and weld interface regions. The magnitudes of the residual strain and stress were observed to have variation between compressive and tensile values across the weld region.

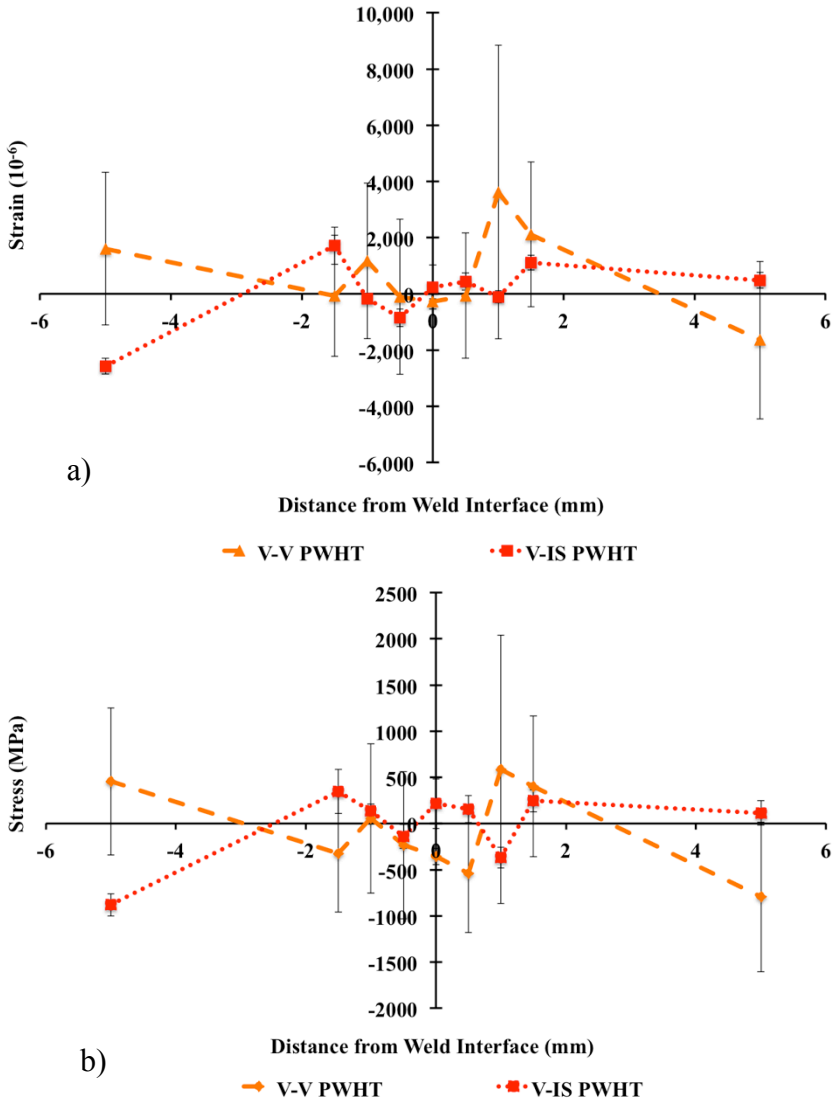

Figure 81: *X*-direction low resolution scans of the PWHT V-V and V-IS residual: a) Strain, b) Stress. Error bars show uncertainty.

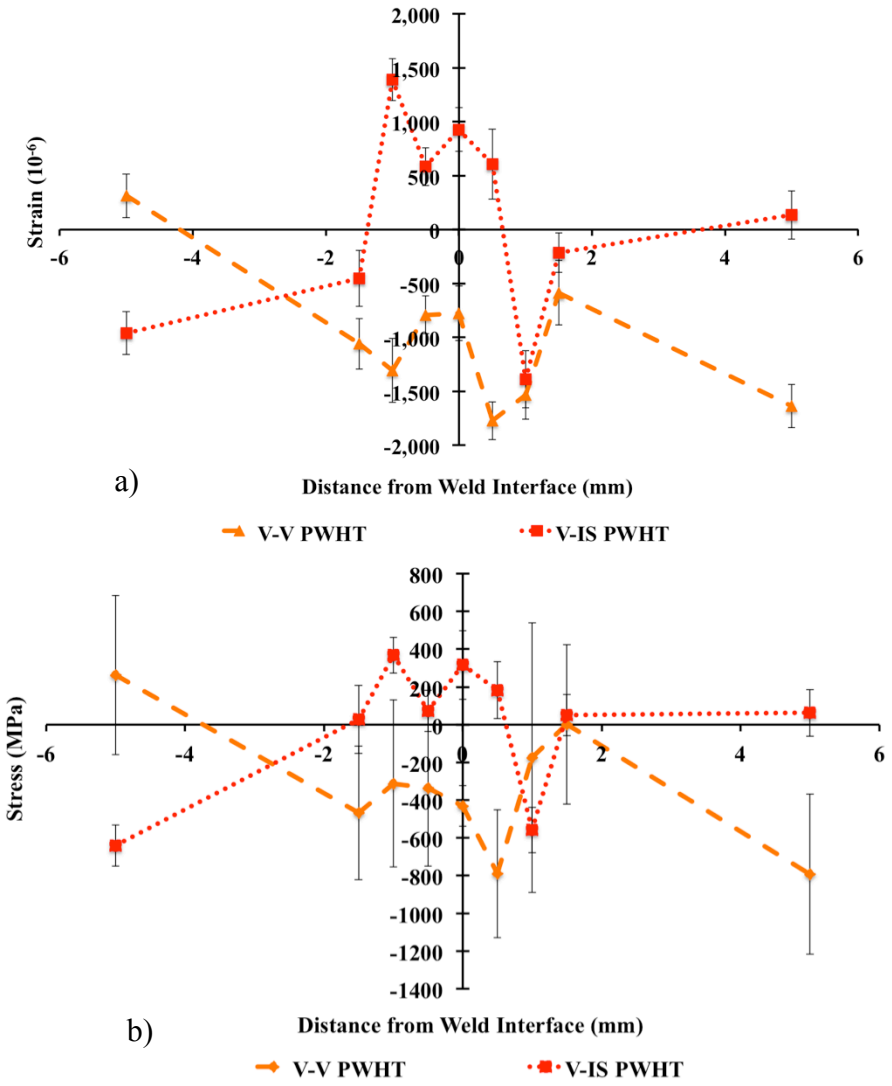

Figure 82: *Y*-direction low resolution scans of the PWHT V-V and V-IS residual: a) Strain, b) Stress. Error bars show uncertainty.

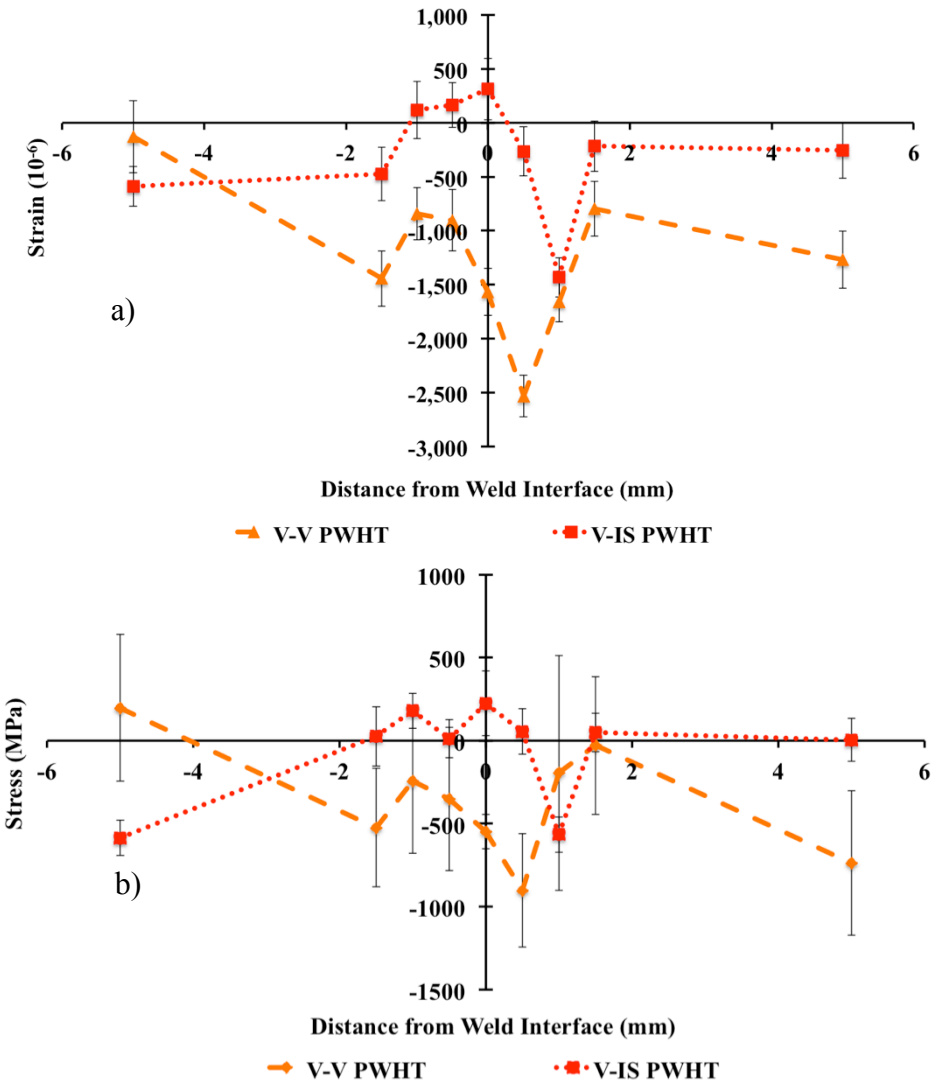

Figure 83: *Z*-direction low resolution scans of the PWHT V-V and V-IS residual: a) Strain, b) Stress. Error bars show uncertainty.

Upon initial inspection of the residual strain and stress values in the *x*-direction of the V-V PWHT sample, it became clear that the measured strain values might not represent the bulk material (*y*- and *z*- directions are discussed further in Section 5.2.3). The primary feature observed that supported this conclusion was the appearance of a double peak in the *x*-direction of the V-V PWHT diffraction data (discussed further in Section 5.2.2). Therefore, in order to find the strain and calculate the stress, one of the peaks had to be selected. This presented a problem of determining which peak to select for the stress calculations. Consequently, to successfully eliminate the occurrence of the double peak in the remaining scan locations during the remaining beam time allotted for the V-V and V-IS PWHT sample experiments, a 4° – 6° sample oscillation was used.

5.2.2 Difficulties Associated with Neutron Diffraction in the PWHTed Samples

Although the neutron diffraction experiments were set up to monitor a single diffraction peak (shown in Figure 84a), the *x*-direction of V-V PWHT material posed a significant challenge since double peaks were detected in regions where the grain size was observed to be between 80 μm – 100 μm. Examples of the different diffraction peaks observed are shown in Figure 84.

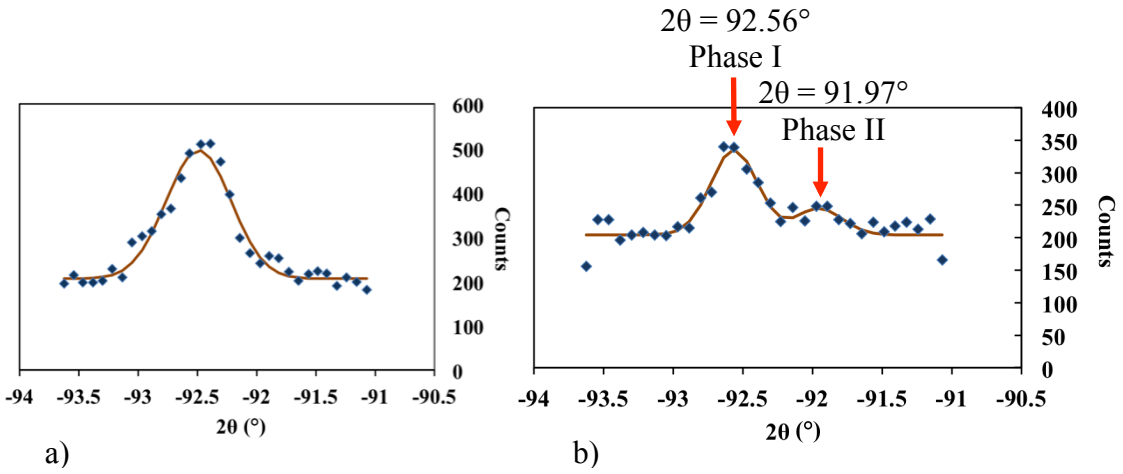

Figure 84: Experimental neutron diffraction data for: a) Single diffraction peak observed in the V-V PWHT sample at the weld interface in the *x*-direction, b) Double peak observed in the V-V PWHT sample in the *x*-direction.

Multiple peaks in alloys with large grains were reported by Mukherji *et al.* [*105*] in their study of γ' and γ'' lattice misfit in Inconel 706. However, in the study by Mukherji *et al.* [*105*] a significant manipulation of the x-ray and synchrotron diffraction data was necessary in order to clearly observe the multiple peaks.

To identify the phases responsible for the multiple peaks in the neutron diffraction data of the *x*-direction of the V-V PWHT sample, the diffraction angle of each peak was used to calculate the lattice parameter for each peak. The calculated lattice parameter for each individual peak was then plotted against the maximum and minimum lattice parameters for the γ' and γ phases for IN 718 obtained from the literature, as shown in Figure 85. The average lattice parameter calculated from the single peak detected for the V-V as-welded material is also shown for comparison. A more detailed discussion on how the lattice parameters were calculated and compared is presented in Appendix D.

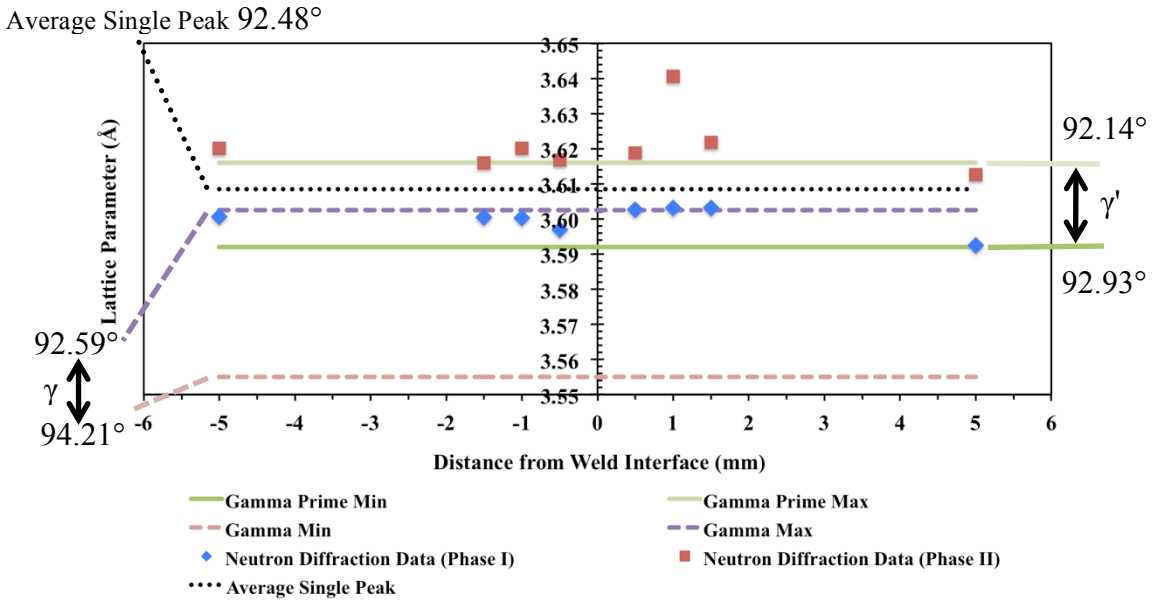

Figure 85: Neutron diffraction data for sites with double peaks in the V ST + DA material along the *x*-direction. Maximum and minimum lattice parameter for the γ' and γ phases based on results reported in [*102*] [*106*] [*107*].

From Figure 85, it can be observed that Phase I (blue data points) are in good agreement with the upper limit of the γ (matrix) phase, while Phase II (red data points) are in general agreement with the upper limit of the γ' phase. As a result, this analysis enabled a more reliable identification of the origin of the double peaks.

Issues with the neutron experimental setup and acquisition (as discussed in Section 5.1.2), material-neutron interaction (mosaic) effects and inaccuracies with the curve fitting may have contributed to the larger lattice parameters calculated for the detected phases (as seen in the outlier point in Figure 85 for Phase II at x = 1 mm) as compared to values presented in the literature. Furthermore, difference in composition between V material used in the current work with that from the literature may have also contributed to the variation in the calculated lattice parameters. According to the literature [*5*] [*101*] [*102*] [*106*], γ' and γ''

morphology is affected by element substitutions in the lattice structure that occurs during heat treatment (exposure). Maniar *et al.* [*101*] studied the effect of heat treatment on lattice parameters for several Ni-based alloys. The authors observed that when the alloys were subjected to similar heat treatment temperatures and durations, the variations in initial alloy composition resulted in lattice substitutions and changes to the morphology and lattice parameters of the precipitates that developed.

As discussed in Section 2.7.1.3 with the larger grains in the PWHT samples, there were fewer grains to contribute to diffraction, which allowed for multiple peaks to be clearly visible. With sample oscillation, the number of grains that contributed to diffraction increased, which resulted in a broader single diffraction peak (loss of dual peaks). In addition, there may have been some preferred orientation of the γ' precipitates in the PWHT samples (based on high magnification FEG-SEM micrographs, as shown in Figure 62 and discussed in Section 4.3.3), which may have also contributed to the appearance of a double peak. Preferred orientation of the precipitates may have reduced the number of suitably aligned planes that would contribute to the diffraction profile, thereby resulting in some diffraction angles contributing less to the overall diffraction profile, subsequently creating a double peak. However, further investigation into precipitate preferred orientation and neutron interaction is required to confirm this hypothesis.

For the remaining *y*- and *z*-directions in the V-V PWHT sample and all the scans in the V-IS PWHT sample, specimen oscillation removed the double peak from the data (i.e., a single peak profile was detected in all directions), but with an associated peak broadening. Peak broadening, measured as the FWHM, for the IS material at $x = 1.0$ of the V-IS PWHT sample (Figure 86a) was 1.077 ± 0.12, while the FWHM of the IS as-received material

(Figure 86b) was 0.3822 ± 0.02. As discussed in Section 2.7.1.3, the lower number of grains contributing to diffraction (larger grain size) in the PWHT material should contribute to more resolved peaks, as compared to the as-welded material. However, the results presented in Figure 86, do not confirm this trend.

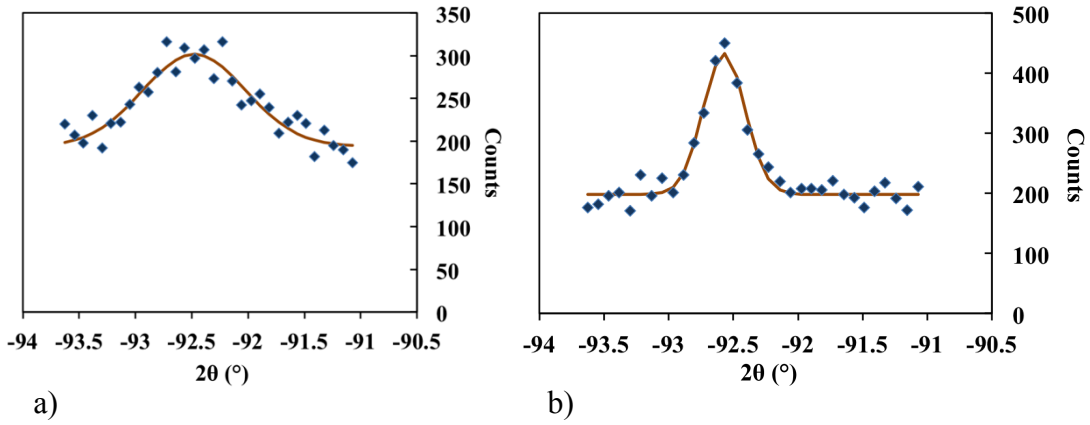

Figure 86: Experimental neutron diffraction data for: a) V-IS PWHT *x*-direction IS material at x = 1.0 mm, b) IS as-received base material.

It is likely that the observed broader single peak in the PWHT samples was the result of the double peak contributions (contributions from multiple phases) that were not fully resolved in the diffraction data (i.e., the data represents a point just prior to the instance where a double peak could be resolved). This conclusion is further supported when comparing the fully defined individual fitted double peak curves (FWHM between 0.38 – 0.45) to the single peaks measured for the as-welded material (FWHM between 0.38 – 0.62). The similarity between FWHM values for the individual peaks in the PWHT and as-welded samples suggests that the broadening in the single peaks of PWHT material (where sample oscillation was used) was likely a result of the peak fitting (i.e., fitting a single peak to data with multiple peaks). Peak broadening in the PWHT material resulting from the presence of

intergranular residual stresses or phase coherency strain induced residual stresses (Type II residual stresses), mosaic effects (Type III residual stresses) and texture were not likely as influential as the contributions from multiple phases. This was because the PWHT is designed to relieve residual stresses within the material and enhance random crystal orientation and re-orientation/destruction of crystal defects (e.g., dislocations). Therefore, the Type II residual stresses, mosaic (Type III residual stresses) and texture contributions to peak broadening in the PWHT material in this work were likely minimal.

The single peaks produced in the V-V PWHTed and V-IS PWHTed material (where sample oscillation was used) diffraction data was a result of the contributions of both phases. Therefore, the diffraction peak of these regions within the PWHT material is representative of the strain in bulk material and can be directly compared with the as-welded samples.

5.2.3 As-Welded and PWHTed Residual Stress Comparison

Comparison of the residual stress from the V-V PWHTed sample performed with the low resolution (0.5 mm X 4.6 mm scan) and the high resolution V-V as-welded sample (0.3 mm X 4.6 mm scan) is provided in Figure 87. From Figure 87a, the residual stress in the *x*-direction of the V-V PWHTed sample varied considerably across the weld interface with a large uncertainty (represented by the error bars). This variation was associated with the double peak that was observed along the *x*-direction (as discussed in Section 5.2.2). Since the strain calculated from the measured diffraction angle of each peak would produce the strain associated with the individual phases and not represent the bulk material, the measured diffraction angles were averaged. The average diffraction angle was then used to calculate the strain and associated stress in order to approximate the bulk material strain and stress along the *x*-direction. The uncertainty in the average diffraction angle position included the

peaks of both phases. Since the stress in the *y*- and *z*-directions of the V-V PWHTed sample used the generalized Hooke's law, the error associated with the average diffraction peak position in the *x*-direction was also transferred to the stress calculated for these directions. However, the literature does report on the residual stresses after PWHT of friction welded superalloys in the virgin state. For example, in the work done by Preuss *et al*. [*17*] [*19*], where superalloys were friction welded and the residual strains measured by neutron diffraction in the as-welded and PWHT states, the authors reported that the calculated residual stresses after heat treatment were near zero or followed a similar profile as the as-welded residual stresses but at a lower residual stress magnitudes.

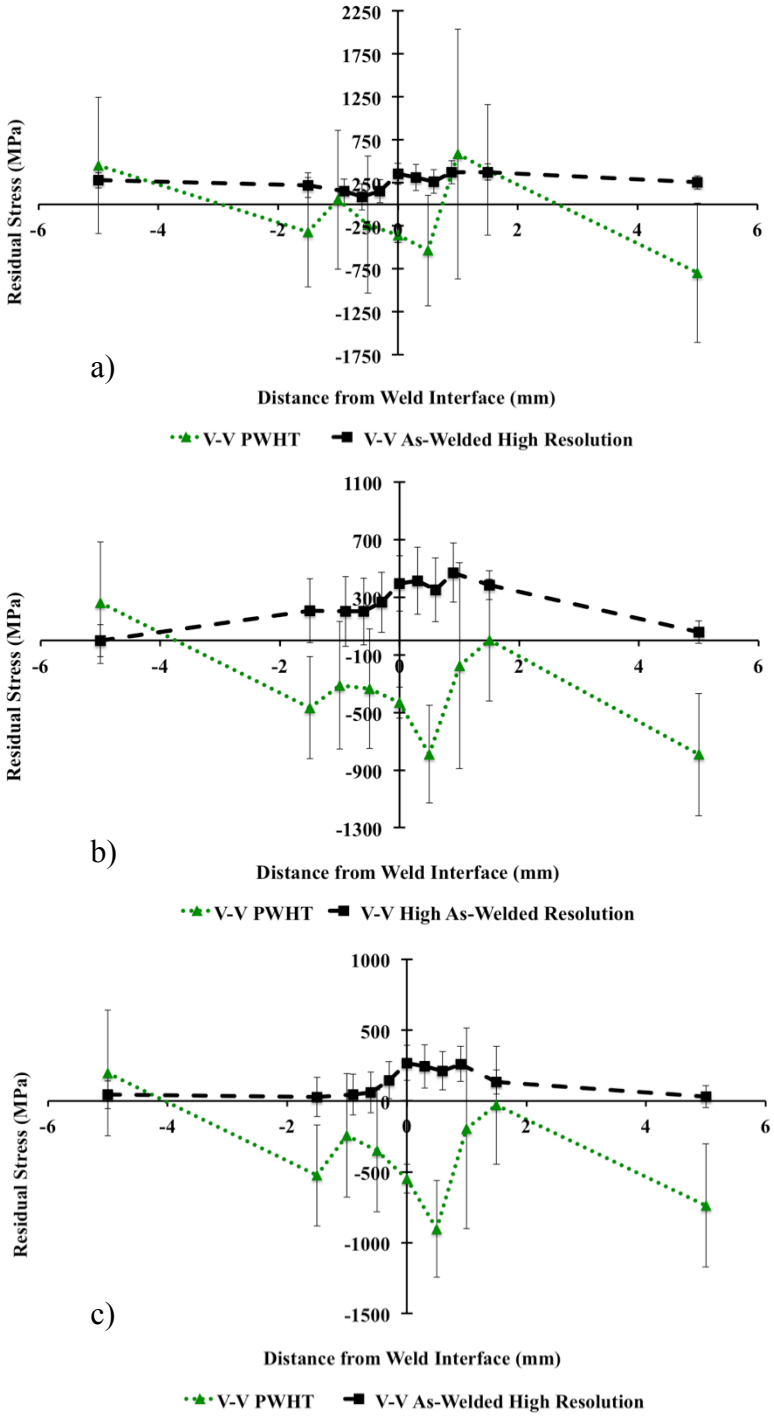

Figure 87: V-V residual stress measurements for high resolution (0.3 mm X 4.6 mm beam size) and PWHT (0.5 X 4.6 mm beam size) scans: a) *x*-direction, b) *y*-direction, c) *z*-direction. Error bars show uncertainty.

Comparison of the residual stress profile from the V-IS PWHTed (0.5 mm X 4.6 mm scan) sample and the high resolution V-IS as-welded sample (0.3 mm X 4.6 mm scan) is provided in Figure 88. The general residual stress trend of the V-IS PWHTed sample followed a similar trend as the as-welded V-IS sample, but at a relatively lower residual stress magnitudes, which agrees with the literature [*17*] [*19*].

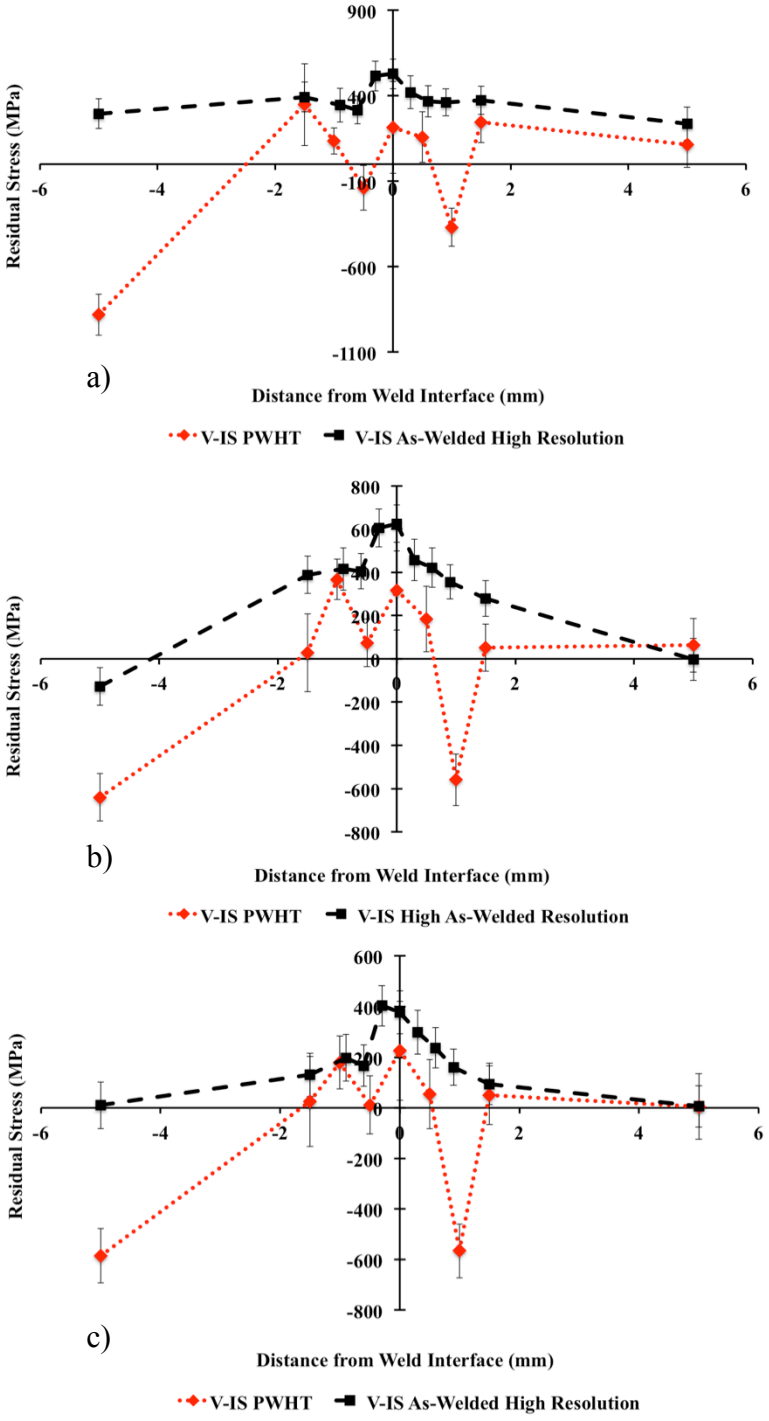

Figure 88: V-IS residual stress measurements for high resolution (0.3 mm X 4.6 mm beam size) and PWHT (0.5 X 4.6 mm beam size) scans: a) *x*-direction, b) *y*-direction, c) *z*-direction. Error bars show uncertainty.

Since a single peak was detected at all locations in the V-IS PWHTed sample (as discussed in Section 5.2.2), the residual stresses can be directly compared to the V-IS as-welded sample. From Figure 88 at x = 1 mm and x = 5 mm the residual stresses have been reduced or were at near zero magnitudes in the V-IS PWHTed sample. For the y- and z-directions, the residual stress was observed to be near zero for most locations. Therefore, it can be concluded that the PWHT had an effect on relieving some of the residual stresses associated with LFWing the V-IS material.

Chapter 6: Conclusions

Microstructural analyses using SEM, EDS and EBSD were performed on V and IS as-received IN 718 material and V-V and V-IS LFWed IN 718 material in the as-welded and PWHT states. Residual strain in the V-V and V-IS as-welded and PWHT samples was measured with the neutron diffraction technique using both a high resolution and low resolution scans to examine the magnitude of the residual strains in the various weld regions. From the measured strain, stress was also calculated for each location of interest across the weld interface of the as-welded and PWHT samples.

The findings of this work relating to each phase of experimentation are summarized as follows:

6.1 Phase I: Base Material Characterization

1) The IS material had a high volume fraction of the δ phase particles at intergranular and intragranular sites, which may be partially attributed to the long exposure of the IN 718 disk to elevated temperature during service or due to the forging/forming operations on the disk. The δ phase volume fraction is an important parameter to consider when developing suitable maintenance and heat treatment parameters in order to fully restore or maintain the mechanical properties of IN 718.

2) No significant difference was observed in the grain size between the outer, mid and inner radius of the IS IN 718 disks. This

suggests that the post service solution heat treatment was successful in creating or maintaining a consistent grain size across the disks. Consistent microstructure across the disks implies uniform mechanical properties and therefore allows for a reliable and consistent repair of the material across these regions.

3) According to EBSD analysis, grain texture was not observed in the V or IS IN 718 as-received materials. The increase in hardness observed across the outer to inner regions of the disks may partially be attributed to other parameters, such as the γ' and γ'' distribution, which was not fully characterized in this work. However, the results discussed in this work offer excellent microstructural and mechanical properties evaluation of IN 718 material that has been subjected to service conditions and has not reached its end-of-life (time expiration) limit.

6.2 Phase I: LFWed As-Welded and PWHT Characterization

1) A successful joint between V and IS IN 718 material was achieved using LFWing. No oxides, voids or contamination of the weld interface and no texture changes across the weld region were observed.

2) Liquation of low melting point phases was not observed in any of the welds examined and therefore cracking associated with the formation of a liquid/matrix interface was not expected. The absence of liquation of constituents may be attributed to the low LFW process temperatures, applied compressive load and small initial precipitate size.

3) Hardness across the weld interface of the as-welded V-V material increased to a peak at the weld interface, which may be associated with grain refinement in the DRX region and a larger volume fraction of the γ'' phase associated with the dissolution of the δ phase in the DRX region. Hardness of the as-welded V-IS material also increased to a peak at the weld interface and may be attributed to complex interactions between the grain size and the morphology, distribution and coherency strains of strengthening precipitates, as well as compositional differences.

4) The offset of the DRX region from the exact center of the weld interface may be attributed to different thermomechanical response of the weld coupons during welding, which may also have influenced the offset in the hardness and the magnitude of the residual strain and stress.

5) PWHT resulted in complete δ phase dissolution at all locations in the sample along with a substantial increase in the grain size across the weld interface in both the V-V and V-IS PWHTed samples.

6) The PWHT of the LFWed samples improved the room temperature hardness and tensile properties of the welded material, which may be partially attributed to the larger volume fraction of the γ'' phase resulting from complete δ phase dissolution.

7) The PWHT was seen to re-solutionize the δ phase uniformly even if the starting materials had a large variation in the δ phase volume fraction. Therefore, the PWHT was compatible for use on LFWed samples.

8) The room temperature hardness and tensile properties of the IS material suggest that the IS material time expiration limit was not reached. Therefore, the simulated repair of BLISKs done in this work using IN 718 material extracted from the IS disk provides important information that validates the feasibility of utilizing LFWing to repair damaged BLISKs and other aero-engine components made of IN 718.

9) LFWing is not sensitive to slight variations in the composition between different IN 718 materials. Therefore, LFWing shows potential for use in manufacturing and repair of aerospace components.

6.3 Phase II: Residual Stress and Strain Measurement

1) Reference lattice parameters and beam width were carefully selected in this work based on microstructural observations. A large tensile stress gradient was present roughly at the centerline of the V-V and V-IS as-welded samples, which was in agreement with the literature.

2) Including the uncertainty of the measurement, the as-welded residual stresses measured with the high resolution neutron beam were lower than the material yield strength at all locations. It is likely that the peak residual stresses were lower than the actual material yield strength within the weld region for reasons highlighted in Section 5.1.2.1.

3) There were several experimental challenges with accurately measuring the residual strain measurements in the V material in the V-V PWHTed samples, thus making direct comparisons between the as-welded and PWHT material impossible. However, for the V-IS PWHTed sample, the residual stresses were observed to be reduced by the PWHT.

The results also suggest that several important considerations must be taken into account before direct comparisons of experiments presented in the open literature can be made. It was demonstrated in this work that variation in the beam size had a significant effect on the measured residual strain and calculated residual stresses due to beam overlap with adjacent weld regions. This overlap may result in inaccurate d/d_0 measurement and result in stress magnitudes that are higher than in reality.

Misalignment of the d/d_0 scans and overlap (vertical and/or horizontal) of the neutron beam with the adjacent weld regions was possibly a contributing factor to the larger uncertainty in the V-V high resolution scans. Due to the lack of clarity in the open literature regarding the compatibility of the gauge volume to the weld region size, proper accounting for variations in d_0 –spacing across the weld interface and sample alignment, it is therefore important to use caution when comparing residual stress magnitudes between studies.

Chapter 7: Future Work

To build on the foundation set in this work, additional testing should be performed to more completely understand how LFWing affects the microstructure and the mechanical properties of IN 718 under simulated repair conditions. The following tests (among others) should be considered:

1) In-depth analysis of the mechanisms resulting in the high residual stresses of the LFWed material.

2) Weld parameter optimization including an in-depth analysis and characterization of the welded material's microstructure (i.e., how microstructure/mechanical properties vary with changes in the LFW process parameters).

3) Finite element model simulation of the LFW process to aid in the determination of the evolution of residual stresses in the material and how variation in weld parameters affects the weld microstructural development.

4) Thermomechanical fatigue and creep tests of LFWed (as-welded and PWHT) material with failure analysis to determine the mechanisms leading to failure.

5) In-depth characterization of the γ' and γ'' phases in the as-welded regions and the influence of weld parameter optimization on these phases and their relation to the mechanical properties of the welded material.

6) Transmission electron microscopy analysis of the γ' and γ'' phases at various locations in each of the weld regions of the as-welded and PWHTed V-V and V-IS materials to confirm *d*-spacing (to compare to the values of *d*-spacing obtained from neutron diffraction experiments).

7) Measurement of the residual strain and stress in the as-welded material via the contour method to validate the values obtained using the neutron diffraction technique. The contour method will also provide the residual strain and stress map across the entire sample surface, which may allow for analysis of regions that may have been missed during the diffraction experiments.

References

[1] A. Chamanfar, L. Sarrat, M. Jahazi, M. Asadi, A. Weck and A. Koul, "Microstructural characteristics of forged and heat treated Inconel 718 disks," *Materials and Design*, pp. 791-800, 2013.

[2] Y. Wang, W. Shao, L. Zhen and B. Zhang, "Hot deformation behavior of delta-processed superalloy 718," *Material Science and Engineering A*, vol. 528, pp. 3218-3227, 2011.

[3] C. Rathod, V. Livescu, B. Clausen and M. Bourke, "Neutron diffraction characterization of residual strain in welded Inconel 718 for NASA space shuttle flow liners," *Advances in Cryogenic Engineering: Transactions of the International Cryogenic Materials Conference - ICMC*, vol. 50, pp. 167-175, 2004.

[4] M. Chaturvedi and Y. Han, "Strengthening mechanisms in Inconel 718 superalloy," *Metal Science*, vol. 17, no. 3, pp. 145-149, 1983.

[5] ASM International, *ASM metals handbook special volume: heat resistant material*.: ASM International, 1997.

[6] M. Qian and J. Lippold, "Liquation phenomena in the simulated heat-affected zone of Alloy 718 after multiple postweld heat treatment cycles," *Welding Journal*, pp. 145-150, 2003.

[7] M. Mehl and J. Lippold, "Effect of delta phase precipitation on the repair weldability of Alloy 718," *Superalloys 718, 625, 706 and Various Derivatives*, pp. 731-741, 1997.

[8] Kh. Al-hatab, M. Al-bukhaiti, U. Krupp and M. Kantehm, "Cyclic oxidation behavior of IN 718 superalloy in air at high temperatures," *Oxidation of Materials*, pp. 209-228, 2011.

[9] M. Mecham. (2011, June) Aviation Week Network. [Online]. http://aviationweek.com/awin/blue-arc-advancement

[10] A. Mateo Garcia, "BLISK fabrication by linear friction welding," *Advances in Gas Turbine Technology*, pp. 411-434, 2011.

[11] R. Messler, Jr., *Principles of welding: Processes, physics, chemistry and metallurgy*.: Wiley-VCH, 2004.

[12] ASM, *ASM metals handbook - Welding, brazing and soldering*.: ASM International, 1997.

[13] P. Mendez and T. Eagar, "Welding processes for aeronautics," *Adcanced Materials & Processes*, pp. 39-43, May 2001.

[14] M. Karadge, M. Preuss, P. Withers and S. Bray, "Importance of crystal orientation in inear friction joining of single crystal to polycrystalline nickel based superalloys," *Materials Science and Engineering A*, vol. 491, pp. 446-453, 2008.

[15] Z. Huang, H. Li, M. Preuss, M. Karadge, P. Bowen, S. Bray and G. Bazter, "Inertia friction welding dissimilar nickel based superalloys Alloy 720Li to IN 718," *Metallurgical and Materials Transactions A* , vol. 38A, pp. 1608-1620, 2007.

[16] M. Preuss, J. Pang, P. Withers and G. Baxter, "Inertia welding nickel based superalloy: Part I metallurgical characterization," *Metallurgical and Materials Transactions A*, vol. 33, pp. 3215-3225, 2002.

[17] M. Preuss, J. Pang, P. Withers and G. Baxter, "Inertia welding nickel-based superalloy: Part II. Residual stress characterization," *Metallurgical and Materials Transactions A*, vol. 33A, pp. 3227-3234, 2002.

[18] N. Iqbal, J. Rolph, R. Moat, D. Hughes, M. Hofmann, J. Kelleher, G. Baxter, P. Withers and M. Preuss, "A comparison of residual stress development in inertia friction welded fine grain and coarse grain nickel-based superalloy," *Metallurgical and Materials Transaction A*, vol. 42A, no. 13, pp. 4056-4063, 2011.

[19] M. Preuss, P. Withers and G. Baxter, "A comparison of inertia friction welds in three nickel base superalloys," *Materials Science and Engineering A*, vol. 437, no. 1, pp. 38-45, 2006.

[20] A. Chamanfar, M. Jahazi, J. Gholipour, P. Wanjara and S. Yue, "Mechanical property and microstructure of linear friction welded WASPALOY," *Metallurgical and Materials Transactions A*, vol. 42A, no. 3, pp. 729-744, 2011.

[21] A. Chamanfar, M. Jahazi, J. Gholipour, P. Wanjara and S. Yue, "Suppressed liquation and microcracking in linear friction welded WASPALOY," *Materials and Design*, vol. 36, pp. 113-122, 2012.

[22] O. Ola, O. Ojo, P. Wanjara and M. Chaturvedi, "Analysis of microstructural changes induced by linear friction welding in a nickel-base superalloy," *Metallurgical and Materials Transactions A*, vol. 42A, pp. 3761-3777, 2011.

[23] O. Ola, O. Ojo, P. Wanjara and M. Chaturvedi, "A study of linear friction weld microstructure in single crystal CMSX-486 superalloy," *Metallurgical and Materials Transactions A*, vol. 43A, pp. 921-933, 2011.

[24] R. Damodaram, S. Ganesh Sundara Raman and K. Prasad Rao, "Microstructure and mechanical properties of friction welded alloy 718," *Materials Science and Engineering A*, vol. 560, pp. 781-786, 2013.

[25] C. Mary and M. Jahazi, "Linear friction welding of In 718 process optimization and microstructure evolution," *Advanced Materials Research*, vol. 15-17, pp. 357-362, 2007.

[26] R. Damodaram, K. Ganesh Sundara Raman and K. Prasad Rao, "Effect of post-weld heat treatments on microstructure and mechanical properties of friction welded alloy 718 joints," *Materials and Design*, vol. 53, pp. 954-961, 2013.

[27] C. Mary and M. Jahazi, "Multi-scale analysis of IN 718 microstructure evolution during linear friction welding," *Adcanced Engineering Materials*, vol. 10, no. 6, pp. 573-578, 2008.

[28] M. Daymond and N. Bonner, "Measurement of strain in a titanium linear friction weld by neutron diffraction," *Physica B*, vol. 325, pp. 130-137, 2003.

[29] J. Romero, M. Attallah, M. Preuss, M. Karadge and S. Bray, "Effect of the forging pressure on the microstructure and residual stress development in Ti-6Al-4V linear friction welds," *Acta Materialia*, vol. 57, pp. 5582-5592, 2009.

[30] M. Chaturvedi, "Liquation cracking in heat affected zone in Ni superalloy welds," *Progress in Light Metals, Aerpspace Materials and Superconductors*, vol. 546-549, pp. 1163-1170, 2007.

[31] H. Bhadeshia. (2003) University of Cambridge. [Online].

http://www.msm.cam.ac.uk/phasetrans/2003/Superalloys/superalloys.html

[32] N. Birks, G. Meier and F. Pettit, *Introduction to the High Temperature Oxidation of Metals*.: University of Cambridge, 2006.

[33] T. Pollock and S. Tin, "Nickel-based superalloys for advanced turbine engines: Chemistry, microstructure and properties," *Journal of Propulsion and Power*, vol. 22, no. 2, pp. 361-374, 2006.

[34] The University of Manchester, *Shreir's Corrosion*, 4th ed., R. A. Cottis et al., Eds. Amsterdam, Netherlands: Elsevier Ltd., 2010, vol. 1.

[35] P. Caron and T. Khan, "Evolution of Ni-based superalloys for single crystal gas turbine blade applications," *Aerospace Science Technology*, vol. 3, pp. 513-523, 1999.

[36] K. Harris and J. Wahl, "Improved single crystal superalloys, CMSX-4 (SLS)[La+Y] and CMSX-486," *Superalloys 2004*, 2004.

[37] A. Lingenfelter, "Welding of Inconel Alloy 718: A historical overview," *Superalloy 718 - Metallurgy and Applicaitons*, pp. 673-683, 1989.

[38] G. Sabol and R. Stickler, "Microstructure of nickel-based superalloys," *Physica Status Solidi*, vol. 35, no. 1, pp. 11-52, 1969.

[39] J. Oblak, D. Paulonis and D. Duvall, "Coherency strengthening in Ni base alloys hardened by DO22 gamma double prime precipitates," *Metallurgical Transactions*, vol. 5, pp. 143-153, 1974.

[40] A. Devaux, L. Naze, R. Molins, A. Pineau, A. Organista, J. Guedou, J. Uginet and P. Heritier, "Gamma double prime precipitation kinetic in Alloy 718," *Materials Science and Engineering A*, vol. 486, pp. 117-122, 2008.

[41] G. Smith and S. Patel, "The role of niobium in wrought precipitation hardened nickel base alloys," in *Superalloys 718, 625,706 and Derivatives 2005*, 2005, pp. 135-154.

[42] Y. Huang and T. Langdon, "The evolution of delta-phase in a superplastic Inconel 718 alloy," *Journal of Materials Science*, vol. 42, pp. 421-247, 2007.

[43] N. Saunders, M. Fahrmann and C. Small, "The application of CALPHAD calculations to Ni-based superalloys," in *Superalloys 2000*, Warrendale, 2000.

[44] P. Milella, *Fatigue and corrosion in metals*.: Springer, 2013.

[45] R. Ambriz and D. Jaramillo, "Chapter 2: Mechanical behavior of precipitation hardened aluminum alloys welds," in *Light metal alloys applications*, W. Monteiro, Ed.: INTECH, 2014, ttp://www.intechopen.com/books/export/citation/EndNote/light-metal-alloys-applications/mechanical-behavior-of-precipitation-hardened-aluminum-alloys-welds.

[46] A. Vairis and M. Frost, "High frequency linear friction welding of a titanium alloy," *Wear*, vol. 217, pp. 117-131, 1998.

[47] A. Vairis and M. Frost, "On the extrusion stage of linear friction welding of Ti-6Al-4V," *Materials Science and Engineering A*, vol. 271, pp. 477-484, 1999.

[48] K. Vishwakarma, N. Richards, and M. Chaturvedi, "Microstructural analysis of fusion and heat affected zones in electron beam welded ALLVAC 718Plus superalloy," *Materials Science and Engineering A*, vol. 480, pp. 517-528, 2008.

[49] O. Ojo, N. Richards and M. Chaturvedi, "Contribution of constitutional liquation of

gamma prime precipitate to weld HAZ cracking of cast Inconel 738 superalloy," *Scripta Materialia*, vol. 50, pp. 641-646, 2004.

[50] O. Ojo and M. Chaturvedi, "On the role of liquated gamma prime precipitates in weld heat affected zone microfissuring of a nickel based superalloy," *Material Science and Engineering A*, vol. 403, no. 1-2, pp. 77-86, 2005.

[51] S. Ernst, W. Baeslack III and J. Lippold, "Weldability of high-strength low expanison superalloys," *Welding Journal, Research Supplement*, pp. 418-430, 1989.

[52] B. Radhakrishnan and R. Thompson, "A phase diagram approach to study liquation cracking in Alloy 718," *Metallurgical Transactions A*, vol. 22, no. 4, pp. 887-902, 1991.

[53] R. Thompson, B. Radhakrishnan and D. Mayo, "Grain boundary chemistry contributions to intergranular hot cracking," *Journal de Physique Colloques*, vol. 49, no. C5, pp. C5-471-C5-479, 1988.

[54] X. Huang, M. Chaturvedi, N. Richards and J. Jackman, "The effect of grain boundary segregation of boron in cast alloy 718 on HAZ microfissuring - A SIMS analysis," *Acta Materialia*, vol. 45, no. 8, pp. 3095-3107, 1997.

[55] R. Thompson, D. Mayo and B. Radhakrishnan, "The relationship between carbon content microstructure and intergranular liquation cracking in cast nickel Alloy 718," *Matallurgical Transaction A*, vol. 22A, pp. 557-567, 1991.

[56] W. Miller and G. Chadwick, "On the magnitude of the solid/liquid interfacial energy of pure metals and its relation to grain boundary melting," *Acta Metallurgica*, vol. 15, no. 4, pp. 607-614, 1967.

[57] J. Pepe and W. Savage, "Effects of constitutional liquation in 18-Ni maraging steel weldments," *Welding Journal Research Supplement*, pp. 411s-422s, September 1967.

[58] J. Pepe and W. Savage, "The weld heat affected zone of the 18-Ni maraging steels," *Welding Journal, Reserach Supplement* , pp. 545s-553s, December 1970.

[59] R. Thompson, J. Cassimus, D. Mayo and J. Dobbs, "The relationship between grain size and microfissuring in Alloy 718," *Welding Journal Supplement*, pp. 91s-96s, April 1985.

[60] M. Soucail and Y. Bienvenu, "Dissolution of the gamma prime phase in a nickel base superalloy at equilibrium and under rapid heating," *Materials Science and Engineering A*, vol. 220, pp. 215-222, 1996.

[61] D. Ping, Y. Gu, C. Cui and H. Harada, "Grain boundary segregation in a Ni-Fe-based (Alloy 718) superalloy," *Materials Science and Engineering A*, vol. 456, pp. 99-102, 2007.

[62] J. Hooijmans and J. Lippold, "Effect of multiple postweld heat treatment on the weldability of Alloy 718," *[1] J. W. Hooijmans, J. C. Lippold, and W. Lin, "Effect of Multiple Postweld Heat Treatment on the Weldability of Alloy 718," Superalloys 718, 625, 706 Var. Derrivatives.*, pp. 721-730, 1997.

[63] D. Harries and A. Marwick, "Non-equilibrium segregation in metals and alloys," *Philosophical Transactions of the Royal Society of London. Series A, Mathematical and Physical Sciences*, vol. 295, no. 1413, pp. 197-207, 1980.

[64] F. Humphreys and M. Hatherly, *Recrystallization and related annealing phenomena*.:

Elsevier, 2004.

[65] Y. Wang, W. Shao, L. Zhen and X. Zhang, "Microstructure evolution during dynamic recrystallization of hot deformed superalloy 718," *Materials Science and Engineering A*, vol. 486, pp. 321-332, 2008.

[66] M. Azarbarmas, M. Aghaie-Khafri, J. Cabrera and J. Calvo, "Dynamic recrystallization mechanisms and twinning evolution during hot deformation of Inconel 718," *Materials Science and Engineering A*, vol. 678, pp. 137-152, 2016.

[67] D. Dye, S. Roberts, P. Withers and R. Reed, "The determination of the residual strains and stresses in a tungsten inert gas welded sheet of IN718 superalloy using neutron diffraction," *Journal of Strain Analysis for Engineering Design*, vol. 35, no. 4, pp. 247-259, 2000.

[68] U. Cihak, M. Stockinger, P. Staron, J. Tockner and H. Clemens, "Characterization of residual stresses in compressor discs for aeroengines: Neutron diffraction and finite element simulation," *Superalloys 718, 625, 706 and Derivatives*, pp. 517-526, 2005.

[69] P. Withers, "Mapping residual and internal stress in materials by neutron diffraction," *Physique* , vol. 8, pp. 806-820, 2007.

[70] P. Withers and H. Bhadeshia, "Residual Stress Part 1: Measurement techniques," *Materials Science and Technology*, vol. 17, pp. 355-365, 2001.

[71] G. Schajer, *Practical residual stress measurement methods*.: Wiley, 2013.

[72] R. Pynn, "Neutron scattering A primer," Los Alamos Neutron Science Center, 1990.

[73] D. Williams and C. Barry Carter, *Transmission Electron Microscopy*, 2nd ed.: Springer, 2009.

[74] W. Callister Jr., *Materials science and engineering an introduction*, 7th ed.: Wiley, 2007.

[75] C. Weidenthaler, "Pitfalls in the characterization of nanoporous and nanosized materials," in *Nanoscale*.: The Royal Society of Chemistry, 2011, vol. 3, pp. 792-810.

[76] B. Cullity, *Elements of x-ray diffraction*.: Addison-Wesley Publishing Company INC., 1956.

[77] B. He, *Two-dimensional x-ray diffraction*.: John Wiley & Sons, INC., 2009.

[78] ASM International, *ASM metals handbook - materials characterization*.: ASM International, 1992.

[79] Rolled Alloys Inc., "Certified Materials Test Report," 2014.

[80] P. Wanjara and M. Jahazi, "Linear friction welding of Ti-6Al-4V: Processing, microstructure and mechanical property inter-relationships," *Metallurgical and Materials Transactions A*, vol. 36A, pp. 2149-2164, 2005.

[81] M. Smith, L. Bichler, J. Gholipour and P. Wanjara, "Mechanical properties and microstructural evolution of in-service Inconel 718 superalloy repaired by linear friction welding," *The International Journal of Advanced Manufacturing Technology*, pp. 1-16, 2016.

[82] FLIR, ResearchIR Max Software - How To Manual, 2012.

[83] ASTM, Standard test methods for Knoop and Vickers hardness of materials, 2011.

[84] ASTM, Standard test methods fo tension testing of metallic materials (Metric), 2004.

[85] R. Rogge, T. Holden and J. Root, "Standard diffractiometer set-up procedure for applied neutron diffraction for industry experiments," Atomic Energy of Canada Ltd. (AECL), RC-1652/ANDI-101,.

[86] M. Smith, J. -B. Levesque, L. Bichler, D. Sediako, J. Gholipour and P. Wanjara, "Residual stress analysis in linear friction welded in-service Inconel 718 superalloy via neutron diffraction and contour method approaches," *Material Science & Engineering A*, vol. 691, pp. 168-179, March 2017.

[87] ASTM, Standard guide for preparation of metallographic specimens, 2001.

[88] ASTM, Standard practice for microetching metals and alloys, 1999.

[89] J. Radavich, "Electron Metallography of Alloy 718," *Superalloys 718, 625, 706 and Various Derivatives*, pp. 17-26, 1997.

[90] ASTM, Standard test methods for determining average grain size, 1996.

[91] ASTM, Standard test method for determining volume fraction by systematic manual point count, 2002.

[92] Y. Zhang, Z. Li, P. Nie and Y. Wu, "Carbide and nitride precipitation during laser cladding of Inconel 718 alloy coatings," *Optics and Laser Technology*, vol. 52, pp. 30-36, 2013.

[93] R. Vincent, "Precipitation around welds in the nickel base superalloy Inconel 718," *Elements*, vol. 33, no. 7, pp. 1205-1216, 1985.

[94] W. Liu, M. Yao, Z. Chen and S. Wang, "Niobium segregation in Inconel 718," *Journal of Materials Science*, vol. 34, pp. 2583-2586, 1999.

[95] M. Smith, L. Bichler, S. Yannacopoulos, J. Gholipour and P. Wanjara, "Characterization of in-service and virgin Inconel 718 superallloy," in *Confrence of Metallurgists*, Vancouver, 2014.

[96] S. Azadian, L. Wei and R. Warren, "Delta phase precipitation in Inconel 718," *Materials Characterization* , vol. 53, pp. 7-16, 2004.

[97] C. Kuo, Y. Yang, H. Bor, C. Wei and C. Tai, "Aging effects on the microstructure and creep behavior of Inconel 718 superalloy," *Materials Science and Engineering A*, vol. 510-511, pp. 289-294, 2009.

[98] J. Brooks and P. Bridges, "Metallurgical stability of Inconel alloy 718," *Superalloys 1988*, pp. 33-42, 1988.

[99] A. Chamanfar, M. Jahazi, J. Gholipour, P. Wanjara and S. Yue, "Analysis of integrity and microstructure of linear friction welded WASPALOY," *Materials Characterization* , vol. 104, pp. 149-161, 2015.

[100] G. Knorovsky, M. Cieslak, T. Headley, A. Romig and W. Hammetter, "Inconel 718: A solidification diagram," *Metallurgical Transactions A*, vol. 20A, pp. 2149-2158, 1989.

[101] G. Maniar, J. Bridge, H. James, Jr. and G. Heydt, "Correlation of gamma-gamma prime mismatch and strengthening in Ni/Fe-Ni base allys contanining aluminum and titanium as hardeners," *Metallurgical Transactions*, vol. 1, pp. 31-42, 1970.

[102] C. Slama and M. Abdellaoui, "Structural characterization of the aged Inconel 718," *Journal of Alloys and Compounds*, vol. 306, pp. 277-284, 2000.

[103] M. Smith, L. Bichler, D. Sediako, J. Gholipour and P. Wanjara, "Measurement of

residual stresses in linear friction welded in-service Inconel 718 superalloy," in *Thermec 2016*, Graz, pp. 1800-1806.

[104] J. Santisteban, A. Steuwer, L. Edwards, P. Withers and M. Fitzpatrick, "Mapping of unstressed lattice parameters using pulsed neutron transmission diffraction," *Applied Crystallography*, vol. 35, pp. 497-504, 2002.

[105] D. Mukherji, R. Gilles, B. Barbier, D. Genovese, B. Hasse, P. Strunz, T. Wroblewski, H. Fuess and J. Rosler, "Lattice misfit measurement in Inconel 706 containing coherent gamma prime and gamma double prime precipitates," *Scripta Materialia*, vol. 48, pp. 333-339, 2003.

[106] K. Kusabiraki, S. Ikeuchi and T. Ooka, "Morphology and lattice constants of gamma double prime precipitates in a Ni-18Cr-16Fe-5Nb-3Mo Alloy," *Materials Transactions*, vol. 37, no. 5, pp. 1050-1055, 1996.

[107] A. Niang, J. Huez, J. Lacaze and B. Viguier, "Characterizing precipitation defects in nickel based 718 alloy," *Materials Science Forum*, vol. 636-637, pp. 517-522, 2010.

Appendices

Appendix A: Composite EBSD Map of the V-V & V-IS As-Welded Samples

See attached data disk

Appendix B: Composite EBSD Map of the V-V & V-IS PWHT Samples

See attached data disk

Appendix C: SEM Map Across the V-V & V-IS As-Welded Samples

See attached data disk

Appendix D: PWHT Neutron Diffraction Multi-peak Analysis

The following appendix provides an example calculation that was performed in order to characterize the double peak present in the V material of the PWHT samples.

From the literature [*106*] [*107*] the maximum and minimum lattice parameters (a) for the γ, γ' and γ'' phases were recorded. For each of the maximum and minimum lattice parameters, the theoretical diffraction angle (2θ) was calculated.

Example:

The minimum lattice parameter for γ (matrix) phase was given as 3.5550 Å [*107*].

For a FCC material, the interplanar spacing (d) for a given lattice parameter and a plane with miller indices (hkl) is given as:

$$d = \frac{a}{\sqrt{h^2+k^2+l^2}} \tag{A.1}$$

Therefore, using Equation A.1 and the minimum lattice parameter for the γ (matrix) phase and the {311} plane:

$$d = \frac{3.5550E-10}{\sqrt{3^2+1^2+1^2}} \tag{A.2}$$

$$d = 1.07187287\text{E-}10 \text{ m} \quad \text{(A.3)}$$

For the particular PWHT neutron diffraction experiment, the wavelength (λ) used was 1.5704 Å. Based on Bragg's Law (Equation 5), the theoretical diffraction angle (2θ) can be calculated as follows:

With d = 1.072 Å and a λ = 1.5704 Å, Bragg's law can be re-written as:

$$\theta = \sin^{-1}\left(\frac{\lambda}{2d}\right) \quad \text{(A.4)}$$

$$\theta = \sin^{-1}\left(\frac{1.5704\text{E}-10}{2(1.072E-10)}\right) \quad \text{(A.5)}$$

$$\theta = 47.1005° \quad \text{(A.6)}$$

Therefore, $2\theta = \sim 94.20°$ (A.7)

This was repeated for the minimum and maximum lattice parameters of each phase. The theoretical diffraction angles were then compared to the double diffraction peaks to see which phase was likely contributing to the diffraction patterns. It was found that the theoretical diffraction peaks (2θ) for the γ, γ' and γ'' phases were between 92.59° – 94.20°, 92.14° – 92.94° and 86.83° – 88.39°, respectively. The δ phase theoretical diffraction angle was found to be around 60°, which was sufficiently far away from the actual experimental diffraction data to not be considered further.

It was observed that the γ and γ' phases best corresponded to the observed diffraction peaks in the actual diffraction data. Once the phases of interest were determined, the lattice parameters from the actual experimental data moving across the V material was found at each location as follows:

The diffraction peak angle was used for each of the double peaks. For example, in Figure 84 (for x = 0.5 mm) Peak I 2θ = 92.56° and Peak II 2θ = 91.97°, corresponding to θ = 46.28° and 45.99°, respectively. Re-writing Bragg's law to solve for the interplanar spacing (d):

$$d = \frac{\lambda}{2\sin\theta} \tag{A.8}$$

$$d = \frac{1.5704\text{E}{-10}}{2\sin(46.28)} \tag{A.9}$$

$$d_I = 1.08644226\text{E-}10 \text{ m} \tag{A.10}$$

and similarly for Peak II: $d_{II} = 1.09183252\text{E-}10$ m (A.11)

Using Equation (A.1) and solving for the lattice parameter (a), we get:

$$a_I = 3.60332132\text{E-}10 \text{ m} \tag{A.11}$$

and similarly for Peak II: $a_{II} = 3.62119881\text{E-}10$ m (A.12)

All the lattice parameters across the V PWHT material were calculated in this way for the γ and γ' phases and plotted along with the theoretical maximum and minimum lattice

parameters (and their corresponding diffraction peak angles (2θ)) from the literature, as shown in Figure 85.